Spectroscopic characterization of local valence change processes in resistively switching complex oxides

Christoph Bäumer

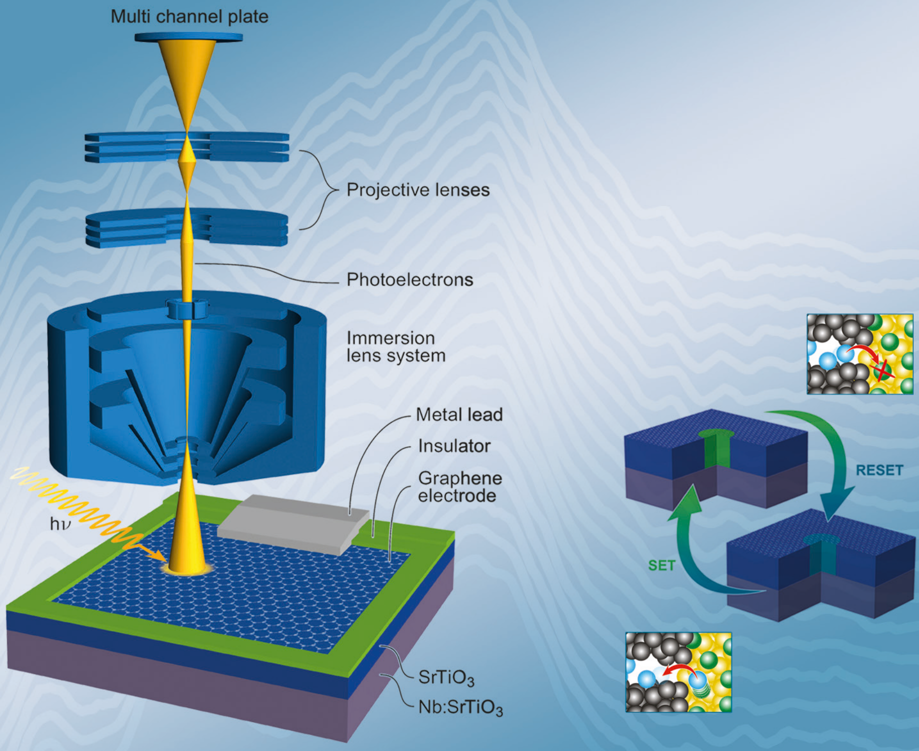

Schlüsseltechnologien / Key Technologies
Band / Volume 150
ISBN 978-3-95806-246-7

JÜLICH
FORSCHUNGSZENTRUM

Schriften des Forschungszentrums Jülich
Reihe Schlüsseltechnologien / Key Technologies Band / Volume 150

Forschungszentrum Jülich GmbH
Peter Grünberg Institute (PGI)
Electronic Materials (PGI-7)

Spectroscopic characterization of local valence change processes in resistively switching complex oxides

Christoph Bäumer

Schriften des Forschungszentrums Jülich
Reihe Schlüsseltechnologien / Key Technologies Band / Volume 150

ISSN 1866-1807 ISBN 978-3-95806-246-7

Bibliographic information published by the Deutsche Nationalbibliothek.
The Deutsche Nationalbibliothek lists this publication in the Deutsche
Nationalbibliografie; detailed bibliographic data are available in the
Internet at http://dnb.d-nb.de.

Publisher and Distributor: Forschungszentrum Jülich GmbH
Zentralbibliothek
52425 Jülich
Tel: +49 2461 61-5368
Fax: +49 2461 61-6103
Email: zb-publikation@fz-juelich.de
www.fz-juelich.de/zb

Cover Design: Grafische Medien, Forschungszentrum Jülich GmbH

Printer: Grafische Medien, Forschungszentrum Jülich GmbH

Schriften des Forschungszentrums Jülich
Reihe Schlüsseltechnologien / Key Technologies, Band / Volume 150

D 82 (Diss. RWTH Aachen University, 2016)

ISSN 1866-1807
ISBN 978-3-95806-246-7

Abstract

An increasingly interconnected world creates a high demand for high-density and low-cost data storage. Redox-based memristive devices, which allow switching between high and low electrical resistances through the application of voltages, are highly attractive candidates for next-generation non-volatile memory. But their control and rational design is complicated by poorly understood switching and failure mechanisms. The complex nanoscale redox processes that are suspected to drive so-called resistive switching in these devices remain inadequately characterized. Especially, quantitative information about these processes, which is essential for further advances in the educated design, has been experimentally inaccessible so far.

Therefore, spectroscopic tools with high spatial resolution are employed in this work to elucidate both switching and failure mechanism of memristive devices based on the model material $SrTiO_3$. After thorough electrical characterization, two alternative photoelectron emission microscopy approaches are used. As photoemission is a surface sensitive process, the top electrodes of the devices are removed before investigation in the first approach. In the second step, thin graphene electrodes are employed, enabling *in operando* characterization. In combination with cross sectional, *in operando* transmission electron microscopy and spectroscopy, a clear evidence of a reversible, localized redox reaction is identified. In the low resistance state, a nanoscale filament in the $SrTiO_3$ is oxygen-deficient, while it is nearly stoichiometric in the high resistance state, resulting in a valence change between Ti^{3+} and Ti^{4+}. The carrier concentration modulation resulting from this valence change is quantified through comparison with calibration spectra. A carrier concentration change by a factor of two causes two orders of magnitude change in device resistance through a modulation of the effective Schottky barrier at the electrode/oxide interface.

The microscopic origin of the polarity of the resistance hysteresis in these devices has long been debated, as it cannot be explained by the typically involved purely internal redistribution of oxygen vacancies. The spectroscopic results of this work reveal that instead, oxygen evolution and reincorporation reactions at the electrode/oxide interface are responsible for the valence change in the $SrTiO_3$.

Regarding the failure mechanism, it is found that fast reoxidation frequently results in retention failure in $SrTiO_3$ devices, which can be inhibited by incidental, local phase separations. Mimicking this phase separation by intentionally introducing retention-stabilization layers with slow oxygen transport is therefore derived as a design rule for retention-failure-resistant devices.

Kurzfassung

Eine zunehmend vernetzte Welt bedingt eine immer stärkere Nachfrage nach hochintegrierter und kostengünstiger Datenspeicherung. Redox-basierte memristive Bauteile, die das Schalten zwischen hohem und niedrigem elektrischen Widerstand durch das Anlegen einer Spannung ermöglichen, sind hochattraktive Kandidaten für nichtflüchtigen Speicher der nächsten Generation. Die Herstellung von Bauelementen mit maßgeschneiderten Eigenschaften wird dadurch erschwert, dass die Schalt- und Ausfallmechanismen nur unzulänglich verstanden sind. Es wird vermutet, dass komplexe, nanoskalige Redoxprozesse das sogenannte resistive Schalten in diesen Bauteilen ermöglicht. Doch diese Prozesse sind bisher unzureichend charakterisiert worden. Insbesondere waren quantitative Informationen experimentell bis dato noch unzugänglich, obwohl diese für ein auf physikalischem Verständnis beruhenden Design essentiell sind.

Deshalb werden in dieser Arbeit spektroskopische Messungen mit hoher Ortsauflösung durchgeführt um sowohl den Schaltmechanismus als auch den Ausfallmechanismus in Zellen aus dem Modellmaterial $SrTiO_3$ aufzuklären. Nach eingehender elektrischer Charakterisierung werden zwei alternative Herangehensweisen mittels Photoemissionselektronenmikroskopie genutzt. Weil die Photoemission oberflächensensitiv ist, werden im ersten Ansatz die Topelektroden entfernt. Im zweiten Schritt werden dünne Graphenelektroden genutzt, um die Zellen *in operando* untersuchen zu können. In Kombination mit *in operando* Transmissionselektronenmikroskopie und -spektroskopie des Probenquerschnitts wird eine lokale, reversible Redoxreaktion eindeutig nachgewiesen. Im niederohmigen Zustand ist ein nanoskaliges Filament innerhalb des $SrTiO_3$ sauerstoffdefizitär, während es im hochohmigen Zustand annähernd stöchiometrisch ist. Das führt zu einem Valenzwechsel zwischen Ti^{3+} und Ti^{4+}. Die daraus resultierende Ladungsträgerkonzentrationsänderung wird durch den Vergleich mit Kalibrationsspektren quantifiziert. Eine Änderung um einen Faktor zwei verursacht durch Veränderung der effektiven Schottkybarriere an der Elektroden-Oxid-Grenzfläche eine Widerstandsänderung um zwei Größenordnungen.

Der mikroskopische Ursprung der Polarität der Widerstandshysterese dieser Zellen wird seit langem kontrovers diskutiert, weil sie nicht mit dem üblichen Modell der rein internen Sauerstoffleerstellenumverteilung erklärt werden kann. Die spektroskopischen Ergebnisse dieser Arbeit zeigen, dass stattdessen Ausbau und Wiedereinbau von Sauerstoff an der Elektroden-Oxid-Grenzfläche den Valenzwechsel im $SrTiO_3$ verursachen.

Bezüglich des Ausfallmechanismus wird festgestellt, dass Reoxidation häufig zu einem Verlust der Langzeitstabilität führt. Diese kann durch zufällig auftretende lokale Phasenseparation verhindert werden. Darauf basierend wird die Design-Regel entwickelt, dass durch bewusste Einführung einer Stabilisierungsschicht mit langsamen Sauerstofftransporteigenschaften die beobachtete Phasenseparation nachgeahmt werden kann, was zu ausfallsichereren Bauteilen führt.

Contents

1 Introduction

In order to meet the high demand for the high-density and low-cost future data storage and logic circuits that are required for an ever increasingly interconnected world, novel devices and new modalities of operation are required. These devices and modalities will ultimately be enabled by the nanoscale design of materials and inventive means of manipulating them [1]. So-called "resistive switching" or "memristive phenomena" are intensively investigated due to the potential use in future non-volatile memory or as novel neuromorphic circuits, even allowing for a local synergy of logic and memory [2–7]. In these devices the application of voltages allows switching between a low resistance state (LRS) and a high resistance state (HRS), or even intermediate states.

Excellent device performance that combines fast switching, long retention (the time for which information can be stored in memory devices) and high-density stacking has already been demonstrated for devices based on transition metal oxide films sandwiched between two metal electrodes – one of the most promising candidate systems for memristive devices. But research and development are still mainly based on purely empirical strategies, rather than on predictive concepts [6], hampering the technological exploitation. At the heart of this roadblock lies an inadequate understanding of the nanoscale operation mechanisms. It is generally agreed upon in the scientific community that resistive switching can be attributed to the motion of mobile donor-type defects, such as oxygen vacancies, and a corresponding valence change in the transition metal cation [2, 4, 6]. Simulations have shown that even small modulations of the oxygen vacancy concentration can induce significant changes of the charge-carrier transport and can therefore account for the resistance change [8–12].

The exact mechanism and especially the quantitative details of the related nanoscale redox-processes, however, are still inadequately characterized experimentally due to the absence of analysis methods that can be used to provide information about electronic structure and chemical composition with sufficient spatial resolution and sensitivity to detect small variations. This roadblock can in principle be overcome using spectromicroscopic tools or transmission electron microscopy (TEM) techniques. For TEM, it is very challenging to place the active region of a device within the thickness of a TEM specimen (typically 100 nm or less). Therefore, direct evidence of the suspected redox processes is difficult to obtain using TEM. On the other hand, a variety of spectromicroscopic studies have identified the formation of an oxygen vacancy rich filament during the first biasing step, which is a first indication of the suspected mechanism [13–17]. But in many cases, these studies have been limited to non-functioning, post-mortem devices (for example after top electrode removal [17]). This approach, of course, makes the examination of the same device in both resistance states inaccessible. For the desired elucidation and quantitative description of the switching process between LRS and HRS, however, it is mandatory to image and characterize the active region in the same device in both resistance states.

Non-destructive, *in operando* spectroscopy techniques using hard X-rays [18] or transmission X-ray microscopy [19,20] have provided insightful information about the role of Joule heating and failure mechanisms. But they have failed to supply spatially resolved, quantitative spectroscopic differences between different resistance states. Therefore, a combination of the successful but previously destructive photoemission electron microscopy (PEEM) studies, which allow for spectroscopic evaluation with high spatial resolution and interface- or surface sensitivity, with a non-destructive *in operando* approach is highly desirable. Similarly, *in operando* TEM, a sophisticated technique under development, which allows application of biases to a TEM specimen, may enable the desired high-resolution mapping of chemical and electronic changes during switching.

Accordingly, the goal of this thesis is the development and utilization of *in operando* approaches using PEEM and TEM to identify and quantify the mechanisms underlying resistive switching. The main challenge in the implementation of *in operando* PEEM characterization is to overcome the high surface sensitivity of photoemission, which limits the probing depth to few nanometers and practically prevents access to the active region covered by top electrodes. Graphene as a highly conductive and photoelectron-transparent material of atomic thickness may circumvent this limitation, when used as top electrode. Graphene electrodes have already been integrated successfully in memristive devices [21–23] and will be used here for the spectromicroscopic investigation of $SrTiO_3$-based memristive devices. $SrTiO_3$ constitutes a resistive switching model material because of its well understood defect chemistry and feasible fabrication as an epitaxial thin film, i.e., a grain boundary-free platform with a low defect density. Moreover, $SrTiO_3$ exhibits well-characterized spectroscopic fingerprints, facilitating the interpretation of the spectroscopic changes during switching.

After reviewing the fundamentals of the model material $SrTiO_3$ and the existing knowledge about resistive switching in $SrTiO_3$ in chapter 2, the sample preparation and analysis techniques will be briefly introduced in chapter 3. Chapter 4 presents an evaluation and calibration of the available spectroscopic signatures of $SrTiO_3$, resulting in a calibration curve for the determination of carrier densities in $SrTiO_3$ based on the O K X-ray absorption edge. In addition, a detailed spectroscopic characterization of as-grown $SrTiO_3$ is performed as a foundation for the following analysis of resistive switching in these films.

Resistive switching in $SrTiO_3$-based devices of different architectures will be presented in chapter 5. The effect of electrode material, film thickness, the surrounding atmosphere and temperature was investigated. A special focus lies on the retention time of the devices – one of the most important parameters for memory devices.

Chapter 6 will show how the previously developed PEEM analysis of post-mortem devices can be applied to derive a first spectromicroscopic fingerprint of the expected changes. It was found that in addition to oxygen-migration induced valence changes, cation-migration can lead to structural changes during memristive operation. The occurrence of such structural changes is closely connected with the retention time.

Chapter 7 contains the central experimental achievement of this thesis, the *in operando* characterization of memristive devices using PEEM with graphene electrodes and cross-sectional TEM analysis of functioning devices. The combination of both approaches offers a three-dimensional perspective. It was found that a localized valence change is indeed the origin of the switching effects and the amount of the valence-change-induced carrier density modulations was quantified. These results show that *in operando* characterization is indeed a powerful tool to characterize nanoscale redox phenomena, yielding an understanding of the switching effect.

Based on these insights, the mechanism driving resistive switching in $SrTiO_3$-based devices will be derived in chapter 8. Using the information from chapters 5 and 7, it will be deduced that the resistance change in these devices is not based on a purely internal redistribution of oxygen vacancies in the $SrTiO_3$ film, which is the typically-invoked scenario. Instead, oxygen species are removed from the $SrTiO_3$ lattice when switching to the LRS and reincorporated into the $SrTiO_3$ when switching to the HRS.

This understanding helps to explain the connection between the structural changes and the retention times described in chapter 6. It will be shown that the observed structural changes inhibit the reincorporation of oxygen into the $SrTiO_3$ layer, resulting in longer retention of the LRS state. A design rule for the development of retention-failure-resistant devices will also be derived in chapter 8.

The thesis will be completed by concluding remarks about resistive switching and data retention in $SrTiO_3$-based devices, a brief consideration of the impact of these insights for resistive switching in transition metal oxides in general and an outlook in chapter 9.

2 Background

2.1 Fundamentals of $SrTiO_3$

Crystal structure

At room temperature, undoped $SrTiO_3$ is an ionic crystal with a perovskite structure with a lattice constant of 3.905 Å and a cubic crystallographic point group $Pm\bar{3}m$ consisting of layers of SrO and TiO_2 stacked in the [001] direction [24]. Cornersharing TiO_6 octahedra form a framework with anticuboctahedrally coordinated Sr ions at the interstices.

Electronic structure

Undoped $SrTiO_3$ is an insulator with an experimentally determined band-gap of 3.2 eV [25]. In a strictly ionic picture, the valence electrons of the Ti 3d, Ti 4s and Sr 5s orbitals are fully transferred into the O 2p orbital and the nominal oxidation states of the ions are Ti^{4+}, Sr^{2+} and O^{2-}. Accordingly, O 2p states form the valence band and the conduction band is formed by empty Ti 3d and Sr 5s states. However, especially the Ti-O bond reveals a significantly covalent contribution. Thus the electronic structure should rather be described by hybridized bands with mixed character [26]. The site projected density of states is shown in Fig. 2.1. While it can be seen that the main contribution to the valence band stems from O states and the bottom of the conduction band is mainly formed by Ti states, a significant admixture of metal states in the valence band and especially of O states at the bottom of the conduction band is apparent.

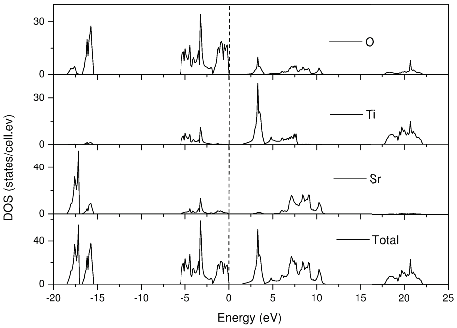

Figure 2.1: Calculated total and partial density of states of undoped $SrTiO_3$. Reproduced from ref. 27.

Defect chemistry and the effect of dopants

For small defect concentrations the interplay of the intrinsic defects with the surrounding atmosphere as well as extrinsic doping in $SrTiO_3$ can be described by defect chemistry [28]. Using the Kröger-Vink notation [29], crystallographic defects can be described by their electronic charge with respect to the perfect lattice. Each species on its regular lattice site are written as $O_O^\times$, $Sr_{Sr}^\times$ or $Ti_{Ti}^\times$, where indices indicate the regular species found on this lattice site and $^\times$ indicates neutral charge compared to the lattice. In the same way, substitutional dopants such as Nb^{5+} substituted for Ti^{4+} is written as $Nb_{Ti}^\bullet$, where $^\bullet$ indicates the positive charge of the defect with respect to the perfect lattice. In the same notation, oxygen vacancies and cation vacancies can be written as $V_O^{\bullet\bullet}$ and $V_M^{\prime\prime}$ with $^\prime$ indicating a negative charge.

Within the temperature regime relevant for this work (typically below 1100 K) the cation sublattice of $SrTiO_3$ is typically considered to be inactive [28]. In contrast, it will be discussed that Joule heating during memristive device operation may lead to extreme temperatures exceeding 1200 K in some cases, as will be discussed in chapter 6. In these cases, the cation sublattice may become active. As the formation energy for $V_{Ti}^{\prime\prime\prime\prime}$ is very high, cation vacancies are mostly formed on the Sr sublattice, leading to the following reaction:

$$Sr_{Sr}^\times + O_O^\times \longleftrightarrow V_{Sr}^{\prime\prime} + V_O^{\bullet\bullet} + (SrO)_{SP}. \tag{2.1}$$

The generation of a V_{Sr}''-$V_O^{\bullet\bullet}$ pair is thus accompanied by the formation of a $(SrO)_{SP}$ secondary phase either at the surface of the $SrTiO_3$ crystal [30,31], or in a Ruddelsden-Popper-like phase within the crystal lattice [32].

While this phase separation is only active at very high temperatures, the creation of oxygen vacancies *via* exchange of the bare $SrTiO_3$ surface with the surrounding atmosphere is already activated at temperatures above 700 K and can even be activated at significantly lower temperatures in the presence of catalytic metals like Pt [28]:

$$\mathrm{O_O^{\times}} \longleftrightarrow \frac{1}{2}\,\mathrm{O_2} + \mathrm{V_O^{\bullet\bullet}} + 2\,\mathrm{e}'. \tag{2.2}$$

From left to right, equation 2.2 can be understood as an oxygen evolution reaction. From right to left, it represents an oxygen incorporation reaction. According to equation 2.2, oxygen vacancies act as donors in $SrTiO_3$. The electrons which are generated through the generation of oxygen vacancies are transferred to the conduction band. Upon doping with oxygen vacancies, the Fermi energy is shifted from a position within the band gap closer to or even into the conduction band as shown in Fig. 2.2. As the conduction band edge is mainly composed of Ti 3d states as discussed above, the doping effect may be understood in an ionic picture as a valence change between Ti^{4+} and Ti^{3+}:

$$2\,\mathrm{Ti^{4+}} + \mathrm{O_O^{\times}} \longleftrightarrow \frac{1}{2}\,\mathrm{O_2} + 2\,\mathrm{Ti^{3+}} + \mathrm{V_O^{\bullet\bullet}}. \tag{2.3}$$

The same doping effect can be obtained using Nb doping ($Nb_{Ti}^{\bullet}$). Nb-doping with concentrations exceeding $10^{18}\,\mathrm{cm^{-3}}$ leads to metallic conductivity [24] making Nb-doped $SrTiO_3$ crystals an ideal candidate for a bottom electrode with an ohmic contact to $SrTiO_3$ thin films. Both $V_O^{\bullet\bullet}$ and $Nb_{Ti}^{\bullet}$ are shallow donors, meaning that the donor levels lie close to the conduction band with a difference of less than 0.1 eV. These donor states are easily ionized at room temperature.

While defect chemistry can be used very successfully to describe many experimental findings for bulk $SrTiO_3$ under equilibrium conditions [28], one needs to recognize its limitations. In particular all defect chemical derivations are based on the assumption of a homogeneous crystal with low defect and dopant concentrations as no interaction

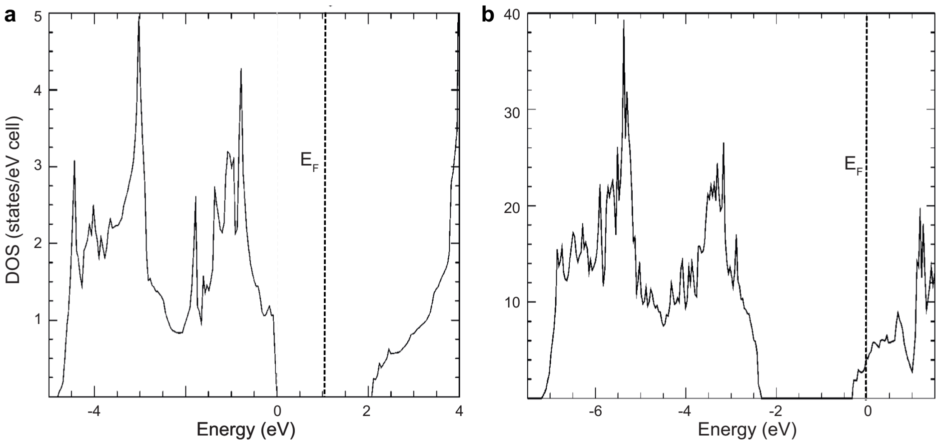

Figure 2.2: Calculated total density of states. (a) Undoped $SrTiO_3$. (b) $SrTiO_3$ with $\approx 4\,\%\,V_O^{\bullet\bullet}$. Modified from ref. 33.

between the defects is included in the defect chemical models. These requirements are not necessarily fulfilled by the pulsed laser deposition (PLD) grown thin films investigated in this work. The strongly kinetically limited growth conditions and the plasma plume chemistry can result in situations far from equilibrium with significant amounts of cation vacancies and even extended defects like Ruddlesden-Popper type faults (as will be shown in chapter 4.2). Therefore, the characteristics of PLD grown thin films can deviate significantly from the behavior predicted by defect chemistry. Nevertheless, the considerations described above are a useful tool to describe the nanoscale chemical processes taking place during resistive switching, as this thesis will demonstrate.

2.2 Electronic transport

The electronic transport properties across noble metal/$SrTiO_3$ interfaces can generally be considered as transport across a Schottky barrier due to the band alignment of a high work function metal with $SrTiO_3$, which can be regarded as a semiconductor with an electron affinity of 4.1 eV (Fig. 2.3a) [34–37]. The electronic transport across a Schottky junction is described in detail in ref. 38. Here, only a brief account of

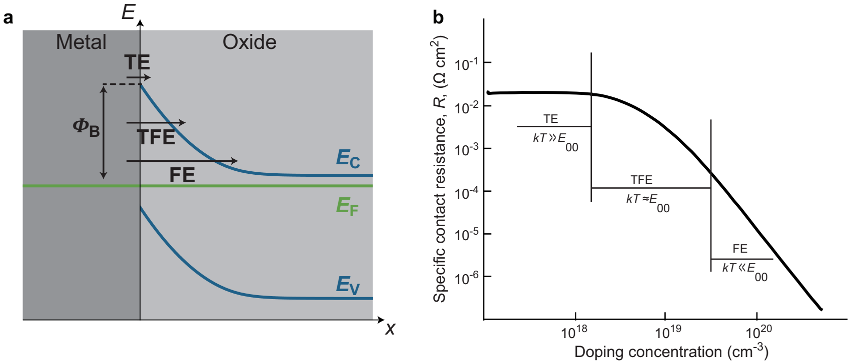

Figure 2.3: Transport across Schottky barriers. (a) Schematic of a Schottky barrier with the Fermi level E_F, the oxide conduction band edge E_C and valence band edge E_V and the resulting Schottky barrier height Φ_B. Different transport characteristics across the barrier are indicated as thermionic emission (TE), thermionic field emission (TFE) and field emission (FE). (b) Specific contact resistance as a function of doping concentration. Modified from ref. 38.

the most relevant transport mechanisms will be provided based on the description in ref. 38.

Thermionic emission

Thermionic or Schottky emission describes the possibility that electrons gain enough energy through thermal activation to overcome the barrier at the metal-semiconductor interface. The resulting current density J_TE is given by

$$J_\mathrm{TE} = A^* T^2 \exp\left[\frac{-q\left(\phi_\mathrm{B} - (\varDelta\phi + V)\right)}{kT}\right] \tag{2.4}$$

with the temperature T, elemental charge q, barrier lowering due to image-force $\varDelta\phi$, supplied bias V, Boltzmann constant k, and the effective Richardson constant

$$A^* = \frac{4\pi q m^* k^2}{h^3} = 120 \frac{m^*}{m_0} \cdot \frac{\mathrm{A}}{\mathrm{cm}^2\,\mathrm{K}^2} \tag{2.5}$$

with the Planck constant h, the electron rest mass m_0 and the effective mass m^*.

Field emission

Electrons with energies lower than the barrier height cannot overcome the energy barrier through thermionic emission. Instead, they may be able to tunnel through the barrier, especially under high electric fields which deform the barrier. This phenomenon is called field emission and is differentiated from direct tunneling where electrons tunnel through the complete barrier width [39]. The field emission current density J_{FE} in the forward and reverse direction (positive or negative bias applied to the high work function (top) electrode, respectively) is given by

$$J_{\mathrm{FE}} \approx \frac{A^{*} T \pi \exp\left[-q\left(\phi_{\mathrm{B}}-V\right)/E_{00}\right]}{c_{1} k \sin\left(\pi c_{1} k T\right)} \qquad \text{(forward)} \qquad (2.6)$$

$$J_{\mathrm{FE}} = A^{*}\left(\frac{E_{00}}{k}\right)^{2}\left(\frac{\phi_{\mathrm{B}}+V}{\phi_{\mathrm{B}}}\right)\exp\left(-\frac{2q\phi_{\mathrm{B}}^{3/2}}{3E_{00}\sqrt{\phi_{\mathrm{B}}+V}}\right) \qquad \text{(reverse)} \qquad (2.7)$$

with

$$E_{00} \equiv \frac{q\hbar}{2}\sqrt{\frac{N}{m^{*}\varepsilon_{s}}} \qquad (2.8)$$

and

$$c_{1} = \frac{1}{2E_{00}}\log\left[\frac{-4\left(\phi_{\mathrm{B}}-V\right)}{-\phi_{\mathrm{B}}}\right] \qquad (2.9)$$

with the donor concentration N (or acceptor concentration in the case of p-type semiconductors), the reduced Planck constant $\hbar$ and the dielectric permittivity ε_s of the semiconductor.

While the shape of an I-V curve may be similar for different conduction mechanisms, the much weaker temperature dependence of field emission compared to thermionic emission has to be noted, i.e., the absence of exponential dependence on temperature.

Equations 2.4 and 2.6/2.7 describe two extreme cases, where thermionic emission (equation 2.4) dominates the transport at high temperatures and low dopant concentrations, i.e., for $kT \gg E_{00}$, while tunneling currents (field emission, equations 2.6/2.7) dominate for $kT \ll E_{00}$. For intermediate temperatures and dopant concentrations ($kT \approx E_{00}$), so-called thermionic-field emission can describe the electronic transport. Thermionic-field emission can be understood as a combination of field emission and thermionic emission. Thermally excited electrons with energies lower than the barrier height can tunnel through the thinner part of the barrier at energies between the conduction band edge of the semiconductor and the Fermi level of the metal.

Therefore, different transport mechanisms dominate the transport for different doping concentrations at a given temperature (Fig. 2.3b). The transport in the extreme case of an ohmic contact between a metal and a degenerately doped semiconductor can in this sense be defined as a tunneling current.

Bulk electronic transport in $SrTiO_3$

For nominally undoped $SrTiO_3$ films, only small carrier concentrations can exist at room temperature due to the rather large band gap, thus limiting the bulk conductivity. Based on the analysis in $SrTiO_3$ capacitors, however, one finds experimentally that significant leakage currents always occur due to residual carriers, for example from oxygen vacancies [40]. In two extreme cases, the resulting bulk conductivity can be described either by band conduction or through so-called Poole-Frenkel emission, which describes transport phenomenologically as thermionic field emission of electrons between isolated trap states.

From a more fundamental perspective, the characteristics of excess electrons in $SrTiO_3$ results from interaction with the lattice through electron-phonon coupling (or electron-electron interaction in the very high carrier regime [41]), as comprehensively reviewed recently by Hao *et al.* [42]. Electron-phonon coupling results in the formation of a polaron, a quasiparticle formed by the excess electron and a polarization cloud of the crystal lattice that follows the electron as it propagates through the crystal [43]. Depending on the spatial extent of the polaronic wave function and associated structural distortions two types of polarons are distinguished, both of which have been reported for $SrTiO_3$ [43–45]: in the small-polaron model the range of the distortion is about one lattice constant, whereas in the large polaron model the wave function spreads over several unit cells. Small polarons form highly localized in-gap states, which might be responsible for the phenomenological Poole-Frenkel emission. Large polarons, on the other hand, preserve band-like transport, but lead to an increased effective electron mass. Using density functional theory, it was suggested that the spatial extent of the polaron may be the result of the carrier density [42].

In summary, the bulk conduction in $SrTiO_3$, which is still an active research area, certainly depends on the details of the defect structure and carrier density. For the purpose of this thesis, it is sufficient to note that the transport of Schottky junctions between high work function metals and $SrTiO_3$ typically appears to be limited by the interface, i.e., the Schottky barrier described above. The transport across this barrier will therefore be used for the qualitative interpretation of $SrTiO_3$-based devices. This is certainly valid for very high carrier concentrations, but the bulk conductivity may play a role at lower concentrations. Quantitative description of current transport in $SrTiO_3$ should therefore take into account both contributions, as shown in ref. 8.

2.3 Resistive switching in $SrTiO_3$

In general, the term resistive switching refers to a reversible change of resistance in metal-insulator-metal (MIM)-structures upon electrical stimulus. The LRS can be interpreted as a logical "1" and the HRS represents the "0" in a binary memory or logic applications.

While many different nanoscale mechanisms can lead to resistive switching in different classes of materials, this thesis focuses on the so-called valence change mechanism, which is the predominant process in transition metal oxides. This mechanism is widely accepted to be a nanoscale redox reaction, induced by oxygen-ion migration [2,4,6,13]. So-called "electroforming" or "forming" steps, which describe the first application of a high bias to the system, enable the following resistive switching. It is suspected that after this treatment, a local accumulation of oxygen vacancies forms a so-called switching filament. The resulting local dopant distribution is suspected to modify the Schottky barrier at the interface with the top electrode and to lead to the LRS. Reset operations with opposite bias recover the HRS by disrupting or re-oxidizing the switching filament. The LRS can be re-obtained through the Set process, the application of the opposite bias compared to the Reset. If the voltages necessary for the forming and Set operation have a similar value, one typically speaks of "soft-forming".

While CMOS-compatible oxides like HfO_2 and Ta_2O_5 are of highest technological relevance for the implementation of memristive devices for logic or memory applications, the prototypical model material for the study of valence-change-driven resistive switching is single-crystalline $SrTiO_3$. Typically, epitaxial $SrTiO_3$ thin films are contacted with a noble metal top electrode, forming a Schottky barrier. Degenerately doped Nb-doped $SrTiO_3$ (Nb:$SrTiO_3$) substrates, which form an ohmic contact, serve as bottom electrodes. $SrTiO_3$ is chosen because of its availability in form of homogeneous, epitaxial thin films without grain boundaries as well as the extensive existing knowledge about defect chemistry, oxygen diffusion and cation diffusion available in literature [46–52]. Another prominent example for such resistive switching materials is the interface between noble metal top electrodes and Nb:$SrTiO_3$ single crystals. In this case, the fundamental mechanism giving rise to the resistance change is under strong debate. In the following, the existing knowledge and suspected mechanisms will be introduced for both model materials.

$SrTiO_3$ thin films

In Fe:$SrTiO_3$ thin film devices, it has been observed that the switching polarity can vary between a so-called eightwise switching, where positive voltages applied to the top electrode enable the Set process, and counter-eightwise switching, where negative voltages applied to the top electrode induce the Set process [53–55]. Both switching polarities can be achieved in the same device through the appropriate selection of switching parameters like the applied voltages and the time these are applied to the device, suggesting that competing mechanisms are at play.

Systematic conductive atomic force microscopy (C-AFM) analysis revealed that even the location of the resistance change varies between the two polarities (Fig. 2.4) [53]. For the counter-eightwise switching, the filament appears to be more spatially localized compared to the eightwise polarity, which gave rise to the terms "filamentary" and "homogeneous" resistive switching, suggesting that eightwise switching would be an area-dependent effect. While this may be true for some materials under some circumstances (such as Pt/Nb:$SrTiO_3$ junctions operated at low current limits, as discussed in

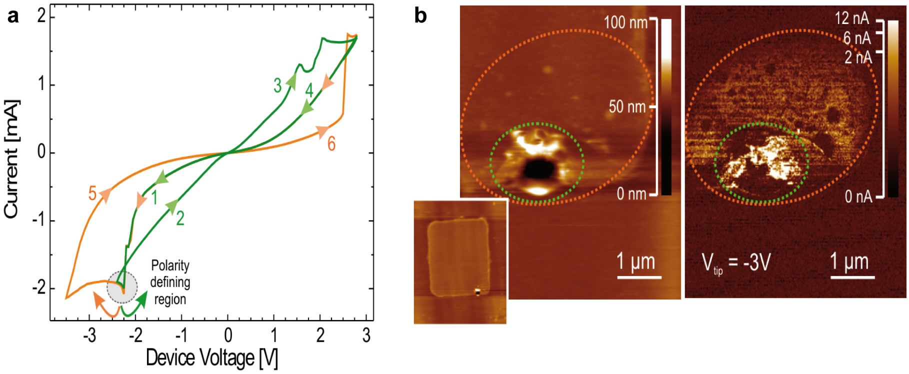

Figure 2.4: Competing switching polarities in Fe:SrTiO$_3$ thin film devices. (a) I-V-characteristic for one device operated at different voltages, resulting in counter-eightwise resistive switching for lower voltages (green curve) and eightwise resistive switching for higher voltages (orange curve), respectively. (b) Conductive AFM topography and current image of a junction after electroforming and top electrode removal. A well conducting crater (green) as well as a medium conducting region around the crater (orange) can be seen. Modified from ref. 53.

chapter 5), eightwise switching is not necessarily area-dependent. Using the terms "filamentary" and "homogeneous" must therefore be avoided.

Interestingly, while counter-eightwise switching in SrTiO$_3$ can be well described qualitatively through the textbook resistive switching model based on the internal redistribution of oxygen vacancies within a switching filament at the Schottky-type noble metal/SrTiO$_3$ interface [2, 4, 8, 9, 56–58], the spatial extent and the redox process itself which could give rise to eightwise switching are still beyond comprehension. While both switching polarities may be observed in the same device, eightwise switching is generally dominating the switching behavior observed in devices with low defect density and small film thickness [54, 59]. All devices in this thesis exhibit only eightwise switching.

For the internal redistribution of oxygen vacancies within a switching filament (counter-eightwise switching), the suspected microscopic mechanism is described as the voltage- and temperature-driven modification of a switching filament as depicted in Fig. 2.5. In the HRS (Fig. 2.5A), the filament consists of a so-called plug, which is a highly n-conductive region of the oxide film and a potential barrier (called disc) between the top electrode and the plug. Upon application of a negative V_{Set}, oxygen vacancies

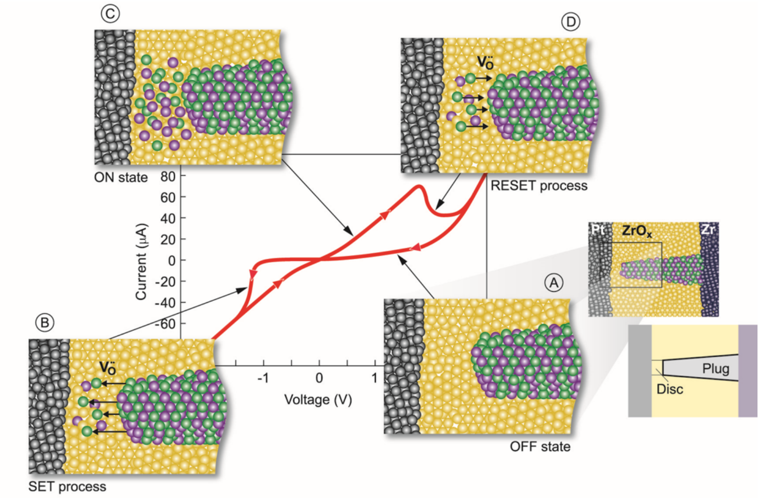

Figure 2.5: Schematic of the proposed switching mechanism for counter-eightwise switching. The I-V-curve can be understood in terms of $V_O^{\bullet\bullet}$ drift and diffusion within a switching filament. $V_O^{\bullet\bullet}$ are depicted in green. Neighboring transition metal ions undergo a valence change and are depicted in violet in a fully oxidized matrix (yellow). The schematic is drawn for a Pt/ZrO/Zr MIM-structure, but it is representative for all valence change resistive switching systems, including $SrTiO_3$. Reproduced from ref. 56.

from the plug part of the filament are attracted into the barrier (Fig. 2.5B), which results in a significant decrease of the barrier height and width due to a local reduction process (compare Fig. 2.3), which turns the cell into the LRS (Fig. 2.5C). For the Reset, a positive voltage V_{Reset} is applied to the active interface which repels the oxygen vacancies (Fig. 2.5D), leading to a local reoxidation, and turns the cell into the HRS again. Going beyond this graphical representation, this type of resistive switching can be accurately modeled using a numerical drift-diffusion model of electronic-ionic transport combined with a Schottky contact barrier [8]. Calculating the electronic transport across the Schottky barrier as well as the drift-diffusion of oxygen under the applied electric field and due to concentration gradients, the model correctly describes the I-V-switching characteristics and reveals that the resistance change is induced by temperature-accelerated ion migration. The necessary temperature is induced through Joule heating within the switching filament [8, 57].

With direct experimental evidence of the redox reactions being inaccessible so far, several phenomenological models have been suggested to explain the eightwise

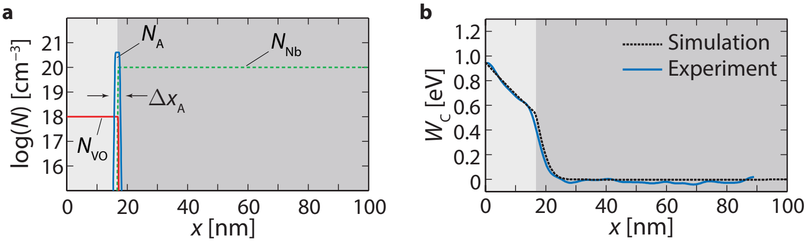

Figure 2.6: Indication for an additional barrier at the $SrTiO_3$/Nb:$SrTiO_3$ interface. (a) Dopant distributions used to fit the experimental data; acceptor doping at the interface must be used to reproduce the experimental data in (b). (b) Comparison between the simulated and the experimentally measured energy-band profile. Modified from ref. 37.

switching phenomenon as described below. For instance, it was shown that the Nb:$SrTiO_3$/$SrTiO_3$ interface is not free from space charges (Fig. 2.6) [37], which may result in a significant potential barrier rather than an ohmic contact at the bottom electrode interface. A possible scenario of eightwise switching could therefore be that resistive switching takes place at the bottom electrode interface instead of at the top Pt interface because of an increased potential barrier, which is modulated by the near-interface $V_O^{\bullet\bullet}$ concentration. Such a change of the active interface has been suggested for multiple resistive switching systems exhibiting coexisting switching polarities [36, 60, 61].

Another proposed mechanism considers that when $V_O^{\bullet\bullet}$ are attracted to the top electrode and are highly concentrated near the interface, the region below may become $V_O^{\bullet\bullet}$-deficient (Fig. 2.7) [10, 53, 62]. The increased resistance of this region then causes the HRS.

As chapter 8 will demonstrate, these proposed mechanisms do not agree with the experimental findings presented in chapter 7. Accordingly, an alternative switching mechanism for eightwise switching must be introduced.

Noble metal/Nb:$SrTiO_3$ interfaces

Similar to eightwise resistive switching in $SrTiO_3$ thin films, typical noble metal/Nb:$SrTiO_3$ interfaces can be Set to the LRS by applying a positive voltage to the

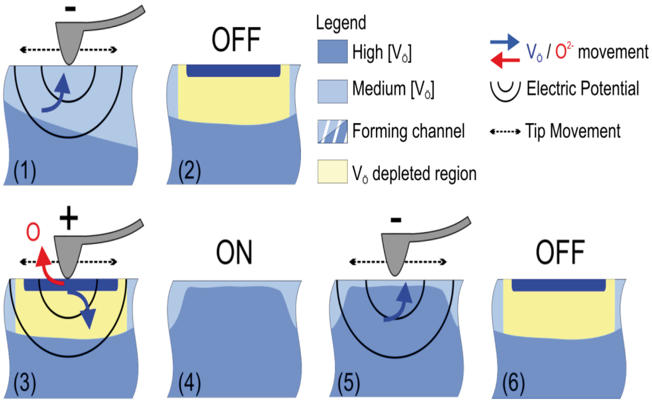

Figure 2.7: Proposed mechanism for switching far from the top electrode interface to explain eightwise switching. Modified from ref. 53.

top electrode, while a negative voltage Resets the device to the HRS [10, 34, 35, 63–68]. Again, the underlying resistive switching mechanism of these junctions is not understood in detail and contradicting interpretations prevail.

Many reports have connected resistive switching in Pt/Nb:SrTiO$_3$ with changes in the oxygen stoichiometry within a thin interfacial dead layer, corresponding to an electron depletion layer caused by the formation of a Schottky barrier [64–66, 69]. Some reports suggested that this interfacial dead layer may be caused by a deviation from the nominal cation stoichiometry in the near-surface region of Nb:SrTiO$_3$ [70], potentially modifying the Schottky-type interfacial space charge region [37].

Regarding the spatial extent of eightwise resistive switching, it has been inferred based on capacitive measurements that the resistance change in Pt/Nb:SrTiO$_3$ devices occurs in a homogeneous manner for small current limits, while higher voltages have been suggested to cause a filamentary change of the resistance [65]. In the latter case, the switching process is commonly interpreted as a locally confined change in the Schottky barrier height [63], while the majority of the interface remains unchanged.

Indeed, there exists both theoretical [71] and experimental evidence [72] that oxygen vacancies in the surface layer of Nb:SrTiO$_3$ lead to a reversible reduction of the effective Schottky barrier height, which can again be understood as a decrease of the contact resistance due to increased carrier concentrations as shown in Fig. 2.3b.

It was observed that resistive switching in Pt/Nb:$SrTiO_3$ devices strongly depends on the oxygen partial pressure of the surrounding atmosphere [64]. The creation of additional oxygen vacancies at the interface yields improved memory characteristics [67] while removal of oxygen vacancies can prevent resistive switching entirely [68]. These observations support the interpretation of the oxygen-ion migration being responsible for resistive switching in this system as well.

Despite the abundant evidence for a dependence on the oxygen partial pressure and the corresponding interpretation of the resistance change in transition metal oxides as an effect caused by the movement of oxygen-ions, however, direct proof of oxygen migration and the associated valence change is rare, resulting in competing interpretations. While some reports try to describe the resistance change in a purely electronic picture [73–76] comparative studies show that both electronic effects such as trapping and detrapping of defect states as well as oxygen-ion migration can explain the electrical data [74, 77]. Accordingly, direct evidence for one or the other mechanism is indispensable. Chapter 6 therefore attempts to experimentally shed light on the microscopic mechanism.

Retention

The ultimate aim regarding memristive device performance is high uniformity for all devices on a single chip, an endurance (write cyclability) of at least 10^7 cycles, scalability down to the nanometer regime and the potential for multibit operation [4, 6]. Most of all, the ultra-nonlinear switching kinetics (also called voltage-time dilemma) between extremely fast switching times ($\leq 10-100$ ns) and long so-called retention times exceeding 10 years has to be met for non-volatile memory applications [4]. Retention refers to the time in which the devices remains in a resistance state which is clearly distinguishable from the opposite resistance state.

While excellent retention has been demonstrated for many binary and ternary oxides in conjunction with fast switching, Noman et al. showed that in the absence of internal electric fields, $SrTiO_3$ cannot exhibit both properties simultaneously [78]. In fact, retention failure after short times was reported for the LRS in single crystalline $SrTiO_3$

thin films and Nb:$SrTiO_3$ [65,79,80]. Polycrystalline and single crystalline $SrTiO_3$ films with considerable amounts of extended defects, on the other hand, exhibit much better retention behavior [80,81].

Based on simulations of the I-V-characteristics and retention times, one finds that the retention failure mechanism for the LRS is based on the rupture of conducting filaments caused by reoxidation due to oxygen diffusion from the side [82,83] or along the vertical direction [84]. Recent studies on the technologically most relevant systems of HfO_{2-x} [85–89] and Ta_2O_{5-x} [82,83,90,91] however, reveal that extremely high retention times can be achieved with oxidizable electrodes or interlayers (the so-called oxygen scavenging layer). Phenomenologically, this finding was attributed to the stability of certain oxygen distributions in the layer stack and filaments with sufficient oxygen vacancy concentrations to be stable against reoxidation due to oxygen diffusion in the lateral direction. Some qualitative conclusions from these simulation-based studies [82,83,92] such as the importance of the filament size and the oxygen vacancy concentration within the filament and the adjacent layers certainly hold true. Experimental evidence for the role of local redox reactions for both the device function (resistance change between LRS and HRS) and for the retention failure, however, remains elusive so far.

3 Experimental methods

In this thesis, $SrTiO_3$ thin films and $SrTiO_3/LaAlO_3$, $SrTiO_3/SrO$, $SrTiO_3/Y{:}ZrO_2$ and $SrTiO_3/Al_2O_3$ heterostructures were fabricated and characterized. In a next step, MIM structures based on these oxide films were fabricated and applied as memristive devices. In general, the oxide films were fabricated via PLD on single crystalline $SrTiO_3$ substrates, which were Nb doped in the case of MIM structures to serve as conductive bottom electrode. For all PLD-grown oxide films, the morphology was characterized by atomic force microscopy (AFM). Most films were characterized *ex situ* using a Surface Analysis Systems Picostation AFM in tapping mode. For *in situ* characterization, ultra-high vacuum (UHV) AFM was performed using an Omicron VT SPM operated in contact mode with a single crystalline diamond tip with a nominal tip radius of 10 nm (Advanced Diamond Technologies)[1]. (C-)AFM measurements on memristive devices were performed using a Asylum Research Cypher AFM with platinum silicide tips or conductive diamond coated tips (Nanosensors PtSi-FM tips and CDT-FMR tips, respectively, Nanoworld, Neuchâtel, Switzerland) in contact mode or tapping mode. In this chapter, the deposition processes of the different films, the device fabrication and the spectroscopic characterization tools will be introduced.

3.1 Pulsed laser deposition

All PLD-grown films were fabricated on 0.5 wt%-Nb:$SrTiO_3$ or $SrTiO_3$ substrates (CrysTec GmbH, Germany). The targets were ablated using a KrF excimer laser ($\lambda = 248\,\mathrm{nm}$) with a repetition rate of 1 or 5 Hz at a specified laser fluence[2]. The film

---

[1] UHV AFM analysis was performed by Dr. Chencheng Xu, Peter Grünberg Institute, Forschungszentrum Jülich GmbH, Jülich, Germany.

[2] The fluences listed in this thesis are measured outside the PLD chamber. The transmission of the laser window of the chamber is around 67 %.

growth at high temperatures was always monitored using reflection high energy electron diffraction (RHEED, akSA400 system).

Pulsed laser deposition of $SrTiO_3$ thin films

Single-crystalline, nominally undoped $SrTiO_3$ thin films were fabricated using a single crystalline $SrTiO_3$ target and a laser fluence of 1.05-2.25 $J{\cdot}cm^{-2}$ in an atmosphere of 0.1 mbar O_2. The spot-size was 2 mm^2 at a target-to-substrate distance of 44 mm. The substrate temperature was 800 °C. The film growth is described in detail refs. 54, 93 and 94. Through the choice of the laser fluence, the film stoichiometry can be tuned, as will be discussed in more detail in chapter 4.2.

SrO growth on $SrTiO_3$ single crytalline substrates and thin films

To achieve $SrTiO_3$ single crystals with different amounts of TiO_2- or SrO-termination (which will be used for the calibration of the angle dependence of the X-ray photoelectron intensities in chapter 4.2), SrO was deposited via PLD on substrates obtained from one $SrTiO_3$ single crystal, which was HF-etched for complete TiO_2-termination [96]. A polycrystalline SrO_2 target was ablated with a repetition rate of 1 Hz and a laser fluence of 1.3 $J{\cdot}cm^{-2}$ (spot size 2 mm^2) at a target-substrate distance of 44 mm in an atmosphere of 10^{-7} mbar O_2; the substrate temperature was 800 °C.

The film growth was monitored using RHEED along <110> direction, as shown for an exemplary deposition of 14 pulses of SrO in Fig. 3.1a. While the intensity of the specular spot continuously decreases with the amount of SrO deposited on the surface, the intensities of the (10) and (-10) 1st order diffracted electrons have a maximum once the coverage of approximately one complete layer of SrO on the $SrTiO_3$ crystal is reached after nine pulses. This relative change of RHEED intensity between the specular point (00) and the (10) and (-10) points has also been observed in MBE-growth of SrO monolayers [97]. For more than one monolayer of SrO one expects the additional appearance of half-integer RHEED streaks. Therefore, the absence of such streaks is an additional indication that none of the SrO films with up to nine pulses exceeded the thickness of one monolayer.

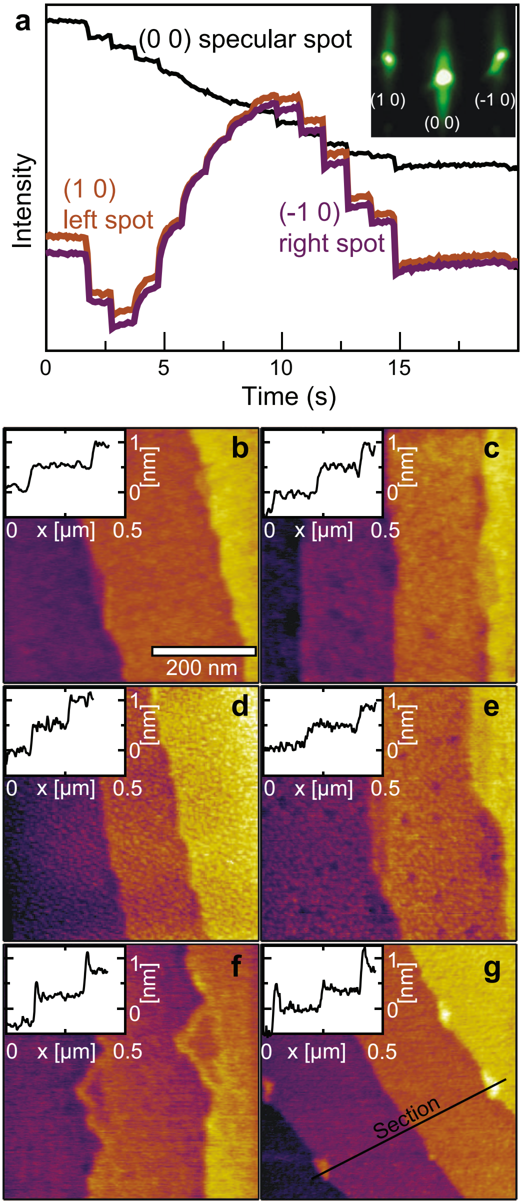

Figure 3.1: Systematic surface termination variation in $SrTiO_3$ single crystals. (a) Representative RHEED intensity during SrO deposition. Inset: Exemplary RHEED pattern after SrO growth (14 pulses). (b)-(g) AFM morphology after deposition of 2, 4, 6, 8, 10, and 12 pulses of SrO, respectively. Step terraces are of unit cell height (≈ 4 Å). Insets: Representative line profiles from the AFM scans along sections like the one depicted in (g). Modified from ref. 95.

The morphology evolution after the deposition of increasing amounts of SrO on single crystalline substrates was monitored with a UHV AFM after *in situ* UHV transfer from the PLD system. Each image was taken at room temperature after quenching the sample directly after the PLD process. The surface morphology for different amounts of SrO termination is depicted in Figs. 3.1b-g. The deposition of less than one monolayer of SrO results in the creation of small islands. The $SrTiO_3$ step terraces remain sharp and no islands of one $SrTiO_3$ unit cell height or more can be observed, confirming that only the surface termination of the crystal changes. Only when ten or more pulses of SrO are deposited, higher islands begin to form at the step edges as can be seen from the line profiles in the insets of Fig. 3.1f and g; it can be assumed that SrO starts to nucleate as a separate phase. These AFM scans support the conclusion from the RHEED analysis that the deposition of nine pulses of SrO results in the deposition of a nearly complete SrO terminating layer on previously perfectly TiO_2-terminated $SrTiO_3$.

$SrTiO_3$/SrO thin film heterostructures were obtained by subsequent *in situ* PLD of 2 nm undoped, slightly Sr-deficient $SrTiO_3$ thin films (laser fluence $1.75\,\mathrm{J\cdot cm^{-2}}$, oxygen atmosphere of 0.1 mbar) and 36 pulses of SrO deposition as described above, resulting in a ≈ 1 nm SrO film of polycrystalline morphology (as confirmed by the RHEED pattern and AFM). 0.5 wt%-Nb:$SrTiO_3$ substrates were used (Crystec GmbH, Germany).

Pulsed laser deposition of $SrTiO_3$/Y:ZrO_2 and $SrTiO_3$/Al_2O_3 heterostructures

$SrTiO_3$/Y:ZrO_2 and $SrTiO_3$/Al_2O_3 heterostructures were obtained in a similar way as $SrTiO_3$/SrO heterostructures. After $SrTiO_3$ deposition as described above, the samples were cooled down to room temperature prior to *ex situ* pulsed laser deposition of Y:ZrO_2 (8 at.% doping level) or Al_2O_3 at room temperature. For both cases, the laser fluence was $2.1\,\mathrm{J\cdot cm^{-2}}$, with a repetition rate of 5 Hz and a spot-size of $1.5\,\mathrm{mm^2}$ at a target-to-substrate distance of 60 mm in an oxygen atmosphere of 10^{-4} mbar[3].

---

[3] Y:ZrO_2 and Al_2O_3 deposition was partially performed by Benedikt Arndt, Peter Grünberg Institute, Forschungszentrum Jülich GmbH, Jülich, Germany.

3.2 Device fabrication and electrical characterization

Noble metal top electrodes for electrical characterization

For regular top electrodes, a 30 nm Pt or Au layer was electron-beam evaporated or sputter deposited, respectively, onto the as-prepared films and structured into $10 \times 10\,\mu m^2$ electrode pads by optical lithography and dry etching in a Reactive Ion Beam Etching tool (Ionfab 300plus, Oxford Instruments). Details of the available top electrode materials and individual fabrication steps are listed in appendix A.

Sample architecture for *in situ* biasing

For *in situ* biasing experiments where no contact with a probe is possible or for extremely thin electrodes, which would not withstand the mechanical contacting with a probe, lithographically defined metallic leads were fabricated through a series of lithography and deposition steps (Fig. 3.2). After fabrication of the top electrodes as described above, the electrode is partially covered by a 100 nm insulating layer (optical lithography). This insulating layer allows for contacting the electrode with Pt/Au leads, which are separated from the continuous bottom electrode. The leads connect to the electrode in one specific position. The leads were prepared via optical lithography and electron beam evaporation of 10 nm Pt followed by 130 nm Au. Details of the different fabrication steps are also listed in the appendix A.

Graphene top electrodes for *in operando* spectroscopy

Graphene layers were used to achieve ultimately thin top electrodes as shown in Fig. 3.3. The graphene was grown via chemical vapor deposition on Cu foil[4] and subsequently transferred to the $SrTiO_3$ samples as described elsewhere [98]. For the structuring of top electrodes, the graphene layer was patterned through optical lithography and oxygen plasma etching. Before photoresist lift-off, a thin insulating layer was deposited via pulsed laser deposition at room temperature. This layer allows for lithographical

---

[4] The graphene growth was performed by Steven Rogers, University of Illinois at Urbana-Champaign, USA, as part of a collaboration

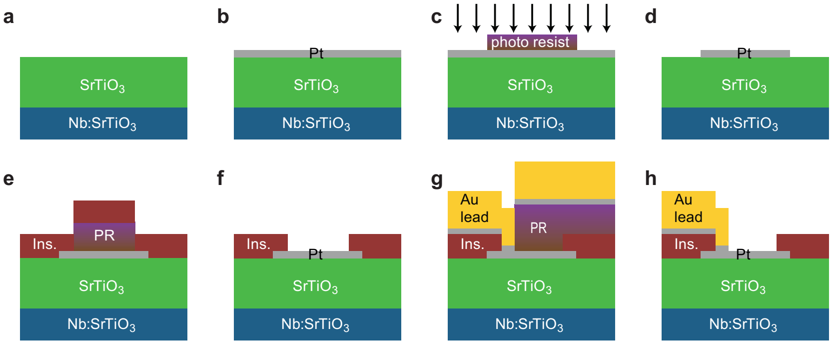

Figure 3.2: Sample fabrication for *in situ* biasing. (a) $SrTiO_3$ film after PLD. (b) A layer of the desired top electrode material (e.g. Pt) is deposited. (c) The desired top electrode area is protected during dry etching using photo resist. (d) The MIM device consisting of a continuous bottom electrode, the $SrTiO_3$ film and the structured top electrode is finished after photo resist lift-off. (e) An insulating layer, such as $Y{:}ZrO_2$ is deposited. The central part of the device is protected by photo resist. (f) After lift-off, the edges of the device and the exposed $SrTiO_3$ surface are covered by the insulator. (g) Metallic leads are deposited while most of the sample surface is protected with photo resist, allowing contact between top electrode and metallic lead only in a defined spot. (h) The device is ready for *in situ* biasing.

alignment in the following step. This is necessary as graphene on $SrTiO_3$ is invisible in an optical microscope. Afterwards, the graphene electrode was partially covered by an additional insulating layer and contacted with a metallic lead as described above.

Electrical characterization

For electrical characterization, the Pt or Au electrodes leads were contacted with W whisker probes for regular top electrodes. Pt/Au leads were contacted with W whisker probes for *ex situ* and atmosphere-dependent characterization and through Al wire bonding or silver paste for *in situ* switching within PEEM instruments. The $Nb{:}SrTiO_3$ substrate served as an electrically grounded bottom electrode and was contacted through Al wire bonding or silver paste. I-V sweeps were performed with a Keithley 2611A SourceMeter. The different sweeps were performed using the following voltage cycles: 0 V to positive voltages (maximum +5 V) for forming and Set, 0 V to negative voltages (maximum -5 V) for Reset and +0.2 V to -0.2 V (in some cases

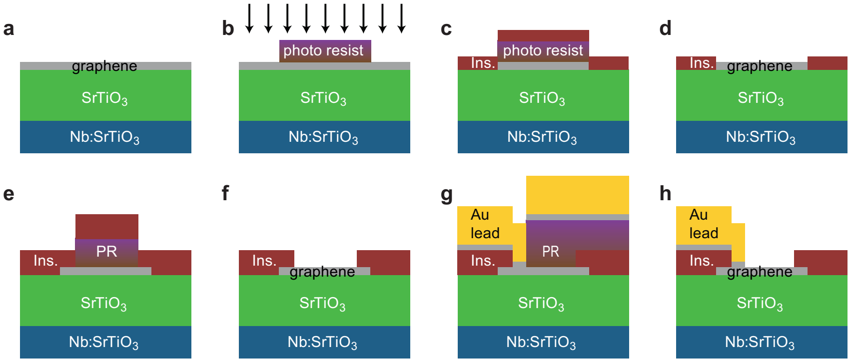

Figure 3.3: Sample fabrication for graphene electrodes. (a) $SrTiO_3$ film after graphene transfer. (b) The desired top electrode area is protected during oxygen plasma etching using photo resist. (c) Before lift-off, a thin insulating layer is deposited. (d) The MIM device consisting of a continuous bottom electrode, the $SrTiO_3$ film and the structured graphene top electrode is finished after photo resist lift-off. (e) Another, thicker insulating layer is deposited. The central part of the device is protected by photo resist. (f) After lift-off, the edges of the device and the exposed $SrTiO_3$ surface are covered by the insulator. (g) Metallic leads are deposited while most of the sample surface is protected with photo resist, allowing contact between top electrode and metallic lead only in a defined spot. (h) the device is ready for *in situ* biasing.

+0.5 V to -0.5 V) for read-out. The device resistance was obtained from the slope of a linear fit of the read-out sweeps between -0.1 V and +0.1 V. The step size was 20 mV and the holding time before measurement was 5 ms; the current compliance for the forming step and the Set process is specified for each device under consideration. During the Reset sweeps no current compliance was necessary. Current compliance, maximum positive and maximum negative voltage compose the so-called switching parameters.

Impedance spectroscopy was performed on virgin cells and representative cells in the HRS and LRS using an HP 4291B RF Impedance/Material Analyzer with a sampling voltage of 300 mV and a frequency range from 20 to 10^6 Hz. The impedance data were fitted with the commercially available software Zplot/Zview (Scibner Associates Inc.). An equivalent circuit consisting of a parallel circuit of a capacitor and a resistor was used to fit the data over the entire frequency range.

3.3 X-ray absorption spectroscopy

X-ray absorption describes the interaction of a solid with electromagnetic irradiation. In this process, an electron can be promoted to an unoccupied, excited state while abiding the dipole selection rules, i.e., the spin quantum number must not change and the change in angular momentum ($\mathit{\Delta} L$) must equal ±1 [26]. If the photon energy becomes sufficient to excite electrons from a specific core level into the lowest-lying unoccupied electronic states allowed by the selection rules the absorption is strongly increased giving rise to a so-called absorption edge (for energies below this edge the absorption probability is low, above this edge the absorption probability is high).

According to Fermi's golden rule, the transition probability per unit time $P_{i \mapsto f}$ from the initial state $|i\rangle$ to the final state $|f\rangle$ can be described as

$$P_{i \mapsto f} = \sum_f \frac{2\pi}{\hbar} |\, \langle f \,|\, H' \,|\, i \rangle \,|^2 \, \delta(h\nu + E_i - E_f) \tag{3.1}$$

with the interaction Hamiltonian H' between the electrons and the electromagnetic field of the photon and the energies of the initial and final states E_i and E_f [99–101]. The delta function ensures energy conservation in the excitation process.

The final state $|f\rangle$ consists of the excited electron and a core hole and can be regarded as a delocalized scattering state. The propagation of the excited electron can be described using the multiple scattering formalism [99]. Through interference between the outgoing photoelectron wave and the reflected waves from the surrounding atoms, this scattering process modifies the matrix element $\langle f \,|\, H' \,|\, i \rangle$ of the absorption probability. $\langle f \,|\, H' \,|\, i \rangle$ depends on the local electronic structure and arrangement of the atoms and results in an additional modulation of the absorption coefficient which depends on the energy $h\nu$ of the electromagnetic irradiation, giving rise to a fine structure of the absorption edge. X-ray absorption spectroscopy (XAS) refers to the measurement of this energy dependent absorption. In a first approximation, the resulting edges can be thought of as an image of the electronic structure of the sample, i.e., the binding energy of the core levels (the initial state $|i\rangle$) and the density of states of the unoccupied level (the final state $|f\rangle$). These edges are therefore element selective and sensitive to the valence state of each involved species.

The absorption edges are labeled according to the initial core level of the electron (K, L, M,...) with a numerical index indicating the subshell. Accordingly, the absorption edges studied in this thesis – the O K-edge and the Ti $L_{2,3}$-edge – indicate an excitation from the O 1s level (angular momentum $L = 0$) to the O 2p level ($L = 1$) or from the Ti $2p_{\frac{1}{2}}$ or Ti $2p_{\frac{3}{2}}$ level ($L = 1$) to the Ti 3d level ($L = 2$), respectively.

Generally, the features of the absorption edges can be interpreted in the near-edge region ($\leq$50 eV above the edge), which is referred to as X-ray absorption near edge spectroscopy (XANES), or the extended structure ($\geq$50 eV above the edge), which is called extended X-ray absorption fine structure (EXAFS). In this thesis, only XANES will be employed. For reasons of simplicity, the resulting measurements will be only referred to as XAS.

Traditionally, XAS was measured from the transmission intensity of X-rays penetrating a thin specimen. Due to difficulties in preparing thin specimen [54], indirect measurements by photoyield or electron yield have become dominant. These measurement techniques rely on the processes occurring after the actual absorption. The final state $|f\rangle$ has a limited lifetime and decays to the the ground state $|i\rangle$ through radiative decay (yielding fluoresence radiation, which is used for the detection in photoyield) or non-radiative decay. This decay path is typically described through the Auger process, where the core hole is filled by an electron from an outer shell. The energy released in this process is transferred to another electron (the Auger electron), which is emitted from the atom. The Auger electrons (as well as the photons created during radiative decay) further interact with the sample through a series of elastic and inelastic scattering events, which creates a secondary electron cascade [102]. This cascade contains a large number of low energy secondary electrons. Under the condition that the mean absorption length is large compared to the inelastic mean free path of the secondary electrons (which is the typical case), the number of these electrons is proportional to the absorption probability [99], which is the basis for XAS based on electron yield. In practice, this can be measured through the sample current or the detection of the electrons that leave the sample. For this thesis, the low-energy secondary electron yield will be detected in a photoemission electron microscope.

3.4 Photoemission electron spectroscopy

X-ray photoelectron spectroscopy (XPS) is a versatile tool for the determination of the valence state and stoichiometry of solids. A detailed description XPS can be found in ref. 103. Similar to XAS, it is based on the absorption of photons, which excite electrons. If the energy above the Fermi level of the photo-excited electrons is higher than the work function of the solid, the electrons leave the surface with a specific kinetic energy and can be detected. The electron kinetic energy E_{kin} is related to the binding energy of the initial core level E_{bin} according to

$$E_{\mathrm{kin}} = h\nu - E_{\mathrm{bin}} - \varPhi \tag{3.2}$$

with the photon energy $h\nu$ and the work function $\varPhi$. As $\varPhi$ is frequently unknown, equation 3.2 can also be expressed as

$$E_{\mathrm{bin}} = h\nu - (E - E_{\mathrm{F}}) \tag{3.3}$$

where $E - E_{\mathrm{F}}$ indicates the electron energy above the Fermi level.

As the binding energy of the core level electrons is characteristic for each element, XPS is an element-sensitive technique. The exact energy position of each core level depends on the local chemical environment. Changes in the binding to the neighboring atoms lead to so-called chemical shifts, allowing for valence-sensitive measurements.

After leaving the sample, photoelectrons are energy-analyzed using a semi-spherical energy analyzer. For this purpose, they are retarded to the analyzer pass energy. Scanning the retarding field in the input lens of the analyzer and detecting the electrons using a micro-channel plate allows for the collection of a spectrum, which plots the photoelectron intensity as a function of the binding energy.

The integrated intensities of the characteristic peaks are a measure of the relative atomic concentrations. Due to differences in the cross sections for the photoelectric effect for different elements and core levels, so-called relative sensitivity factors are necessary to calculate the relative atomic concentration from the integrated peak area. These sensitivity factors can be found in literature, but they may vary by 10-20 %

for the same element in different chemical environments, making careful calibration indispensable.

X-rays can penetrate the sample and excite photoelectrons from a depth of several hundred nanometers. However, as the generated photoelectrons move through the sample, they scatter elastically and inelastically. Therefore, electrons which are created near the surface have a higher probability of leaving the sample with their characteristic energy. If electrons scatter inelastically, they can only contribute to the background of the spectrum (and generate secondary electrons). Accordingly, XPS is a surface sensitive technique and the information depth t is typically described as

$$t = 3\lambda \cos\theta \tag{3.4}$$

with the inelastic mean free path λ (the average distance an electron travels before undergoing inelastic scattering) and the photoemission angle θ, which indicates the angle between the surface normal and the energy analyzer. t is typically on the order of very few nanometers, depending on the electron kinetic energy and the material through which it is traveling. Using the kinetic energy and the electronic structure of the material as an input, λ values can be calculated according to ref. 104.

The XPS measurements described in chapter 4.2 were performed with a PHI 5000 Versa Probe (Physical Electronics Inc., USA) with monochromatic Al K_α X-ray illumination, a pass energy of 29.35 eV and at various photoemission angles using electron neutralization. All spectra in this thesis were evaluated using CasaXPS Version 2.3.16 and a Shirley background was subtracted prior to quantitative analysis.

3.5 Photoemission electron microscopy

Photoemission electron microscopy (PEEM, also XPEEM if the electrons are excited using X-ray sources) images electrons which leave the sample using a set of lenses, which allows for imaging of the sample surface.

For the PEEM studies presented in this thesis, three different PEEM instruments are used: The NanoEsca from Scienta Omicron GmbH, Taunusstein, Germany (described in detail in ref. 105 and 106), the P90 AC LEEMPEEM from SPECS Surface Nano Analysis GmbH, Berlin, Germany (described in detail in refs. 107) and SPELEEM from Elmitec GmbH, Clausthal-Zellerfeld, Germany (described in detail in ref. 108).

PEEM allows for work function-selective and element-specific, direct imaging of surfaces and interfaces as well as imaging of the k-space. For the purpose of this thesis, chemical sensitivity was achieved operating PEEM in XAS mode and through energy-filtered imaging, which contains spatially resolved XPS and so-called work function scans, as described below.

Photoemission electron microscopy in absorption mode

The operation of a photoemission microscope is depicted exemplarily in Fig. 3.4. Here, the NanoESCA is shown, but the fundamental imaging unit in the other microscopes is similar. A high electric field is applied between the objective immersion lens and the sample, accelerating the emitted photoelectrons into the imaging column, where a first image is formed in the plane of the iris aperture. This image is further magnified through a set of electrostatic or magnetic lenses. An image of the sample surface can thus be obtained using a detection unit composed of micro-channel plate, a scintillator screen and a CCD camera.

The majority of the electrons that leave the sample that are imaged in this manner are secondary electrons. As the intensity of the secondary electrons is proportional to the number of absorbed photons, tuning the photon energy to the characteristic absorption edges of the material under investigation allows spatially resolved XAS characterization.

For this purpose, various series of images are taken at increasing photon energies with a step size of 0.1 eV for the Ti L-edge and 0.2 eV for the O K-edge. These image stacks are analyzed using the IGOR Pro software. Before spectra can be extracted from regions of interest in the images, some data treatment is necessary. First, the background-camera-noise is removed through subtraction of a reference image obtained without emitted electrons. Secondly, inhomogeneities in the detection unit (especially

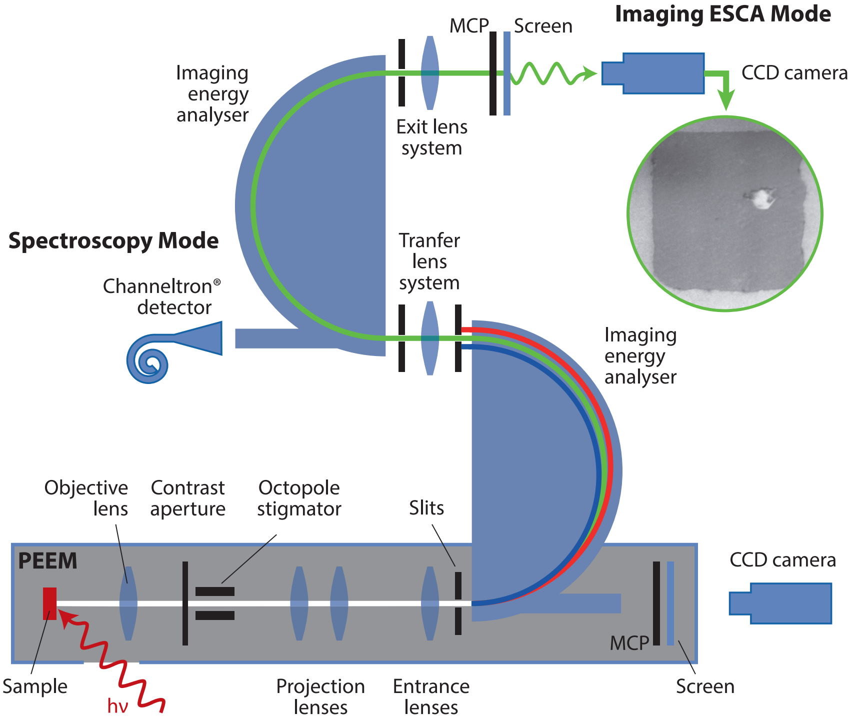

Figure 3.4: Schematic layout of the NanoEsca from Omicron NanoTechnology GmbH, one of the PEEM instruments used in this thesis. Modified from ref. 54. Photoelectrons, which are excited using a UV lamp or synchrotron light, are imaged using a set of electron lenses. The image plane is either the entrance slit of an energy analyzer or a micro-channel plate. The green-framed inset is a representative energy filtered image.

the micro-channel plate) can be corrected by the normalization with a featureless "flat-field" image. In order to highlight the variations of the secondary electron intensity due to an absorption edge in XAS mode, it is important to remove the photon energy independent contrast due to a variation of the local work function. For this purpose, several images at photon energies far from the absorption edge are averaged to get a high statistics image of the work function contrast. Afterwards, the entire image stack is divided by this reference image. The remaining contrast is then only due to different absorption characteristics.

In the next step, absorption spectra can be extracted from regions of interest by plotting the average intensity of the selected region as a function of photon energy. The influence of unavoidable variations of the photon intensity $I_0(E)$ are removed through normalization to the drain current from a gold grid in the beam path measured at the same time as the PEEM measurement.

For easier comparison, the resulting spectra can be background corrected by a linear fit of the pre-edge and subsequent normalization by fitting a third-order polynomial to the post-edge using the Athena software [109]. To avoid artifacts from normalization, only relative peak intensity changes and shifts will be discussed. The relative peak ratio trends described in the following chapters are the same before and after normalization.

Energy-filtered photoemission electron microscopy

If the image of the sample surface is formed in the entrance slit of an energy analyzer (e.g. the double hemispherical energy analyzer of the NanoESCA shown in Fig. 3.4), the photoelectrons can be distinguished based on their kinetic energy. Using a single channeltron detector, regular photoelectron spectra can be obtained, as described in section 3.4. Using a second set of lenses and a two-dimensional detector as described for PEEM in absorption mode, energy-filtered imaging of core level, valence and secondary electrons is possible. Again, series of images are obtained, which now correspond to increasing electron kinetic energies. Core level photoemission spectra can be extracted from the resulting image stack in different regions of interest as described above. The fitting of these spectra was performed after principal component analysis with CasaXPS Version 2.3.16, which is a common tool for noise reduction in large data sets. The components were constrained to have the same peak position and width for each fit.

For core level imaging, the photon energy was 200 eV. The total energy resolution determined from both the spectrometer broadening (pass energy 50 eV and entrance slit 1 mm) and the photon bandwidth is 200 meV. For work function spectra, a UV lamp with $h\nu = 4.9\,\mathrm{eV}$ is used, which allows for imaging of low energy electrons close to the photoemission threshold only. The work function is defined as the lowest energy electrons need to leave the sample. On the energy scale $E - E_\mathrm{F} = E_{kin} + \Phi$, which is typically used for these measurements, the low energy side of the threshold spectra

($E_{kin} = 0$) can be fitted using a convolution of Gauss and Heaviside functions to determine the work function [110].

The calculated theoretical resolution of the aberration corrected instruments in the PEEM mode using secondary electrons is on the order of 10-50 nm, for core levels it is $\approx$150 nm [106–108]. But the actual resolution can be negatively influenced by imperfect alignment of the microscope and by space charge effects [111]. An estimate of the actual resolution will be provided in section 7.2.

4 Spectroscopic signatures of $SrTiO_3$: the influence of doping and non-stoichiometry

Since small changes in the electronic and chemical structure are expected to have a large impact on the resistivity of complex oxides (compare chapter 2), the spectroscopic signatures of $SrTiO_3$ have to be analyzed carefully for their suitability to characterize the as-prepared thin films on the one hand and to resolve the changes during switching on the other hand. Accordingly, characteristic XPS and XAS signatures of $SrTiO_3$ will be introduced and the effect of both anion and cation non-stoichiometry will be analyzed in this chapter. As the suspected valence changes during switching are spatially confined to switching filaments, the effect of anion non-stoichiometry (i.e., donor doping) will be considered for XAS only, because the lateral resolution of PEEM in absorption mode is much better than in XPS mode. Moreover, XAS in principle contains the same information as electron energy loss spectroscopy (EELS), a highly attractive tool for spectroscopic characterization with atomic resolution in a transmission electron microscope, which will also be utilized as part of this thesis. The XPS analysis will focus on the impact of cation non-stoichiometry for the surface and the bulk of $SrTiO_3$ thin films.

4.1 X-ray absorption signature of $SrTiO_3$

The accessible X-ray absorption edges will be carefully evaluated below to examine their suitability to resolve small changes of the electronic structure during resistive switching.

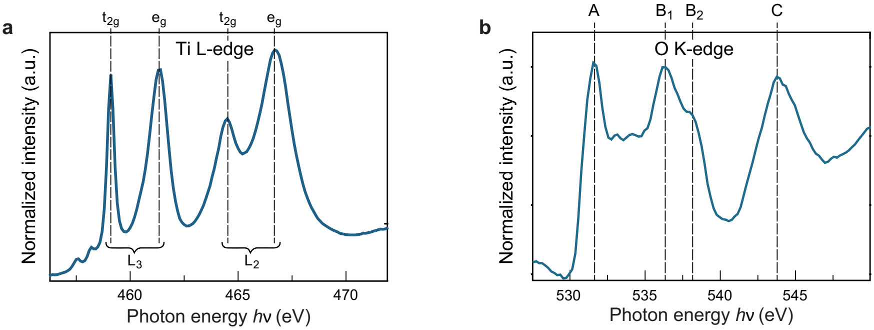

Figure 4.1: Characteristic X-ray absorption edges in $SrTiO_3$. (a) Ti L-edge and (b) O K-edge absorption spectra from a $SrTiO_3$ film.

For EELS, the same spectroscopic signatures are expected. The results presented in this section have been published in part in ref. 112.

4.1.1 Titanium L-edge

For stoichiometric $SrTiO_3$, the Ti L-edge which is described in more detail in refs. 54 and 113 consists of four characteristic peaks (Fig. 4.1a). The origin of these peaks lies in the spin orbit splitting of the Ti 2p level, which splits the spectrum into the L_2 and L_3 edge, and the additional crystal field splitting of the Ti 3d level. In the octahedral coordination in $SrTiO_3$, d_{yz}, d_{xz} and d_{xy} orbitals, which point between the ligands, exhibit t_{2g} symmetry. On the other hand, $d_{\mathrm{x}^2-\mathrm{y}^2}$ and d_{z^2} orbitals point towards the oxygen ligands and possess e_g symmetry, with stronger interaction with the ligands. Consequently, the antibonding e_g orbitals have a higher energy compared to the antibonding t_{2g} orbitals.

It is well-known that oxygen vacancies in $SrTiO_3$ (which are suspected to drive the resistance change as described above) lead to Ti^{3+} states, i.e., partial filling of the conduction band, which is mainly composed of Ti 3d states (compare Fig. 2.2). Due to its nature, the Ti L-edge is sensitive for the filling of the Ti 3d band and Ti^{3+} concentrations can be derived from the shape of the Ti L-edge spectrum for concentrations exceeding 10-20 % [54, 114, 115]. Here, PEEM operated in XAS mode was used to reproduce this observation (Fig. 4.2a). The Ti^{3+} concentration indicated in Fig. 4.2 is derived from the following procedure. An area exhibiting different amounts

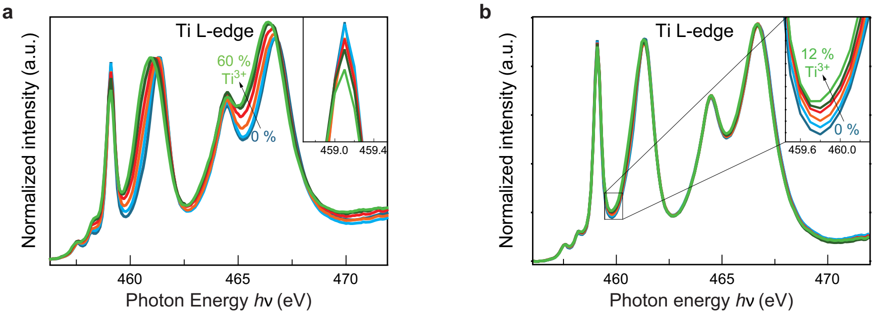

Figure 4.2: Ti L-edge for increasing Ti^{3+} concentrations. (a) High Ti^{3+} concentrations (0-60 %). (b) Low Ti^{3+} concentrations (0-12 %). Insets: Zoom to the L_3 t_{2g} edge and to the photon energy of the Ti^{3+} L_3 e_g edge, respectively. Modified from ref. 112.

of Ti^{3+} was identified and the Ti L-edge spectra were extracted from each point (2×2 pixels) of the image stack and numerically described through a linear combination of two reference spectra, i.e., the spectrum with the highest Ti^{3+} concentration observed here and the 0 % Ti^{3+} spectrum. By comparison with the work of Abbate et al. it was determined that the reference spectrum with the highest Ti^{3+} concentration corresponds to $\approx 60\,\%$ Ti^{3+} [114]. The relative intensity of both reference spectra in the linear combination therefore yields the Ti^{3+} concentration for each point. Points with the same amount of Ti^{3+} were grouped as region of interests (ROIs) and used to extract the spectra displayed in Fig. 4.2. As described in literature, there are significant changes in the Ti L-edge spectrum for different Ti^{3+} concentrations. The L_3 e_g and L_2 e_g peaks are broadened and shifted to lower photon energies for increasing amounts of Ti^{3+}. At the same time, the relative intensity of the L_3 t_{2g} peak decreases (Fig. 4.2a, Inset).

In comparison, the spectral changes for small Ti^{3+} concentrations ($\lesssim 10\,\%$, Fig. 4.2b)), are only very subtle in the Ti L-edge spectra, which can only be identified through numerical least-square fitting of each spectrum as a linear combination of reference spectra as described in refs. 54 and 112. But the trend of the spectral changes is the same as for high concentrations. A shoulder at the low energy side of the L_3 e_g and L_2 e_g peaks occurs and the relative intensity of the L_3 t_{2g} peak decreases.

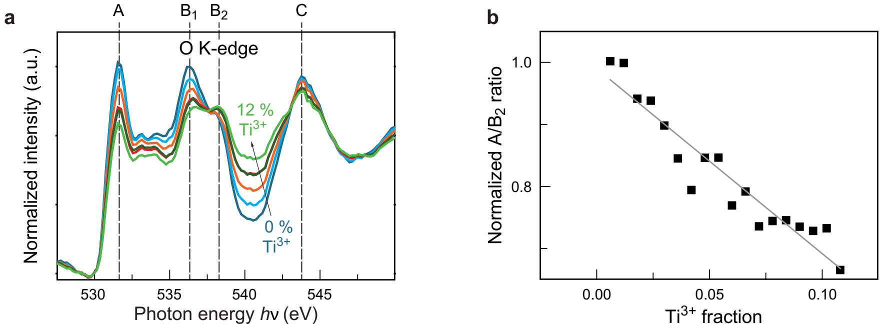

Figure 4.3: Calibrating X-ray absorption spectroscopy for the detection of subtle changes in oxygen vacancy concentration. (a) O K-edge for the same Ti^{3+} concentrations as for the Ti L-edge in Fig. 4.2b. (b) Normalized A/B_2 peak ratio for different Ti^{3+} concentrations. Peak intensities are obtained from the maximum absolute intensities for each peak. Grey line is a linear fit to the data and serves as a calibration curve. Modified from ref. 112.

4.1.2 Oxygen K-edge

In general, the O K-edge stems from the excitation of O 1s core level electrons into unoccupied states of O 2p character [26,116] and therefore represents a measure for the O 2p projected unoccupied density of states. In a strictly ionic picture, accordingly, the O K-edge cannot exist as the O 2p states should be occupied. However, the partial densities of states for $SrTiO_3$ show that the electronic structure should rather be described by hybridized bands with mixed character as described before (Fig. 2.1). While the conduction band is mainly formed by empty Ti and Sr states, there is also a contribution from O 2p states, especially the Ti-O bond possesses a significantly covalent contribution.

The O K-edge of stoichiometric $SrTiO_3$ (Fig. 4.1b) can therefore be regarded as a probe for the interaction of oxygen states with metal bands and each characteristic peak has been assigned to a specific interaction [116]. As is obvious from Fig. 2.1, the first O K-edge peak (peak A) corresponds to a transition from the O 1s level to a hybrid level between O 2p and Ti t_{2g} states. In contrast to peak A, which is interpreted unambiguously in the literature, the following peaks B_1, B_2 and C have been assigned to different interactions of Ti, Sr, and even antibonding O-O character [116, 117]. As the bottom of the conduction band is most relevant for electronic transport, the interpretation of

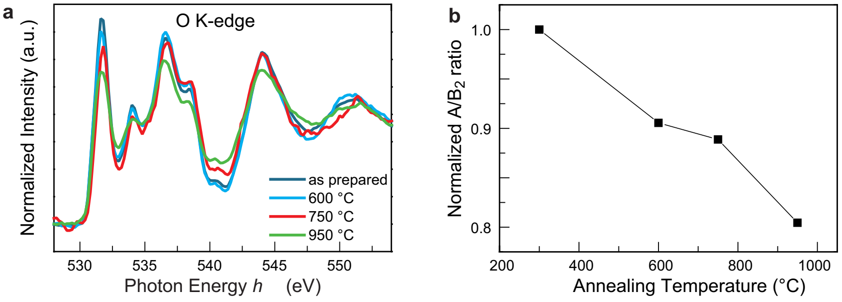

Figure 4.4: O K-edge for a $SrTiO_3$ vacuum annealing series. (a) O K-edge after vacuum annealing at different temperatures. (b) Normalized A/B_2 peak ratio for each temperature. Modified from ref. 112.

the O K-edge in this thesis will focus on peak A (which will be normalized to peak B_2 to avoid artifacts from scan-to-scan variation).

Fig. 4.3 shows the O K-edge spectra for the same small Ti^{3+} concentrations shown for the Ti L-edge in Fig. 4.2b. While there were hardly any changes observable in the Ti L-edge for these concentrations, the O K-edge exhibits much more pronounced spectral changes. The most obvious trend with increasing Ti^{3+} concentration is the decrease of the peak A and an increase in the intensity of the valley between peaks B_2 and C.

As described above, Peak A corresponds to a transition from the O 1s level to a hybrid level between O 2p and Ti t_{2g} states. The observed decrease of peak A can, therefore, be understood as a decrease in the number of unoccupied hybridized O 2p-Ti t_{2g} states available for the transition from the O 1s level, i.e., decreased X-ray absorption probability at this photon energy. In the first approximation, therefore, the peak A intensity should decrease linearly with increasing number of electrons in the conduction band [26]. Qualitatively similar trends have previously observed for a series of different transition metal oxides [26] and in aliovalent substitution series of $La_xSr_{1-x}TiO_3$ [118] and $Nd_{1-x}O_3$ [119]. In $SrTiO_3$ thin films with oxygen vacancies induced by fabrication [120, 121] or via electroforming in resistive switching devices [122, 123] a decrease in peak A intensity was also observed qualitatively. Here, a nearly linear trend of the A/B_2 peak intensity ratio for Ti^{3+} concentrations below 10 %

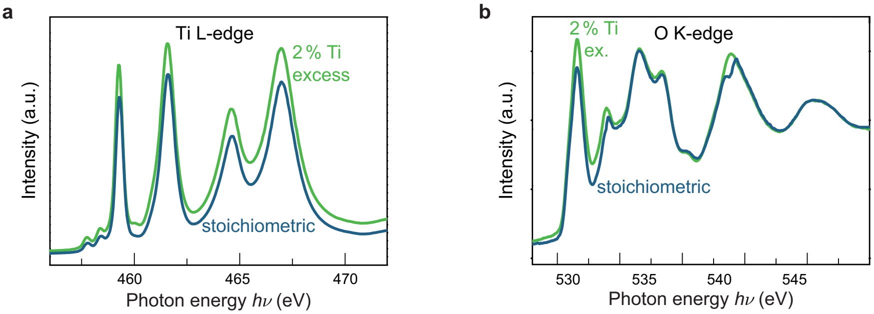

Figure 4.5: X-ray absorption edges in non-stoichiometric $SrTiO_3$. (a) Ti L-edge and (b) O K-edge absorption spectra from a stoichiometric and a Ti-rich $SrTiO_3$ film (blue and green line, respectively). Using angle-dependent XPS, the Ti-excess was determined to be roughly 2 %.

(Fig. 4.3b) is observed, which yields a distinct, quantitative calibration for the purpose of this work.

With the decrease of peak A, the valley between peaks B_2 and C becomes shallower and peak B_2 increases slightly with increasing oxygen vacancy concentration. Compared to the absorption edge around peak A, this change in intensity cannot be easily understood in a simple band-structure model and remains an open question for future investigation. The experimental calibration of the A/B_2 ratio with increasing Ti^{3+} concentration, on the other hand, supplies a valid measure for the charge carrier density.

Comparing the spectral changes in the Ti L-edge and O K-edge for small concentrations of Ti^{3+}, it is obvious that the O K-edge is more sensitive to the anticipated changes of the electronic structure upon resistive switching than the commonly used Ti L-edge. Consequently, the O K-edge will be used for the detection of small changes and quantitative measurements of the electronic structure.

It is worth noting that the same trend in the A/B_2 ratio can be reproduced through annealing of $SrTiO_3$ thin films in vacuum (Fig. 4.4). As a result of defect equilibria, an increased concentration of donor-type oxygen vacancies is expected for increasing annealing temperature [124].

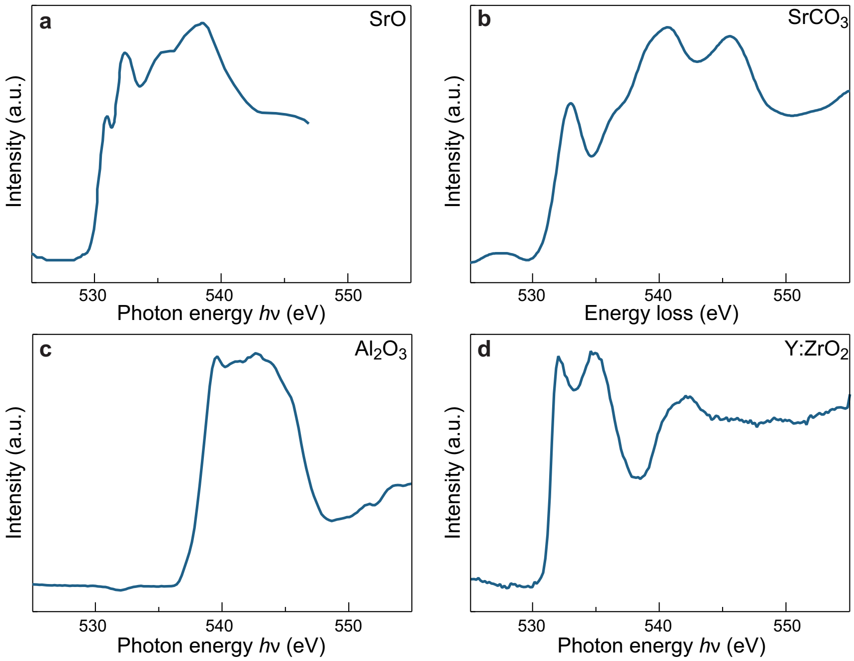

Figure 4.6: O K-edge in different oxides. (a) O K-edge of SrO. Modified from ref. 125. (b) O K-edge of $SrCO_3$ measured using EELS. Measurement performed by Dr. Hongchu Du, Peter Grünberg Institut and Ernst Ruska-Centre, Forschungszentrum Jülich GmbH, Jülich, Germany. (c) O K-edge of an α-Al_2O_3 single crystal measured using PEEM. (d) O K-edge of a 100 nm 8 at.%-Y:ZrO_2 thin film measured using PEEM.

A change in the A/B_2 ratio was also observed in $SrTiO_3$ films of different cation stoichiometry (Fig. 4.5). Comparing a film with roughly 2 % Ti excess (determined through angle-dependent XPS as described in the following section) with a rather stoichiometric film first of all shows differences in the overall intensity of the Ti L-edge for both the characteristic peaks and the edge jump (difference in intensity of pre- and postedge). This is expected from the different total Ti content of the sample. In addition, the peak A intensity of the O K-edge varies between both samples. For the Ti-rich sample, one finds a higher peak A intensity. This may be indicative of a decreased electron concentration in the conduction band, which is expected from defect chemistry. In Ti-rich films, the major defects are acceptor-type Sr vacancies. As the electron density decreases with increasing acceptor concentration, this trend would be expected. It cannot be ruled out, however, that the change in the O K-edge is also directly caused by the Ti-excess, as peak A is caused by the hybridization of Ti and O states.

As oxide heterostructures will be analyzed in addition to $SrTiO_3$ thin film devices, Fig. 4.6 shows the O K-edge of several oxides of interest as a reference for further discussions. The O K-edge of SrO exhibits several broad features between 530 and 540 eV. $SrCO_3$, which commonly forms on the surface of SrO in ambient atmospheres, shows a sharp feature around 532 eV and two broad features at 540 and 545 eV, making it clearly distinguishable from SrO. In this case, the O K-edge was measured using EELS, which in principle contains the same information as XAS even though subtle differences may occur due to excitation by electrons or photons, respectively [126]. The Al_2O_3 spectrum possesses only one broad peak between 538 and 545 eV, similar to literature references [127]. The spectrum obtained from an $Y:ZrO_2$ thin film exhibits two sharp features at 532 and 535 eV and a broad peak at 542 eV, again similar to literature references [128, 129]. All of these spectra can easily be differentiated from the $SrTiO_3$ spectrum.

4.2 X-ray photoelectron spectroscopy of $SrTiO_3$ single crystals and thin films

As was demonstrated recently, the cation stoichiometry of complex oxide thin films for memristive devices has a large impact on the switching and retention properties [80, 130, 131]. At the same time, non-stoichiometric surface (termination) layers can have a similar impact, as will be discussed in chapters 6 and8. During growth of complex oxide thin films, unintentional change of surface termination was observed [97], and the accomodation of non-stoichiometries and possibly resulting defect formation during growth are still under debate [132–134]. It is therefore imperative to precisely determine and control both stoichiometry and surface termination of complex oxide thin films and their substrates to tailor their properties and their interplay.

To date, both quantities are typically determined separately using established non-destructive techniques such as X-ray photoelectron diffraction [135, 136], ion scattering spectroscopy [137], coaxial impact collision ion scattering spectroscopy [138], scanning transmission electron microscopy [139, 140], and scanning probe microscopy [96, 141–143] for the termination and Rutherford backscattering spectrometry as well as XPS for the stoichiometry [144–146]. While XPS presents the most accessible tool for the determination of thin film stoichiometry, the impact of the termination layer is usually not taken into account when the films are compared to reference data, although Zhang et al. pointed out that different terminations of single crystals lead to differences in the intensity ratios by as much as 17 %, which can lead to dramatic errors in the stoichiometry estimate [147].

At the same time, as this section will demonstrate, analysis of the angle dependence inherent to this termination-dependent X-ray photoelectron intensity renormalization provides a unique tool to directly determine the substrate or thin film termination and stoichiometry simultaneously. A simple analytical model is presented, which accurately describes the angle dependent cation X-ray photoelectron intensity ratio of $SrTiO_3$ single crystals with different terminations. In a second step, this model is applied to demonstrate that during homoepitaxial $SrTiO_3$ growth, excess cations are indeed consumed in a self-organized surface termination conversion before cation defects are incorporated into the film. The results presented in this section have been published in part in ref. 95.

4.2.1 Analytical consideration

In order to quantitatively describe the cation photoelectron intensities, a $SrTiO_3$ single crystal composed of equally spaced layers of TiO_2 and SrO under X-ray illumination is considered as shown in Fig. 4.7. For regions of perfect TiO_2-termination, Ti 2p photoelectrons excited in the first monolayer can leave the crystal unattenuated with intensity $\mathrm{I}_0^{\mathrm{Ti2p}}$, while Ti 2p photoelectrons from deeper layers are attenuated by each $SrTiO_3$ unit cell they have to penetrate. The intensity contribution $\mathrm{I}_k^{\mathrm{Ti2p}}$ from each layer k ($k = 0, 1, 2, ...$) can then be expressed as

$$I_k^{\mathrm{Ti2p}} = I_0^{\mathrm{Ti2p}}\exp(-\frac{ak}{\cos\theta\lambda^{\mathrm{Ti2p}}}) =: I_0^{\mathrm{Ti2p}}\exp(-\xi_k^{\mathrm{Ti2p}}) \tag{4.1}$$

with the lattice parameter $a = 3.905\,\mathrm{Å}$, the inelastic mean free path (IMFP) λ^{Ti2p} for photoelectrons at the characteristic kinetic energy and the photoemission angle θ.

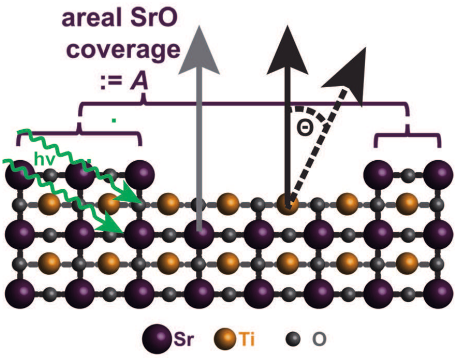

Figure 4.7: Schematic illustration of the photoemission process from $SrTiO_3$ single crystals. Black and grey arrows represent electrons emitted at Ti and Sr ions, respectively. Modified from ref. 95.

Sr 3d electrons, however, are even attenuated if they are excited within the first unit cell, since they have to penetrate the terminating TiO_2-monolayer. Consequently, Sr 3d photoelectrons from layer k are attenuated by $k + 0.5$ unit cells and their intensity can be expressed as

$$I_k^{\mathrm{Sr3d}} = I_0^{\mathrm{Sr3d}} \exp(-\frac{a/2}{\cos\theta\lambda^{\mathrm{Sr3d}}}) \exp(-\xi_k^{\mathrm{Sr3d}}). \tag{4.2}$$

Following the same considerations for regions of perfect SrO-termination, one arrives at the following expressions for the total intensities:

$$I_{\mathrm{tot,TiO_2-term}}^{\mathrm{Ti2p}} = I_0^{\mathrm{Ti2p}} \sum_{k=0}^{\infty} \exp(-\xi_k^{\mathrm{Ti2p}}) \tag{4.3}$$

$$I_{\mathrm{tot,TiO_2-term}}^{\mathrm{Sr3d}} = I_0^{Sr3d} \exp(-\frac{a/2}{\cos\theta\lambda^{\mathrm{Sr3d}}}) \sum_{k=0}^{\infty} \exp(-\xi_k^{\mathrm{Sr3d}}) \tag{4.4}$$

$$I_{\mathrm{tot,SrO-term}}^{\mathrm{Ti2p}} = I_0^{\mathrm{Ti2p}} \exp(-\frac{a/2}{\cos\theta\lambda^{\mathrm{Ti2p}}}) \sum_{k=0}^{\infty} \exp(-\xi_k^{\mathrm{Ti2p}}) \tag{4.5}$$

$$I_{\mathrm{tot,SrO-term}}^{\mathrm{Sr3d}} = I_0^{\mathrm{Sr3d}} \sum_{k=0}^{\infty} \exp(-\xi_k^{\mathrm{Sr3d}}) \tag{4.6}$$

Equations 4.3 and 4.4 represent the total intensity of Ti 2p and Sr 3d photoelectrons for perfect TiO_2-termination, respectively, while equations 4.5 and 4.6 represent the total intensity of Ti 2p and Sr 3d photoelectrons for perfect SrO-termination.

For a mixed termination, which can be imagined as a perfectly TiO_2-terminated $SrTiO_3$ single crystal with an areal coverage A of a SrO monolayer, as depicted in Fig. 4.7, one arrives at

$$\frac{I_{total}^{\mathrm{Sr3d}}}{I_{total}^{\mathrm{Sr3d}} + I_{total}^{\mathrm{Ti2p}}} = \frac{(A + B\exp(-\frac{a/2}{\cos\theta\lambda^{\mathrm{Sr3d}}}))N_0^{\mathrm{Sr}}\sigma^{\mathrm{Sr}}}{(A + B\exp(-\frac{a/2}{\cos\theta\lambda^{\mathrm{Sr3d}}}))N_0^{\mathrm{Sr}}\sigma^{\mathrm{Sr}} + (A\exp(-\frac{a/2}{\cos\theta\lambda^{\mathrm{Ti2p}}}) + B)N_0^{\mathrm{Ti}}\sigma^{\mathrm{Ti}}} \tag{4.7}$$

with the total atomic concentrations N_0^x and the sensitivity factor σ^x for cation x and the areal coverage of TiO_2-termination $B = 1 - A$.

Equation 4.7 describes the cation photoelectron intensity ratio as a function of only the photoemission angle θ for a given surface termination and stoichiometry. While this model does not include the positions of scattering atoms within the crystal, which are the essential part of the complex photoelectron diffraction models, it treats the crystal semi-continuously. This leads to much easier fitting of the model to experimental data and does not require a high angular resolution, as will be shown in the following sections.

The stoichiometry of the crystal is represented through the total atomic concentrations N_0^{Ti} and N_0^{Sr} in equation 4.7. This expression is valid as long as the approximate position of each species (i.e., the depth k, at which the photoelectron is excited) remains the same as in the stoichiometric crystal. It is therefore evident that this model accurately represents crystals with homogeneously distributed point defects, while quantitative errors may occur in the descriptions of highly non-stoichiometric $SrTiO_3$ crystals, which have been shown to possess extended defects like Ruddlesden-Popper phases [148]. This is discussed in detail in section 4.2.4.

The transmission efficiencies of the XPS lens system may vary with photoelectron energy (i.e., between Ti 2p photoelectrons and Sr 3d photoelectrons). Resulting energy dependences of $\sum_{k=1}^{\infty}\exp(-\xi_k)$, however, are included in the calibration of the sensitivity factors, which is performed using $SrTiO_3$ single crystals of known termination and stoichiometry, as shown below.

4.2.2 Termination determination in $SrTiO_3$ single crystals

After fabrication and *in situ* AFM analysis, $SrTiO_3$ single crystals with increasing amounts of SrO-termination (i.e., samples with 0, 2, 4, 6, and 8 pulses of SrO deposition,

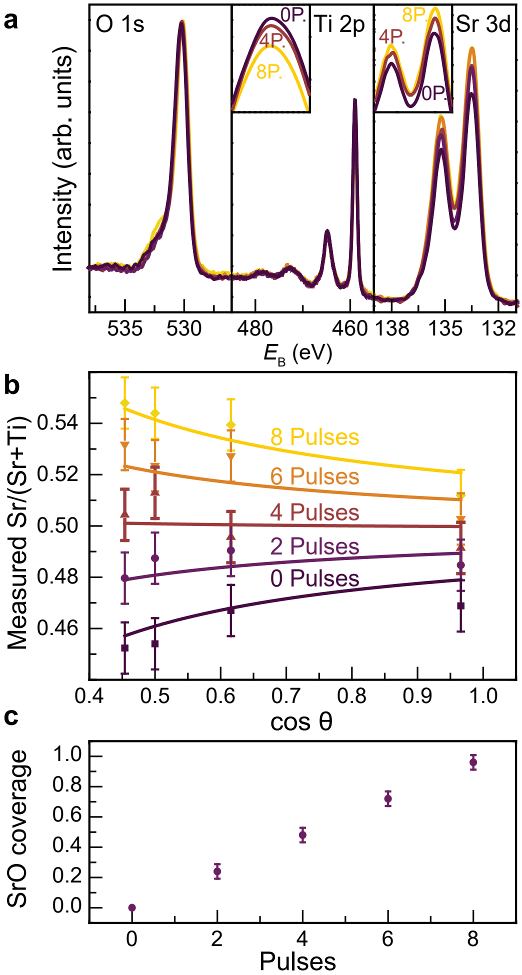

Figure 4.8: XPS analysis and termination determination of $SrTiO_3$ single crystals. (a) Representative XPS spectra for $SrTiO_3$ crystals with increasing amounts of SrO coverage normalized to the O 1s peak intensity. The Ti 2p and Sr 3d peaks have the same shape and binding energy for each sample, indicating the absence of a second phase. Insets: Zoom-in on the peaks for films with 0, 4 and 8 pulses of SrO. (b) Measured cation ratios (data points) as a function of the photoemission angle and fits (solid lines) according to equation 4.7. (c) SrO coverage extracted from the fits in (b). Modified from ref. 95.

compare section 3.1) were characterized by XPS at various photoemission angles. The samples were transferred from one analysis tool to the next in ultra-high vacuum. For each angle, the O 1s, Ti 2p and Sr 3d peaks were measured, indicating relative intensity changes between Ti 2p and Sr 3d but no second phases, as is apparent from the identical peak shapes (Fig. 4.8a). The apparent atomic concentration was extracted for each angle based on the intensity ratios as shown in Fig. 4.8b. As expected, TiO_2 terminated samples show a measured Sr/(Sr+Ti) ratio of less than 0.5 with a further decrease towards more surface sensitive measurements. Mixed termination leads to a rather constant cation ratio, while SrO termination leads to the opposite trend observed for the TiO_2 termination.

For quantitative analysis, this angle dependence was fitted according to equation 4.7. The cation ratio of each sample was constrained to ideal stoichiometry (i.e., $N_0^{\mathrm{Sr}} = N_0^{\mathrm{Ti}}$) and the sensitivity factors were calibrated during the fitting routine. The IMFPss were constrained to literature values of $\lambda^{\mathrm{Ti2p}} = 21$ Å and $\lambda^{\mathrm{Sr3d}} = 26$ Å [104] and the surface termination A – the only physical variation between the samples – was allowed to vary under the constraint of linear increase of SrO termination with the number of pulses. The measured, angle dependent cation ratios and the fits are shown in Fig. 4.8(b), indicating an excellent agreement of the analytical model with the measurement. The generality of the model is underlined by the fact that opening the constraint on IMFP and the linear increase in SrO coverage resulted in very similar IMFP and A values. The results of the fits are summarized in Fig. 4.8c, where a linear increase of SrO termination from 0 % to nearly complete coverage is apparent, which agrees very well with the reflection high energy electron diffraction (RHEED) and AFM results (compare section 3.1).

Accordingly, the model described in equation 4.7 can accurately describe the termination-induced angle dependence of the photoelectron intensity ratios. Therefore, this straightforward measurement (total measurement time of only 3 hours for each sample) can determine the fraction of each terminating layer with high accuracy. It is furthermore obvious that although all of these samples have an ideal cation stoichiometry of 50 % Sr and 50 % Ti, the differences in surface termination would lead to a measurement error of several percent points even for close-to-normal photoemission angles if the termination effects were not included in the analysis of XPS data.

4.2.3 Termination conversion during $SrTiO_3$ thin film deposition

In the next step, four homoepitaxial $SrTiO_3$ thin films were deposited with varying laser fluence, which presents a well-known tool for the fabrication of thin films with different cation ratios [144–146]. After ultra-high vacuum transfer the films were analyzed via AFM and XPS. 20 nm films were obtained as described in section 3.1 on multiple pieces of one TiO_2-terminated $SrTiO_3$ single crystal.

The surface morphology for each film is shown in Fig. 4.9a-d. For the films with lower fluences, the vicinal step surface structure of the substrate is well preserved. For films with higher fluences, the step edges are not as apparent, but the surfaces are equally smooth with a root-mean-square roughness below 0.25 nm. RHEED intensity profiles were obtained through line-by-line integration of the RHEED intensity perpendicular to the diffraction streaks of (-10), (00) and (10). These profiles qualitatively indicate an increase of SrO-termination fraction with decreasing laser fluence (insets of Fig. 4.9a-d), which is apparent from the increasing intensity of the 1st order diffracted electrons compared to the specular spot (compare RHEED intensity plot in Fig. 4.7a and ref. 97).

This qualitative observation is further supported by angle dependent XPS measurements for films deposited with low laser fluences (Fig. 4.9e), which show cation ratio trends indicative of SrO termination (increase of the measured Sr/(Sr+Ti) ratio for increasingly surface sensitive measurements). The opposite trend is observed for higher fluences. Quantitative values for the termination and stoichiometry can be extracted by fitting the angle dependent XPS-measurements according to equation 4.7. For these fits, which are also shown in Fig. 4.9e, the IMFPss and sensitivity factors were fixed to the values determined for single crystals and the amount of SrO-termination and the atomic concentration of Sr, N_0^{Sr}, were allowed to vary. The IMFP values are typically calculated for stoichiometric samples; given the weak dependence of the IMFPs on the stoichiometry or possible defects, however, utilizing these literature values for slightly non-stoichiometric samples is justified. The fit parameters for the thin film stoichiometry and termination are shown in Table 4.1.

From the values for the $SrTiO_3$ thin film stoichiometry and termination extracted simultaneously through these fits, it is obvious that despite appreciable error bars the previously reported qualitative trends of Ti-rich films for high fluences, close to

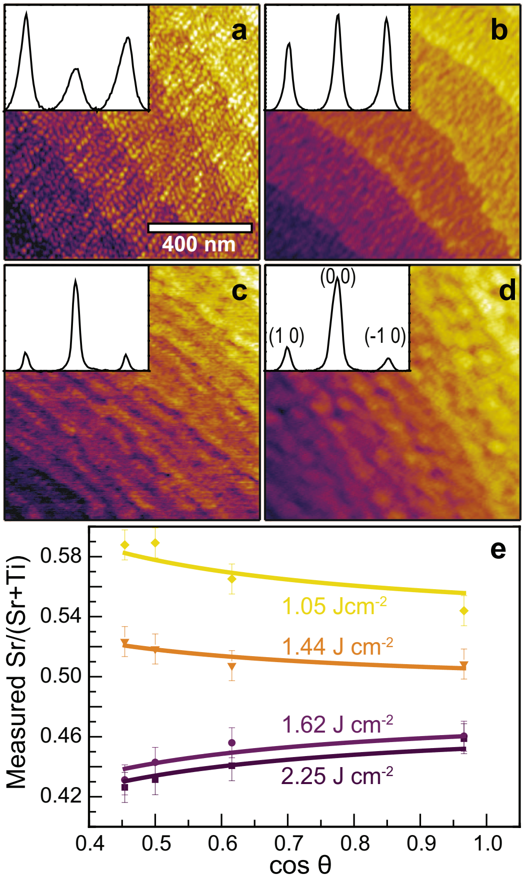

Figure 4.9: Termination and stoichiometry determination for $SrTiO_3$ thin films. (a)-(d) AFM morphology of 20 nm homoepitaxial $SrTiO_3$ thin films grown with a laser fluence of 1.05, 1.44, 1.62 and 2.25 $J{\cdot}cm^{-2}$, respectively. Step terraces are of unit cell height ($\approx 4\,\text{Å}$). Inset: Line profiles extracted from the RHEED pattern after growth. For each case, only the specular spot and 1st order diffracted electrons are detected (each peak is labeled exemplary in (d)). (e) Measured cation ratios (data points) as a function of the photoemission angle and fits (solid lines) according to equation 4.7. Modified from ref. 95.

Table 4.1: Thin film surface termination and stoichiometry.

Fluence (J·cm^{-2})	SrO-term, A	$N_0^{\mathrm{Sr}}/(N_0^{\mathrm{Sr}} + N_0^{\mathrm{Ti}})$
1.05	100 %	54.0 ± 2.0 %
1.44	76 %	49.8 ± 1.6 %
1.62	0 %	48.5 ± 1.6 %
2.25	0 %	47.7 ± 1.6 %

stoichiometric films for medium fluences and Sr-rich films for low fluences holds [144, 146]. It is obvious that the cation ratio difference of films with a similar stoichiometry but different termination layers can be heavily underestimated or overestimated if the termination effect is not considered. This is most apparent for the samples grown at 1.44 J·cm^{-2} and 1.62 J·cm^{-2}. They exhibit a cation ratio difference of just roughly one percent point, but they could be misinterpreted to possess a difference of 5 percent points even for normal emission.

Even more importantly, these results add the additional information of preferential SrO-termination for films grown at lower fluences, for Sr-rich but also for close-to-stoichiometric films. Since the substrates were perfectly TiO_2-terminated, this means that during the growth process, excess Sr ions are consumed in a self-organized surface termination conversion from TiO_2-termination to SrO-termination on a nearly stoichiometric film rather than through incorporation of substantial amounts of defects into the film. This is most apparent for the sample grown at 1.44 J·cm^{-2}, which is stoichiometric but possesses predominant SrO termination. Only upon further decrease of the laser fluence (1.05 J·cm^{-2}) does one observe significant incorporation of this Sr excess into the film. It can therefore be inferred that this incorporation of large amounts of defects starts after the surface termination conversion is completed or if rather large amounts of excess Sr are present.

The evolution of the Sr-excess accommodation during film growth is investigated in more detail using TEM (Fig. 4.10). In line with the assumption based on the XPS measurements, most of the $SrTiO_3$ film (the lower 15 nm) does not exhibit high amounts of defects despite the severe Sr excess during deposition. Instead, only the topmost few nanometers have an increased defect density. This upper layer appears to be separated from the film underneath through the appearance of antiphase boundaries, which are double layers of SrO in a matrix of regular TiO_2-SrO-TiO_2 stacking. These boundaries might nucleate once the surface termination conversion described above is completed

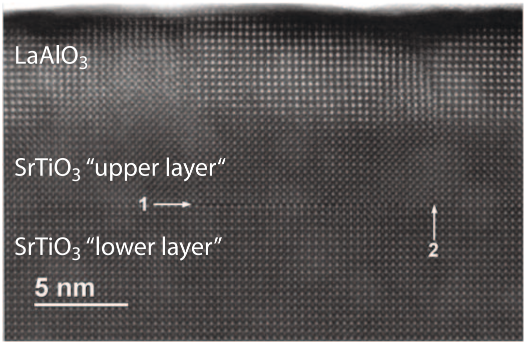

Figure 4.10: High-angle annular dark-field TEM image of the Sr-rich $SrTiO_3$ film. The film was covered by a $LaAlO_3$ protective layer. The bright region at the top of the image is $LaAlO_3$. For the $SrTiO_3$ thin film, two regions can be distinguished: A surface region with a high concentration of defects, and a "bulk" region with a smaller number of defects. The arrows indicate antiphase boundaries separating these regions and penetrating the surface region[1].

and additional SrO needs to be incorporated through another mechanism. One may surmise that they are created through the growth of islands of SrO monolayers on a SrO-terminated $SrTiO_3$ film and subsequent growth of $SrTiO_3$ as described in detail in ref. 93. These additional SrO layers may play an important role in the different resistive switching properties between stoichiometric and Sr-rich devices described below.

4.2.4 Deviations from the point defect model

As extended defects are not taken into account in the analytical consideration presented above, quantitative errors may occur if equation 4.7 is used to describe highly non-stoichiometric $SrTiO_3$ thin films. This section will present two worst case scenarios for this misrepresentation. First, a SrO double layer is incorporated close to the surface of the crystal. In a second step, the entire crystal possesses a Ruddlesden-Popper-type layered structure.

For this purpose, the expected measured cation intensity ratios of the crystals containing these extended defects were analytically calculated and the resulting data points

---

[1] Image courtesy of Dr. Hongchu Du, Peter Grünberg Institut and Ernst Ruska-Centre, Forschungszentrum Jülich GmbH, Jülich, Germany.

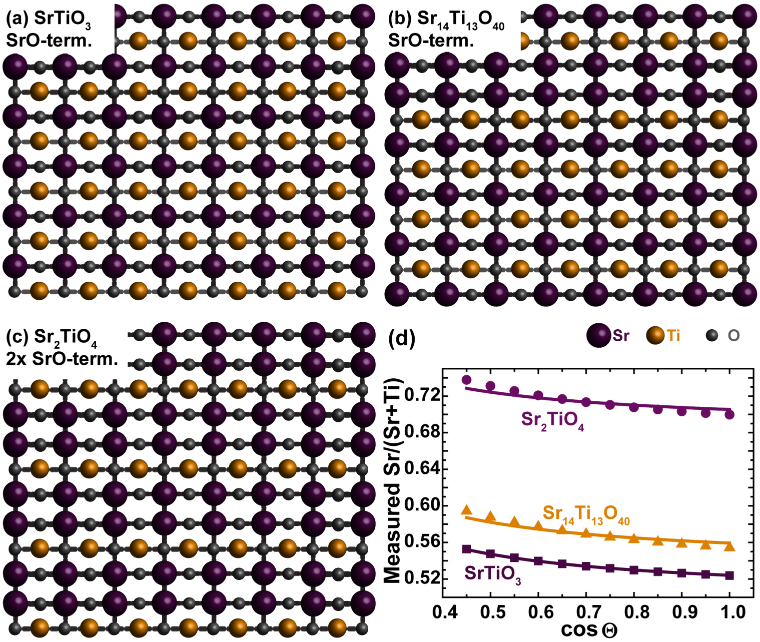

Figure 4.11: Termination and stoichiometry determination for $SrTiO_3$ thin films with severe Sr excess. (a) Schematic illustration of a $SrTiO_3$ single crystals with SrO termination. (b) Schematic illustration of a $Sr_{14}Ti_{13}O_{40}$ single crystals with SrO termination and a double SrO layer burried one unit cell underneath the surface. (c) Schematic illustration of a Sr_2TiO_4 single crystals with a two-layer-SrO termination. (d) calculated cation intensity ratio (data points) as a function of the photoemission angle and fits (solid lines) according to equation 4.7. Modified from ref. 95.

were fitted with the model for the perfect crystal. As shown in Fig. 4.11a, a stoichiometric $SrTiO_3$ crystal with SrO termination, which can be described accurately using equation 4.7 is used as a point of comparison for the defective structures. For the first case of extended defects which might be induced by non-stoichiometric growth, one additional layer of SrO is inserted below the first unit cell (Fig. 4.11b). This could correspond to a 5 nm $SrTiO_3$ film with 2 % Sr-excess, if the entire Sr-excess was consumed in the formation of this Ruddelsden-Popper-type defect. Alternatively, this can be regarded as a Ruddelsden-Popper-phase film with the stoichiometry $Sr_{14}Ti_{13}O_{40}$. This defect is intentionally incorporated as close to the surface as possible to demonstrate the most severe effect such extended defects my have on the measured film stoichiometry. Note that a SrO double layer at the surface of the $SrTiO_3$ crystal is an unrealistic scenario, as it is energetically unfavorable [149].

In a second step, further SrO layers were inserted into the crystal, yielding a Ruddelsden-Popper-phase film with the stoichiometry Sr_2TiO_4 (Fig. 4.11c). This film can hardly be regarded as a non-stoichiometric $SrTiO_3$ film, but it is included in this analysis to demonstrate the maximum effect extended defects like Ruddelsden-Popper-phases can have. For both cases described above, the relative cation photoemission intensities were calculated layer by layer, in a similar way as described in section 4.2.1. For the $Sr_{14}Ti_{13}O_{40}$ film one obtains

$$I_0^{\mathrm{Sr3d}} = I_0^{\mathrm{Sr3d}} \tag{4.8}$$

$$I_1^{\mathrm{Ti2p}} = I_0^{\mathrm{Ti2p}}\exp(-\frac{a}{2\cos\theta\lambda^{\mathrm{Ti2p}}}) \tag{4.9}$$

$$I_2^{\mathrm{Sr3d}} = I_0^{\mathrm{Sr3d}}\exp(-\frac{a}{\cos\theta\lambda^{\mathrm{Sr3d}}}) \tag{4.10}$$

$$I_3^{\mathrm{Sr3d}} = I_0^{\mathrm{Sr3d}}\exp(-\frac{3a}{2\cos\theta\lambda^{\mathrm{Sr3d}}}) \tag{4.11}$$

$$I_4^{\mathrm{Ti2p}} = I_0^{\mathrm{Ti2p}}\exp(-\frac{2a}{\cos\theta\lambda^{\mathrm{Ti2p}}}) \tag{4.12}$$

$$I_5^{\mathrm{Sr3d}} = I_0^{\mathrm{Sr3d}}\exp(-\frac{5a}{2\cos\theta\lambda^{\mathrm{Sr3d}}}) \tag{4.13}$$

$$\ldots \tag{4.14}$$

for the intensity I_k^{Sr3d} or I_k^{Ti2p} from layer k. Summing over all layers of a 5 nm film, one arrives at the angle-dependent intensities indicated in Fig. 4.11d.

For Sr_2TiO_4 one obtains

$$I_k^{\mathrm{Sr3d,layer\,1}} = I_0^{\mathrm{Sr3d}}(\,-\,\xi_k'^{\mathrm{Sr3d}}) \tag{4.15}$$

$$I_k^{\mathrm{Sr3d,layer\,2}} = I_0^{\mathrm{Sr3d}}\exp(-\frac{a'/3}{\cos\theta\lambda^{\mathrm{Sr3d}}})\exp(-\xi_k'^{\mathrm{Sr3d}}) \tag{4.16}$$

$$I_k^{\mathrm{Ti2p,layer\,3}} = I_0^{\mathrm{Ti2p}}\exp(-\frac{2a'/3}{\cos\theta\lambda^{\mathrm{Ti2p}}})\exp(-\xi_k'^{\mathrm{Ti2p}}) \tag{4.17}$$

for the intensity $I_k^{\mathrm{Sr3d,layer\,1}}$, $I_k^{\mathrm{Sr3d,layer\,2}}$ or $I_k^{\mathrm{Ti2p,layer\,3}}$ from the first and second SrO layer and the TiO_2 layer from unit cell k, respectively, with the Sr_2TiO_4 out-of-plane lattice parameter $a' \approx 6$Å and $\xi_k'^{\mathrm{Ti2p}} = \frac{a'k}{\cos\theta\lambda^{\mathrm{Ti2p}}}$. Summing over all layers of a 5 nm film, the angle-dependent intensities indicated in Fig. 4.11d are obtained.

These analytically determined cation intensity ratios for the defective $SrTiO_3$ films were now treated like the measured XPS data analyzed in section 4.2.3 and fitted using equation 4.7. For these fits, which are also shown in Fig. 4.11d, the fraction of SrO-termination and the atomic concentration of Sr, N_0^{Sr}, were allowed to vary. For each case, the best fit is obtained with 100 % Sr-termination. The stoichiometry is summarized in Table 4.2 along with the nominal stoichiometry for each film. For both highly-nonstoichiometric films with extended defects, a reasonable fit with a relative error of below 3.5 % is obtained. This indicates that extended defects can in fact lead to an overestimation or underestimation of the true cation ratio of a given film. At the same time, these worst case scenarios yield a comparably small relative error, especially when compared to the experimental uncertainty or the enormous effect pure termination effects can have (up to 17 %, compare ref. 147 and Fig. 4.9). This analytical model therefore presents a very useful tool for the simultaneous determination of termination and stoichiometry.

Given the appearance of extended defects in the Sr rich film presented in Fig. 4.9a and e and Fig. 4.10, it is imperative to consider the impact these extended defects have on the fit with equation 4.7. As was discussed above, even for the worst case scenarios of extended defects, this fitting routine will result in a relative error below 3.5 %. Careful inspection of the inaccurate fits in Fig 4.11 reveals that the neglect of extended defects in the analytical description results in a misrepresentation of the slope of the measured Sr/(Sr+Ti) ratio, which is compensated by an overestimation of $N_0^{\mathrm{Sr}}/(N_0^{\mathrm{Sr}} + N_0^{\mathrm{Ti}})$ (compare Table 4.1). For thin films free of extended defects, on

Table 4.2: Nominal film stoichiometry and best fit obtained with equation 4.7.

Chemical Formula	True $N_0^{\mathrm{Sr}}/(N_0^{\mathrm{Sr}}+N_0^{\mathrm{Ti}})$	$N_0^{\mathrm{Sr}}/(N_0^{\mathrm{Sr}}+N_0^{\mathrm{Ti}})$ from the fit
$SrTiO_3$	50.0 %	50.0 %
$Sr_{14}Ti_{13}O_{40}$	51.9 %	53.6 %
Sr_2TiO_4	66.7 %	68.6 %

the other hand, the fit perfectly matches the experimental slope. The accuracy of the fit with respect to the slope in the measured cation ratio may therefore be considered as a qualitative hint at the presence or absence of considerable amounts of extended defects.

Coming back to Fig. 4.9e, one can therefore assess the types of defects expected from the XPS analysis. For all films grown with Ti excess or slight Sr excess, the slope of the fitted curve matches the experimental results fairly well. For the Sr-rich film (grown with a laser fluence of $1.05\,\mathrm{J{\cdot}cm^{-2}}$), however, an appreciable deviation between data points and fits is apparent. Based on the XPS analysis one would therefore expect Sr-rich extended defects to be present in the near-surface region of the film, which is exactly what was observed in TEM (Fig. 4.10). In conclusion, the XPS analysis presented in this section - while providing important and fairly accurate information about the film stoichiometry and surface termination - also contains qualitative indications about the defect structure of the near-surface region.

4.3 Summary

In this chapter, the spectroscopic signatures of $SrTiO_3$ were analyzed for both cation non-stoichiometry and anion non-stoichiometry (donor doping). In the first section it was demonstrated that small doping-induced changes in the electronic structure can be determined using XAS or EELS, spectroscopic tools available with high lateral resolution in PEEM or TEM, respectively. While the Ti L-edge is commonly used in literature to determine the carrier density in $SrTiO_3$, it was found here that the O K-edge is much more sensitive for small changes. Based on a comparison with literature, a calibration curve for the A/B_2 peak ratio was obtained as a function of the carrier concentration in the conduction band (i.e., the Ti^{3+} concentration). This calibration curve will be used in section 7.2 to quantify the valence change during resistive switching in $SrTiO_3$.

In the second section, an analytical model for the analysis of angle-dependent cation photoelectron intensity ratios was introduced. The model takes into account both the influence of termination layers and the stoichiometry of the thin film or single crystal. Fitting angle-dependent XPS data with this model allows the extraction of both quantities simultaneously. This was used for the characterization of the as-prepared $SrTiO_3$ thin films grown with different laser fluences. A self-organized surface termination conversion from TiO_2-termination to SrO-termination was observed for films grown at lower laser fluences. Once this termination conversion is completed, additional significant Sr excess appears to be incorporated as Sr-rich extended defects like Ruddlesden-Popper-type antiphase boundaries. Such extended defects are not included in the analytical model and therefore lead to small but noticeable deviations between true angle-dependent cation photoelectron intensity ratios and the fit using the model. Nevertheless, as the relative errors between true cation ratio and the cation ratios determined from the model remain small even for the worst case scenarios considered here, this analytical description presents a novel and straightforward tool for the characterization of oxide thin films and surfaces.

5 Resistive switching and retention in $SrTiO_3$ thin film devices

In this chapter, the resistive switching properties of $SrTiO_3$ thin film devices and noble metal/Nb:$SrTiO_3$ devices will be studied in detail before further spectromicroscopic characterization in the following chapters.

5.1 General switching characteristics and dependence on current compliance

Figs. 5.1a and b show exemplary I-V-curves of memristive devices consisting of a 20 nm $SrTiO_3$ thin film sandwiched between a Nb:$SrTiO_3$ bottom electrode and a square Pt top electrode of $10 \times 10\ \mu m^2$ with 30 nm thickness as discussed in detail in ref. 80. The stoichiometry of the film was determined through variation of the laser fluence as described in section 4.2.3, resulting in a nearly stoichiometric film with Sr/(Sr+Ti)≈0.50 and a Sr-rich film with with Sr/(Sr+Ti)≈0.52, respectively. As these are prototypical I-V-curves for eightwise switching in $SrTiO_3$-based devices, several common features will be briefly introduced.

Before applying high biases, the device exhibits a very high resistance ($\geq 10^8\ \Omega$). Upon application of positive biases on the order of 2-3 V to the top electrode, the device undergoes a soft-forming step (blue lines in Fig. 5.1). At a certain positive bias, the resistance of the device dramatically decreases. To prevent damage to the device, a current limit of several tens of mA is used in the measurement setup. This can be seen by the sudden kink in the forming curve in panel b. After forming, the device is in the LRS with typical resistances of 10^3-$10^5\ \Omega$.

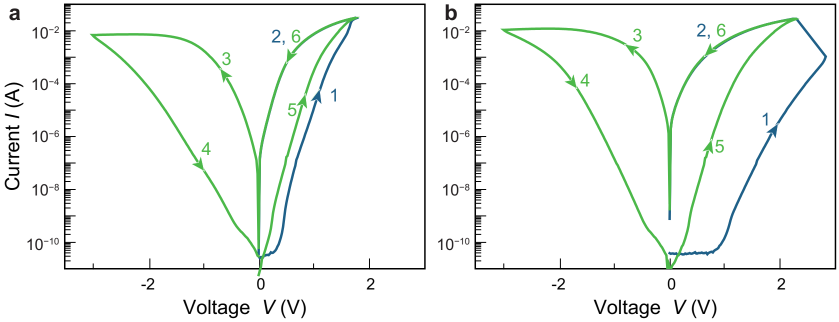

Figure 5.1: Exemplary I-V-curves. (a) Pt/SrTiO$_3$/Nb:SrTiO$_3$ device with Sr/(Sr+Ti)≈0.50. (b) Pt/SrTiO$_3$/Nb:SrTiO$_3$ device with Sr/(Sr+Ti)≈0.52. The forming step is indicated in blue for each case[1].

The device can then be reversibly switched between the HRS (10^8-$10^{10}\,\Omega$) and the LRS through so-called Reset and Set operations, that means through the application of negative voltages on the order of 3-5 V and positive voltages on the order of 1.5-2.5 V, respectively (green line in Fig. 5.1). The Set voltages are typically close to or smaller than the voltage needed for forming.

The influence of the SrTiO$_3$ stoichiometry is discussed at length in ref. 80. The most important differences lie in the lower initial resistance of the stoichiometric devices, which result in a less pronounced forming step. Additionally, the retention times for Sr-rich devices are generally higher than for stoichiometric devices [80]. For the purpose of this work, both stoichiometric and Sr-rich devices were used to study different phenomena. In the following, the SrTiO$_3$ stoichiometry will therefore be indicated for each device under consideration.

As Joule heating plays a significant role in the operation of memristive devices, the current limit plays a crucial role for the switching characteristics. If no current limit is used or the limit is chosen too high, a breakdown due to excessive heat may occur. Inappropriately low current limits, on the other hand, may suppress resistive switching entirely. For intermediate values, the extent of the observed I-V-hysteresis varies. For example, the hysteresis of Au/SrTiO$_3$/Nb:SrTiO$_3$ devices is rather small for 10 mA, while 30 mA already leads to a much larger hysteresis (Fig. 5.2a and b). In particular,

---

[1] Samples fabricated and measurement performed by Nicolas Raab, Peter Grünberg Institute, Forschungszentrum Jülich GmbH, Jülich, Germany.

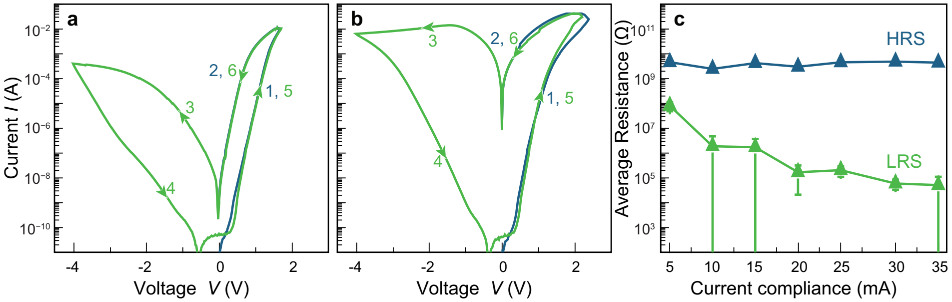

Figure 5.2: Dependence of the switching characteristics on the current limit for Au/$SrTiO_3$/Nb:$SrTiO_3$ devices with Sr/(Sr+Ti)≈0.50. Top electrode size was $10\times10\,\mu m^2$ with a thickness of 30 nm. (a) Representative I-V-curve for a current limit of 10 mA. (b) Representative I-V-curve for a current limit of 30 mA. (c) Average resistance for the LRS and HRS as function of current limit. For each data point, 5 devices were averaged. Error bars indicate the standard deviation.

the value of the LRS is much lower for higher current compliances, while the HRS remains rather constant, leading to an increased $\frac{R_{\text{off}}}{R_{\text{on}}}$-ratio or so-called memory window. This is most obvious when plotting both LRS and HRS as a function of current limit (Fig. 5.2c). In the following, the current limit will therefore be indicated for each device under consideration.

5.2 I-V-characteristics for different top electrode materials

As the Schottky barrier between top electrode and the $SrTiO_3$ dominates the transport mechanism in the device (compare sections 2.2 and 2.3), the choice of top electrode material may have a large impact on the virgin resistance as well as on LRS and HRS values. Throughout this thesis, different top electrode materials will be used for specific purposes, making a top electrode comparison imperative. Specifically, Pt top electrodes are the standard choice for $SrTiO_3$-based devices, Au top electrodes were used to enable spectromicroscopic analysis after electrode removal (see chapter 6), and ultrathin Rh and graphene electrodes were used for *in operando* spectromicroscopy.

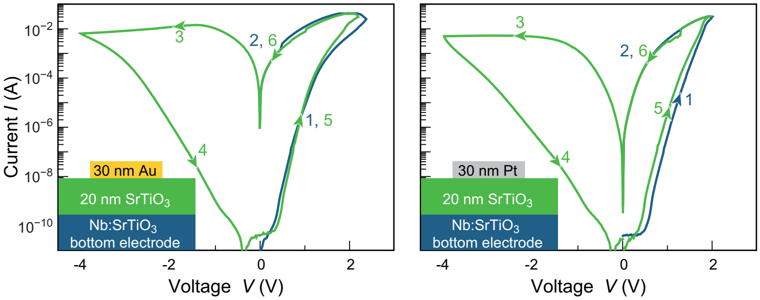

Figure 5.3: Comparison between Au and Pt top electrodes for devices with Sr/(Sr+Ti)≈0.50 with a current limit of 30 mA. (a) Au top electrode. (b) Pt top electrode. Top electrode size was 10×10 µm^2 with thickness of 30 nm.

Representative I-V-curves for Pt and Au top electrodes are shown in Fig. 5.3. Similar eightwise switching is observed and similar resistance values can be obtained using the same switching parameters. Only subtle differences can be seen in the shape of the I-V-characteristics and the absolute resistance values, mainly for the LRS. This might be due to sample-to-sample variations, e.g. because of subtle differences in the $SrTiO_3$ stoichiometry, or due to differences in the microstructure of the electrode, which is very important for the switching mechanism, as will be discussed in chapter 8. Differences in the Schottky barrier, which might be expected given the slightly different work functions of 5.0-5.5 eV for Au and 5.1-5.9 eV for Pt [150] are apparently not as important as the HRS appears to be less affected.

Typically, the top electrodes of these devices are contacted using a W whisker probe, allowing easy access without the need for complex fabrication steps. For *in operando* measurements or operation in different atmospheres, however, this is not suitable and a more sophisticated architecture using metal leads for the contacting of the top electrodes was used as described in section 3.2. Fig. 5.4 shows that this results in similar switching characteristics, validating this approach. Again, small variations in the sample stoichiometry might be responsible for the differently shaped LRS curve. Due to small but detectable leakage currents between metal lead and bottom electrode, the minimum currents measured in the HRS using the metal leads are slightly higher than for the devices contacted directly (compare the minimum currents of the forming steps in Fig. 5.4a and b). But these leakage currents do not appear to impact the resistive switching.

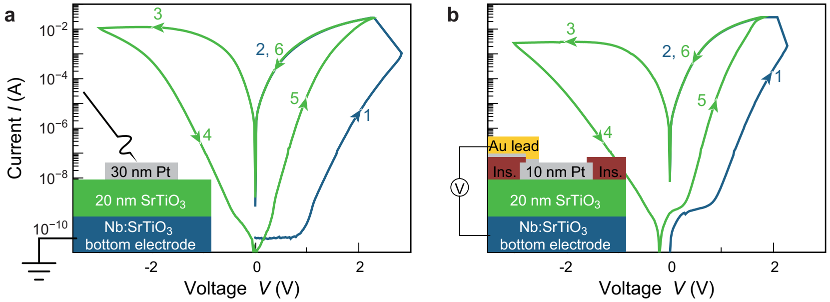

Figure 5.4: Comparison between Pt top electrodes contacted with a tungsten probe (a) or a Pt/Au lead (b) for devices with Sr/(Sr+Ti)≈0.52 and a current limit of 30 mA. Top electrode size was 10×10 µm^2 with thickness of 30 nm for (a) and 16×19 µm^2 with thickness of 10 nm for (b).[2]

As discussed in the introduction, *in operando* PEEM characterization is a highly desirable approach for the investigation of memristive devices. The main challenge in the implementation is to overcome the high surface sensitivity of photoemission. Therefore, two ultra-thin top electrode materials are investigated. Due to the small thickness, contacting with whisker probes was not possible and metal leads were used as described above. In a first step, a thin layer of Rh was used. Rh has the benefit of weaker photoelectron absorption compared to Pt or Au [123] while it is chemically similar with a work function around 5.0-5.2 eV [150]. A thin layer of just 2 nm Rh was sufficient to achieve complete coverage of the SrTiO$_3$ thin film, as confirmed by AFM. Again, eightwise switching was observed, but the shape of the I-V-curve exhibits some differences compared to Pt or Au electrodes (Fig. 5.5a). In particular, higher positive voltages were needed for the Set operation and the HRS is not quite as insulating as before. The higher voltages necessary for the Set may be connected with the observation that no forming or Set was possible for thicker Rh top electrodes with a thickness of 30 nm. Notwithstanding these differences, operation with Rh electrodes allows typical resistive switching and is therefore suitable for *in operando* measurements.

To achieve even thinner electrodes, graphene monolayers were used. Graphene - though strictly speaking not a metal - is highly conductive and has a work function comparable

---

[2] The impact of electrode size will be described in detail in the PhD thesis of Nicolas Raab, Peter Grünberg Institute, Forschungszentrum Jülich GmbH, Jülich, Germany.

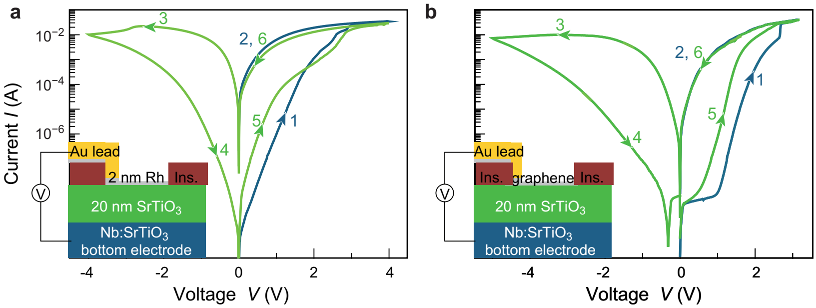

Figure 5.5: Comparison between Rh (a) and graphene (b) top electrodes for devices with Sr/(Sr+Ti)≈0.52. The current limit was set to 35 mA and 40 mA, respectively. Top electrode size was $16 \times 19\,\mu m^2$. Modified from ref. 112.

to noble metals (4-5 eV depending on production method and chemical and electrostatic doping) [151], making it an attractive electrode candidate. Resistive switching in $SrTiO_3$-based devices with graphene top electrodes yields astonishingly similar I-V-curves compared to Au or Pt (Fig. 5.5b). Combined with the atomic thickness, this makes graphene the ideal candidate to study buried layers using spectromicroscopy as will be verified in chapter 7.

5.3 Thickness dependence

As different film thicknesses can lead to the observation of opposite switching polarities [54,59], $SrTiO_3$ thin film based devices of different film thickness were characterized and compared with noble metal/Nb:$SrTiO_3$ junctions[3]. Interestingly, qualitatively similar eightwise switching with only subtle differences in the switching parameters was observed for Nb:$SrTiO_3$ and all $SrTiO_3$ thicknesses up to 40 nm, which is in contrast to the observations for Sr_2TiO_4 [59] and Fe:$SrTiO_3$ [54].

---

[3] A part of the I-V-measurements presented in this section was performed by Philipp Michael Müller, Peter Grünberg Institute, Forschungszentrum Jülich GmbH, Jülich, Germany, as part of his master's thesis.

Nb:$SrTiO_3$

In a first step, the low-current switching regime ($\leq$ 100 µA) of Pt/Nb:$SrTiO_3$ devices with different electrode size was characterized. All devices show qualitatively similar I-V-hystereses, which superpose each other when normalized to the junction area (Fig. 5.6a). Both HRS and LRS accordingly show linear scaling of the resistance with the junction area. Thus, one can conclude that the current distribution below the Pt electrode exhibits a laterally homogeneous, non-filamentary character with eightwise switching polarity. A similar behavior was observed before for Pt/Nb:$SrTiO_3$ junctions operated with such small currents limits [65].

Upon application of significantly higher current limits, however, the normalized I-V-hystereses do not superpose each other. Instead, smaller devices show a higher LRS current density and a higher HRS current density than larger devices (Fig. 5.6b). This behavior is due to a more pronounced forming step. The homogeneous switching for low current compliances observed above is forming free, the HRS current is equal to the virgin current and the first Set sweep and subsequent sweeps superpose each other. Higher currents in the mA range, on the other hand, lead to a soft-forming step, the first Set sweep and subsequent Set sweeps do not superpose each other (Fig. 5.6c). The difference between the first and the second Set increases with decreasing junction area for a given current limit, i.e., with increasing current density. In line with the vanishing of the area scaling of both LRS and HRS observed here, forming steps in such junctions have been proposed to yield filamentary switching [65]. However, the switching polarity as well as the shape of the I-V curves do not change upon forming, indicating a similar underlying mechanism.

To verify the filamentary switching and to visualize switching-induced local changes of the electronic and chemical structure, memristive Au/Nb:$SrTiO_3$ devices were characterized using XPEEM as shown in section 6.3.

$SrTiO_3$ thin films

As described above, eightwise switching can also be obtained in $SrTiO_3$ thin film devices. In a first step, 20 nm $SrTiO_3$ devices with different electrode size were characterized for a comparison of the low-current switching regime ($\leq$ 100 µA) with the

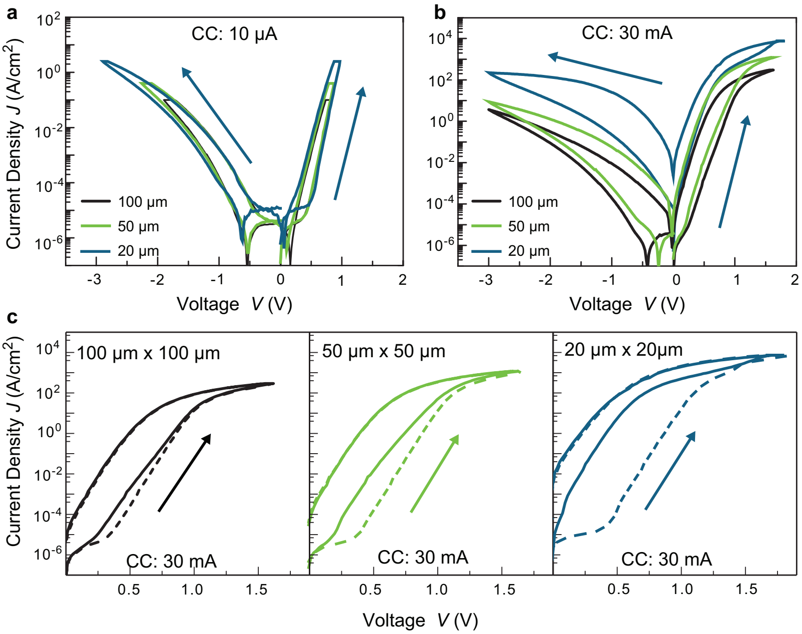

Figure 5.6: Resistive switching in Nb:SrTiO$_3$ with dependence on electrode size and current limit. (a) I-V-characteristic of Pt/Nb:SrTiO$_3$ junctions with different electrode size, normalized to the junction area. In each case, the current limit was set to 10 μA. (b) I-V-characteristic of Pt/Nb:SrTiO$_3$ junctions with different electrode size, normalized to the junction area. In each case, the current limit was set to 30 mA. (c) Forming process (dashed line) and subsequent Set (solid line) for the devices presented in b. The current limit was set to 30 mA for forming and switching.

homogeneous switching observed for Pt/Nb:SrTiO$_3$. All devices show eightwise I-V-hystereses, but the curves do not superpose each other when normalized to the junction area (Fig. 5.7a and b), indicating that no spatially homogeneous switching can be obtained in SrTiO$_3$ thin film devices even for the small currents used here. This is connected with the appearance of a pronounced forming step for much lower current densities than for Nb:SrTiO$_3$ devices (compare Fig. 5.6). As an example, Fig. 5.7c shows the forming step observed for small SrTiO$_3$ thin film devices operated with a current limit of 100 μm. For this current limit, no forming was observed for the Nb:SrTiO$_3$ devices.

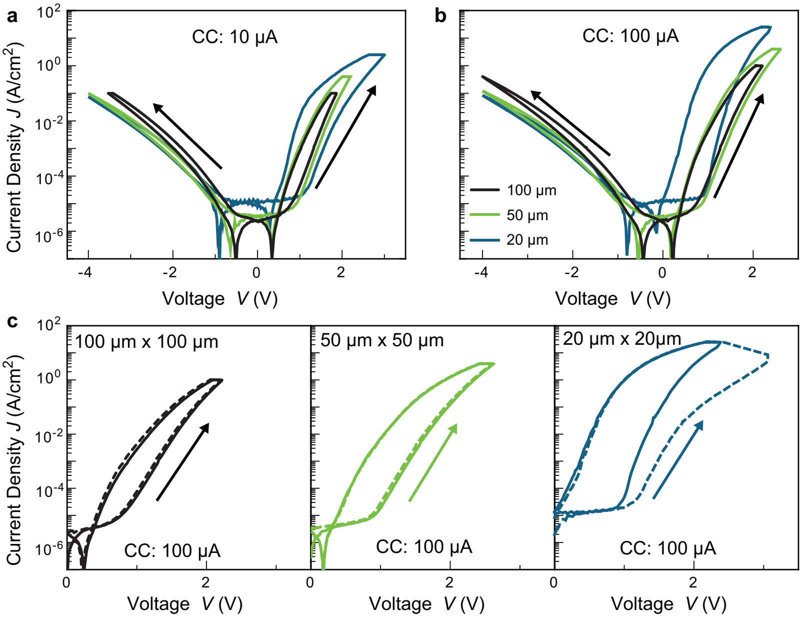

Figure 5.7: Resistive switching in 20 nm $SrTiO_3$ (Sr/(Sr+Ti)≈0.52) with dependence on electrode size and current limit. (a) I-V-characteristic for different electrode sizes, normalized to the junction area. In each case, the current limit was set to 10 µA. (b) I-V-characteristic for different electrode sizes, normalized to the junction area. In each case, the current limit was set to 100 µA. (c) Forming process (dashed line) and subsequent Set (solid line) for the devices presented in (b). The current limit was set to 100 µA for forming and switching.

For higher current limits in the mA range, eightwise switching with a pronounced forming step can be observed for Pt/$SrTiO_3$/Nb:$SrTiO_3$ devices of varying $SrTiO_3$ thickness up to 40 nm[4]. Fig 5.8 shows representative I-V-curves for Nb:$SrTiO_3$ and $SrTiO_3$ thin films of increasing thickness and table 5.1 summarizes the switching parameters. While the general shape of the curves is similar, subtle changes occur. With increasing film thickness, both forming voltage V^{form} and Set voltage V^{Set} increase, which are defined as the voltage at which the current limit is reached. V^{form} increases from 1.78 V to 3.29 V from Nb:$SrTiO_3$ to 40 nm $SrTiO_3$ devices, V^{Set} from 1.74 V to 2.68 V. Interest-

---

[4] For even thicker $SrTiO_3$ thin films, counter-eightwise switching can also be observed, as will be described in detail in the master's thesis of Thomas Heisig, Peter Grünberg Institute, Forschungszentrum Jülich GmbH, Jülich, Germany.

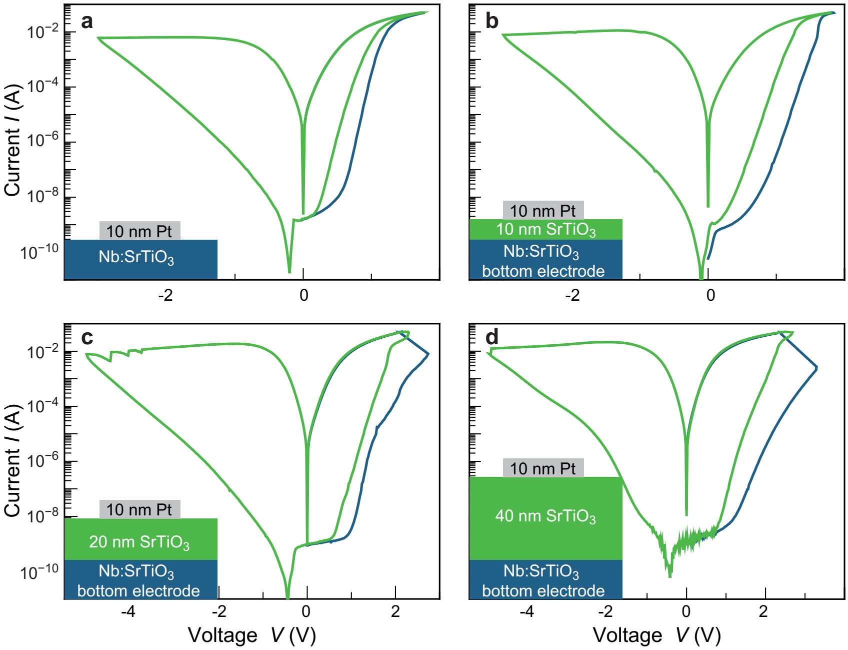

Figure 5.8: I-V-curves for different SrTiO$_3$ thicknesses. (a) Nb:SrTiO$_3$. (b) 10 nm SrTiO$_3$. (c) 20 nm SrTiO$_3$. (d) 40 nm SrTiO$_3$. For the thin films, Sr/(Sr+Ti) was ≈0.52. 10 nm Pt top electrodes with a size of $16 \times 19\,\mu m^2$ were used which were contacted using lithographically defined metal leads as described above. Current limit was set to 50 mA.

Table 5.1: Switching parameters for different film thicknesses

	Nb:SrTiO$_3$	10 nm SrTiO$_3$	20 nm SrTiO$_3$	40 nm SrTiO$_3$
R^{initial}	$5.1 \times 10^7\,\Omega$	$3.8 \times 10^8\,\Omega$	$3.5 \times 10^8\,\Omega$	$3.3 \times 10^8\,\Omega$
R^{LRS}	$1.5 \times 10^4\,\Omega$	$3.2 \times 10^3\,\Omega$	$1.2 \times 10^4\,\Omega$	$6.5 \times 10^3\,\Omega$
R^{HRS}	$1.3 \times 10^7\,\Omega$	$1.2 \times 10^8\,\Omega$	$1.7 \times 10^7\,\Omega$	$2.6 \times 10^8\,\Omega$
V^{form}	1.78 V	1.84 V	2.74 V	3.29 V
V^{Set}	1.74 V	1.81 V	2.30 V	2.68 V
V^{Reset}	-3 V	-3 V	-5 V	-5 V

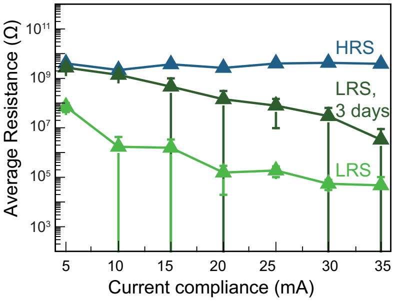

Figure 5.9: Retention as a function of current compliance. Average resistance of the devices plotted in Fig. 5.2c after 3 days. Au top electrodes and 20 nm $SrTiO_3$ thin films with Sr/(Sr+Ti)≈0.50 were used. For each data point, 5 devices were averaged. Error bars indicate the standard deviation.

ingly, it can be observed that the forming step for Nb:$SrTiO_3$ devices and rather thin $SrTiO_3$ films is less pronounced than the forming step for 20 or 40 nm thick devices, i.e., the difference between V^{form} and V^{Set} increases with the film thickness. This goes along with an increase of the initial resistance and HRS resistance with increasing film thickness. For the initial resistance, this trend cannot be observed for the devices presented here due to the aforementioned leakage current from the metal leads, but it was confirmed using top electrodes contacted directly with W probes (data not shown). For the LRS resistance, no clear trend can be observed.

Similar to V^{Set}, the Reset voltage V^{Reset} increases with the film thickness as well. As the Reset is a gradual process [8], the Reset voltage is defined here as the lowest voltage which yields the highest obtainable resistance.

5.4 Data retention and the influence of the surrounding atmosphere

As discussed in the section 2.3, long retention times are mandatory for nonvolatile memory application, but are not necessarily observed in all memristive devices. In this section, the typical room-temperature retention behavior of the devices investigated in this thesis will be briefly summarized.

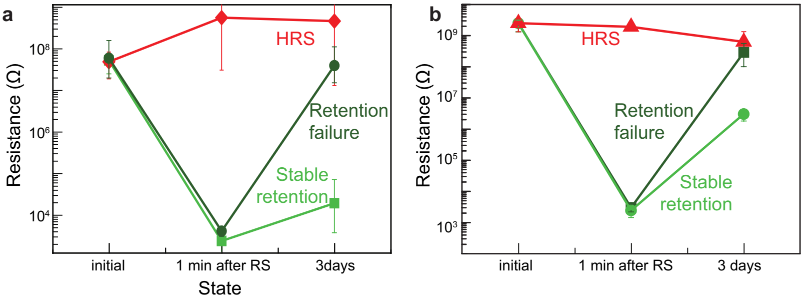

Figure 5.10: Characteristic retention behavior. (a) Retention behavior of different devices on the same chip. Au electrodes on 2 nm $SrTiO_3$ with Sr/(Sr+Ti)≈0.50. The current limit was set to 50 mA. Devices reset into the HRS remain at a constant resistance over several days (red curve). Devices that were set into the LRS show two classes of retention behavior: stable retention and retention failure (bright green and dark green curves, respectively). For each class of retention behavior, the resistance was averaged for five representative devices. Error bars indicate the minimum and maximum values obtained for each resistance state. (b) Retention behavior for Nb:$SrTiO_3$ devices. Modified from refs. 152 and 153.

In transition metal oxide memristive devices, it is generally observed that higher current limits yield improved LRS retention times [83]. The same trend can also be observed for the $SrTiO_3$ thin film devices investigated here (Fig. 5.9). For comparably small current limits of 5-10 mA, the LRS is indistinguishable from the HRS after 3 days, while an average memory window of two orders of magnitude can be maintained for current limits on the order of 35 mA. The rather large error bars indicate a significant device-to-device variation of the retention behavior.

This device-to-device variation becomes even more pronounced for higher current limits (Fig. 5.10a). While the HRS was stable for each device investigated here, two classes of retention characteristics of the LRS were observed, which is the reason for the large error bars observed above. For most devices in the LRS, the resistance increased by several orders of magnitude, indicative of a retention failure, while some devices (≈ 20 %) retained a resistance below 10^5 Ω. A qualitatively similar observation can be made for Nb:$SrTiO_3$ devices (Fig. 5.10b). In the following, these devices will be referred to as devices with a retention failure and devices with stable retention, respectively.

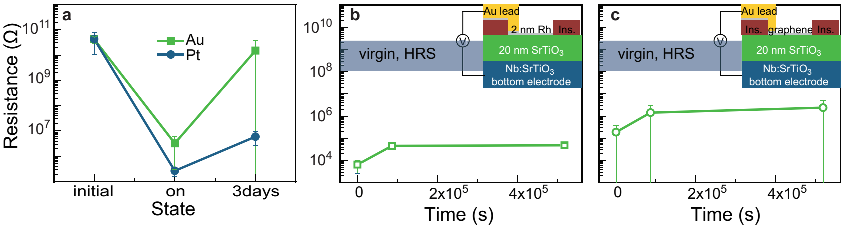

Figure 5.11: Characteristic retention behavior for different top electrodes. (a) Comparison between Pt and Au, current limit was set to 30 mA. LRS retention for Rh top electrodes (b) and graphene top electrodes (c). Current limit was set to 35 and 40 mA, respectively. In each case, Sr/(Sr+Ti)≈0.52 and the resistance was averaged for five representative devices. Error bars indicate the standard deviation.

In the following chapters, these devices will be studied spectromicroscopically to shed light on the switching process itself as well as on the potential retention failure mechanisms. For the investigation of the failure mechanism, devices with different retention times will be compared. For the study of the switching process, devices with stable retention were selected. As different electrode materials will be used for this purpose, the influence of the top electrode on the retention behavior will be briefly reviewed below.

Compared to the devices with Au electrodes discussed above, devices with Pt top electrodes exhibit strongly improved retention times (Fig. 5.11a). From the smaller error bars it can be inferred that they also exhibit a smaller device-to-device variation. For the ultra-thin electrodes, a similarly stable LRS retention can be obtained (Fig. 5.11b and c). Here, it is worth noting that the device-to-device variation is smaller for the Rh top electrodes compared to graphene electrodes, which also exhibit higher LRS resistance in general. The increased variation may be a result of differences in the quality of the graphene-$SrTiO_3$ interface, which are inherent to the fabrication method with a wet transfer of the graphene sheets.

As discussed in section 2.3, reoxidation of the switching filament is believed to be responsible for the retention failure of the LRS and previous studies reported some dependence of the switching characteristics and retention times on the oxygen partial pressure of the surrounding atmosphere [154]. Accordingly, it was investigated if the surrounding atmosphere has an impact on the switching properties and the retention times.

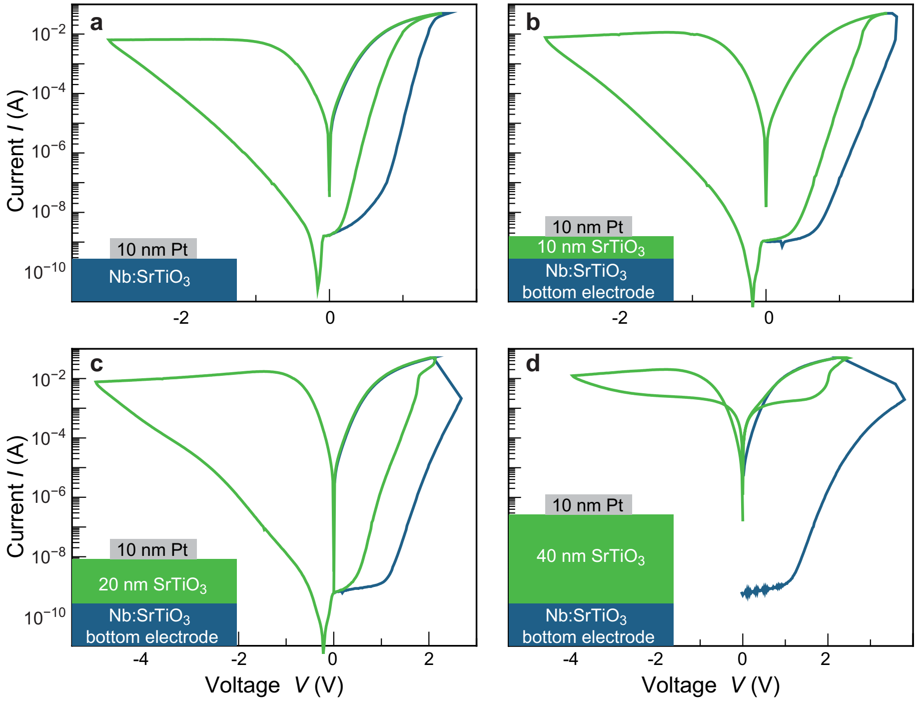

Figure 5.12: I-V-curves in vacuum for different SrTiO$_3$ thicknesses. (a) Nb:SrTiO$_3$. (b) 10 nm SrTiO$_3$. (c) 20 nm SrTiO$_3$. (d) 40 nm SrTiO$_3$. The current limit was set to 50 mA.

Table 5.2: Switching parameters in vacuum for different film thicknesses.

	Nb:SrTiO$_3$	10 nm SrTiO$_3$	20 nm SrTiO$_3$	40 nm SrTiO$_3$
R^{LRS}	$1.0 \times 10^4\,\Omega$	$2.7 \times 10^3\,\Omega$	$5.3 \times 10^3\,\Omega$	$6.4 \times 10^3\,\Omega$
R^{HRS}	$5.0 \times 10^7\,\Omega$	$8.2 \times 10^7\,\Omega$	$1.6 \times 10^7\,\Omega$	-
V^{form}	1.62 V	1.78 V	2.68 V	3.80 V
V^{Set}	1.53 V	1.64 V	2.14 V	2.48 V
V^{Reset}	-3 V	-3 V	-5 V	-
f	0/3	0/4	2/4	4/4

In a first step, all samples from the thickness series were stored in a vacuum of $\approx 10^{-6}$ mbar for 3 days and several devices for each sample were electrically switched in the vacuum environment. Representative I-V-curves are shown in Fig. 5.12 and typical switching parameters are given in Table 5.2. Again, the same trend of increased forming, Set and Reset voltage with increasing film thickness can be seen, but the required voltages are lower than in air for each thickness. At the same time, the HRS values decreased compared to operation in air. Interestingly, some of the devices on the 20 nm sample could not be reset into the HRS at all. The same is true for all devices on the 40 nm sample (compare Fig. 5.12d). Therefore the failure rate f of devices which could not be reset into the HRS in vacuum is listed in table 5.2.

In order to investigate the retention times in vacuum and in ambient atmosphere, several devices of each thickness were set into the LRS and HRS and the resistance of each device was monitored over a period of several days while the devices were exposed to ambient atmosphere or stored in vacuum ($p^{\mathrm{tot}} \approx 10^{-6}$ mbar, Fig. 5.13). One can observe dramatic differences of the retention behavior. For Nb:SrTiO$_3$ devices, the LRS resistance under ambient conditions increases by three orders of magnitude within one day and consequently becomes indistinguishable from the HRS. Under vacuum conditions, however, the LRS resistance remains two orders of magnitude lower (Fig. 5.13a). This indicates that the retention failure of the LRS is caused by a reoxidation through an exchange with the surrounding atmosphere, which can be inhibited through storage in vacuum. In fact, the LRS resistance in vacuum does not change over time after an initial increase. To understand this, it has to be noted that these devices were set to the LRS in air, before the chamber was evacuated. As the resistance increase over time is strongest directly after switching [153], it is reasonable to assume that the Pt/Nb:SrTiO$_3$ devices were partially reoxidized before the chamber was evacuated. Once a vacuum is obtained, the resistance does not appear to change over time. As is evident from the small error bars, all of the devices stored in the same atmosphere exhibited almost identical retention behavior, rendering this a general phenomenon.

Interestingly, the retention behavior of 10 nm SrTiO$_3$ is rather different compared to Nb:SrTiO$_3$. Even in ambient atmosphere, LRS and HRS remain well distinguishable after few days; storage in vacuum only yields a small improvement (Fig. 5.13b). For 20 nm SrTiO$_3$, the LRS is again more stable under vacuum conditions, indicating a

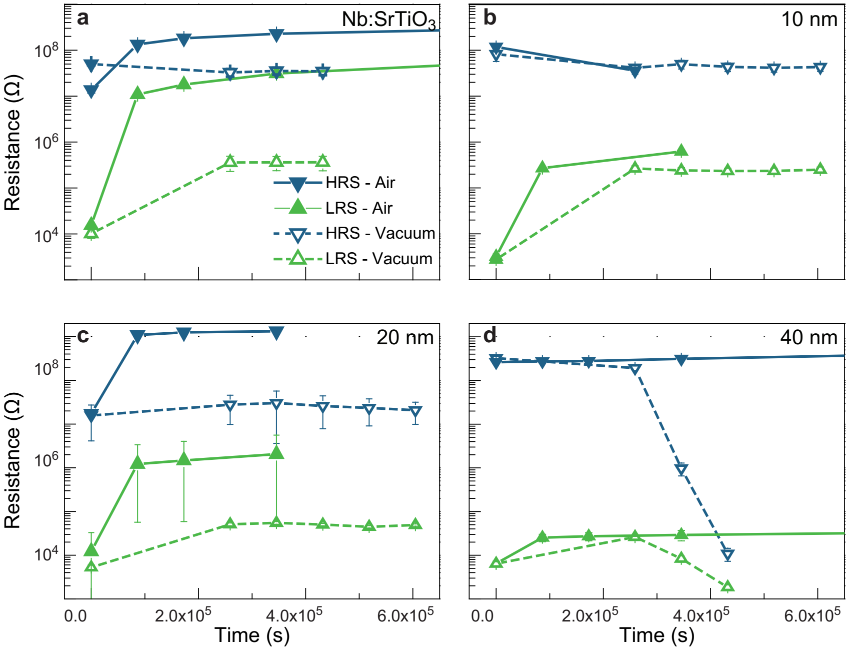

Figure 5.13: Resistance as a function of time for different $SrTiO_3$ thicknesses in air and in vacuum. (a) Nb:$SrTiO_3$. (b) 10 nm $SrTiO_3$. (c) 20 nm $SrTiO_3$. In this case, the measurements in air and in vacuum were performed on two separate samples. (d) 40 nm $SrTiO_3$. The current limit was 50 mA. All devices were switched in air. For retention measurements in vacuum, the chamber was evacuated after each devices was switched and read-out in air. Therefore, only the second data point in the corresponding curves was measured in vacuum.

similar behavior compared to Nb:$SrTiO_3$ (Fig. 5.13c). For 40 nm $SrTiO_3$ films, the retention in air is already stable for all devices in the HRS and LRS investigated here. Storage and read-out in vacuum, however, results in a strong decrease of both resistance states with each read-out. Although read-out voltages (here: read-out sweeps of ±0.5 V) are typically not sufficient to alter the resistance state of a device, there appears to be a so-called read disturb [87] for the 40 nm film in vacuum. This indicates a rather unstable LRS and HRS; for both states oxygen appears to be removed from the $SrTiO_3$ film during read-out sweeps in vacuum. Possibly, this is connected to the occurrence of more severe changes of the top electrode metal with increasing film thickness (Fig. 5.14). For thin films, only slight contrast changes of the electrode appear after switching, which are possibly connected to recrystallization of the Pt due to Joule heat-

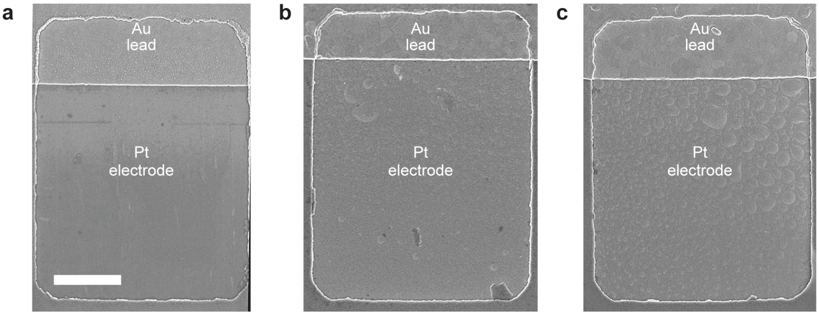

Figure 5.14: SEM images after resistive switching for different film thicknesses. (a) 10 nm. (b) 20 nm. (c) 40 nm $SrTiO_3$. Scale bar, 2 µm. Current limit was set to 50 mA in each case.

ing [54, 155]. For thicker films, bubbles can be observed, which indicate a pronounced release of oxygen from the $SrTiO_3$ film during forming [156]. The significantly modified top electrode structure resulting from bubble formation and potential bursting of the bubbles, in turn, may be responsible for increased interaction with the surrounding atmosphere, it appears to be more permeable to oxygen.

Given the obvious dependence of the switching behavior on the surrounding atmosphere, devices on each sample were also switched in gas atmospheres with different oxygen partial pressures to further elucidate the cause of the difference observed in air and in vacuum. Representative I-V-curves for switching of Nb:$SrTiO_3$ and $SrTiO_3$ devices of different thickness in O_2, N_2 and Ar/H_2 (4% H_2 in Ar) environments are shown in Fig. 5.15. An O_2 atmosphere represents highly oxidizing conditions, N_2 is less oxidizing but nominally not reducing due to some O_2 contamination (99.999 % N_2). Ar/H_2 is a completely reducing atmosphere. While some differences between the different thicknesses are apparent, certain general trends of the switching behavior in different atmospheres can be observed, which can be most easily recognized for the 40 nm film (Fig. 5.15l). The individual resistances (initial, LRS and HRS) are different for each atmosphere, which gives rise to differences in the forming steps and I-V-hysteresis. For all samples, there is a trend to lower resistances with increasingly reducing conditions, indicating an interaction of the active layer (which is burried underneath a Pt electrode) in the virgin state (!), the HRS and the LRS. As panels (a, d, g, j) compare multiple de-

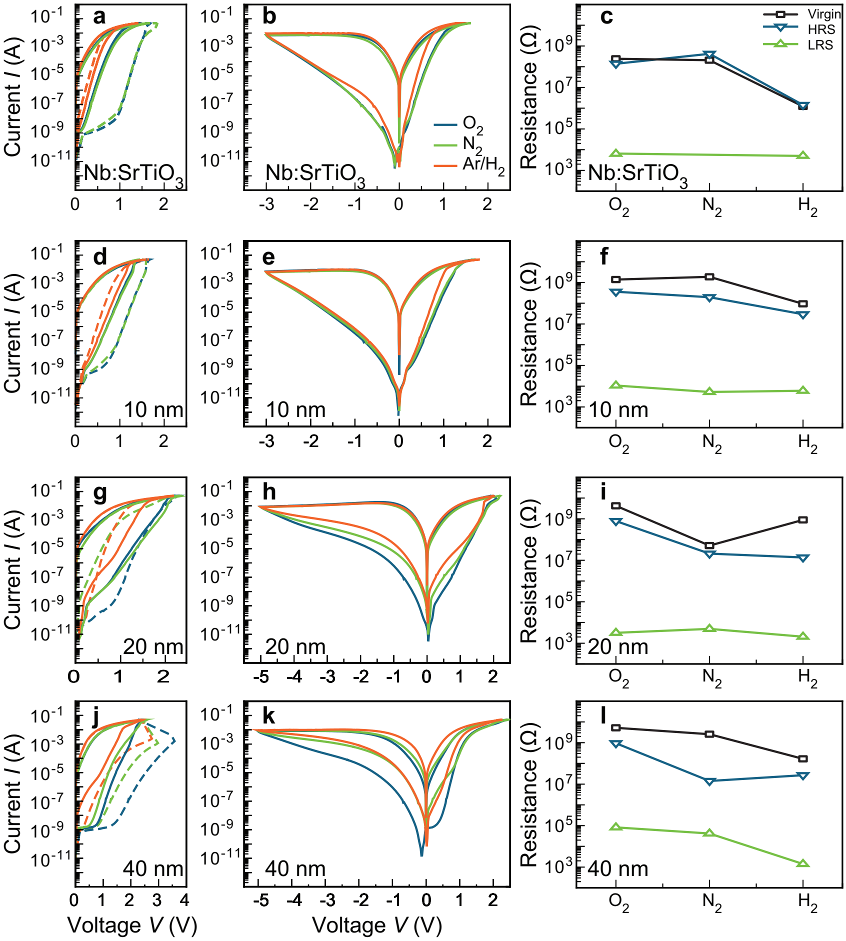

Figure 5.15: Atmosphere-dependent resistive switching for different film thicknesses. (a, d, g, j) Forming step (dashed lines) and subsequent Set sweep (solid lines) for Nb:$SrTiO_3$ devices, 10 nm, 20 nm and 40 nm $SrTiO_3$ devices, respectively. For each atmosphere, a different, previously unaddressed devices was used. (b, e, h, k) *I*-*V*-curves for the same device in different atmospheres. (c, f, i, l) Virgin resistance, HRS and LRS resistance as a function of atmosphere for the devices shown in panels (a, d, g, j) along with the HRS and LRS resistance obtained from the devices in panels (b, e, h, k). Gas pressure for O_2, N_2 and Ar/H_2 was 3 mbar in each case.

vices on the same sample, device-to-device variation gives rise to some data scattering. This is reduced through the comparison of the same device in different atmospheres (panels (b, e, h, k)). Since the oxygen partial pressure of the N_2 atmosphere is given by impurities, some scatter may also be expected for these resistances. Despite these difficulties, the observed trends are certainly indicative of device interaction with the atmosphere during switching as well as without applied biases, which is in line with the observations for operation in vacuum. The reason for the altered switching characteristics and for the stabilized retention in vacuum therefore is confirmed to be connected to oxygen partial pressure of the surrounding atmosphere. This interaction with the surrounding appears to be most pronounced for the 40 nm film. In general, operation in vacuum and in reducing atmosphere is possible for the majority of the devices. This means that the Reset operation requires oxygen from the surrounding atmosphere to achieve the highest possible HRS, but even without oxygen from the surrounding a Reset of about two orders of magnitude remains possible.

It can be concluded that $SrTiO_3$-based memristive devices interact with the surrounding atmosphere - in particular the oxygen partial pressure or chemical potential - before, during and after operation. The implications of this observation will be discussed in detail in chapter 8.

5.5 Oxygen detection experiments

Because of this dependence on oxygen partial pressure, one may surmise that the resistance change involves oxygen evolution during Set and reincorporation during Reset rather than internal oxygen vacancy redistribution during resistive switching as has been suggested for other material systems such as TiO_2 [157] and Si rich SiO_x [158,159]. To test this hypothesis, oxygen evolution during device operation was monitored as described in ref. 159 (Fig. 5.16).[5]

A Pt/Nb:$SrTiO_3$ device and a Pt/20 nm $SrTiO_3$/Nb:$SrTiO_3$ device were switched multiple times in a vacuum chamber using piezo-controlled tungsten probes for electrical con-

---

[5] These measurements were performed in collaboration with Mark Buckwell, Luca Montesi and Prof. Anthony J. Kenyon, Department of Electronic and Electrical Engineering, University College London, London, UK, with the generous help of Dr. Richard J. Chater, Department of Materials, Imperial College London, London, UK.

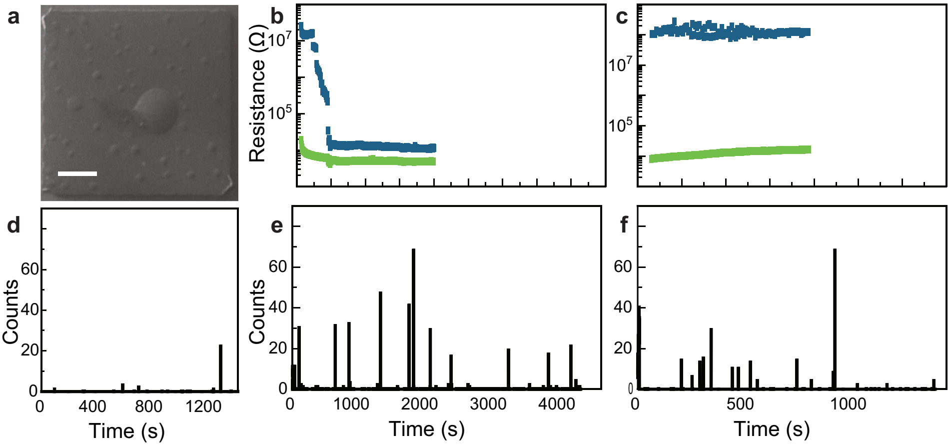

Figure 5.16: Oxygen detection experiments. (a) Secondary electron image of a Pt/Nb:$SrTiO_3$ device after operation and breakdown in vacuum. Scale bar, 2 µm. (b) LRS and HRS resistance of the Pt/Nb:$SrTiO_3$ device as a function of time during cycling with positive and negative voltage pulses. (c) LRS and HRS resistance of the Pt/20 nm $SrTiO_3$/Nb:$SrTiO_3$ device (Sr/(Sr+Ti)≈0.50) as a function of time during cycling with positive and negative voltage pulses. In both cases, the current limit was set to 20 mA. (d) O_2^- ion count as a function of time without applied bias. (e) O_2^- ion count as a function of time during and after the device operation and breakdown in panel (b). (f) O_2^- ion count as a function of time during and after the device operation in panel (c).

tact. The chamber is equipped for secondary electron and secondary ion imaging (using a Ga primary ion beam), a secondary-ion mass spectrometer detector and a residual gas analyzer (RGA). Fig. 5.16a shows a secondary electron image of the Pt/Nb:$SrTiO_3$ device after switching and breakdown exhibiting many small bubbles and one large bubble. The device was switched several tens of times with LRS and HRS values similar to typical operation in air, before the HRS became increasingly low resistive and the device was stuck in the LRS (Fig. 5.16b). The Pt/20 nm $SrTiO_3$/Nb:$SrTiO_3$ device could be switched several hundreds of times without significant changes to the LRS or HRS values (Fig. 5.16c). During the operation of both devices, O_2^- ions could be detected (Fig. 5.16e-f). These O_2^- ions are suspected to be created during oxygen evolution from solid oxides and may therefore be connected to the switching events [159]. The detection events – though not directly related to single switching events – appear to be connected with the operation of the devices as no such events (or at least dramatically fewer in number) can be detected without applied bias (Fig. 5.16d).

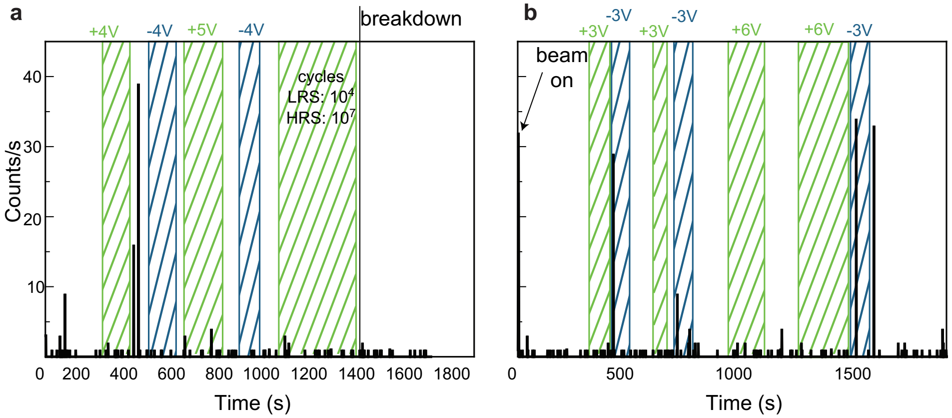

Figure 5.17: ^{18}O detection experiments. (a) $^{18}O_2^-$ ion count as a function of time during and after the device operation and breakdown. Single, individual voltage pulses of increasing magnitude with maximum voltages as indicated were applied during the time intervals which are indicated by the shaded boxes. In a next step, Set and Reset pulses were applied during the time indicated as "cycles". (b) $^{18}O_2^-$ ion count as a function of time during and after the device operation without breakdown. Single, individual voltage pulses of increasing magnitude were applied in the indicated time intervals. The counts at $t = 0\,s$ is caused by the ion beam, which was blanked after this initial peak.

The apparently random distribution of the switching events in time and the occurrence of some events even minutes after the application of biases might be connected to the bubble-burst-mechanism described in ref. 159. This would mean that oxygen-containing bubbles are created during the Set operation and that these bubbles burst at some point in time, releasing the O_2^- ions. Gaseous oxygen would then also be expected to be released, however, measurements with an RGA for similar devices did not detect any increase in O_2 partial pressure. This might be related to the relatively high background count rate during experiments and smaller amounts of oxygen being released for each Set operation of these devices as compared to the electroforming step in SiO_x-devices with brittle TiN top electrodes, where such oxygen release could be detected during forming [159].

In order to confirm that the O_2^- ions are emitted from the $SrTiO_3$ thin film rather than from extrinsic sources such as surface adsorbates, which might be released due to Joule heating, the ion detection experiment was repeated with Pt/20 nm $SrTiO_3$/Nb:$SrTiO_3$ devices where the $SrTiO_3$ thin film had been enriched with oxygen atoms of molecular mass 18 (^{18}O) through isotope exchange at 800 °C for one hour before top electrode deposition. The results are shown in Fig. 5.17, indicating that the detected ions are in fact emitted from the film itself. Unfortunately, no clear connection between individual switching events and ion detection events could be obtained for the reason explained above.

These measurements therefore indicate that oxygen release during each Set operation is a possible mechanism for the resistance change, but do not yield reliable proof of this mechanism, which will rather be presented in chapter 7.

5.6 Temperature dependence

As discussed in section 2.2, the exact transport mechanism in noble metal/$SrTiO_3$ and Nb:$SrTiO_3$ junctions, while potentially containing valuable information about the switching process, cannot be easily inferred from the bare I-V-curve as many different transport mechanisms exhibit a similar I-V dependence at a given temperature (e.g. an exponential dependece). More information may be gained from the temperature dependent transport behavior as the different mechanisms have significantly different dependences on temperature. Therefore, temperature-dependent I-V-hystereses were obtained from several devices operational in vacuum. In addition, the LRS resistance of devices which were switched in air and at room temperature was read-out as a function of temperature for each sample from the thickness series investigated in sections 5.3 and 5.4[6].

Fig. 5.18 shows the temperature-dependent I-V-curves for Nb:$SrTiO_3$ devices and 10 nm $SrTiO_3$ films. While the room temperature measurements for both types of devices are qualitatively similar as discussed above, their temperature-dependence shows noticeable differences. But some general trends can be found in both types of devices which will be discussed first.

The resistance of both devices generally increases with decreasing temperature. This is most easily seen in the right shift of the I-V-curve for both LRS and HRS under positive bias (refer to the upper and lower branches of the I-V-curves in Fig. 5.18 for

---

[6] These measurements were performed by Philipp Michael Müller, Peter Grünberg Institute, Forschungszentrum Jülich GmbH, Jülich, Germany as part of his master's thesis.

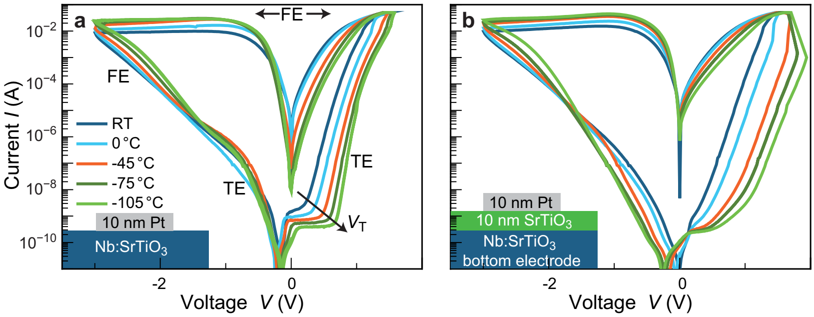

Figure 5.18: Temperature-dependent I-V-curves for (a) Nb:SrTiO$_3$ devices and (b) 10 nm SrTiO$_3$ films. The development of the threshold voltage V_T is indicated. The different regions of the I-V-curves are tentatively assigned to thermionic emission (TE) and field emission (FE) as dominating transport mechanisms as described in the text.

the LRS and HRS, respectively). This shift is most pronounced for the HRS and less so for the LRS.

For negative biases, the LRS exhibits a less temperature-dependent behavior. This results in a higher absolute current for negative biases of the same absolute values compared to positive voltages of the same value (e.g., the absolute current at -0.1 V is higher than at +0.1 V). This is very untypical for regular Schottky barriers where thermionic emission or thermionic-field emission usually dominate. It is indicative of very pronounced field emission contributions, which in turn indicate very high n-doping levels [38]. This unusual behavior may also be the reason for the cross-over of the temperature-dependent I-V-curves in the HRS at negative biases (around -1 to -2 V). At high voltages, the high carrier concentrations play a strong role, resulting in a decreased resistance with decreasing temperature (a metallic behavior, as was also observed for Fe-doped SrTiO$_3$ devices [123]), while at low biases these processes are not as dominant, resulting in the opposite trend. In general, the temperature dependence of the I-V-data at high currents or voltages need to be interpreted carefully as Joule heating may play a significant role. But the trends described here for the HRS and LRS are evident for voltages close to zero, where the impact of Joule heating may still be small.

While these trends can be observed for both Nb:SrTiO$_3$ and SrTiO$_3$ devices, the shape of the I-V-curves at low temperatures are very different. For Nb:SrTiO$_3$ devices, there

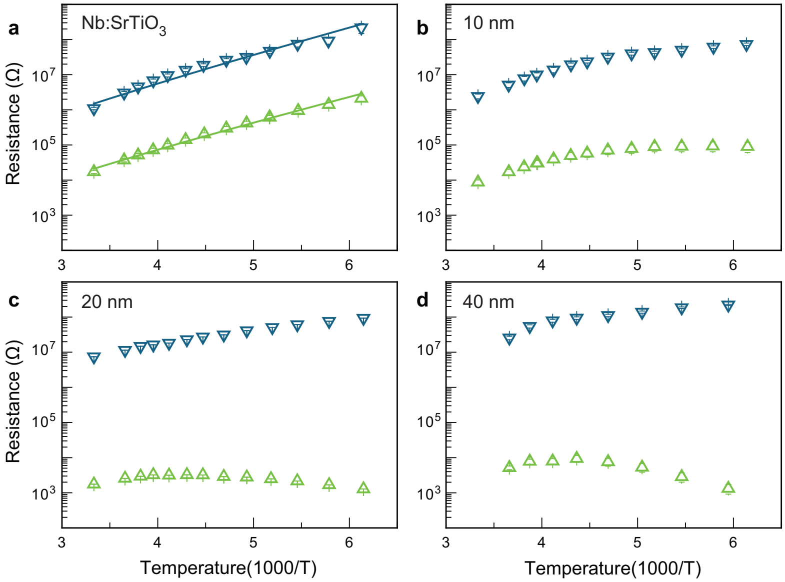

Figure 5.19: Temperature dependence of the LRS (green triangles) and the HRS (blue triangles) for different thicknesses. (a) Nb:SrTiO$_3$. (b) 10 nm SrTiO$_3$. (c) 20 nm SrTiO$_3$. (d) 40 nm SrTiO$_3$.

is an increasingly pronounced threshold voltage V_T for decreasing temperatures, i.e., a transition from an insulating behavior at low voltages to a highly conductive behavior at high positive voltages. Similar to the curves at room temperature, the Set process is rather gradual; there is no sudden jump into the current limit. For 10 nm SrTiO$_3$ devices, V_T is much less pronounced. Instead, a gradual transition to higher conductivity is observed before the Set process occurs. In contrast, the Set process itself becomes increasingly sharp with decreasing temperature, leading to a sudden jump into the current compliance at low temperatures.

As the I-V-behavior at higher voltages is a more complex situation and the switching in vacuum may not be the same as under usual operating conditions, the low-voltage ("read-out") response of devices pre-switched in air will be presented next. Fig. 5.19a shows the LRS and HRS dependence on temperature for Nb:SrTiO$_3$ devices. The same resistance trend with decreasing temperature is obvious as observed in Fig. 5.18. For both LRS and HRS, the resistance increases with decreasing temperature. In fact, the data can be fitted in first approximation with the simple dependency

$$R_{\mathrm{TE}} \propto \frac{1}{J_{\mathrm{TE}}} \propto \frac{c'}{T^2} \exp\left[\frac{c''}{T}\right] \tag{5.1}$$

derived from equation 2.4 with the fitting parameters c' and c''. The fits for both LRS and HRS are shown in Fig. 5.19a, suggesting a different barrier height but the same dominating transport mechanism for both resistance states. Of course, this is an oversimplification as the current over the barrier is certainly more complex, as described in section 2.2, but the agreement between data and simple fit does indicate a thermionic emission-like transport for both resistance states.

An increase with decreasing temperature is again observed for the 10 nm $SrTiO_3$ film (Fig. 5.19b), but a kink in the slope of the linear trend occurs for both LRS and HRS at low temperatures. For the 20 nm $SrTiO_3$ film (Fig. 5.19c), the HRS still exhibits this thermionic emission-like behavior, but the LRS exhibits only very week temperature dependence, which is indicative of field emission currents dominating the transport [38]. The LRS temperature dependence even shows a decrease with decreasing temperature for the 40 nm $SrTiO_3$ film, a 'curvature' from a positive to a negative slope can be observed (Fig. 5.19d). This indicates an almost ohmic contact due to extremely high carrier density. In general, an increased 'curvature' of the LRS resistance can be observed for increasing film thicknesses. For Nb:$SrTiO_3$, only one slope is observed, while the slope decreases for lower temperatures for thicker films.

Based on these observations, the HRS transport mechanism appears to be rather independent of the film thickness and reflects emission over a Schottky-like barrier, as observed for many memristive devices [160]. But the thickness dependence of the absolute values (compare also table 5.1) indicates that the resistance is not completely governed by the interface, but possesses an additional contribution from the $SrTiO_3$ film itself, e.g. through Poole-Frenkel emission or polaron hopping. For the LRS, the transport mechanism is also dominated by emission over the barrier for both Nb:$SrTiO_3$ and thin $SrTiO_3$ films, but the field emission contribution *increases* with film thickness. This is unexpected on first sight and will be considered in detail during the discussion of the switching mechanism (cf. chapter 8).

As was indicated before, the processes dominating the transport across the barrier may vary with the applied voltage. Therefore, Fig. 5.20 shows a comparison of the

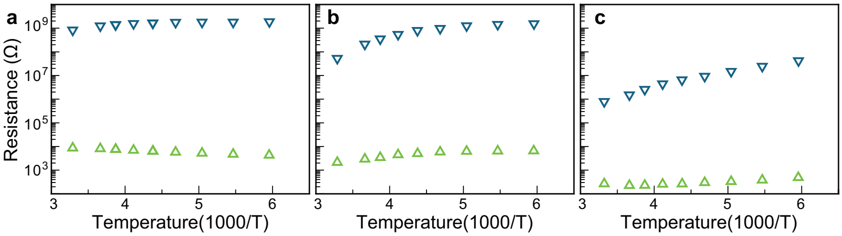

Figure 5.20: Temperature dependence of the LRS (green triangles) and the HRS (blue triangles) for a 20 nm $SrTiO_3$ device for different read-out voltages. (a) Measured at 0 V. (b) Measured at 0.5 V. (c) Measured at 1 V.

resistance of a single device evaluated at different positive voltages (the slope was fitted linearly in a ±0.1 V interval around the specified voltage). For this particular device, the HRS was rather close to the measurement limit, which gives rise to a nearly constant value in Fig. 5.20a. Apart from this, the same trends of thermionic emission over the barrier dominating for the HRS and a field emission-dominated LRS hold for all voltages, justifying why the resistance close to zero was plotted in Fig. 5.19.

5.7 Summary

In summary, resistive switching properties of Nb:$SrTiO_3$ and $SrTiO_3$ thin film devices were investigated comparing different stoichiometries, top electrode materials and film thicknesses. On first sight, all devices exhibit similar eightwise switching, but differences in retention times and switching parameters can be observed. A general trend was observed where thicker $SrTiO_3$ films exhibit a more pronounced forming step and higher HRS values while requiring higher switching voltages.

Regarding the choice of the top electrode material, differences in the I-V-characteristics between different top electrode materials are small, which can be expected based on a similar work function of the electrode materials investigated here. Au top electrodes yield generally bad LRS retention times compared to devices with the regular Pt top electrodes; only few devices show a stable retention. Because of this, they present an attractive platform to investigate the origin of stable retention and retention failure using spectromicroscopy, as presented in chapter 6. Ultra-thin Rh and graphene top electrodes show suitable switching characteristics and sufficient retention for *in operando* characterization as presented in chapter 7.

Importantly, a dependence of both I-V-characteristics and retention times on the oxygen partial pressure of the external atmosphere was found. Reducing atmospheres lead to improved LRS retention and a less pronounced Reset, which leads to a lower HRS value and therefore a decrease of the memory window. This indicates a certain interaction with the surrounding both during and after operation. Oxygen species appear to be necessary for a complete Reset. But for most thicknesses, operation in reducing atmospheres proved to be possible (with the drawback of a lower memory window).

Temperature dependent measurements indicate that the charge carrier transport in Nb:$SrTiO_3$ and $SrTiO_3$ thin film devices is dominated by the Schottky barrier between the high work function top electrode and the $SrTiO_3$. The dominating transport mechanism to overcome the Schottky barrier appears to be thermionic emission in the HRS and the LRS for Nb:$SrTiO_3$ and thin $SrTiO_3$ film (up to $\approx$10 nm) and shifts towards field emission for the LRS in thicker $SrTiO_3$ films.

6 Photoelectron emission microscopy after top electrode delamination

As discussed in chapter 2, the ultimate aim regarding device performance for non-volatile memory applications includes long retention times exceeding 10 years. Excellent retention has been demonstrated for individual devices composed of many different binary and ternary oxides. But for each case, at least a fraction of the devices exhibits very poor retention. The failure mechanism giving rise to this poor retention as well as the switching mechanism itself are not well understood, both have just been loosely connected to oxygen-migration. The details of the switching and and failure mechanism may therefore be elucidated using spectromicroscopy.

In this chapter, spectromicroscopy after top electrode delamination is applied to investigate the local valence state of $SrTiO_3$ devices after device operation and retention failure. For this purpose, memristive devices with Au electrodes were examined. On the one hand, these devices allow for mechanical removal of the top electrodes, which allows for studying the active layer with a surface-sensitive technique such as PEEM. On the other hand, the retention in these devices is typically very poor, but some devices exhibit strongly improved retention, which makes them an intriguing platform for the study of retention failure and stabilization mechanisms. In the first part of this chapter, the method for mechanical removal of the top electrodes will be introduced. Afterwards, the spectromicroscopic signature of the switching and failure mechanisms will be presented for $SrTiO_3$ thin film devices and Nb:$SrTiO_3$/metal junctions. These signatures reveal that both regular device operation and failure are caused by spatially confined redox reactions. The results presented in this chapter have been published in part in refs. 152 and 153.

6.1 *In situ* delamination of the top electrodes

The main challenge in the PEEM characterization of MIM structures is to overcome the high surface sensitivity of photoemission, which limits the probing depth to few nanometers and practically prevents access to the active region covered by top electrodes. For the spectromicroscopic analysis presented in this chapter, the top electrodes were mechanically removed (delaminated) under UHV conditions with an adhesive copper tape after sputter deposition of a homogeneous 30 nm Au layer onto the entire sample. The delaminated sample was transferred into the XPEEM chamber under UHV conditions. Details of the mechanical removal can be found in ref. 54. The complete removal of the Au top electrode is checked by recording the spatially resolved Au 4f XPS spectrum on the former device area and for all presented devices the absence of any gold signal has been verified (with the exception of a small amount of Au residue for the device in the HRS). All XPEEM experiments have been performed at the NanoESCA beamline at Elettra synchrotron laboratory (Trieste, Italy) using the endstation described elsewhere [106].

6.2 $SrTiO_3$ thin film devices

6.2.1 Titanium L-edge

In order to visualize switching-induced local changes of the electronic and chemical structures of $SrTiO_3$, memristive Au/$SrTiO_3$ (2 nm)/Nb:$SrTiO_3$ devices as described in chapter 5 were investigated using XPEEM. As discussed in section 5.4, individual devices on the same sample exhibit retention failure or stable retention, respectively.

Devices with stable retention

In a first step, the devices with stable retention were used to examine the valence change mechanism which is expected to be responsible for the memristive operation of $SrTiO_3$-based cells. After delamination of the top electrode, XPEEM imaging of a representative device with stable retention revealed a switching filament with enhanced

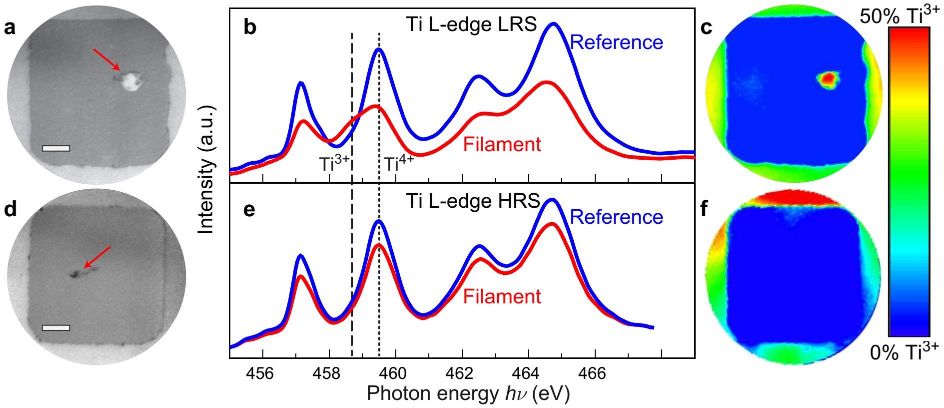

Figure 6.1: XPEEM comparison between LRS and HRS. (a) XPEEM image of a device with a stable retention in the LRS recorded with a photon energy of 458.5 eV. Filament indicated by a red arrow. Scale bar, 2 µm. (b) Ti L-edge spectra extracted from the XPEEM image stack for a region inside the bright filament discernible in (a) (red line) and for the surrounding device area (blue line). (c) False color map of the Ti^{3+} contribution for the device in (a). (d) XPEEM image of a device in the HRS recorded with a photon energy of 458.5 eV. Filament indicated by a red arrow. Scale bar, 2 µm. (e) Ti L-edge spectra extracted from the XPEEM image stack for a region inside the bright filament discernable in (d) (red line) and for the surrounding device area (blue line). (f) False color map of the Ti^{3+} contribution for the device in (d). Modified from ref. 152.

contrast (Fig. 6.1a). As the photon energy $h\nu = 458.5\,\text{eV}$ used in this case corresponds to the Ti^{3+} L_3 e_g absorption edge, one may surmise that the contrast arises because of a reduced Ti valence state inside this filament, which has been expected to be the origin of the low resistance [4, 15–17, 53]. In fact, extracting Ti L-edge absorption spectra for a ROI within this filament and for a reference area from the surrounding reveals a strong contribution of Ti^{3+} within the filament[1], indicated by the dashed line, while the surrounding device area only shows Ti^{4+} contributions, as is expected for stoichiometric $SrTiO_3$ (Fig. 6.1b) [15, 114].

In order to analyze the spatial extent of the Ti^{3+} contribution, false color maps were created by fitting the spectra at each pixel using model absorption spectra for Ti^{3+} and Ti^{4+} in $SrTiO_3$. A color image is created, where the color scale

---

[1] As will be shown below, the 50 mA current limit used here leads to a phase separation. Therefore - in contrast to most devices presented in chapter 7 - the O K-edge cannot be used here for the determination of the carrier density and the Ti L-edge is used instead.

represents the spectral contribution of the Ti^{3+} signal. Before such treatments, the linear, vertical energy dispersion of the beamline exit slit and the parabolic, vertical energy dispersion of the NanoESCA energy filter were corrected as described in ref. 161.

The local confinement of the observed valence change is directly evident from the false color map of the Ti^{3+} contribution for the entire device area as shown in Fig. 6.1c: only for the filament area does one find a significant contribution. Since Ti^{3+} states in $SrTiO_3$ correspond to electrons in the conduction band [4], this region can in fact be regarded as the switching filament. The enhanced contrast surrounding the active device is caused by the dry etching involved in the electrode structuring and is not associated with the device conductance. One may therefore conclude that the resistive switching occurs within this filament due to a local reduction of the Ti.

The difference between LRS and HRS is investigated next. For a device which was switched back to the HRS, no Ti^{3+} spectral contributions could be detected (Fig. 6.1d-f) although XPEEM images indicate the presence of a locally modified area, which can be ascribed to the reoxidized switching filament. This means that during Reset, the switching filament has been reoxidized, as was speculated in chapter 5. This reoxidation occurred in such a way that no Ti^{3+} can be detected using the Ti L-edge, i.e., at least the top few nanometers of the filament have been reoxidized. As a very thin film (2 nm) was investigated here, this indicates reoxidation of the entire filament.

It is interesting to note that in the PEEM image at this photon energy, the HRS filament has a dark contrast compared to the surrounding, which is in contrast to the LRS filament. This indicates that (i) there does not appear to be a strong Ti^{3+} component (which is confirmed by the Ti L-edge spectrum and the false color map) and (ii) that there is a decreased overall Ti intensity in this region, as was also the case for the LRS. The reason for the decrease in intensity will be discussed in section 6.2.2.

Based on the remarkable difference between the spectra extracted for the switching filaments in the LRS and the HRS and the corresponding false color maps in Fig. 6.1, it is directly obvious that there is indeed a pronounced valence change between the different resistance states. In other words, these results demonstrate explicitly that

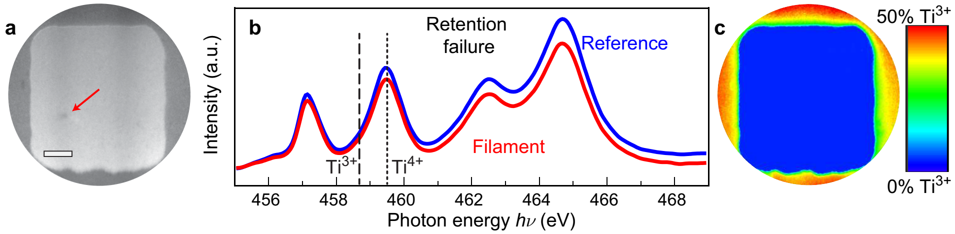

Figure 6.2: Ti L-edge of a device with retention failure. (a) XPEEM image of a device with an LRS retention failure recorded with a photon energy of 459.5 eV. Filament indicated by a red arrow. Scale bar, 2 µm. (b) Ti L-edge spectra extracted from the XPEEM image stack for a region inside the bright filament discernible in (a) (red line) and for the surrounding device area (blue line). (c) False color map of the Ti^{3+} contribution for the device in (a). Modified from ref. 152.

local reduction and reoxidation indeed constitute the fundamental mechanism behind resistive switching in this model system.

Devices with retention failure

As discussed in section 5.4, reoxidation of the switching filament is believed to be responsible for the retention failure of the LRS. Therefore, the local electronic structure of devices with retention failure was analyzed in a next step, as shown for an exemplary device in Fig. 6.2. While the XPEEM images show a small area with a darker contrast, which might be the remainder of a switching filament, the Ti L-edge absorption spectra for this region and the surroundings, and in particular the false color map of Ti^{3+}, reveal that no significant Ti^{3+} contribution is present in the entire device area. Similar to the case of the device in the HRS, this means that the initially reduced switching filament is reoxidized during retention failure.

The role of oxygen migration for the retention of $SrTiO_3$-based devices has already been discussed based on the comparison of the retention characteristics in different atmospheres (cf. section 5.4). The retention times are improved in the absence of oxygen, because reoxidation of the switching filament from the environment appears to be inhibited. Consequently, these results experimentally verify the hypotheses of previous simulation-based models [84], which propose the retention failure of the LRS to be due to oxygen diffusion along the vertical direction.

6.2.2 Oxygen K-edge

The question arises why some devices on the same chip show stable retention, while most devices exhibit retention failure. In order to elucidate the microscopic mechanism for retention stabilization, the local chemical configuration of the switching filaments of the devices shown in section 6.2.1 are investigated in more detail. O K-edge absorption spectra for the filament and the surroundings of the device with stable retention reveal a strong modification of the local environment of the O ions within the filament (Fig. 6.3a). From comparison with literature, it can be assumed that this modification stems from a significant SrO contribution, as the individual peaks A, A', B_1 and B_2 are smeared out into one broad feature and peak C is strongly reduced in intensity [125]. Considering the role of Joule heating during resistive switching (cf. chapter 2), the formation of SrO on the surface of $SrTiO_3$ is plausible as such SrO islands have been previously observed after high temperature treatments exceeding 1000 °C [162–164]. In fact, it has already been shown that Joule heating during electrical treatment is sufficient to promote this phase separation [15, 17, 165].

Performing similar false color mapping as described above (using O K-edge reference spectra for SrO and $SrTiO_3$), Fig. 6.3b,d,f) reveals that this modified O environment is only present within the switching filament for the LRS device with stable retention and the device in the HRS, while it is absent for the device with retention failure. The phase separation is also the reason for the observed decrease in the overall intensity of the Ti L-edge for the devices in Fig. 6.1. On the one hand, this confirms that the difference in the Ti valence rather than the existence or absence of a phase separation is responsible for the resistance change. The different spatial extent of the SrO contribution is suspected to be caused by device-to-device variation. On the other hand, the absence of any SrO signal for the LRS device with retention failure (Fig. 6.3e,f) suggests a connection between the occurrence of the phase separation with the retention behavior. A comparison of all measured devices reveals that this is a reliable trend. Four LRS devices with retention failure and four devices with stable LRS retention were investigated as described above for the representative devices. For all of these devices, no Ti^{3+} or SrO spectral contribution was observed for the devices with retention failure, while all devices with stable retention exhibited a filament with a Ti^{3+} contribution and an SrO interface component. Therefore, the role of this SrO layer for the device retention will be discussed in detail in chapter 8.

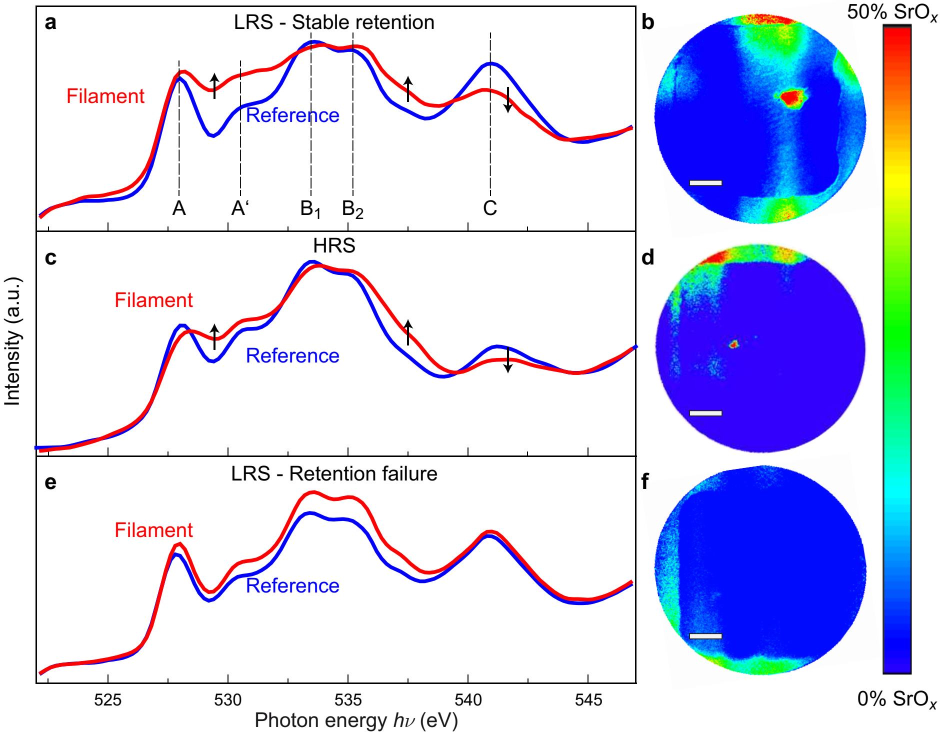

Figure 6.3: Spectromicroscopic fingerprint of the filament chemistry. (a) O K-edge spectra extracted from the XPEEM image stack for the switching filament (red line) and for the surrounding device area (blue line) for the device with stable retention (the same device as in Fig. 6.1(a)-(c)). (b) False color map of the SrO contribution for the same device. The apparent vertical stripe in the center of the device is an artifact from the uncorrected but small horizontal energy dispersion of the NanoESCA energy filter. (c) O K-edge spectra extracted from the XPEEM image stack for a region within the switching filament (red line) and for the surrounding device area (blue line) for the device in the HRS (the same device as in Fig. 6.1(d)-(f)). (d) False color map of the SrO contribution for the same device. (e) O K-edge spectra extracted from the XPEEM image stack for a region within the switching filament (red line) and for the surrounding device area (blue line) for the device with retention failure (the same device as in Fig. 6.2). (f) False color map of the SrO contribution for the same device. Modified from ref. 152.

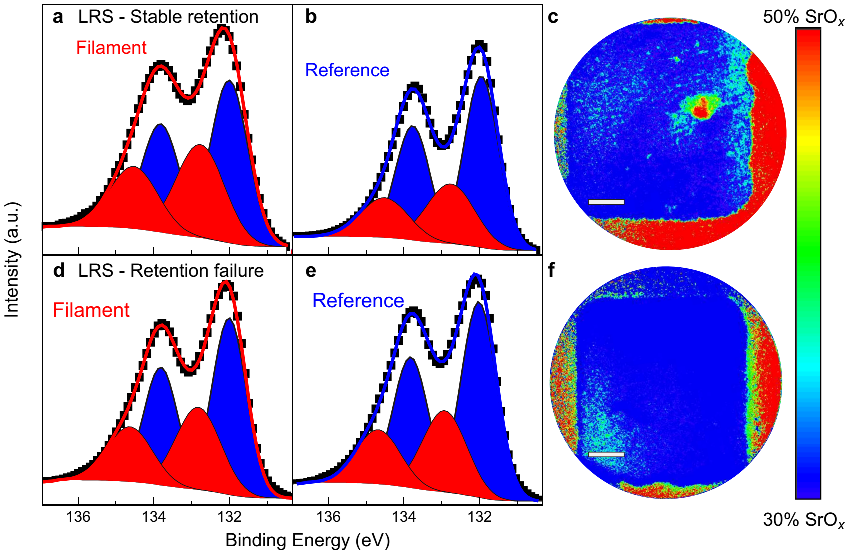

Figure 6.4: XPS analysis of the filament chemistry. (a) Sr 3d spectrum for the switching filament (black data points) for the device with stable retention with a fit (red line) consisting of a bulk component (blue doublet) and a SrO-like surface component (red doublet). (b) Sr 3d spectrum extracted from a region surrounding the switching filament (black data points) for the same device with a similar fit (blue line). The SrO-like surface component is suppressed in comparison with (a). (c) False color map of the SrO contribution for the same device. (d) Sr 3d spectrum for the suspected switching filament (black data points) for the device with retention failure with a similar fit (red line). (e) Sr 3d spectrum extracted from a region surrounding the switching filament (black data points) for the same device and a similar fit (blue line). (f) False color map of the SrO contribution for the same device. Modified from ref. [152].

6.2.3 Sr 3d XPS

As SrO surface components have been detected using XPS before [30, 165], energy-resolved XPEEM was performed for the Sr 3d level to verify the observed phase separation independently. As typically observed for $SrTiO_3$ thin films, the Sr 3d spectra extracted from these scans can be fitted well with a doublet for the bulk contribution and an additional doublet found at 0.8 eV higher binding energy, which corresponds to SrO-type surface components (Fig. 6.4a,b) [30, 165]. As was observed using the O K-edge, the amount of this SrO-type component is significantly higher within the filament of the device with stable retention, as is evident from the representative spectra for the filament and the surrounding and the false color map of the SrO contribution shown in Fig. 6.4a-c. In this case the false color maps were created by fitting the spectra at each pixel using the peak model shown in Fig. 6.4a. For the device with retention failure, there is no indication of this local phase separation in the XPS analysis (Fig. 6.4d-f). The components for the SrO surface component are almost equal in height for the filament and the surrounding. This is confirmed by the false color map, which reveals no significant additional contribution of SrO for the entire device area.

The electron kinetic energy used here was around 60-70 eV, corresponding to the minimum of the kinetic-energy-dependent inelastic mean free path of just 0.5 nm [166]. The surface sensitivity of the XPS analysis thus confirms that the observed phase separation for devices with stable retention yields a Sr-deficient filament with a SrO layer in the surface region (i.e., the electrode-oxide interface before electrode removal).

6.3 Nb:SrTiO$_3$ devices

After the characterization of SrTiO$_3$ thin film devices, Au/Nb:SrTiO$_3$ junctions as described in detail in section 5.3 are investigated spectromicroscopically. As discussed before, large currents in the mA range lead to a pronounced forming step and the suspicion of filamentary switching in these devices, which will now be verified.

After delamination of the top electrode, XPEEM imaging of a representative device in the LRS reveals an area with darker contrast (Fig 6.5a) at a photon energy of 459.5 eV, which corresponds to the Ti^{4+} L$_3$ e$_g$ absorption edge. A direct comparison of the XPEEM image with a C-AFM image of the same device reveals that this area is the only area with increased conductivity (Fig. 6.5d), yielding direct evidence for the filamentary change of the resistance. If the valence change mechanism is responsible for this change of resistance, one would consequently expect this area to exhibit a spectroscopic signature of reduced SrTiO$_3$. Similar to the case of thin film devices, a comparison of the Ti L absorption edge reveals that this switching filament in fact consists of a mixture of Ti^{4+} and Ti^{3+} states [15,114], while the insulating surrounding only

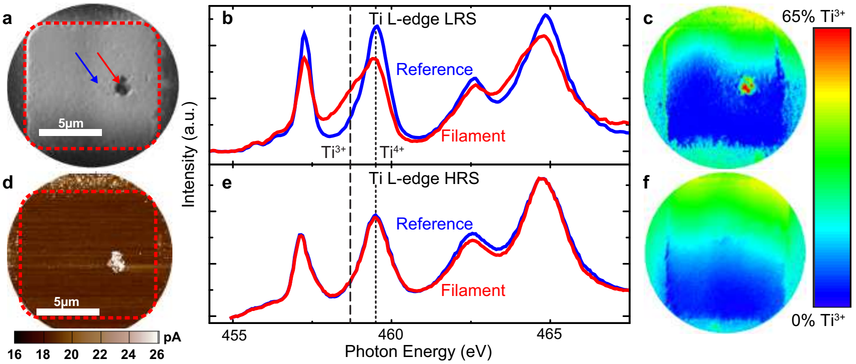

Figure 6.5: Fingerprint of the localized valence change in Nb:$SrTiO_3$ devices. (a) XPEEM image of a device in the LRS recorded with a photon energy of 459.5 eV. (b) Ti L-edge spectra extracted from the XPEEM image stack for a region within the filament (red line) and for the surrounding device area (blue line) as indicated with the arrows in a. (c) False color map of the Ti^{3+} contribution for the device in (a). (d) C-AFM current image of the device shown in (a). (e) Ti L-edge spectra extracted from the XPEEM image stack for a device in the HRS from a region within the suspected filament (red line) and for the surrounding device area (blue line) as indicated with the arrows in (d). (f) False color map of the Ti^{3+} contribution for the device in (e). No Ti^{3+} contribution is discernible for the entire device area. The apparent vertical gradient in the false color maps is an artifact from the uncorrected but small energy dispersion. The resulting contrast is much lower, however, than the real contrast detected for the filament. Modified from ref. 153.

exhibits Ti^{4+} states (Fig. 6.5b). The local confinement of this valence change is again evident from the false color map of the Ti^{3+} contribution (Fig. 6.5c): only within the filament area does one find a significant Ti^{3+} contribution.

For comparison, a device that was reset to the HRS was also analyzed (Fig. 6.5e-f). XPEEM images indicate the presence of a locally modified area, which can be ascribed to the switching filament in the HRS (i.e., a reoxidized switching filament, data not shown). Again, no Ti^{3+} spectral contributions could be detected in this region (Fig. 6.5e). False color mapping does not show any significant Ti^{3+} contribution for the entire device area. In consequence, these results demonstrate explicitly that a change of the Ti valence in a locally confined filament is indeed also responsible for the resistive switching in Au/Nb:$SrTiO_3$ junctions operated at high current limits.

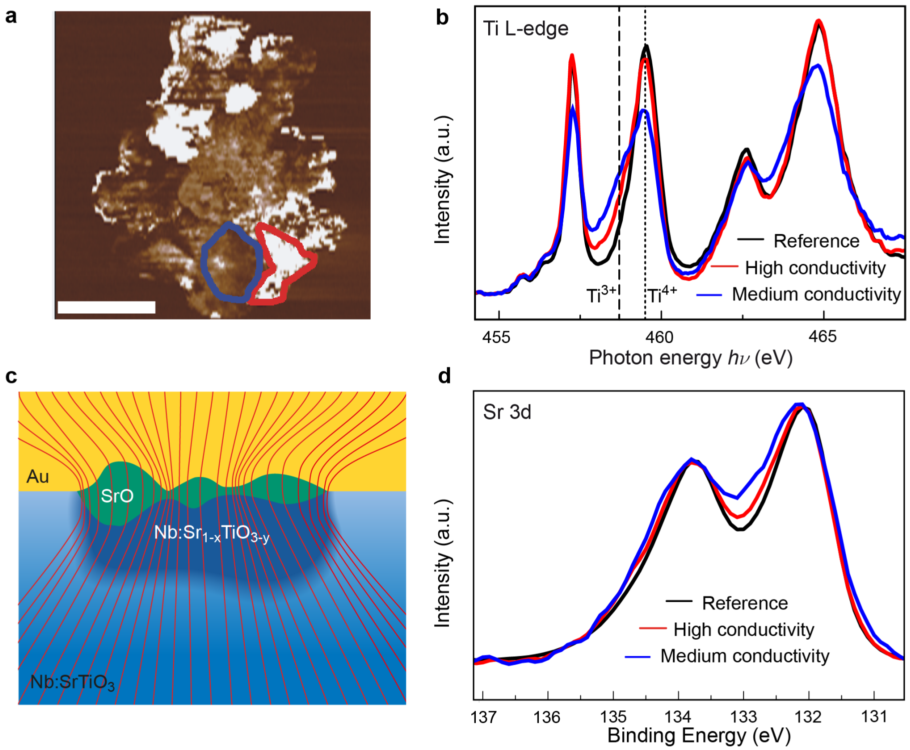

Figure 6.6: Fine-structure of a switching filament in $Nb:SrTiO_3$. (a) High-magnification C-AFM image of the switching filament for the LRS device in Fig. 6.5. Representative regions of high conductivity (red) and mediocre conductivity (blue) were chosen for spectroscopic evaluation. (b) Ti L-edge spectra extracted from the XPEEM image stack for two regions inside the filament outlined in (a) (red and blue lines) and for the surrounding device area (black line). (c) Schematic illustration of the phase separation in the switching filament. $Nb:SrTiO_3$ single crystal in blue with an insulating surface layer (light blue) underneath the Au top electrode. The switching filament consists of a well-conducting, $Nb:Sr_{1-x}TiO_{3-y}$ region (dark blue) which penetrates the insulating surface layer. This filament is covered by a SrO layer (green) of non-uniform thickness. The thickness dependent series resistance of this SrO layer leads to non-uniform conductance, as depicted by the current density lines (red lines). The lines are drawn such that the density of lines indicates the current density. (d) Sr 3d XPS spectra for the same regions as in (b). Modified from ref. 153.

While Fig. 6.5 already validates the valence change mechanism, closer inspection of the switching filament is essential to shed light onto the details of the switching process itself and on possible implications of the filament chemistry on the retention times as described above. In order to analyze the link between conductivity and the valence state in more detail, regions with different conductivity were selected based on the C-AFM data and used as reference for the analysis of the spectromicroscopic data (Fig. 6.6a). For each of these regions, Ti L-edge absorption spectra were extracted (Fig. 6.6b). Comparison of the two representative spectra extracted within the switching filament indicates an inhomogeneous distribution of Ti^{3+} states within the filament. Upon first sight, one may expect that areas with a high Ti^{3+} concentration should correspond to the areas of highest conductivity inside this switching filament. The C-AFM data, however, indicate the opposite behavior: areas of high conductivity correspond to mediocre Ti^{3+} concentrations, while areas of mediocre conductivity correspond to high Ti^{3+} concentrations.

This apparent contradiction can be explained through the consideration of the spatially resolved Sr 3d spectra extracted from the same regions as the Ti L-edge spectra (Fig. 6.6d). As described above for $SrTiO_3$ thin film devices, one finds a local phase separation into Sr-deficient $SrTiO_3$ with a SrO coverage of the switching filament. This SrO coverage is apparent from the high binding energy shoulder of the Sr 3d spectra. Comparison of the Sr 3d spectra and the C-AFM data reveals that the SrO layer is responsible for the non-uniform conductivity of the switching filament: Regions with high conductivity show only a slight shoulder, indicative of a thin SrO layer. Regions with lower conductivity, on the other hand, exhibit a more pronounced shoulder, indicative of a thicker SrO layer. This correlation is directly understandable in terms of the electronic structure of SrO: The filament region underneath is well conducting even for small Ti^{3+} contribution. SrO, however, is an insulator and therefore presents an additional tunneling barrier for electronic transport into the filament. Thin SrO layers therefore do not impede electronic transport drastically, while thicker layers lead to a non-negligible series resistance. This scenario is schematically depicted in Fig. 6.6c.

As discussed in chapter 5.4, the LRS of these devices can undergo a retention failure, which appears to be connected to exchange with the ambient atmosphere. As for the $SrTiO_3$ thin film devices, devices with a retention failure and devices with stable retention can be distinguished for the filamentary switching in Nb:$SrTiO_3$ devices. For the XPEEM investigation of the filamentary switching mechanism described above, a representative device with stable retention was selected to allow for the characterization of the LRS state even after the unavoidable delay between switching and XPEEM investigation. Similar to the observations for $SrTiO_3$ tin film devices, all devices with stable retention investigated here exhibit a SrO layer on top of the reduced switching filament. In contrast, no SrO signature was found for devices with a retention failure, indicating a close connection between the appearance of the SrO layer and the LRS retention, similar to the case described in section 6.2.3. The role of this SrO layer for the LRS retention for both types of devices will be therefore discussed in chapter 8.

6.4 Summary

In this chapter, it was demonstrated that spatially confined valence changes between Ti^{3+} and Ti^{4+} within a switching filament are responsible for the resistance change in $SrTiO_3$ thin film devices as well as noble metal/Nb:$SrTiO_3$ junctions operated at high current limits. The same valence change also leads to the LRS retention failure. While reoxidation of previously oxygen-deficient areas causes the frequently observed retention failure of the LRS, Joule-heating-induced local phase separation within the switching filament can stabilize the retention due to the formation of a $SrTiO_3$/SrO interface.

7 *In operando* spectroscopy and microscopy of switching-induced structural and electrical changes

As demonstrated in the previous chapter, resistive switching in transition metal oxides can be attributed to the motion of mobile donor-type defects and the corresponding valence change in the transition metal cation. The exact mechanism and especially the quantitative details of the related nanoscale redox-processes, however, remained elusive due as spectromicroscopic characterization of the same switching filament in each resistance state is mandatory for a quantitative description of the switching effects. The PEEM analysis described in the previous chapter was limited to post-mortem devices as the metallic top electrodes had to be removed due to the surface sensitivity of photoelectrons. This approach, of course, makes the examination of the same device in both resistance states inaccessible. Therefore, a development of the previously destructive PEEM studies towards a non-destructive *in operando* characterization is highly desirable.

In this chapter, uncovered single layer graphene is used as the top electrode for $SrTiO_3$-based memristive devices, allowing simultaneous electrical biasing and imaging inside PEEM instruments, enabling *in operando*, quantitative analysis of the redox processes. In the second part of this chapter, this characterization will be complemented with a cross-sectional, *in operando* TEM analysis, providing atomically resolved spectroscopic information in both the lateral and the vertical direction of the device. The results presented in this chapters have been published in part in ref. 112.

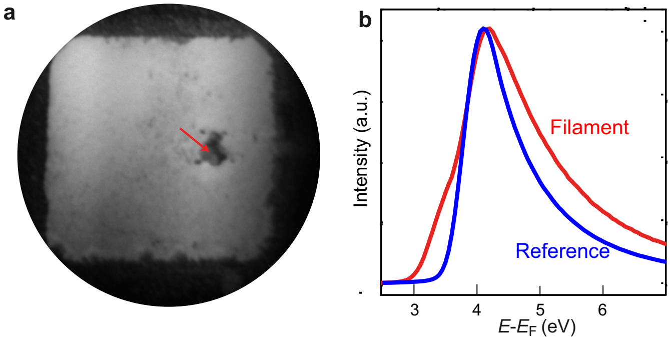

Figure 7.1: Filamentary work function changes. (a) Energy-filtered PEEM image of the same device presented in Fig. 6.5 at an electron energy $E - E_\mathrm{F} = 3.45\,\mathrm{eV}$ with a photon energy of 200 eV. (b) Threshold photoelectron spectra extracted from the filament (red line) and the surrounding (blue line).

7.1 Filament identification via photoelectron threshold spectromicroscopy

As the local work function may contain additional information about the electronic structure resulting from memristive operations [54, 167], the $SrTiO_3$ device in the LRS from the previous chapter was also characterized through work function scans as described in section 3.5. This is shown in Fig. 7.1. Similar to the observations in refs. 54 and 167, a left shift of the rising edge of the threshold photoelectron spectrum, i.e., a decreased work function, is apparent for the filament compared to the surrounding (Fig. 7.1b). This decrease can correspond to a Fermi level shift towards the conduction band, which is in line with the observed Ti^{3+} contribution. However, the observed phase separation may introduce a similar shift of the work function due to the formation of SrO on the surface as well as topographic effects. Therefore, the local work function will has to be considered in detail based on *in operando* measurements.

To achieve the desired *in operando* PEEM characterization of the resistive switching process, $SrTiO_3$-based memristive devices with graphene top electrodes as introduced in section 5.2 were employed (Fig. 7.2). These devices are first characterized through work function scans using the NanoESCA at Forschungszentrum Jülich with UV irradiation

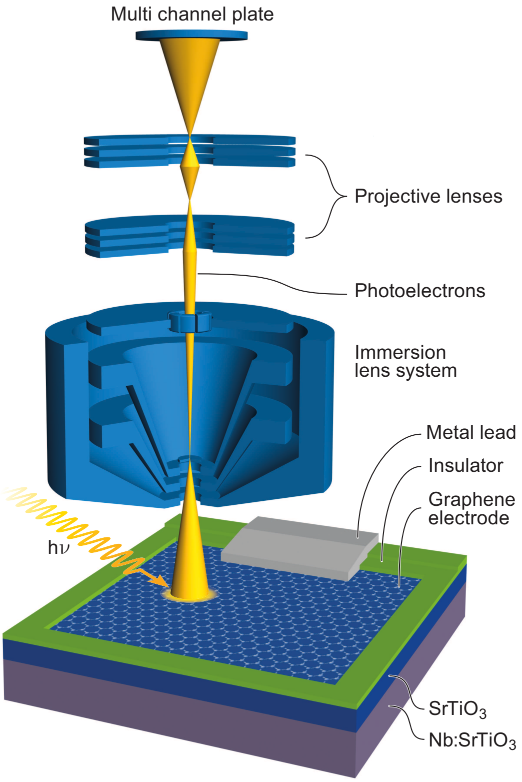

Figure 7.2: Device and measurement setup schematic. An epitaxial $SrTiO_3$ layer (blue) is sandwiched between a $Nb:SrTiO_3$ bottom electrode (violet) and graphene top electrode (grey honeycomb lattice). The graphene electrode is contacted through a metal lead, which is electrically separated from the continuous bottom electrode, allowing for biasing inside PEEM instruments. At the same time, photoelectrons from the $SrTiO_3$ layer can easily escape through the graphene electrode, allowing simultaneous imaging, as depicted with the PEEM lens system. Modified from ref. 112.

from a Hg lamp[1]. This allows a first characterization of several devices with graphene top electrodes in a manageable time and serves as a basis to select devices for further XPEEM analysis (see section 7.2). For the purpose of these measurements, devices were switched in air and mounted into the NanoESCA for each separate switching step as no biasing is possible within the instrument.

An exemplary device is shown in Fig. 7.3. The graphene device is surrounded by an insulating layer and contacted with a metal lead. Using the energy filter unit of the NanoESCA, single images are recorded for different electron energies. As described in section 3.5 this allows the extraction of threshold photoelectron spectra. Fitting the secondary electron cut-off at the rising edge of the spectra with a convolution of Gauss and Heaviside functions, in turn, allows the determination of the work function [110].

In the following, local variations of the work function of graphene/1 nm $Al_2O_3/SrTiO_3$ devices will be analyzed after each switching event[2]. For this purpose, PEEM images with an energy corresponding to the rising edge of the threshold spectrum for the graphene/$Al_2O_3/SrTiO_3$ stack are compared. Contrasts in these images can correspond to work functions variations, which can be caused by changes in the electronic structure or residues and dirt on the graphene surface. If the variation of the work function is caused by switching-induced changes of the electronic structure, one would expect a reproducible change after each switching event. If the contrasts are caused by residues, on the other hand, no reversible change would be expected. Therefore, threshold photoelectron spectra were extracted for each area exhibiting contrast in the respective PEEM images and only those areas exhibiting change upon switching are considered in the following. To avoid artifacts from contamination-induced changes of the work function due to the exposure to air after each step, a reference spectrum from the unmodified device area was taken for each step (not shown in the following for reasons of clarity). The work function of this reference area served for the calibration of the energy scale such that only changes between the reference and the filament work function are considered.

---

[1] NanoESCA characterization was performed as part of the master's thesis of Richard Valenta, Peter Grünberg Institute, Forschungszentrum Jülich GmbH, Jülich, Germany [168].

[2] The influence of a thin Al_2O_3 layer will be discussed in great detail in chapter 8. Graphene/1 nm $Al_2O_3/SrTiO_3$ devices exhibit very similar switching compared to devices without the Al_2O_3 layer.

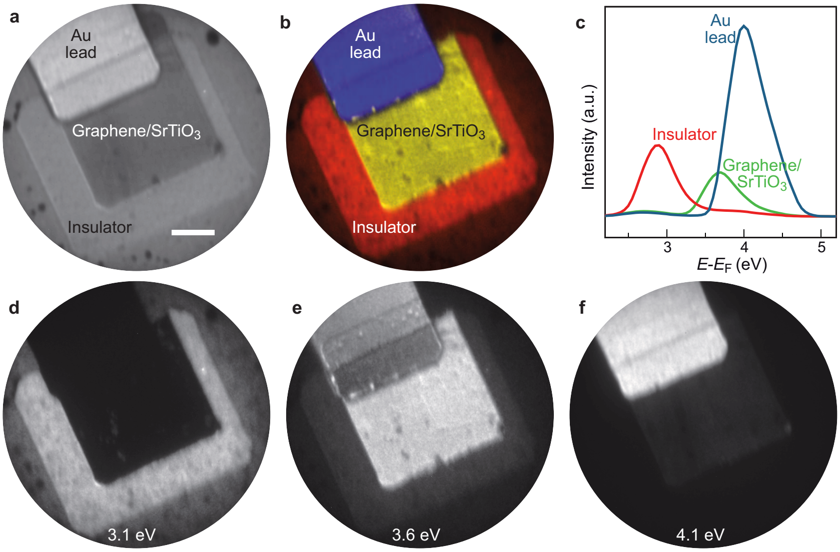

Figure 7.3: Exemplary graphene/SrTiO$_3$ device investigated with energy filtered PEEM. (a) Integrated PEEM image of an exemplary device. The graphene/SrTiO$_3$ device is contacted with a Au lead, which is electrically separated from the bottom electrode through an insulating layer. Scale bar, 5 µm. (b) False color image of the same device created from energy filtered images (panels d-f). The images from panels d-f are overlaid in different color scales. (c) Threshold photoelectron spectra extracted from the different regions of the device. (d) Energy-filtered PEEM image of the same device at an electron energy of 3.1 eV. Only the insulator appears bright. (e) Energy-filtered PEEM image of the same device at an electron energy of 3.6 eV. The graphene/SrTiO$_3$ sandwhich area appears brightest. (f) Energy-filtered PEEM image of the same device at an electron energy of 4.1 eV. Only the Au appears bright.

First, the forming step will be analyzed. In Fig. 7.4, a virgin device is shown, which exhibits some areas of local contrast variations. As this is a virgin device, these features must stem from non-switching related effects such as photo resist residues on the graphene surface, as discussed above, which is confirmed through comparison with the AFM topography (data not shown). After the forming step, an additional contrast appears, which is connected to a decrease in work function (Fig. 7.4b and c). This feature will be referred to as filament in the following. A decrease in work function after forming has been observed previously for post-mortem devices and could be connected to an increase in the oxygen vacancy doping concentration [54, 167]. The fact that this filament is truly connected to a switching event and not an artifact (possibly resulting

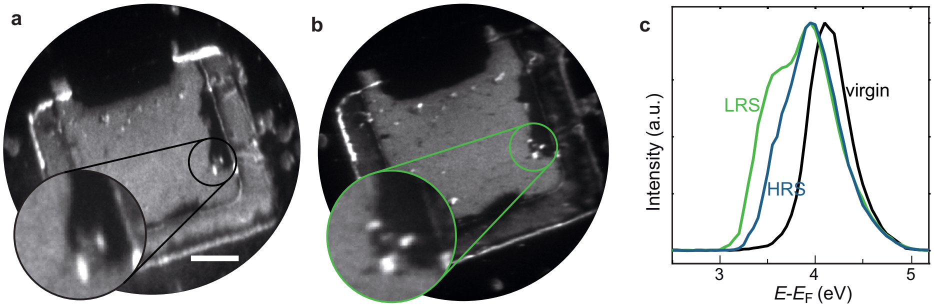

Figure 7.4: PEEM analysis of the forming step. (a) PEEM image of a virgin device at an electron energy of 3.75 eV. Some contrasts are visible within the device area, which must correspond to residues and dirt on the graphene layer, as no electrical treatment was performed yet. Scale bar, 5 µm. (b) PEEM image of the same device after forming. An additional contrast appeared, which was previously absent (compare insets). (c) Threshold photoelectron spectra extracted for the filament area before forming and after Set and Reset operations.

from additional dirt on the sample surface) is verified through an additional switching operation followed by PEEM analysis. After Reset, the work function of the filament is increased again, which indicates a (partially) reversible effect. It can therefore be concluded that during switching, changes in the local work function occur within the switching filament.

In a next step, the reversible change of the filament work function was verified using a second device (Fig. 7.5). This device was formed and reset before the first PEEM image was taken, where no contrasts are visible within the device area (Fig. 7.5a). After setting this device to the LRS, a new contrast appears, which is connected to a strongly decreased work function (Fig. 7.5b). Again, this change in work function is partially reversible, as the following Reset, Set and Reset operations lead to less pronounced, more pronounced and less pronounced contrast, respectively, which is caused by change in work function (Fig. 7.5c-f).

After fitting of the spectra, the work function $\varPhi^{\mathrm{F}}$ of the filament can then be compared to the unaltered surrounding $\varPhi^{\mathrm{R}}$ for each resistance state, yielding

$$\varDelta\varPhi = \varPhi^{\mathrm{F}} - \varPhi^{\mathrm{R}}. \tag{7.1}$$

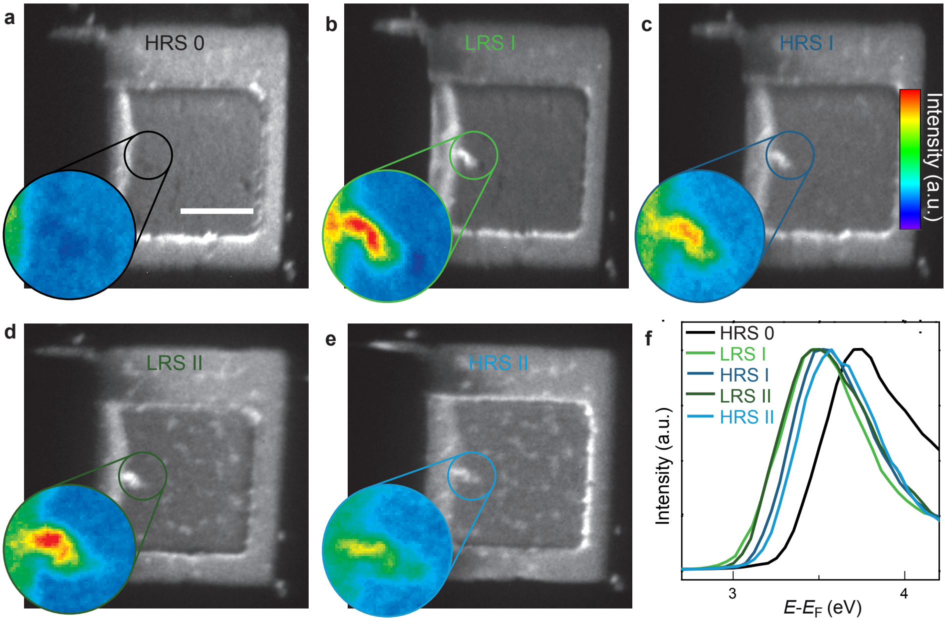

Figure 7.5: Reversible change of the filament work function. (a) PEEM image of another graphene/Al_2O_3/$SrTiO_3$ device in the HRS at an electron energy of 3.4 eV. Scale bar, 5 µm. (b) PEEM image of the same device after Set. (c) PEEM image after Reset. (d) and (e) PEEM images after additional Set and Reset operations, respectively. Insets: magnification of the area around the switching filament, which appeared after the Set operation. A different color scale is used for improved contrast. (f) Threshold photoelectron spectra extracted from the filament.

Fig. 7.6a shows that for the rather reproducible LRS, $\Delta\Phi \approx -0.2\,\text{eV}$, while $\Delta\Phi \approx -0.1$ to $-0.15\,\text{eV}$ for the HRS. A comparison between $\Delta\Phi$ and the device resistance measured directly after each switching event (i.e., before the sample is mounted into the instrument) shows that the resistance value for HRS I and HRS II is almost identical (Fig. 7.6a), so one would expect a similar $\Delta\Phi$ as well. Measuring the device resistance again after each PEEM measurement reveals that the resistance is rather stable for HRS II and just increased slightly during the measurement. This is the typical behavior one would expect from a device kept in air after the switching. For HRS I, on the other hand, the device resistance decreases by approximately two orders of magnitude during the course of the PEEM experiment. This dramatic change in resistance is usually not observed in air for the HRS (see section 5.4) and might be a result of the vacuum

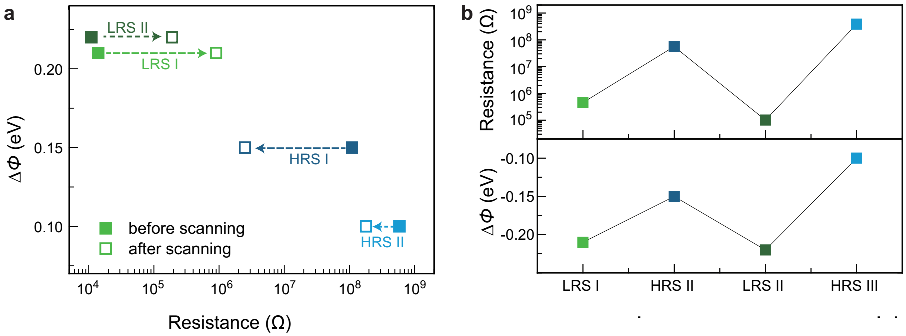

Figure 7.6: Quantification of the filament work function. (a) Work function difference between filament and reference area as a function of device resistance measured before and after PEEM measurement. (b) Evolution of device resistance after PEEM measurement (upper panel) and work function difference between filament and reference area (lower panel) during the switching cycle. As the resistance changes during the course of the experiment, the average value of the resistances measured before and after the PEEM characterization is plotted in panel (b).

surrounding and the irradiation with high intensity UV light [169]. This change in resistance, in turn, may explain the $\Delta\Phi$ value for HRS I.

For the LRS, an increase of the device resistance by 1-2 orders of magnitude is observed before and after the measurement, but this is the typical, fast increase in device resistance after the Set operation (see section 5.4), i.e., the typical short-time retention behavior of the LRS.

Comparing the average value of the resistances measured before and after the PEEM with the measured work function difference, it can be concluded that the change in work function tracks the actual device resistance satisfactorily (Fig. 7.6b), while problems with device retention may be more severe under UV irradiation, complicating the comparison between spectromicroscopic values and the device resistance if the device cannot be operated in the PEEM instrument itself.

The question remains why the filament investigated in Figs. 7.5 and 7.6 does not exhibit any contrast during the first HRS measurement (Fig. 7.5a). One may surmise that the Reset operation leading to this HRS I resulted in a higher resistance than for the following HRS states, which might make the contrast of the filament less apparent. But comparison of the resistance values disproves this suspicion, all HRS values are

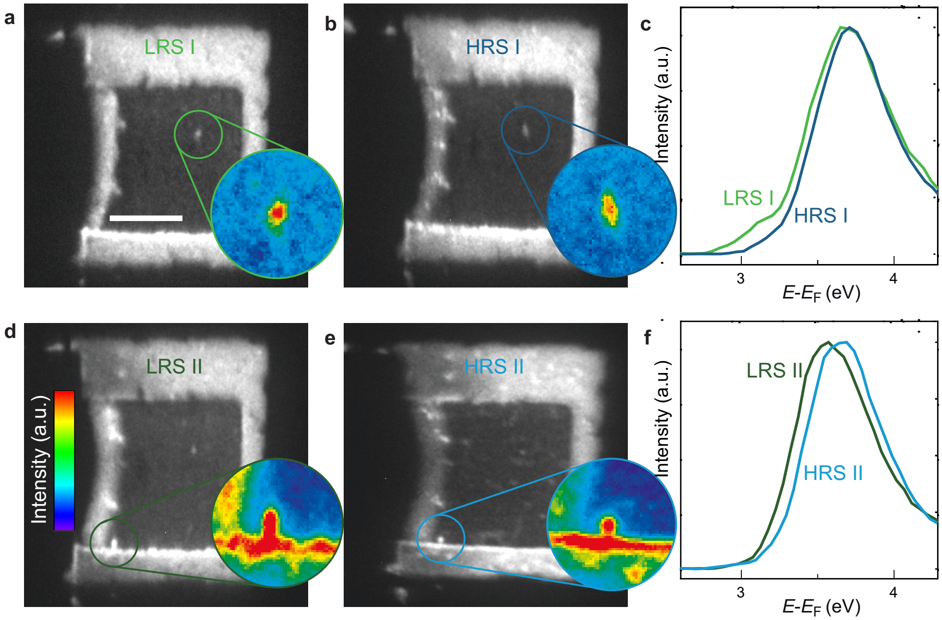

Figure 7.7: Change of the active filament position. (a) PEEM image of another graphene/Al_2O_3/$SrTiO_3$ device in the LRS at an electron energy of 3.45 eV. Scale bar, 5 µm. (b) PEEM image of the same device after Reset. (c) Filament threshold photoemission spectra. (d) PEEM image of the same device after another Set. A new filament was created (see inset) (e) PEEM image of the same device after another Reset. The new filament underwent a change in work function. (f) Filament threshold photoemission spectra.

very similar. Alternatively, the active filament investigated in Figs. 7.5 and 7.6 may be different from the active filament of the first switching cycle leading to the first HRS ("HRS 0" in Fig. 7.5). The active filament for the first switching cycle might then have been located underneath the Au lead, making it impossible to detect with PEEM. As discussed in section 8.1, this is actually a rather likely scenario and agrees well with the fact that in contrast to the devices discussed so far, no evidence of an active filament could be detected via work function scans for many other devices investigated here (data not shown).

As demonstrated in Fig. 7.7, a variation of the filament position is indeed possible for these devices. In Fig. 7.7a and b images of the LRS I and HRS I of another device show a small active filament, which again exhibits an increase of the work function upon switching to the HRS (Fig. 7.7c). After switching back into the LRS II, the work function of this filament does not change, but a new filament appears, which now exhibits a lower work function than the surrounding (Fig. 7.7d-f). The first filament, accordingly, is still visible, but inactive. This observation confirms that the active filament in these devices might change during repeated switching cycles. Unfortunately, further switching could not be performed using this device as the memory window declined and even the switching direction changed after the next Set and Reset operations.

Such a change in the position of the switching filament during repeated cycling has been observed before for so-called electrochemical metalization cells [170,171] where it is assumed that this phenomenon is one of the reasons for cycle-to-cycle variability of the LRS and the HRS, one of the major obstacles that have to be overcome for practical application of resistive switching devices.

It can be concluded that switching filaments in graphene/Al_2O_3/$SrTiO_3$ devices can be identified using threshold photoelectron spectromicroscopy. During forming, a filament with a lower work function compared to the surrounding is created. The active filament might change during the operation of a single device, but under some circumstances the same filament is reproducibly created and reoxidized, which goes along with a reproducible change of the work function. This filament work function appears to have a direct correlation with the device resistance. In the next section, only filaments which occur in the same location for each switching cycle will be considered.

7.2 *In operando* spectromicroscopy: O K-edge as a probe of local, switching-induced carrier density modulations

After the confirmation that switching filaments in devices with graphene electrodes can in principle be identified using PEEM, graphene/$SrTiO_3$ devices are now analyzed using XPEEM, focusing on the O K-edge. The O K-edge was chosen as it is more sensitive to small changes in the electronic structure (see section 4.1). If not specified

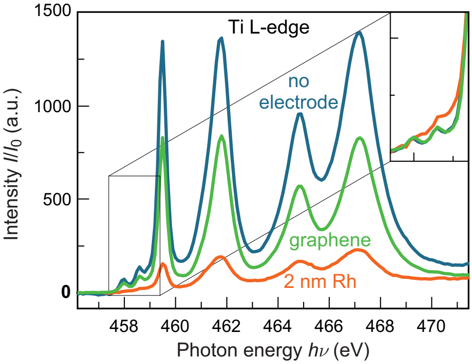

Figure 7.8: Top electrode comparison for sufficient XPEEM signal from the active layer. $SrTiO_3$ Ti L-absorption edge detected from $SrTiO_3$ with a 1 nm Al_2O_3 capping layer without electrode, from underneath a graphene electrode, and from underneath a 2 nm Rh electrode. Inset: Zoom to the prepeak-area after normalization confirming better spectral resolution with graphene electrodes compared to Rh electrodes. Normalized spectra from underneath graphene and from the surface without electrode are practically identical. Modified from ref. 112.

differently, the XPEEM experiments presented in this section have been performed at the beamline UE56/1-SGM at BESSY II (Berlin, Germany) using secondary electrons as detection method.

In a first step, in order to confirm that a sufficient photoelectron signal from the $SrTiO_3$ thin film can be obtained through graphene layers, the absolute electron yield at the Ti L-edge for an $SrTiO_3$ thin film without electrode was compared with a $SrTiO_3$ thin film covered by a graphene electrode and a film covered by a 2 nm Rh electrode as described in section 5.2 at comparable experimental conditions. Compared to the $SrTiO_3$ without electrode, the photoelectron signal underneath the Rh electrode is diminished by a factor of 7 (Fig. 7.8). Thus, the investigation of buried layers underneath ultra-thin metal is in principle possible but very difficult due to low signals. Utilizing graphene electrodes, on the other hand, allows for a much stronger signal, which is only reduced by a factor of 1.6. In contrast to the spectrum from the film covered by Rh, even the small prepeaks on the low-energy side of the L_3 edge are well reproduced, confirming that spectromicroscopy using graphene electrodes is sensitive even for subtle spectroscopic changes of the buried layer (Fig. 7.8, Inset). This electron-transparency is the reason why secondary electron microscopy and X-ray pho-

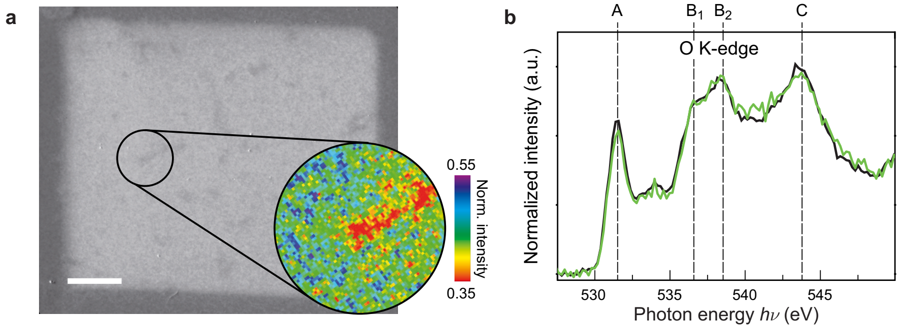

Figure 7.9: O K-edge signature of a switching filament. (a) XPEEM image of the device shown in Fig. 7.5 at a photon energy of 531.6 eV (peak A). Scale bar, 2 µm. The previously observed filament can be identified again as a dark contrast (red contrast in the magnified inset). (b) O K-edge for the switching filament in panel (a) (green line) and the surrounding device area (black line).

toelectron spectroscopy through graphene membranes are possible [172–174]. Based on these findings, it can be concluded that graphene electrodes with their unparalleled conductance-to-thickness ratio [23] are the ideal electrode material to study buried layers using spectromicroscopy[3].

O K-edge

Functioning devices are analyzed in a first step by imaging using a photon energy of 531.6 eV (peak A energy), as the peak A intensity of the O K-edge is the most obvious indication for reduced $SrTiO_3$. For the device shown in Fig. 7.5, the position of the active filament is already known from the threshold photoemission analysis. The same feature is also visible as an area of reduced peak A intensity in Fig. 7.9a. Extracting the entire O K-edge spectrum for this feature and the surrounding area reveals the fingerprint of reduced $SrTiO_3$ for the filament (reduced peak A intensity, increased intensity between peaks B_2 and C, Fig. 7.9b).

In Fig. 7.9a, there also appear other areas with similarly reduced intensity at peak A, which can either be an effect from dirt on the sample surface (reduced intensity for the

---

[3] Therefore, Rh electrodes will be neglected in the remainder of this thesis. *In operando* spectromicroscopy using Rh electrodes was demonstrated in the master's thesis of Richard Valenta, Peter Grünberg Institute, Forschungszentrum Jülich GmbH, Jülich, Germany [168].

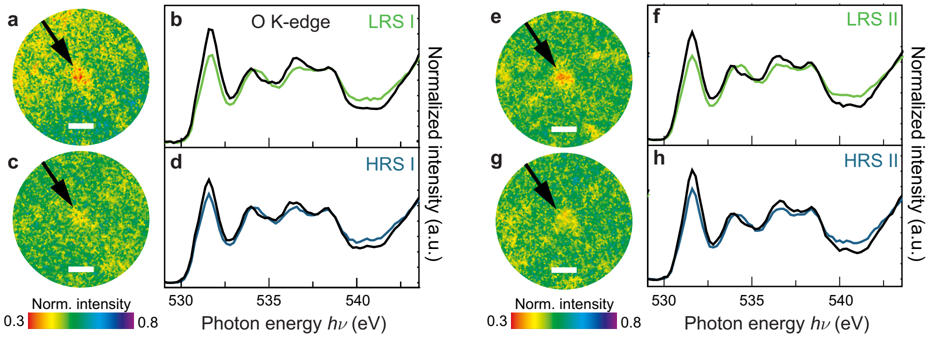

Figure 7.10: Spectromicroscopic fingerprint of a resistive switching filament in the LRS and HRS. (a, c, e, g) PEEM images of the switching filament in the LRS, HRS, LRS II and HRS II, respectively (indicated by the black arrow) for a photon energy of 531.6 eV (peak A). Scale bars, 1 µm. (b, d, f, h) O K-edge for the switching filament in panels (a, c, e, g) (green and blue lines for the LRS and HRS, respectively) and the surrounding device area (black lines). Modified from ref. 112.

entire spectrum), or the indication of partial filaments, i.e., other reduced areas in the $SrTiO_3$ layer. For clarification, each of these features needs to be analyzed after each switching event. Unfortunately, this device (and all other devices on this sample) were destroyed during the next step of the analysis because of a discharge in the PEEM instrument[4].

Therefore, this experiment was repeated several times with new samples. A representative device is shown in Fig. 7.10. The device was analyzed after each switching event during a switching cycle LRS $\mapsto$ HRS $\mapsto$ LRS $\mapsto$ HRS by acquiring O K-edge image stacks after each switching event. Upon close examination of the entire device area, a feature exhibiting reduced intensity in the LRS at peak A was found, which is suspected to be the switching filament (red spot in Fig. 7.10a). Extracting the entire O K-edge spectrum for this feature and the surrounding area again reveals the fingerprint of reduced $SrTiO_3$ for the filament (Fig. 7.10b). The same feature shows much weaker

---

[4] While this appeared to be a random event during the middle of a measurement, such discharges were found to occur with increased probability for samples exhibiting significant outgassing due to improper mounting, or if the stage was very close to the extractor, or if the stage was moved in rather large steps while the synchrotron beam was illuminating the samples. Mounting samples with as little silver paste and plastics components as possible, leaving the sample in the main chamber without imaging for a sufficient amount of time to ensure proper UHV and only moving the stage with small steps (e.g. $\leq 2\,\mu m$), preferably while using only low energy electron or UV light irradiation from a mercury lamp were found to decrease the likelihood of destructive discharges.

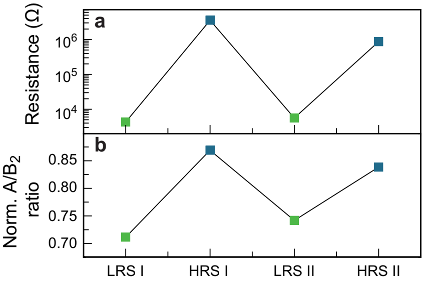

Figure 7.11: Spectromicroscopic quantification of a resistive switching filament. (a) Device resistance and (b) normalized A/B_2 ratio as a function of the device state. Modified from ref. 112.

contrast at peak A in the HRS (Fig. 7.10c). For quantification, the O K-edge spectra for this filament were extracted for each resistance state (Fig. 7.10a-g), which show a reproducible change in the normalized intensity of peak A.

Similar to the correlation between device resistance and filament work function (Fig. 7.6), this change in peak A intensity exhibits a direct correlation with the device resistance (Fig. 7.11). To verify that this region is in fact the active switching filament, all other regions of interest in the entire device area which show contrasts in the O K-edge were also analyzed, but no significant changes during electrical stimulus were found. This reproducible change in the O K-edge can therefore be regarded as the fingerprint of a single active switching filament. Bearing in mind the interpretation of the peak A intensity discussed in section 4.1, the change in the O K-edge is indicative of a high concentration of carriers at the conduction-band edge in the LRS, and a lower concentration in the HRS. Comparison to the reference established in Fig. 4.3 yields approximate values of $9 \pm 2\,\%$ Ti^{3+} in the LRS and $4 \pm 1\,\%$ Ti^{3+} in the HRS. As XPEEM is a highly surface sensitive technique, the resulting charge-carrier densities of $1.5{\times}10^{21}$ electrons per cm^3 (LRS) and $6.7{\times}10^{20}$ electrons per cm^3 (HRS) can be considered as an average value of the top 2-3 nm of the filament. In the lateral direction, the diameter of this filament has an upper limit of 500 nm (this was found to be the necessary size of the ROI used to extract the spectra).

Although experimental uncertainties limit the accuracy of assigning absolute values (compare the relatively large error bars given above), these results provide valuable quantitative information on the charge-carrier density differences between different resistance states. Going beyond the analysis of post-mortem devices presented in chapter 6, these results obtained from reversible changes finally yield unambiguous and quantitative evidence that resistive switching in transition metal oxides is driven by a nanoscale redox reaction: An oxygen vacancy-driven valence change in the Ti leads to a charge carrier density modification by a factor of 2-3. This information can complement existing device simulation models, enabling unprecedented predictive modeling approaches for future memory or logic devices, as will be presented in chapter 8.

As described above, the entire device area was examined in each resistance state for the device shown in Figs. 7.10 and 7.11 to ensure that the active filament is in the field of view in each case. Of course, this approach limits the spatial resolution of the XPEEM characterization. Fitting a sharp edge within the PEEM image with a Gaussian profile convoluted with a step function as described in ref. 175 yields a resolution of 140 nm. Even more importantly, many devices did not exhibit an identifiable switching filament, which may be located underneath the Au lead, as discussed above. To overcome these limitations, the experiment was repeated with a pre-defined switching filament as described below.

Before the graphene electrode was deposited, the W probe was placed directly on the $SrTiO_3$ thin film to form a conductive filament, similar to the process described in ref. 176 (Fig. 7.12a-d)[5]. Applying positive voltages to the W probe then leads to a forming step very similar to the forming step described for MIM devices in chapter 5 (Fig. 7.12h). To avoid structural damage to the $SrTiO_3$ and the phase separation observed in chapter 6, the current was limited to 1 or 2 mA. The structural integrity was confirmed by AFM and spatially resolved XPS measurements during XPEEM analysis. Using C-AFM, the location of the conductive filament could be identified (Fig. 7.12e-g) and it was found that the conductivity increased most significantly in the proximity a small elevation, which indicates small structural alterations. Only

---

[5] For alignment purposes, a 30 nm insulating layer was deposited outside the areas designated to be contacted by graphene top electrodes. This procedure yields "windows" where the $SrTiO_3$ is directly accessible for contacting with the probe tip and for subsequent contacting with graphene electrodes.

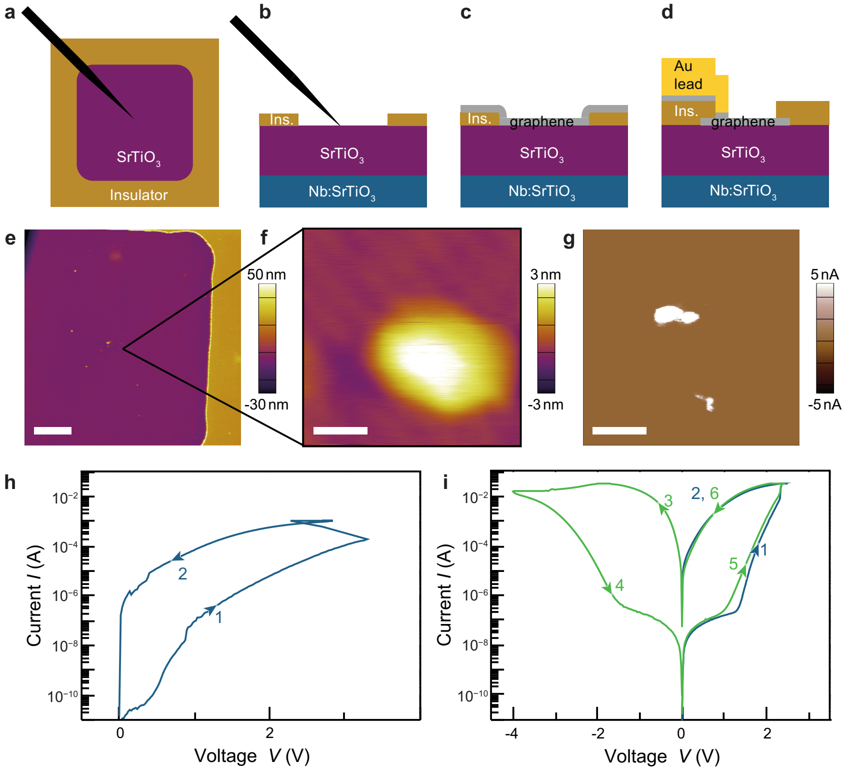

Figure 7.12: Pre-defining a switching filament. (a) Schematic of a window in the insulator, where the W probe can contact the SrTiO$_3$ layer directly. (b) Side view of the same schematic. (c) Schematic of the next step in the fabrication process: graphene is deposited onto the entire surface. (d) Schematic of the device after fabrication. (e) AFM-topography of a representative device after forming with a current limit of 2 mA. The violet area represents the SrTiO$_3$ surface, the insulator appears yellow. Scale bar, 5 µm. (f) Zoom-in of the AFM-topography to the area of contact between W probe and SrTiO$_3$ layer. Scale bar, 50 nm. (g) C-AFM conductivity map of the same area. Scale bar, 50 nm. (h) Forming step of another device (the device that will be used for PEEM analysis). The current limit was 1 mA. (i) First biasing step (blue line) and subsequent I-V-curve after device fabrication.

for larger currents on the order of 10 mA alterations similar to the forming induced phase-separation shown in chapter 6 were found.

After top electrode fabrication, the device exhibited typical eightwise resistive switching, with a very indistinct forming step compared to devices without pre-defined filament (Fig. 7.12i). This could indicate that the pre-defined filament needs some "activation" which can be achieved with a smaller voltage than forming in an undisturbed film. In the following *in operando* XPEEM characterization, O K-edge measurements of the entire device area, as shown exemplarily in Fig. 7.13a, confirmed that the pre-formed area exhibits the signature of reduced $SrTiO_3$. Subsequently, this area was analyzed in both LRS and HRS using a higher magnification (Fig. 7.13b), achieving higher spatial resolution. The resolution was determined to be 20-50 nm depending on which feature was chosen for the fitting routine, indicating operation with almost ideal microscope settings [108]. The switching filament exhibits a complex fine structure, which resembles the fine structure observed in C-AFM but is slightly larger, and which changes during switching from the LRS to the HRS (Fig. 7.13c-f). Extracting the O K-edge spectra for a rather large area including the filament – similar to the procedure used in Fig. 7.10 – results in the same trend as observed before, i.e., an increase of the peak A intensity when going from the LRS to the HRS.

The high spatial resolution achieved here allows to even extract spectra from different regions within the filament. Fig. 7.13g shows the spectrum obtained from the brightest spot in Fig. 7.13d. This spectrum appears to have changed dramatically from the reference spectrum, as peak A is strongly suppressed and a new peak at the original peak B_2 energy occurs. But close comparison to the available reference spectra confirms that this feature cannot be caused by SrO or $SrCO_3$ (compare Fig. 4.6). Instead, it is very similar to the reference spectrum obtained for $\approx 24\,\%$ Ti^{3+}, which is shown in Fig. 7.13h. On first sight, both spectra shown in Fig. 7.13h have a very different shape than the spectra in Fig. 7.13g. The reason for this lies in the machines used to obtain the spectra: The *in operando* experiments in Fig. 7.13a-g were performed at Elettra, while the references were taken at Bessy II. Due to unavoidable, O containing contamination of the X-ray optics within the beamlines, a non-negligible renormalization of the X-ray intensities occurs at these photon energies, which may not be completely correctable through the typical normalization procedures. Therefore, only trends like peak ratio changes between a reference and the ROI or difference spectra

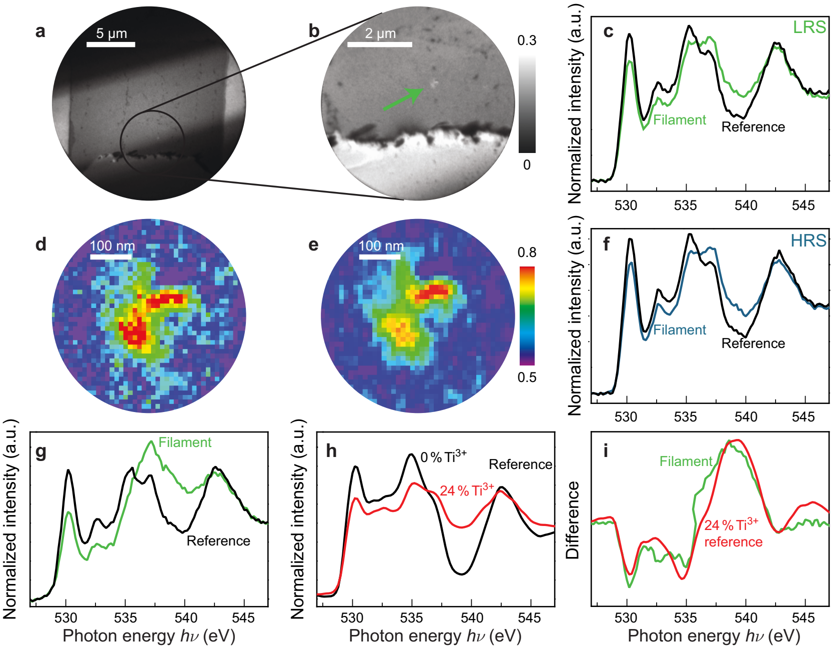

Figure 7.13: O K-edge of a pre-defined switching filament. (a) PEEM image of the device under consideration with a photon energy of 538.2 eV. The diagonal brighter stripe is caused by the synchrotron beam profile. The stripe is the area of the footprint with highest brilliance. (b) PEEM image of the same device with a higher spatial resolution (photon energy of 538.2 eV). The green arrow indicates the pre-formed switching filament. (c) O K-edge for the switching filament (averaged over $\approx 400 \times 400\,\mathrm{nm}^2$) in the LRS (green line) and the surrounding device area (black line). (d) Zoom to the switching filament in the LRS (photon energy of 538.2 eV) using a different color scale for easier contrast visualization. (e) Zoom to the switching filament in the HRS (photon energy of 538.2 eV). (f) O K-edge for the switching filament in the HRS (blue line) and the surrounding device area (black line) extracted from the same ROI as in (c). (g) O K-edge for the switching filament (extracted from the brightest feature in (d) (green line) and the surrounding device area (black lines). (h) O K reference spectra for $\approx 24\,\%$ Ti^{3+} (red line) and $\approx 0\,\%$ Ti^{3+} (black line) extracted from the same reference measurement presented in Fig. 4.2b. (i) Difference spectra between filament and surrounding from (g) (green line) and $\approx 24\,\%$ Ti^{3+} and $\approx 0\,\%$ Ti^{3+} from h (red line). The *in operando* experiments have been performed at the Nanospectroscopy beamline at Elettra synchrotron laboratory (Trieste, Italy) using secondary electrons as detection method.

are directly comparable. Comparing the difference spectra between the filament and the surrounding and the spectra for $\approx 24\,\%$ Ti^{3+} and $\approx 0\,\%$ Ti^{3+}, respectively, confirms that the central part of the filament indeed corresponds to an area with $\approx 24\,\%$ Ti^{3+} (Fig. 7.13i). This indicates that switching filaments are not necessarily homogeneous in their oxygen vacancy concentration, but rather posses a fine structure with higher and lower concentrations. It must be assumed that the fine structure is even more complex than recognizable in Fig. 7.13 and even higher resolution would be necessary to resolve it. Nevertheless, the area-integrated values derived from the full switching cycle presented in Fig. 7.10 provide a valuable starting point for device simulation, as will be shown in chapter 8.

Ti L-edge

As discussed in detail in section 4.1, the O K-edge is more sensitive for small changes in the Ti^{3+} concentration than the Ti L-edge. Nevertheless, subtle trends can also occur in the Ti L-edge even for small Ti^{3+} concentrations. For completeness, the device shown in Fig. 7.13 is therefore also analyzed using the Ti L-edge. As was pointed out in section 4.1, the Ti L_3 t_{2g} peak decreases with increasing Ti^{3+} concentration. Fig. 7.14 shows that the L_3 t_{2g} peak intensity of the filament observed in Fig. 7.13 varies when switching from LRS to HRS. Like peak A of the O K-edge, the Ti L_3 t_{2g} peak is smaller in the LRS, indicating an increased Ti^{3+} concentration. Analysis of the Ti L-edge – while more challenging to use for quantification of the switching induced carrier density variations – therefore supports the conclusions drawn from the O K-edge. It should be noted that reversible changes in the Ti L-edge were found to be easier recognizable using higher magnification XPEEM experiments with high lateral resolution as the small effects tend to be unobservable if additional averaging with neighboring regions occurs due to limited resolution.

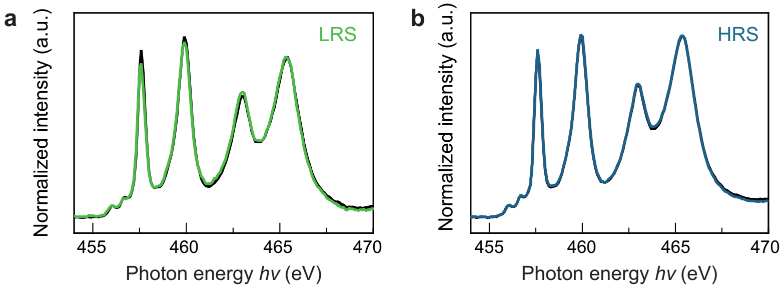

Figure 7.14: Ti L-edge of the same pre-defined resistive switching filament. (a) Ti L-edge for the switching filament shown in Fig. 7.13 in the LRS (green line) and the surrounding device area (black line). (b) Ti L-edge for the switching filament shown in Fig. 7.13 HRS (blue line) and the surrounding device area (black line). The experiments have been performed at the Nanospectroscopy beamline at Elettra synchrotron laboratory (Trieste, Italy) using secondary electrons as detection method.

7.3 *In operando* transmission electron microscopy: vertical and horizontal mapping of switching-induced carrier density modulations

To detect small variations in the electronic and chemical structure within a memristive device at the atomic scale, one has to turn to TEM. The use of modern aberration corrected TEMs allows a range of complimentary characterisation techniques to be performed during one experiment on the same specimen. TEM is ideally suited to study valence change memristive devices because these techniques can include atomic resolution imaging, energy dispersive X-ray spectroscopy (EDX) for composition mapping, and EELS for composition mapping and for characterization of the electronic structure. An additional advantage of its complimentary use in addition to PEEM is that TEM specimen are typically prepared through focused ion beam (FIB) cutting of cross-sectional lamellae, which allows investigation of both top and bottom electrode interfaces simultaneously.

For TEM specimens that have been switched *ex situ*, i.e., before FIB cutting, it is not certain that the active region of a device is contained within the ≈ 100 nm thin TEM specimen and problems with volatility over time [92] or during specimen prepa-

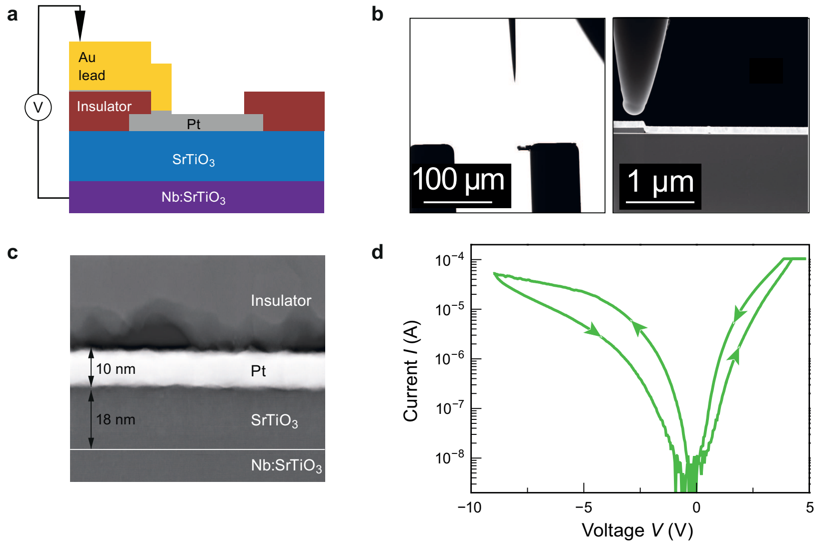

Figure 7.15: *In operando* memristive operation of a $SrTiO_3$ device in a TEM. (a) Schematic of specimen examined. (b) Very low magnification STEM image of specimen and electrical contact (left) and higher magnification of specimen and electrical contact (right). The electrical contact touches the Au lead rather than the actual top electrode to prevent heating effects and mechanical stress to the actual device. (c) Higher magnification HAADF STEM image showing the geometry of the device. (d) I-V-characteristics of the device as examined in the electron microscope.

ration can result in substantial information loss [177]. Additionally, small changes in specimen preparation and experimental procedure will lead to difficulty in accurately interpretating the analytical data. Most importantly and similar to the motivation for *in operando* spectromicroscopy, characterization of the same switching filament in each resistance state is mandatory for a comprehensive analysis of the switching effects. Therefore, TEM characterization must also be employed using an *in operando* approach[6].

Because of its potential for atomic-scale imaging of physical and chemical processes, there have been great efforts towards the development of *in operando* TEM with piezo-controlled electrical probes in the last few years and considerable interest in its appli-

---

[6] The development and application of this *in operando* approach was conducted in cooperation with Dr. David Cooper, CEA LETI, Grenoble, France, who performed all TEM experiments presented in this section.

cation to memristive devices [178–183]. Most reports in the literature are based on either bright field TEM or scanning transmission electron microscopy (STEM) imaging and although they can provide evidence of changes that occur during switching, quantitative physicochemical information about exact valence change switching mechanisms are rare due to an absence of results that use analytical TEM, such as EELS, to show changes in either the atomic concentrations or the changes in electronic states during switching. In addition, the piezo-controlled electrical contact point, which is commonly used in *in operando* TEM experiments, is frequently applied directly to the ROI which will cause destructive local heating effects and mechanical stress [178]. As such extrinsic effects need to be prevented to study fundamental resistive switching processes [179], the key to successful imaging of the memristive operation in a TEM is the careful positioning of the electrical contact.

For these reasons, FIB lamellae were cut from the Pt/20 nm $SrTiO_3$/Nb:$SrTiO_3$ devices (Sr/(Sr+Ti)≈0.52) with lithographically defined electric leads, which were described in sections 3.2 and 5.3 (Fig. 7.15a-c). The device area of the lamellae had a specimen thickness of ≈100 nm and a piezo controlled W tip was landed onto the metal lead far away from the actual device area on a thicker part of the TEM specimen. The specimen was mounted in a Nanofactory biasing holder using conducting epoxy such that the substrate was electrically connected to the holder. The top of the specimen was protected with marker pen ink before specimen preparation which was then removed by oxygen plasma cleaning just before the *in operando* experiments such that the top Au contact was exposed for electrical probing. The $SrTiO_3$ layer did not appear to change because of the plasma cleaning step.

High-angle annular dark-field (HAADF) STEM images were obtained (Fig. 7.15c) and EELS spectra were acquired before the switching experiment to measure the device in the unformed state. Voltage sweeps were then applied to switch the device between HRS and LRS during which further STEM and EELS measurements were performed. The device was switched multiple times between LRS and HRS in eightwise polarity by sweeping to positive or negative voltages, respectively (Fig. 7.15d).

Before and after each switching event, the entire active device area was mapped using EELS. The oxidation state for each region of the device can then be obtained from the intensities and positions of the different characteristic peaks of the EEL spectra as

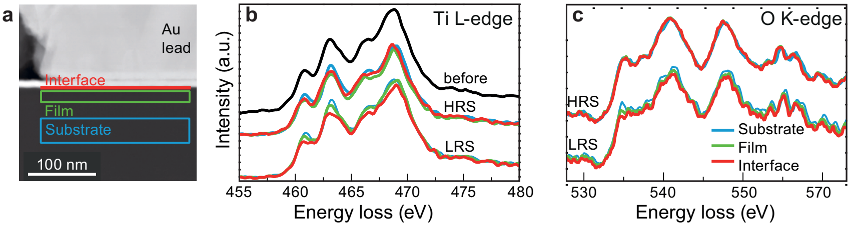

Figure 7.16: TEM-comparison of the same device in the LRS and the HRS. (a) STEM image showing the region examined during the switching experiment. The different ROIs are labeled. (b) Ti L-edge EEL spectra for the regions indicated in a, acquired before and during the switching with the device in LRS and HRS. (c) O K-edge EEL spectra for the same regions as in (c).

these contain the same information as the X-ray absorption spectra introduced in section 4.1. Fig. 7.16a shows a HAADF STEM image of the ROI with the substrate, film and Pt/$SrTiO_3$ interface regions indicated. A representative Ti L-edge EEL spectrum acquired in the pristine state, i.e., before the switching experiments, shows homogeneous, fully oxidized $SrTiO_3$, mainly Ti^{4+} states are present (Fig. 7.16b). This confirms that the specimen preparation procedure did not introduce artifacts. The Ti L-edge after switching to the LRS and the HRS is also shown in Fig. 7.16b. For the device in the HRS it is clear that there are only small changes in the Ti spectra compared to the pristine state for the entire device. However, for the LRS there are reductions in intensity and shifts of the characteristic peaks corresponding to a reduction in Ti^{4+} states and an increase in Ti^{3+} states as is apparent from the decrease of the L_3 t_{2g} peak and the slight shift and broadening of the other peaks.

This trend is confirmed by the trend in the O K-edge spectra for the same regions (Fig. 7.16c). Although the O spectra are noisy compared to the Ti spectra, a reduction in the peak A intensity can be observed in the LRS state. In line with the XPEEM observations from section 7.2, this indicates an increased number of electrons in the conduction band, i.e., an increased amount of Ti^{3+}. In contrast to the XPEEM experiments, however, the O K-edge measured using EELS was too noisy for reliable information about small changes. Therefore, the Ti L-edge will be used for further investigation in the following. First of all, in order to verify that the observed valence changes are reproducible and not due to irreversible heating effects, the device was switched between LRS and HRS several times and further spectra were acquired, resulting in the same observation (Fig. 7.17).

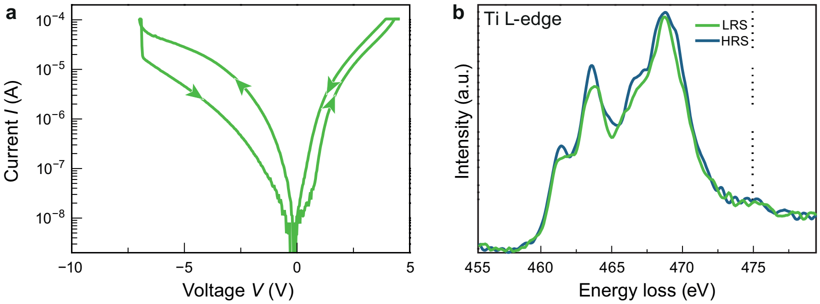

Figure 7.17: Reproducibility of switching effects in the TEM. (a) A second switching cycle for the same device as in Figs. 7.15 and 7.16. (b) Ti L-edge EEL spectra for the interface region indicated in Fig. 7.16a, acquired after the devices was switched again to the LRS and HRS.

In a next step, the oxidation states of the device was mapped with very high spatial resolution. Fig. 7.18a shows an annular dark field STEM image of the ROI in the LRS, Fig. 7.18b and c show series of EEL spectra that have been collected from the $\approx 20\,\mathrm{nm}$ $SrTiO_3$ thin film from the substrate towards the Pt interface with a step of 1.2 nm between each acquisition for the LRS and the HRS. A gradual change in the $\frac{\mathrm{Ti}^{3+}}{\mathrm{Ti}^{4+}}$ ratio is apparent for the LRS (compare Ti L_3 e_g peak position in Fig. 7.18b), which becomes more obvious when plotting the normalized intensity of the L_3 t_{2g} edge (Fig. 7.18d), which gives a direct measure of the oxidation state of the device as discussed in section 4.1. From these spectra it can be seen that the oxidation states are most strongly modified near the Pt electrode, where a shift in the Ti L_3 e_g peak position of $-0.3\,\mathrm{eV}$ can be observed, which is indicative of a low oxygen vacancy concentration of less than 4 at.%, based on a comparison with ref. 115. A map of the L_3 e_g peak width indicates the changes in Ti^{3+} concentration in a two-dimensional manner (Fig. 7.18e). For the LRS, the Ti^{3+} concentration appears only in the $SrTiO_3$ film and it increases linearly from bottom to top while it seems to be laterally rather homogeneous. Comparison of this trend in $\frac{\mathrm{Ti}^{3+}}{\mathrm{Ti}^{4+}}$ ratio for the LRS with the same measurement in the HRS reveals that in the HRS, the entire film shows only Ti^{4+} states (Fig. 7.18c and f). In line with the observations from the XPEEM experiments, the TEM analysis validates a valence change at the Pt/$SrTiO_3$ interface as the origin of eightwise resistive switching.

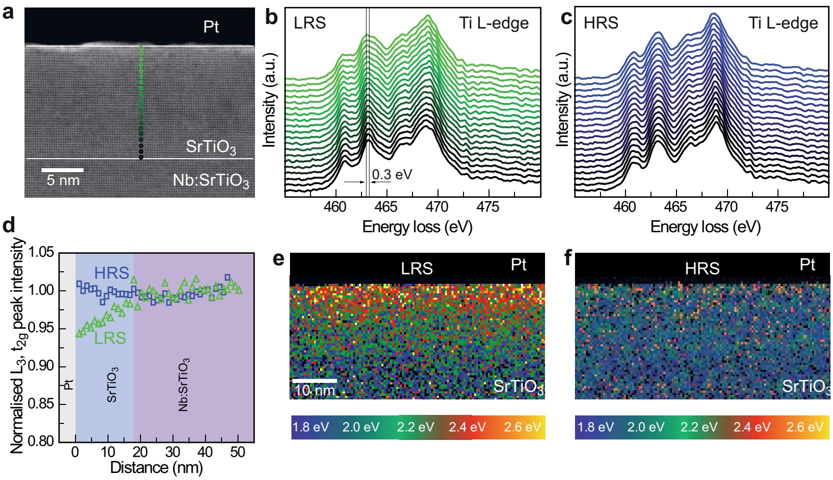

Figure 7.18: Vertical mapping of the redox reaction. (a) High-resolution annular-dark field image of the ROI in the LRS. (b) Ti L-edge EEL spectra for the device in the LRS. The spectra have been acquired across the SrTiO$_3$ film using 1.2 nm steps from bottom to top as indicated in (a) and show the evolution of the edges as a function of position up to a depth of 20 nm into the device. (c) Ti L-edge EEL spectra for the device in the HRS. Again, the spectra have been acquired across the SrTiO$_3$ film using 1.2 nm steps from bottom to top as indicated in (a). (d) The intensity of the L$_3$ t$_{2g}$ edge as a function of depth into the specimen for LRS and HRS acquired to a depth of 55 nm into the device. (e) Map of the fitted Ti L$_3$ e$_g$ peak width in the LRS. (f) Map of the fitted Ti L$_3$ e$_g$ peak width in the HRS.

Interestingly, not only the concentration gradient changes between LRS and HRS, but also the total oxygen vacancy concentration in the entire SrTiO$_3$ film varies reversibly. This is obvious from the difference of the total Ti^{3+} concentration (several at.% Ti^{3+} in the LRS, no Ti^{3+} in the HRS) and can be further confirmed through mapping of the total oxygen concentration obtained using standard EELS signal integration techniques (Fig. 7.19). In the LRS, there is less oxygen in the SrTiO$_3$ film than in the HRS. As expected based on the high formation energy of oxygen vacancies in Nb:STO, the concentration in the substrate remains constant for both HRS and LRS. While background removal can lead to large errors in the quantitative measurements based on this signal integration, the general trend of a different total oxygen concentration in the SrTiO$_3$ film between LRS and HRS certainly holds true.

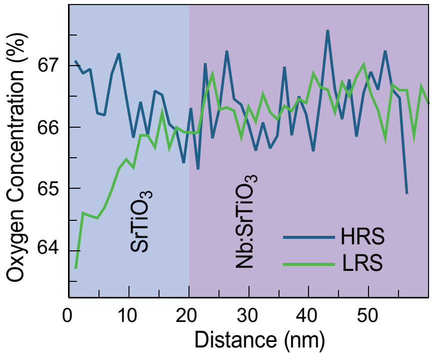

Figure 7.19: Oxygen profiles for the LRS and HRS. Oxygen maps were acquired by integrating the O K EELS edge and the average oxygen concentration is plotted as a function of depth.

A larger field of view was examined to determine the size and position of the redox-active region of the device. EELS maps were acquired across a several µm-wide region to assess the changes in oxidation states. The spectra shown in Figs. 7.16, 7.17 and 7.18 were recorded in the region underneath the contact between the metal lead and the top electrode and closest to the W probe and will be referred to as point A from now on. Fig. 7.20a shows Ti L-edge spectra for different points underneath the contact area between metal lead and top electrode. Here, it can be seen that the $SrTiO_3$ underwent a valence change from Ti^{4+} to Ti^{3+} at point A and point B, which indicates the region underneath the contact between metal lead and top electrode farthest away from the W probe. The same valence change was also found for each point in between points A and B. As was shown in Figs. 7.18 and 7.20, the $SrTiO_3$/Nb:$SrTiO_3$ interface does not exhibit a valence change (points C and D). The Pt/$SrTiO_3$ interface farther away from the contact area between metal lead and top electrode do not exhibit any sign of a valence change (points E and F, Fig. 7.20b), as schematically depicted in Fig. 7.20c. These observations show on the one hand that the redox reaction has a rather large spatial extent of ≈3 µm in the lateral direction, which corresponds well to previous observations [53]. On the other hand, it is clear that the redox reaction does not occur underneath the entire electrode area but rather in a preferred position closest to the metal lead. These observations suggest a rather spatially extended process where localization may be induced by the boundary conditions. As will be discussed in detail in the next chapter, the most obvious reason why the redox reaction could be located

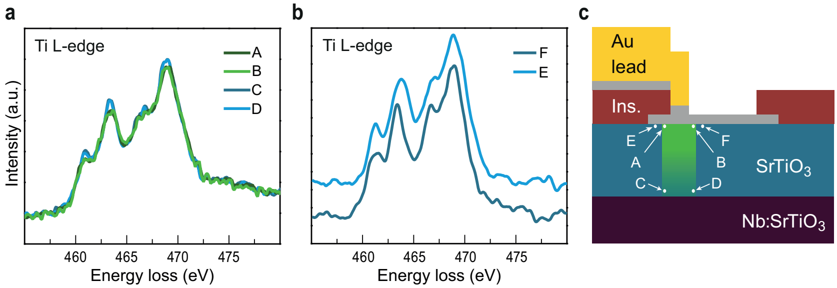

Figure 7.20: Horizontal extent of the redox reaction. (a) Ti L-edge spectra acquired from the different points indicated in (c). A and B are points close to the Pt/$SrTiO_3$ interface within the overlap between metal lead and top electrode, C and D are close to the bottom interface. (b) Ti L-edge EEL spectra acquired from points close to the Pt/$SrTiO_3$ interface outside the contact area but still underneath the top electrode as indicated in (c). (c) Schematic of the specimen indicating the regions where changes occurred during the switching experiments.

in a specific contact-area-defined region is the role of Joule heating, which is typically necessary to enable the valence change [57].

7.4 Summary

In summary, this chapter presented two complimentary *in operando* approaches to characterize the memristive operation in $SrTiO_3$-based devices. Using graphene electrodes, PEEM characterization focusing on work function scans revealed the creation and reproducible work function change of spatially confined switching filaments. In some cases, the location of the active filament may even change from cycle to cycle.

XPEEM analysis based on the O K-edge demonstrates that the resistance change is connected with a valence change of the Ti within the active filament. During Set and Reset operations, the peak A intensity decreases or increases, respectively, which shows an increase or decrease of the carrier concentration at the conduction band edge, which is caused by reversible doping with oxygen vacancies. High resolution XPEEM measurements show that the filaments exhibit an intricate fine structure with an inhomogeneous Ti^{3+} distribution.

Careful comparison of the filament spectra to the references established in section 4.1 even allowed a quantitative assessment of the carrier density change between LRS and HRS – a quantity that has previously been elusive but long-awaited in the resistive switching community for the educated modeling and development of memristive devices.

Using *in operando* TEM of a cross-sectional device, the differences between LRS and HRS could be mapped at the atomic scale in the remaining, third dimension. The valence change occurred through a change in the total oxygen concentration of the film, which is in line with the dependence of the switching and retention characteristics on the external oxygen partial pressure observed in chapter 5. In the LRS, a decrease of the total oxygen concentration leads to a linear Ti^{3+} profile, where high amounts (several at.%) of Ti^{3+} can be observed at the $Pt/SrTiO_3$ interface, which decays towards ≈ 0 at.% at the $SrTiO_3/Nb{:}SrTiO_3$ interface. Lateral mapping revealed that the valence change has a rather large spatial extent, but occurs in a preferred position due to the external boundary conditions.

8 Discussion

After the characterization of the $SrTiO_3$-based devices using atmosphere and temperature dependent electrical characterization, post mortem and *in operando* PEEM and *in operando* TEM analysis, the results will now be discussed to derive the qualitative switching mechanism and to discuss the redox reaction quantitatively (section 8.1). Afterwards, the retention failure mechanism will be deduced and a rational design of retention-failure-resistive devices based on the intentional fabrication of oxide heterostructures will be introduced (section 8.2). In a last step, the switching mechanism in these heterostructures will be discussed (section 8.3). The results and considerations presented in this chapter have been published in part in refs. 112, 152 and 153.

8.1 The switching mechanism of eightwise resitive switching in $SrTiO_3$

As discussed in the introduction, the underlying physicochemical mechanism of so-called eightwise resistive switching is still under controversial debate. With direct experimental evidence of the redox reactions being inaccessible so far, several phenomenological models have been suggested to explain the eightwise switching phenomenon as described below. The atomic-scale insights about the redox reaction derived from the *in operando* TEM and PEEM characterization described in the previous chapter allow for an evaluation of each of the proposed mechanisms.

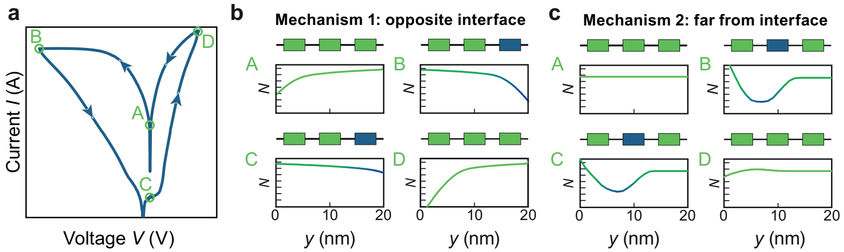

Figure 8.1: Previously proposed mechanisms for eightwise switching in $SrTiO_3$. (a) I-V-curve of an exemplary device exhibiting eightwise switching. (b) Proposed mechanism for switching at the bottom electrode interface located at $y = 20\,\mathrm{nm}$. Schematic oxygen vacancy concentration N in the LRS (A), during Reset (B), in the HRS (C) and during Set (D). (c) Proposed mechanism for switching far from the top electrode interface located at $y = 0\,\mathrm{nm}$ based on ref. [8]. Schematic oxygen vacancy concentration N in the LRS (A), during Reset (B), in the HRS (C) and during Set (D) based on the mechanism suggested in ref. 53. The resistance of the top interface, the filament itself and the bottom interface are represented by electronic symbols for simple resistors connected in series. Low resistance is indicated in green, high resistance is indicated in blue.

8.1.1 Clarifying the switching mechanism

Mechanism 1: Opposite interface. Competing switching polarities have been observed in many memristive systems, and this competition was mostly attributed to the change of the active electrode [36, 60, 61]. Since it was shown that the $SrTiO_3$/Nb:$SrTiO_3$ interface is not free from space charges [37], a possible scenario of eightwise switching could therefore be that resistive switching takes place at the bottom electrode interface instead of at the top Pt interface because of an increased potential barrier, which may be modulated by the near-interface oxygen vacancy concentration $[V_O^{\bullet\bullet}]$ (Fig. 8.1a and b). Here, the potential barrier at the bottom electrode interface would have to be larger than the one at the top electrode interface and therefore the carrier density at the bottom interface would govern the I-V characteristics of the device. For this scenario to be true, however, one would expect high $[V_O^{\bullet\bullet}]$ near the $SrTiO_3$/Nb:$SrTiO_3$ interface in the LRS. But the XPEEM and TEM results indicate exactly the opposite, i.e., oxygen vacancy accumulation at the Pt interface in the LRS and low $[V_O^{\bullet\bullet}]$ near the $SrTiO_3$/Nb:$SrTiO_3$ interface.

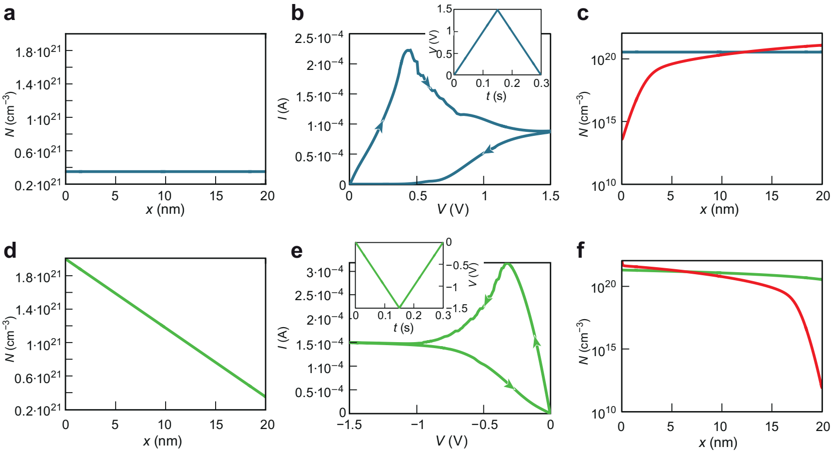

Figure 8.2: Limitations of the drift-diffusion model with ion-blocking electrodes. (a) Oxygen-vacancy profile of the HRS derived from the *in operando* TEM experiments. (b) Simulated I-V-curves for a triangular signal of positive voltages using the vacancy profiles from (a) as initial donor concentration profiles. (c) Vacancy profiles before and after the application of the positive voltage signal (blue line and red line, respectively). (d) Oxygen-vacancy profile of the LRS derived from the experiments. (e) Simulated I-V-curves for a triangular signal of negative voltages using the vacancy profiles from (d) as initial donor concentration profiles. (f) Vacancy profiles before and after the application of the negative voltage signal (green line and red line, respectively). The simulation was performed by Astrid Marchewka.

Mechanism 2: Far from interface. When oxygen vacancies are attracted to the top electrode and are highly concentrated near the interface, the region below may become oxygen vacancy-deficient (Fig. 8.1c). The increased resistance of this region then causes the HRS [10,53,62]. However, $[\mathrm{V}_\mathrm{O}^{\bullet\bullet}]$ in this case would need to be highest near the top electrode interface for the HRS, which is clearly opposite to the flat $[\mathrm{V}_\mathrm{O}^{\bullet\bullet}]$ distribution in the HRS and the $[\mathrm{V}_\mathrm{O}^{\bullet\bullet}]$ increase in the vicinity of the top electrode in the LRS observed using both XPEEM and TEM. Mechanism 2 can therefore not account for eightwise resistive switching in these samples.

Given that these two suggested mechanisms do not agree with the experimental Ti^{3+} fingerprints for the LRS and the HRS, the evolution of the corresponding oxygen vacancy distributions upon electrical bias was investigated using a numerical drift-diffusion model of coupled electronic-ionic transport inside the oxide layer[1] [8]. In the simulations, both electrodes are considered as oxygen blocking, enabling a mere redistribution of the donor-type oxygen vacancies inside the oxide layer. This redistribution is the commonly excepted driving force of resistive switching in redox-based systems, which can describe the counter-eightwise switching convincingly [8].

Starting with the homogeneous oxygen vacancy distribution of the HRS (Fig. 8.2a), a positive triangular voltage signal is applied, resulting in the (intuitively expected) retraction of oxygen vacancies from the Pt interface. Such a distribution causes an increased Schottky barrier, and therefore even increased device resistance (Fig. 8.2b-c). This behavior, which actually corresponds to the regular counter-eightwise switching mechanism, is in stark contrast to the devices investigated here, where the $SrTiO_3$ devices are switched to the LRS using a positive bias resulting in an increased concentration of Ti^{3+} at the Pt electrode interface, corresponding to an increased $[V_O^{\bullet\bullet}]$. Similarly, the evolution of the oxygen vacancy profile of the LRS upon application of a negative triangular voltage signal is simulated (Fig. 8.2d-f), correctly resulting in an increased resistance. But a further increase in $[V_O^{\bullet\bullet}]$ is observed near the Pt electrode interface, while the concentration at the Nb:$SrTiO_3$ electrode decreases. The resulting distribution does not resemble the flat distribution of the HRS that can be derived from the experimental data. In conclusion, redistribution of oxygen vacancies inside the oxide – one of the basic assumptions of many resistive switching models – solely leads to the normal (counter-eightwise) resistive switching. It completely fails to explain eightwise resistive switching as the observed donor profiles for LRS and HRS cannot be transformed into each other.

Based on these shortcomings of existing models, the following model for eightwise switching – which has been phenomenologically proposed for other oxides before – has to be considered for $SrTiO_3$-based memristive devices.

Mechanism 3: Oxygen exchange. As the total oxygen vacancy concentration in the entire $SrTiO_3$ film (not just at one interface) varies reversibly between a high concentration after applying positive voltages (Set to LRS) and a low concentration

---

[1] The simulation was performed by Astrid Marchewka, Institute of Materials in Electrical Engineering and Information Technology II, RWTH Aachen University, Aachen, Germany.

after applying negative voltages (Reset to HRS), oxygen must inevitably be removed from the $SrTiO_3$ lattice during the Set process and reincorporated during the Reset as schematically depicted in Fig. 8.3. In other words, a positive bias on the Pt electrode would result in anodic oxidation of lattice oxygen resulting in the formation of oxygen vacancies in the vicinity of the Pt/$SrTiO_3$ interface and the evolution of oxygen gas (oxygen evolution reaction, equation 2.2). This leaves behind two electrons, which is observed experimentally as a valence change between Ti^{4+} and Ti^{3+} according to equation 2.3. In the same sense, a negative bias results in a reduction reaction at the Pt/$SrTiO_3$ interface (oxygen incorporation reaction, equation 2.2). From an electrochemical perspective, these processes can be regarded as oxygen evolution and oxygen reduction reactions [184].

The mechanisms that are commonly invoked to explain eightwise resistive switching in $SrTiO_3$ (mechanisms 1 and 2) fail to account for the observed Ti^{3+} profiles, and the TEM results explicitly verify a total oxygen concentration difference of the $SrTiO_3$ film between LRS and HRS (Fig. 7.19), which is also consistent with the valence changes observed using XPEEM. Therefore, oxygen evolution and reincorporation (mechanism 3) have been validated as the only mechanism which can account for eightwise switching in $SrTiO_3$.

$SrTiO_3$ thickness dependence and the role of the Pt top electrode

While potentially intermediate steps of the oxygen evolution and reincorporation reactions as well as the influence of extrinsic contributions such as water [177, 185] and carbon-containing species have to remain subject of further research, the question arises where the gaseous oxygen necessary for the Reset operation comes from. It was shown many years ago that oxygen can migrate through Pt [186, 187] and SIMS measurements have shown that it can in fact be stored within Pt electrodes of memristive devices [188], most probably through physisorption or chemisorption within grain boundaries. One may therefore surmise that after Set, O_2 is stored within the Pt grain boundaries and reincorporated into the $SrTiO_3$ during Reset as illustrated in Fig. 8.3.

Coming back to the results from the thickness series presented in chapter 5, a general trend was observed where thicker $SrTiO_3$ films require higher switching voltages

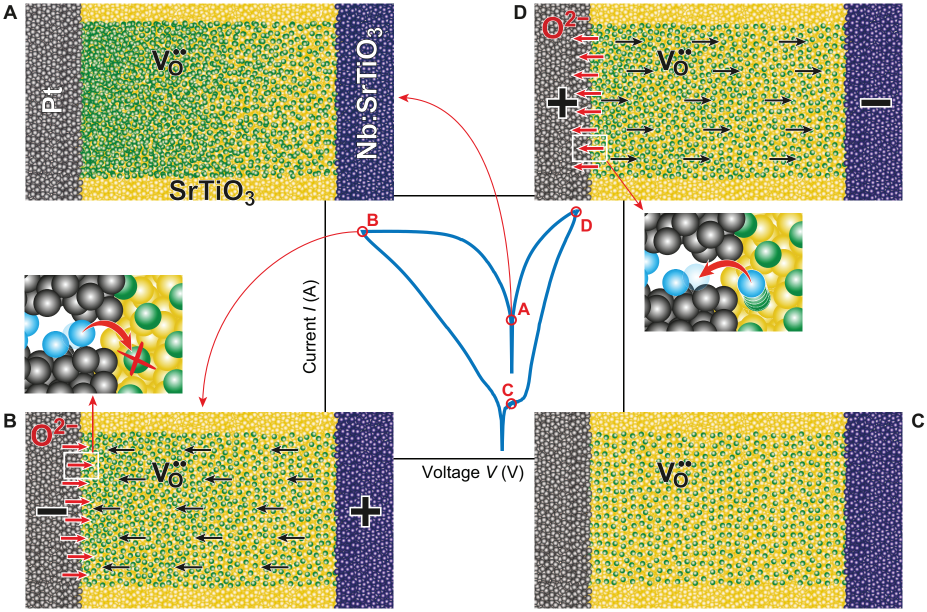

Figure 8.3: Proposed mechanism for eightwise switching through oxygen evolution and reincorporation. An I-V-curve of an exemplary device exhibiting eightwise switching is depicted together with schematics of the proposed mechanism. A: LRS. Oxygen-vacancy filament (green circles) in a matrix of stoichiometric SrTiO$_3$ (yellow circles) sandwiched between a Pt top electrode (grey circles) and a Nb:SrTiO$_3$ bottom electrode (blue circles). B: Reset. oxygen ions are reincorporated into the SrTiO$_3$ lattice and recombine with the oxygen vacancies, reducing the total number of vacancies in the filament. C: HRS. The filament is nearly completely reoxidized. D: Set. Oxygen ions are removed from the SrTiO$_3$ lattice, leaving behind oxygen vacancies.

(Fig. 8.4). In terms of the switching mechanism based on oxygen evolution and reincorporation, this can be understood in the following ways. On first sight, an increased film thickness t may require a higher voltage V_C to achieve the critical field E_C for the oxygen evolution and reincorporation reactions, if one assumes that the electric field mostly drops across the film itself, as $E_\mathrm{C} = -\nabla V_\mathrm{C}$ would yield $E_\mathrm{C} = -\frac{V_\mathrm{C}}{t}$. Based on this crude approximation, one would expect a proportional dependence of V^form and V^Set on t [189]. But this is not the case. While the dependence of V^form on t appears to be rather linear, it clearly does not cross the origin. Instead, one finds $V^\mathrm{form}(t = 0) \approx 1.5 - 1.8\,\mathrm{V}$, indicating that more complex factors must be at play

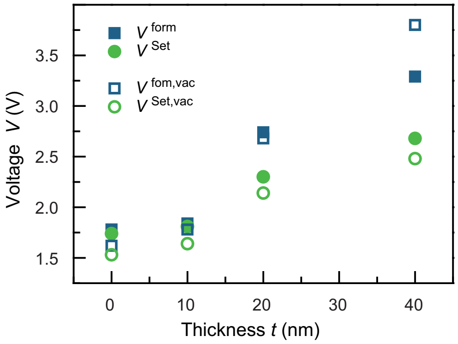

Figure 8.4: Switching parameters in air an in vacuum. Forming voltage V^{form} and Set voltage V^{Set} in air and in vacuum reproduced from tables 5.1 and 5.2.

(Fig. 8.4). This is easily understandable as the electric field must mostly drop in the depletion region of the Schottky barrier, so the critical voltage would depend on t in a more complex way.

In addition to this complex dependence, one has to consider the total amount of oxygen which is removed from the $SrTiO_3$ and reincorporated. One may assume that the observed linear trend of the oxygen vacancy profile between a high $[V_O^{\bullet\bullet}]$ at the Pt interface and a small $[V_O^{\bullet\bullet}]$ at the Nb:$SrTiO_3$ interface needs to be established for the LRS of all film thicknesses. For thicker films, therefore, the total amount of oxygen which must be removed from the lattice is higher. This may be the reason for higher Set voltages, or longer Set times for a given voltage. Similarly, more oxygen needs to be reincorporated to achieve the flat $[V_O^{\bullet\bullet}]$ observed for the HRS, leading to an increase in V^{Reset}. But again, one would expect a proportional dependence of these voltages on t.

An indication that different total amounts are involved in the operation of devices with different film thicknesses can be derived from the SEM images presented in Fig. 5.14. Based on mechanism 3 as described above, one may assume that the oxygen is stored in the grain boundaries of the top electrode. These grain boundaries will have a certain capacity for O_2-storage. For example, the oxygen removed during the operation of a 10 nm $SrTiO_3$ device can be stored in the Pt electrode without any deformations (Fig. 5.14a). For thicker films, increasing amounts of bubbles are observed (Fig. 5.14b-c), indicating that more oxygen is removed from the $SrTiO_3$ than can be stored in the grain boundaries. This is similar to the development of O_2 gas during forming as described in ref. 156, where the number of bubbles in the Pt electrode was found to depend on the volume of the oxide layer of the device.

The influence of the surrounding atmosphere

These different amounts of oxygen gas which are involved in the Set and Reset operations are also responsible for the differently pronounced dependence on the surrounding atmosphere for different thicknesses observed in section 5.4. As more oxygen is necessary for the Reset of thick films, it is rather straightforward that the Reset operation cannot be completed for these films in oxygen-deficient atmospheres. On the microscopic scale, this may have several reasons. For example, oxygen-species stored in the grain boundaries, which – one may speculate – are sufficient for the Reset of thin films, may be stable in vacuum so that the switching in air and in vacuum is very similar (compare the similar forming and switching voltages in Fig. 8.4). For thicker films, the oxygen-species for the Reset may be supplied either from the bubbles underneath the electrode, or from the surrounding atmosphere itself, as proposed in ref. 154. In the first case, O_2 stored underneath mechanically deformed Pt may escape more easily than O_2 stored in Pt grain boundaries, leading to insufficient oxygen supply in reducing atmospheres. In the second case, if the surrounding atmosphere itself supplies the oxygen necessary for Reset, it is clear that low oxygen partial pressures impede the Reset (in fact, one would expect that Reset in vacuum or reducing atmospheres might not be possible at all). For these reasons, a partial Rreset is observed in 20 nm films, while no Reset is possible in 40 nm films.

Other top electrode materials

If the oxygen is indeed removed from the $SrTiO_3$ at the top electrode interface, the electrode material should be suspected to have a large impact on the microscopic details of the switching. For Pt, solubility of O_2 in the grain boundaries has been reported many times, but for Au, this is not commonly observed. This may be the reason why Au top electrodes on $SrTiO_3$ films tend to exhibit numerous holes after memristive operation [54]. Rather than storage in grain boundaries, oxygen-species may create bubbles underneath the Au at an earlier stage than observed for the Pt. Given the low ductility and low melting point of Au compared to Pt [190], these bubbles will burst more easily, leaving behind the observed holes, which may play a significant role in the switching and retention behavior due to the enhanced reaction rates for oxygen evolution and reincorporation at triple-phase-boundaries [15].

Considering the ultra-thin electrodes for *in operando* spectromicroscopy, the high Set voltage for 2 nm Rh is suprising. As noted in section 5.2, no forming or Set was possible for thicker Rh layers. It can therefore be speculated that oxygen evolution is impeded by low solubility in Rh. Because of its high tensile strength and high melting point [190], bubble formation may not be possible to overcome the solubility limit. Therefore, thin Rh layers require higher voltages to drive the oxygen evolution, oxygen-species might be able to penetrate such a thin layer. Thick Rh layers then inhibit oxygen evolution entirely. Another possible reason for the impeded oxygen evolution may be the formation of a thin layer of Rh oxide at the electrode/oxide interface as Rh is a less noble metal than Pt or Au. But this oxide layer cannot account for the observed thickness dependence in a straightforward manner. For graphene electrodes, it has been shown using Raman spectroscopy that oxygen-species may escape from the oxide layer during Set and that they may be stored through chemical bonding to the graphene layer until reincorporation into the oxide during Reset [21].

Nb:SrTiO$_3$

The LRS retention times in noble metal/Nb:SrTiO$_3$ also depend on the availability of oxygen species for the reoxidation of a previously oxygen-deficient Nb:SrTiO$_3$ surface [153]. In combination with the direct spectromicroscopic observation of the valence change mechanism from section 6.3, this indicates that oxygen-ion migration rather than the frequently discussed trapping and detrapping of defect states is responsible for the resistive switching observed here. The retention failure rate in devices switched with low current limits does not scale with the electrode-size [153]. Since these devices exhibit a homogenous current distribution, the whole area of the Pt electrode must also be involved during the reoxidation effect. Therefore, it appears likely that the reoxidation occurs via oxygen transport through the top electrode (most likely along Pt grain boundaries) rather than at the electrode edge.

For these reasons, one may assume that mechanism 3 is also responsible for the resistive switching in noble metal/Nb:$SrTiO_3$ devices, as was suggested before [64, 65]. For example, Buzio *et al.* presented oxygen evolution and incorporation as the only reasonable explanation for the observed p_{O_2}-dependent switching characteristics [64]. This switching mechanism appears to be responsible for both spatially homogeneous switching and filamentary switching, as they exhibit the same switching polarity in line with oxygen evolution leading to the LRS. While switching polarity and the shape of the I-V-curves remains similar, a substantial difference observed for these two cases is that the $\frac{R_{\mathrm{off}}}{R_{\mathrm{on}}}$-ratio for devices operated under the filamentary switching mechanism is orders of magnitude larger. This can be understood as the filamentary switching mechanism leads to considerable Joule heating (higher currents confined to a much smaller area), enabling thermally assisted ion migration. This process can lead to the observed drastic change in resistance due to the evolution of a large amount of oxygen, as is obvious from the Ti^{3+} filament presented in section 6.3. The difference between spatially homogeneous switching and filamentary switching, accordingly, does not lie in the fundamental switching mechanism but in the presence or absence of Joule heating, which can assist in the field-driven ion migration and therefore lead to a more pronounced resistance change.

8.1.2 Location of switching induced redox reactions

From the TEM analysis, it was clear that the redox reaction occurred underneath the overlap between the metal lead and the top electrode, and this was repeatedly observed for all measured devices in the TEM. On first sight, it is surprising that the metallic contact (Pt lead and Pt electrode) should define the location of the switching event, as the electric field distribution has to be homogeneous below the entire top electrode with potential field enhancements at the electrode edges. One would therefore expect the switching to occur preferentially at defects within the film or at the electrode edges [123].

The most obvious reason why the redox reaction could be located instead in a specific contact-area-defined region is the role of Joule heating, which is typically necessary to enable the valence change [57]. This suspicion is verified through thermal imaging of a representative 20 nm $SrTiO_3$ device with metal lead during the Set process (Fig. 8.5a).

Overlaying the thermal image with an optical micrograph reveals that the local hot-spot is located in the contact area between metal lead and top electrode. The absolute temperatures given in Fig. 8.5a cannot represent the true, local temperatures as the limited resolution of infrared imaging (about 8 µm in this case) inevitably smears out the information from the different regions of the sample. Moreover, only the surface temperature is measured rather than the temperature of the buried active layer. Nevertheless, the qualitative localization of the hottest region may explain the preferred switching underneath the contact.

An electro-thermal simulation (Fig. 8.5b) sheds light on the reason for the preferential heating of the contact area[2]. The simulation solves the stationary current continuity and heat equation for the temperature and electric potential in the whole TEM specimen. Assuming metallic contact between the metal lead and the top electrode always resulted in the hottest region of the device exactly in the center of the top electrode. Including a contact resistance above and underneath the Pt top electrode – representative of carbon-containing species resulting from *ex situ* fabrication and photo resist residues – shifts the hot-spot to the part of the top electrode that is in contact with the lead. The occurrence of such residues may be the reason for the dark shadow observable between the metal lead and the top electrode in the STEM image in Fig. 7.16a. The introduction of the contact resistance creates a voltage divider between the oxide and the contact resistances such that more heat is dissipated in the contact area. In conclusion, the thermal and electrical boundary conditions of the entire device including the electrical contacts dictate the location of the resistive switching in these samples.

This may also be the reason why the switching filaments of the devices studied here, which were identified by post-mortem spectromicroscopy and conductive AFM (cf. chapter 6) always occurred at the contact point between the W probe used for electrical contacting and the top electrode. This observation is different from Fe:$SrTiO_3$ devices investigated previously, where defects in the film or the electrode edge were found to be preferential switching locations [123]. One can only speculate that the different defect structure of the Fe:$SrTiO_3$ films and the nominally undoped films is responsible for these differences. In addition, the different resistivity between these films may play a role. For 20 nm Fe:$SrTiO_3$ devices, the device resistance during forming or Set is

---

[2] The simulation was performed by Camilla La Torre, Institute of Materials in Electrical Engineering and Information Technology II, RWTH Aachen University, Aachen, Germany.

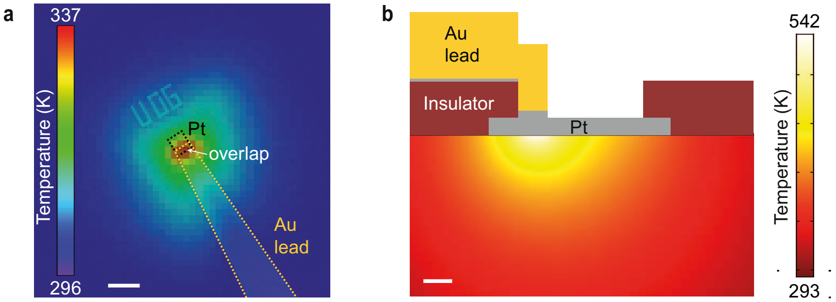

Figure 8.5: Origin of the filament location. (a) Thermal image of a 20 nm $SrTiO_3$ device with metal lead overlaid with an optical micrograph during the Set process. The device possesses the same layer stack and metal lead as the TEM specimen. The top electrode area is indicated with the black, dashed line, the metal lead is indicated with the yellow, dashed line. The hottest temperatures are measured in the overlap area of electrode and metal lead. Scale bar, 30 µm[3]. (b) Excerpt of a 2D electro-thermal simulation. The simulated temperature in the $SrTiO_3$ and Nb:$SrTiO_3$ layers is depicted as color code. The top layers are magnified with respect to their height but not their width to enable the identification of the hot-spot. Clearly, the highest temperature is reached beneath the part of the Pt top electrode that is capped with the Pt/Au lead. Scale bar, 3 µm. The simulation was performed by Camilla La Torre.

typically 3-10 × $10^3\,\Omega$ [54, 123], still dominated by the device resistance itself. For nominally undoped 20 nm $SrTiO_3$ devices used here, it is only the order of $10^2\,\Omega$, where it is much more likely that contact resistances play a role.

Regarding the graphene/$SrTiO_3$ devices, no evidence of switching could be found for many devices under investigation. For these devices, it is very likely that the switching occurred underneath the metal lead, similar to the case of Pt electrode contacted with the metal leads described above. Given the inhomogeneous contact between graphene and an underlying substrate [191], however, it is reasonable that the switching filament can be created in a different location as well. This is obvious from the reproducible changes of the switching filament carrier density observed in Figs. 7.5 and 7.10. The location of the switching filament can be also be pre-defined through forming of a filament using a W probe before electrode deposition (Fig. 7.13). If the active layer (i.e., the $SrTiO_3$) already exhibits a reduced filament even before the electrode and metal lead fabrication, it appears that the boundary conditions given by the contact

---

[3] Thermal imaging was performed with Dr. Christian Rodenbücher, Peter Grünberg Institute, Forschungszentrum Jülich GmbH, Jülich, Germany.

resistance play a smaller role as resistive switching will preferentially occur in the predefined region.

If oxygen is removed from the $SrTiO_3$ lattice during forming and Set, it is conceivable that the quality of the contact between graphene and $SrTiO_3$ will suffer. This may be the reason why the location of the filament was changing for some devices (Fig. 7.7). Alternatively, it can be imagined that once the filament has been completely reoxidized, other regions where pre-filaments were previously created [16, 192] might become the most likely location for the creation of a new filament.

8.1.3 Quantitative analysis of the switching process

In section 5.6 it was shown that during switching, the effective Schottky barrier appears to change. For the LRS, the effective barrier appears narrower and smaller than for the HRS, giving rise to increased tunneling currents, especially for 20 nm and 40 nm films. As the current in the LRS will mostly flow through the reduced filament rather than the entire device area, one may expect a local variation of the barrier.

Along the same line, spatially resolved work function scans during PEEM experiments indicated that the local work function of the active layer may change because of the resistive switching [54, 167]. If the work function of the active layer is reduced, the conduction band edge will be closer to the Fermi energy, resulting in more mobile carriers (Fig. 8.6a). In other words, the doping effect of oxygen vacancies discussed in section 2.1 reduces the oxide work function, which in turn reduces the Schottky barrier (cf. Fig. 2.3).

During the *in operando* PEEM experiments with graphene top electrodes, the same effect was observed. For the LRS, the filament work function was reduced. The interpretation of these results, however, requires more careful consideration. As the work function determined by PEEM experiments typically indicates the work function of the topmost layer, one may question if the changes in the local work function are not related to changes in the graphene layer rather than the $SrTiO_3$. Using Raman spectroscopy, Tian *et al.* have shown that in fact a graphene top electrode may be chemically doped by oxygen species during memristive operation [21]. During Set, oxygen-species leave the $SrTiO_3$ and lead to heavy p-doping in the graphene layer, which is reduced to slight

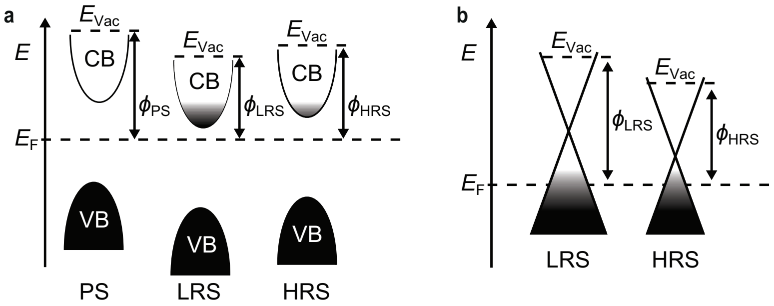

Figure 8.6: Potential origin of the work function changes during switching. (a) Band diagram for the pristine state (PS), LRS and HRS demonstrating how the $SrTiO_3$ work function, valence band (VB) and conduction band (CB) shift for different oxygen vacancy concentrations. Modified from ref. 167. (b) Band diagram for the graphene top electrode due to p-doping from oxygen-species for the LRS and HRS as expected from the observations in ref. 21. Occupied states are indicated in black, unoccupied states are white.

p-doping after Reset. The implications this doping effect will have on the graphene work function is depicted in Fig. 8.6b. In the LRS, the graphene work function would be larger than in the HRS.

This opposite trend compared to the $SrTiO_3$ work function makes it possible to distinguish between the two effects. As the experimental observation is in line with the reduced filament work function expected for the $SrTiO_3$ and contradicting to the expected shift of the graphene work function, it appears that the $SrTiO_3$ rather than the graphene layer dominate the signal. This interpretation is also in line with the observation that the XPEEM analysis of the $SrTiO_3$ layer is possible through the graphene electrode, indicating theat the secondary electrons used to acquire the PEEM image tunnel through the graphene.

As described in section 2.2 and in more detail in ref. 38, the current flowing through a device depends on the barrier height in an exponential manner for most typically considered conduction mechanisms, as can be seen, for example, from equation 2.4. The observed exponential trend between device resistance and filament work function (Fig. 7.6) – while not completely reliable due to the limited number of data points – is therefore also in agreement with the interpretation of the $SrTiO_3$ work function being responsible for the observed shift of the threshold photoemission spectra. The work function of the LRS is $\approx 0.1\,\mathrm{eV}$ lower than for the HRS.

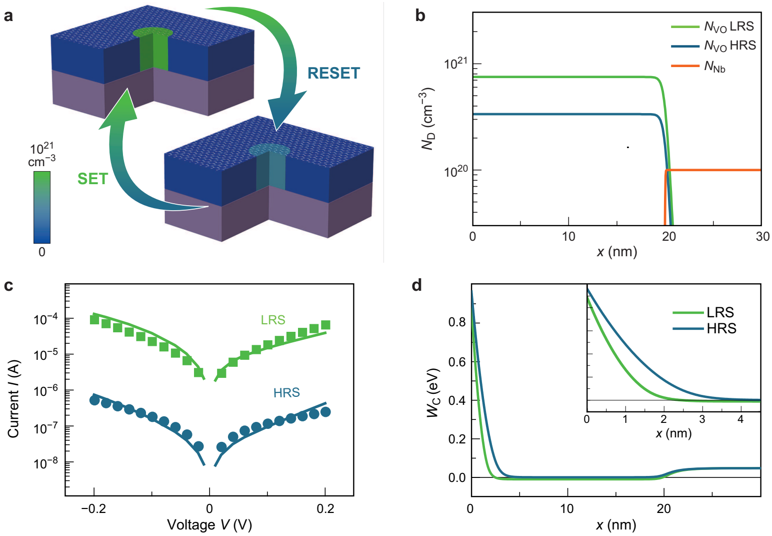

Figure 8.7: Utilizing PEEM-insights for device simulation. (a) Schematic of the switching filament in the HRS and in the LRS derived from the spectromicroscopic information. Filament diameter is 500 nm. The color scale refers to the oxygen vacancy concentration used for the model as described in panel (b). (b) Oxygen vacancy distributions as a function of depth x used for the simulation of the LRS and the HRS. In both cases, a flat distribution was assumed. (c) Experimental read-out sweeps (green and blue data points for the LRS and HRS, respectively) of the device in Fig. 7.10 with simulated I-V characteristics based on the model in (a) and (b) (green and blue lines). (d) Profiles of the energy of the conduction band edge $W_C(x)$ as a function of depth at zero bias for the LRS and the HRS. The simulation was performed by Astrid Marchewka. Modified from ref. 112.

Because of this ambiguous interpretation of the work function scans, which contain only indirect evidence of the valence change mechanism, a quantitative description of the switching process itself should be performed using the valence-sensitive, quantitative chemical information derived from the XPEEM measurements. In section 7.2, the switching induced carrier density variation was determined to be $9 \pm 2\,\%$ Ti^{3+} in the LRS and $4 \pm 1\,\%$ Ti^{3+} in the HRS averaged over a filamentary region of roughly 500 nm in diameter.

These filament dimensions and carrier densities can serve as input into an existing device simulation model to verify that the observed carrier density variations can account for the resistance change of approximately two orders of magnitude for this particular device. Using the model described in ref. 8, which was also used in section 8.1, the I-V characteristic of the device under investigation was calculated in both resistance states[4]. The simulated I-V curves were compared with experimental read-out sweeps at low biases. Focusing on the low voltages typical of the read-out sweeps avoids larger currents and voltages which might lead to unwanted resistance changes and which would necessitate complex temperature treatments in the simulation. Because of the derivation of the switching mechanism described in section 8.1, it was assumed that oxygen is removed from the $SrTiO_3$ lattice during Set and reincorporated during Reset. The low-voltage I-V characteristics of the LRS and HRS are calculated accordingly using static distributions of doubly ionizable donor-type oxygen vacancies in the $SrTiO_3$ thin film (Fig. 8.7a-c). The donor concentrations of both states are derived from the electron densities determined in the XPEEM experiments, i.e., the experimentally quantified values serve as an input parameter for the simulations and are not allowed to vary. All other parameters are identical in the simulations of the LRS and the HRS and their values were checked to be physically meaningful. As a first step, a uniform oxygen vacancy profile throughout the thin film was used for this simulation for the reasons of simplicity.

The results show that spatially confined changes in the oxygen vacancy concentration by a factor of 2-3 at the electrode-oxide interface indeed lead to changes of more than two orders of magnitude in the device resistance (Fig. 8.7c). Fig. 8.7d demonstrates that this resistance change is induced by the modulation of the effective Schottky barrier height and width, as was expected based on the arguments listed above. Considering the experimental uncertainties and simplicity of the model, the simulation yields a remarkable agreement with the experimental data, validating that the observed redox reaction is indeed responsible for the resistance change.

Coming back to the work function scans discussed above, the Schottky barrier height of the filament does change during resistive switching as expected. The Schottky barriers shown in Fig. 8.7d show a difference in the barrier height of $0.07\,\mathrm{eV}$ in addition to a significant barrier narrowing for the LRS. Together, these effects are in good agreement with the experimentally observed work function differences of $\approx 0.1\,\mathrm{eV}$.

---

[4] The simulation was performed by Astrid Marchewka, Institute of Materials in Electrical Engineering and Information Technology II, RWTH Aachen University, Aachen, Germany.

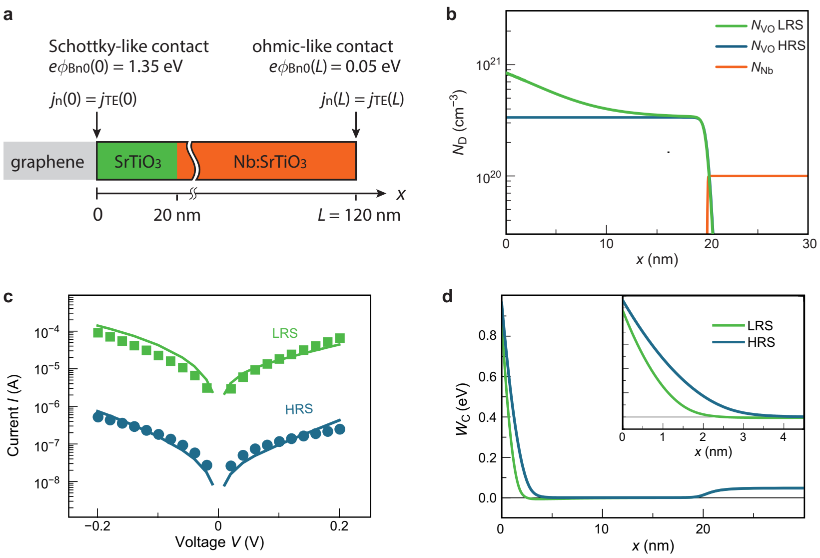

Figure 8.8: Impact of different oxygen vacancy for the simulation. (a) Model geometry. (b) Oxygen vacancy distributions as a function of depth x used for the simulation of the LRS and the HRS. For the LRS, a gradual decay of the oxygen vacancy concentration from the top electrode to the bottom electrode is assumed. (c) Experimental read-out sweeps (green and blue data points for the LRS and HRS, respectively) of the device in Fig. 7.10 with simulated I-V characteristics based on the model in (a) and (b) (green and blue lines). (d) Profiles of the energy of the conduction band edge $W_C(x)$ as a function of depth at zero bias for the LRS and the HRS. The simulation was performed by Astrid Marchewka. Modified from ref. 112.

Because of the observed gradient of the oxygen vacancy profile in the LRS (cf. sections 7.3 and 8.1), the assumed flat distribution used for the calculation presented above is an oversimplification. Therefore, the same simulation was repeated using a decaying oxygen vacancy profile in the LRS (Fig. 8.8). The oxygen vacancy concentration in the near-interface region, which is determined through the XPEEM experiments in this case, is kept constant between both simulations. The conduction band profiles and simulated I-V-characteristics resulting from both simulations with a flat distribution and a gradual decay of the oxygen vacancy concentration are almost identical (compare Figs. 8.7 and 8.8). Therefore, the Schottky barrier appears to be dictated by the interfacial carrier density and not to depend on the carrier density father away from the Schottky-type interface.

8.1.4 Implications for applications of memristive devices

Going beyond the model system $SrTiO_3$, there have already been indications and considerations that oxygen evolution and reincorporation might also drive the resistance change in other valence change memristive systems such as TiO_2 [157], Si rich SiO_x [158,193], CeO_2 [183], $SrRuO_3$ [194], $La_{0.8}Sr_{0.2}MnO_3$ [195], $Pr_{0.67}Ca_{0.33}MnO_3$ [196] and the technologically most relevant HfO_2 [154] and TaO_x [194]. However, these reports were mainly phenomenological and (therefore) oxygen evolution and reincorporation remained largely ignored for the comprehension and modelling of memristive devices, and accordingly their development towards application. Hence, the experimental verification of this switching mechanism demonstrates a fundamentally important insight into redox-based memristive device in general.

On first sight, a switching mechanism based on oxygen evolution and reincorporation is technologically challenging due to exchange with the environment and internal redistribution (i.e., counter-eightwise switching) might be favorable to improve device stability. Accordingly, the recognition of the origin of eightwise resistive switching can help to design memristive devices through educated means of suppression of the eightwise switching. This could be achieved, for example, through engineering of defect density, film thickness and operation conditions to allow intentional architectures which enhance internal redistribution and suppress oxygen exchange. For example, it was observed that eightwise switching typically requires higher operation voltages than counter-eightwise switching. Operation at low voltages – which can now be understood as operation below the critical voltage for oxygen evolution and reincorporation – can therefore suppress the eightwise switching.

Nevertheless, the devices presented in sections 7.3 and 5.4 are operational in a vacuum and in reducing gas atmospheres as well, which may lessen the apparent technological inapplicability. The $\frac{R_{\text{off}}}{R_{\text{on}}}$-ratio is largest in oxidizing atmospheres (compare section 5.4), indicating exchange with the surrounding and therefore verifying the mechanism derived from the TEM results. But the oxygen is evidently (partially) stored within the electrode, making oxygen-exchange-driven resistive switching not entirely atmosphere-dependent. In fact, it has been proposed that the deliberate design of memristive devices with oxygen-exchange active oxides can be beneficial for higher $\frac{R_{\text{off}}}{R_{\text{on}}}$-ratios due to a deeper Reset [197], which can help for fast and easy access in an integrated circuit. In other words, reoxidation of the entire switching filament yields a higher HRS value compared to pure redistribution of vacancies, which is also apparent from the increased $\frac{R_{\text{off}}}{R_{\text{on}}}$-ratio [76]. The use of such electrochemical mechanisms therefore comprises opportunities as well as challenges for technological implementation.

8.2 The retention failure mechanism and rational design of failure-resistant memristive devices

In the previous section, the role of oxygen evolution and reincorporation during resistive switching operations was discussed. During Reset, oxygen-species stored in the top electrode or supplied from the surrounding reoxidize the switching filament due to reincorporation of oxygen. In section 5.4, the retention characteristics in vacuum were compared to the behavior in ambient atmosphere. The LRS retention times were generally significantly improved when the devices were stored in vacuum. It appears that the retention times are improved because no oxygen is available for reoxidation of the switching filament from the environment. Consequently, these results experimentally verify the hypotheses of previous simulation-based models [84] which propose the retention failure of the LRS to be due to oxygen diffusion along the vertical direction. Given that the reoxidation is inhibited in vacuum, oxygen species necessary for retention failure are evidently not supplied from the lateral direction. Instead – as is the case for the Reset operation – the oxygen species are apparently supplied from the interface between the top electrode and the $SrTiO_3$ film, inside the top electrode (e.g. within grain boundaries), or even supplied from the surrounding atmosphere. One can thus conclude that incorporation and vertical diffusion of oxygen from the top electrode or surrounding into $SrTiO_3$ plays a dominant role in the retention failure mechanism.

This interpretation is further corroborated by the observed differences in retention times between different film thicknesses and top electrode materials. For thicker films, the retention behavior was generally found to be more stable than for thin devices. One may attribute this observation to the fact that more oxygen is necessary to reoxidize a filament in a thick film (which was also the explanation for higher Set and Reset voltages for thicker films). Regarding the frequent retention failure using Au top electrodes compared to Pt electrodes, one may surmise that the triple-phase-boundary at the observed holes in the Au electrodes leads to enhanced reaction rates for oxygen reincorporation [15]. Another possible reason could be a difference in the catalytic activity for oxygen incorporation for the different metals.

As discussed in chapter 6, it appears that in the presence of oxidizing atmospheres (e.g. ambient air), a phase separation into a Sr-deficient $SrTiO_3$ and a SrO surface layer is mandatory for stable retention in $SrTiO_3$ thin film devices. Bearing in mind the conclusions from the measurements in vacuum, this phase separation could be presumed to be responsible for strongly suppressed reoxidation of the switching filament from the vertical direction due to impeded oxygen diffusion within and through the SrO layer. Reoxidation from the side is unlikely to contribute significantly due to the filament dimensions, which would require µm diffusion lengths from the side in contrast to only 2 nm in the vertical direction for the device discussed in section 6.2.2.

In contrast to the model material $SrTiO_3$, the oxygen diffusion in SrO, however, is not well understood. A theoretical description of oxygen migration in this system will therefore be provided in section 8.2.1. Beforehand, it is necessary to consider the question of whether the observed phase separation is a side effect of the process leading to stable retention, or indeed its origin. To demonstrate and make use of the influence of the $SrTiO_3$/SrO interface for the device performance, the retention characteristic of devices based on an intentionally created interface between Sr-deficient $SrTiO_3$ and SrO is investigated in the following section.

8.2.1 Retention and oxygen migration in $SrTiO_3$/SrO heterostructures

To mimic the phase separation evidenced in chapter 6, artificial $SrTiO_3$/SrO heterostructures were created by successive pulsed laser deposition of 2 nm $\approx 1\,\%$ Sr-deficient $SrTiO_3$ and 1 nm SrO as described in chapter 3.1. For the quantitative comparison of the retention behavior of $SrTiO_3$ thin film devices with $SrTiO_3$/SrO heterostructures, multiple devices were switched between the HRS and LRS configurations for both samples and the resistance values were monitored over several days. To reveal the retention behavior of the as-prepared films rather than the characteristics

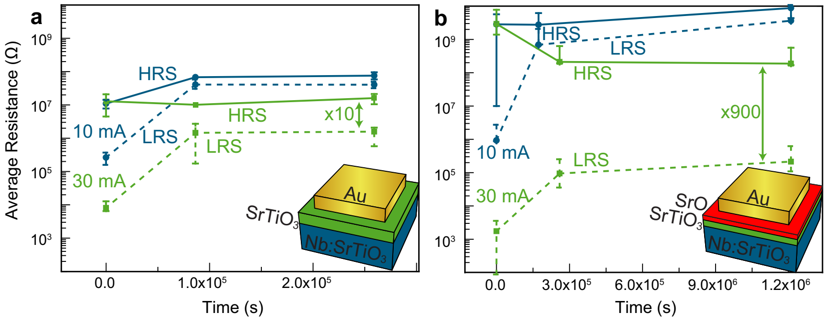

Figure 8.9: Retention behavior of $SrTiO_3$ thin film devices and $SrTiO_3/SrO$ heterostructures. (a) Average resistance of $SrTiO_3$ thin film devices in the LRS (dashed line) and the HRS (solid line) as a function of time after switching for a Set current limit of 10 mA (blue lines) and 30 mA (green lines). The device schematic is shown in the inset. (b) Average resistance of $SrTiO_3/SrO$ heterostructure devices in the LRS (dashed line) and the HRS (solid line) as a function of time after switching for a Set current limit of 10 mA (blue lines) and 30 mA (red lines). Error bars indicate the minimum and maximum values obtained for each resistance state. The device schematic is shown in the inset. Modified from ref. 152.

of local phase separations as described above, the current limits were chosen as low as possible such that the memory window was still larger than 2 orders of magnitude. The I-V-hysteresis for both samples remained similar in shape, indicating that the same fundamental switching mechanism was responsible for the resistance change, as will be discussed in section 8.3. The average resistance as a function of current limit and time is shown in Fig. 8.9. While the retention of the HRS was rather stable for each case, the LRS showed strong differences between both samples, depending on the current limit. For 10 mA, the average LRS increased to a value barely distinguishable from the HRS within a short time for both $SrTiO_3$ thin film devices and $SrTiO_3/SrO$ heterostructures. For 30 mA, on the other hand, LRS and HRS are also very close to each other for $SrTiO_3$ thin film devices after 10^5 s (or even earlier), but $SrTiO_3/SrO$ heterostructures exhibit a large memory window of roughly 3 orders of magnitude even after 10^6 s (note the different time scales in Fig. 8.9a and b).

While the data shown in Fig. 8.9 is averaged over multiple devices, it is worth noting that in contrast to the $SrTiO_3$ thin film devices, no device with a complete retention failure (HRS and LRS indistinguishable) was observed for the $SrTiO_3/SrO$ heterostructures after switching with 30 mA. This improved retention behavior is caused by a rather stable LRS value after an initial relaxation combined with a stable HRS on the order of $10^8\,\Omega$. It was achieved with less power than was necessary for the observation of single $SrTiO_3$ devices with stable retention (cf. Fig. 5.10a), making it less likely that an additional phase separation is responsible for the stable retention. The dispensability of phase separations for good retention times also results in a more uniform behavior of different devices on the same chip: While the devices shown in Figs. 6.1 and 6.2 are vastly different in their retention behavior (as shown in Fig. 5.10a), all devices containing the intentional $SrTiO_3$/SrO interfaces exhibit a similar resistance for all times investigated here.

Given the significant retention improvement through the insertion of a SrO layer, one can conclude that the Joule-heating enabled phase separation is not a side effect of high temperatures during forming, but rather the origin of the observed stable retention for the devices shown in Figs. 6.1a-c 6.5a-c. It can be understood as the separation of the pristine $SrTiO_3$ into a switching element (the oxygen deficient $SrTiO_3$) and an artificial retention-stabilization-layer, the SrO.

Oxygen diffusion in SrO/$SrTiO_3$ heterostructures

Therefore, it needs to be investigated how this phase separation can assist in prolongating the retention times. As discussed above, a retention failure is caused by the reoxidation of the switching filament from the vertical direction. For the $SrTiO_3$/SrO heterostructure, three different scenarios can prevent this reoxidation:

Mechanism i: Oxygen storage capability. Similar to the oxygen exchange between different oxide layers in oxide dual-layer memory elements under applied electric fields [198], oxygen from the $SrTiO_3$ could be incorporated into SrO (as interstitials or into existing vacancies) during the Set operation. The SrO layer can be regarded as an oxygen reservoir. This may lead to a new, (meta-)stable oxygen distribution between the two adjacent oxides eliminating the driving force for reoxidation of the $SrTiO_3$ without applied electric fields and therefore lead to improved retention times.

Mechanism ii: Surface reaction rate of oxygen incorporation. If the storage of additional oxygen in the retention-stabilization-layer is impeded due to a lack of available lattice sites (no vacancies available and unfavorable energy of formation for oxygen interstitials), oxygen evolution at the SrO/eletrode interface must occur during the Set operation, similar to the Set operation and reoxidation in $SrTiO_3$ thin film devices described above. In this case, reoxidation of the $SrTiO_3$ during Reset or retention failure inevitably requires the incorporation and diffusion of additional oxygen into the heterostructure from the top electrode or the surrounding atmosphere. Since conduction band electrons contribute to the rate determining step in the incorporation of oxygen into the oxide lattice [28, 199], this step might be impeded in SrO due to the comparably large band gap (between 5.0 and 6.5 eV). The inhibited oxygen incorporation may therefore be responsible for the enhanced retention times of the heterostructures.

Mechanism iii: Diffusion rate. At the same time, the oxygen needs to migrate from the top surface into the conductive filament within the $SrTiO_3$ after the incorporation into the retention-stabilization-layer. Given the fast diffusion rates in $SrTiO_3$, the improved retention of the heterostructures may be caused by slower ambipolar diffusion rates within the SrO. If the incorporation rate of the retention-stabilization-layer was as fast as in $SrTiO_3$, slow diffusion through the retention-stabilization-layer may become the rate determining step and thus retard the reoxidation of the switching filament.

In order to clarify which of the effects (mechanisms i-iii) are responsible for the improved retention times, the oxygen migration in the heterostructure is investigated through static lattice simulations[5]. Given that both pulsed laser deposition and phase separation during electrical treatments result in oxide layers with considerable amounts of point defects such as anion and cation vacancies, the simulation focuses on the migration of oxygen vacancies within $SrTiO_3$/SrO heterostructures. Fig. 8.10 shows the site and saddle-point energies corresponding to the migration of an oxygen vacancy through the heterostructure. One notices a considerable difference in the migration barriers in the two materials, with the barriers in SrO (≈ 1.2 eV) being twice as high as those in $SrTiO_3$ (≈ 0.6 eV). This suggests that, once oxygen ions are incorporated into SrO_{1-x} under an electric field (which lowers the barrier for migration), their return is hindered. There are also small differences in the site energies within $SrTiO_3$ (this is due to the biaxial strain

---

[5] The simulation was performed by Amr H. H. Ramadan, Institute of Physical Chemistry, RWTH Aachen University, Aachen, Germany.

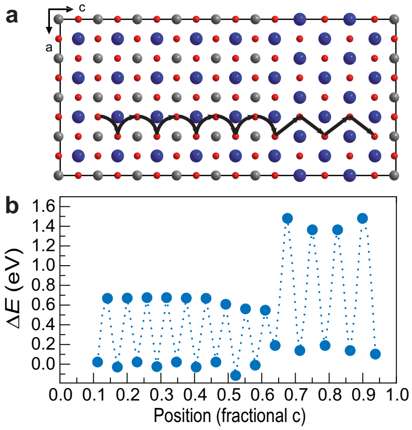

Figure 8.10: Oxygen vacancy migration in the $SrTiO_3/SrO$ heterostructure. (a) Illustration of the simulation cell of the heterostructure, with the simulated migration path indicated schematically by black arrows. Sr in blue, Ti in grey and O in red. (b) Energies of the sites and saddle-points corresponding to an oxygen vacancy migrating through the heterostructure. The x-axis is scaled to the fractional coordinates of the c-axis of the simulation cell. All plotted energies are referenced to the average vacancy formation in the $SrTiO_3$ regime of the simulation cell. The dotted line serves as a guide to the eye for the change in energy during the migration process. Modified from ref. [152].

arising from lattice mismatch) and between $SrTiO_3$ and SrO (suggesting a small amount of vacancy redistribution from SrO to $SrTiO_3$) [199].

Based on these calculations, one may conclude that impeded oxygen transport within the $SrTiO_3/SrO$ heterostructure (mechanism iii) could in fact lead to improved retention times. At the same time, it cannot be excluded that mechanisms i and ii play a similar role in SrO, as oxygen incorporation reactions and the defect structure in SrO are not well understood. Therefore, additional model oxide materials are investigated in a next step to clarify whether the oxygen storage capability or the impeded oxygen transport are the dominating factor of retention improvement through the intentional insertion of retention-stabilization-layers.

8.2.2 Rational design of retention-failure resistant memristive devices

The broad variety of physical properties exhibited by oxides allows the selection of prototypical materials for the retention-stabilization-layer. For this purpose, yttria-stabilized zirconia ($Y{:}ZrO_2$) and Al_2O_3 are selected. These oxides differ most severely in two specific properties: Electronically, both $Y{:}ZrO_2$ and Al_2O_3 are rather inactive insulators with a large band gap, but they are prototypical representatives for fast oxygen transport combined with high oxygen vacancy concentration and slow oxygen transport combined with very low oxygen vacancy concentration, respectively. While $Y{:}ZrO_2$ is the prototypical oxygen-ion conducting electrolyte, with a measured oxygen diffusion coefficient of $D^{Y:ZrO_2}(500\,K) \approx 10^{-13}\,cm^2\,s^{-1}$ and an activation enthalpy of just 1 eV [200], Al_2O_3 exhibits low diffusion coefficients, even close to its melting point; the extrapolated value with an activation energy of $6.5 \pm 0.5\,eV$ [201] is $D^{Al_2O_3}(500\,K) \approx 10^{-65}\,cm^2\,s^{-1}$. Due to the high concentration of oxygen vacancies, $Y{:}ZrO_2$ also exhibits a large amount of available lattice sites for oxygen storage, while Al_2O_3 exhibits very small deviations from nominal stoichiometry.

As described in chapter 3, $SrTiO_3$ (2 nm)/$Y{:}ZrO_2$ (1 nm) and $SrTiO_3$ (2 nm)/Al_2O_3 (1 nm) heterostructures were fabricated by successive pulsed laser deposition. Multiple devices on each chip were switched between the HRS and the LRS. Similar switching characteristics compared to $SrTiO_3$ thin film devices suggest the same underlying mechanism (cf. section 8.3). For $SrTiO_3$/$Y{:}ZrO_2$ heterostructures, a large initial memory window is observed for a current limit of 1 mA (Fig. 8.11a). For a 10 mA current limit, the HRS is comparably low with just $10^7\,\Omega$. Nevertheless, the initial memory window after switching with 10 mA current limit is three orders of magnitude, which is similar to the memory windows obtained for the $SrTiO_3$ thin film devices. For even higher current limits, the devices break down to a low resistance. $SrTiO_3$/Al_2O_3 heterostructures can be switched reliably with 10 mA or 30 mA current limit, resulting in similar initial memory windows of 10^3 and 10^4, respectively (Fig. 8.11b).

As these model oxides are good representatives for fast and slow oxygen transport coupled with high and low oxygen storage capabilities, a comparison of the retention characteristics of these heterostructures, may allow the distinction between mechanisms i and ii-iii In fact, compelling differences are observed: HRS and LRS values were sim-

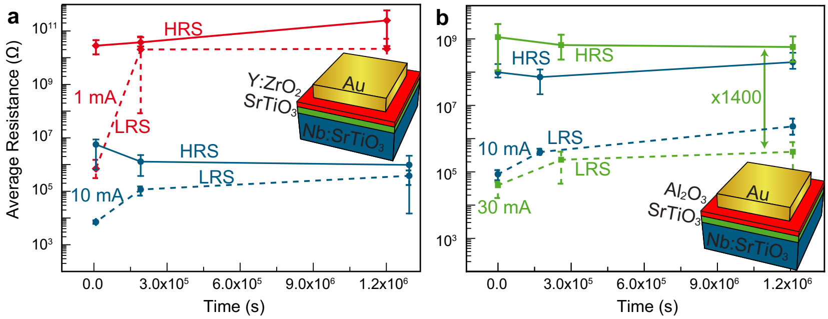

Figure 8.11: Retention behavior of $SrTiO_3$/YSZ heterostructures and $SrTiO_3/Al_2O_3$ heterostructures. (a) Average resistance of $SrTiO_3$/Y:ZrO_2 heterostructure devices in the LRS (dashed line) and the HRS (solid line) as a function of time after switching for a SET current compliance of 1 mA (red lines) and 10 mA (blue lines). The device schematic is shown in the inset. (b) Average resistance of $SrTiO_3/Al_2O_3$ heterostructure devices in the LRS (dashed line) and the HRS (solid line) as a function of time after switching for a SET current compliance of 10 mA (blue lines) and 30 mA (green lines). Error bars indicate the minimum and maximum values obtained for each resistance state. The device schematic is shown in the inset. Note the different resistance scales in panels (a) and (b). Modified from ref. 152.

ilar to each other after short times ($< 10^5$ s) for the case of the oxygen-conducting $SrTiO_3$/Y:ZrO_2 heterostructure for all current limits (Fig. 8.11a). For the oxygen-diffusion-suppressing Al_2O_3, on the other hand, stable retention of both HRS and LRS was obtained for both 10 mA and 30 mA, with a large memory window of several orders of magnitude even after more than 10^6 s (as shown for the average resistance in Fig. 8.11b). As was the case for the $SrTiO_3$/SrO heterostructures, no complete retention failure could be observed in any $SrTiO_3/Al_2O_3$ device.

This is a dramatic improvement compared to devices fabricated without retention-stabilization-layers or retention-stabilization-layers with fast oxygen diffusion. Since these heterostructures exhibit an initial memory window of 10^3 for switching with 10 mA, which is nearly identical to the memory windows for $SrTiO_3$/Y:ZrO_2 heterostructure or $SrTiO_3$ thin film devices, one can conclude that the observed stable retention cannot be explained by initially higher memory windows. Accordingly, inhibiting the back transport of oxygen (at room temperature and without applied electric fields) presents the most effective method to stabilize retention in $SrTiO_3$-based memristive devices (which is in line with the observations from the atmosphere-dependent measurements). The oxygen storage capability (mechanism i) of the retention-stabilization-layer does not appear to play an important role, as the introduction of Y:ZrO$_2$ layers does not improve the retention. Instead, reoxidation of the switching filament can be prevented if no oxygen can enter the SrTiO$_3$ (mechanisms ii and iii).

As is evident from the improved retention with SrO and Al$_2$O$_3$ retention-stabilization-layers, slow oxygen migration within the layer (mechanism iii) can protect the switching filament from fast reoxidation. Incorporation of such layers with slow oxygen diffusion for the protection of the switching filaments may therefore be regarded as a design rule for failure-resistant memristive devices. Since both SrO and Al$_2$O$_3$ are also wide band gap insulators, one cannot exclude that impeded incorporation of oxygen at the surface (mechanism ii) may have a similar or additional effect. However, in this case one may also expect a similar effect from Y:ZrO$_2$, as the high initial resistance of SrTiO$_3$/Y:ZrO$_2$ heterostructures (cf. section 8.3) indicates that only an extremely small concentration of conduction band electrons is present in the Y:ZrO$_2$ layer. Therefore, mechanism iii is the most apparent explanation for the improved retention.

Implications of stable retention times achieved in lower-power operation

It is worth emphasizing that only with Al$_2$O$_3$, the retention-stabilization-layer with the highest oxygen migration enthalpy used here, stable retention could be obtained with a 10 mA current limit. This current is still extremely high regarding the application in integrated circuits. However, the current limits necessary to achieve resistive switching in µm-sized single crystalline SrTiO$_3$ devices are always on this order of magnitude (see chapter 5) and might be attributed to the inherently low defect density. To achieve stable retention in the SrTiO$_3$-based devices shown in Figs. 6.1a-c and 6.5a-c., a much higher current limit of 50 mA was applied, but the majority of devices still showed retention failure after short times. The intentional introduction of suitable retention-stabilization-layer apparently reduces the current necessary for the desired retention performance dramatically.

This power reduction has very beneficial effects: Major structural changes such as phase separations or severe lattice distortions are commonly observed for SrTiO$_3$ thin film devices (compare chapter 6 and refs. 17 and 165). These structural changes apparently

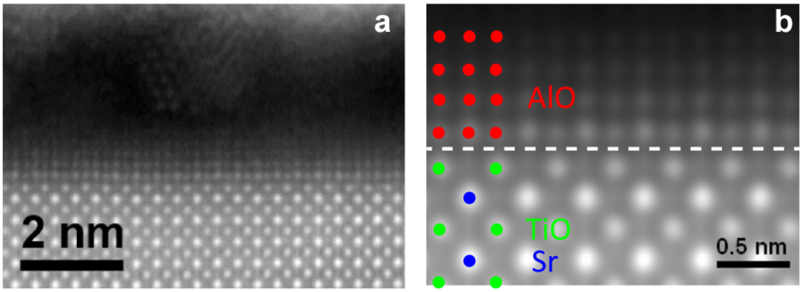

Figure 8.12: TEM imaging of $SrTiO_3/Al_2O_3$ heterostructures. (a) HAADF STEM image of the epitaxial $SrTiO_3/Al_2O_3$ interface (denoised by a nonlinear filter [202]) (b) Magnified one dimensional averaged image better revealing the structure of the epitaxial interfaces. The TiO/AlO interfaces are more evidently seen from the one-dimensional averaged HAADF STEM image. TEM imaging performed by Dr. Hongchu Du. Modified from ref. 152.

did not occur for the $SrTiO_3/Al_2O_3$ heterostructures. For closer inspection, HAADF STEM imaging of an electrically treated device was performed[6]. Fig. 8.12 shows cross sectional HAADF STEM images of the $SrTiO_3$ (2 nm)/Al_2O_3 (1 nm) heterostructures from a switching filament, which was identified by C-AFM prior to the preparation of the TEM lamella.

The STEM images reveal epitaxial growth of the aluminum oxide on top of TiO_2-terminated $SrTiO_3$. The observed atomic structure for the as-grown aluminum oxide is identical for the entire lamella (within the switching filament as well as few µm away from it) and appears to be similar to the reported $SrTiO_3/\gamma$-Al_2O_3 in literature [203]. Within the switching filament shown in Fig. 8.12, the structure in both the $SrTiO_3$ and the Al_2O_3 shows no evident difference compared to the surrounding of the filament, confirming the suspicion that no structural damage occurred during the switching. The absence of structural changes of the active layers during switching is desirable for future memory and logic devices, yielding more uniform and reproducible devices. This is also apparent from the much more uniform retention behavior of $SrTiO_3/Al_2O_3$ heterostructures (Fig. 8.11) compared to the $SrTiO_3$ thin film devices in Fig. 5.10.

---

[6] TEM imaging performed by Dr. Hongchu Du, Peter Grünberg Institut and Ernst Ruska-Centre, Forschungszentrum Jülich GmbH, Jülich, Germany.

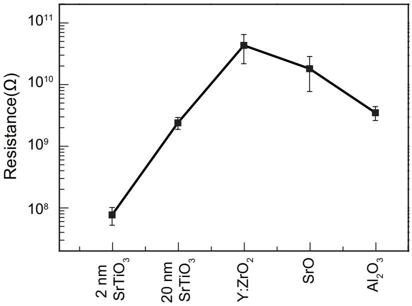

Figure 8.13: Initial resistance of $SrTiO_3$ thin films and heterostructures with Au top electrodes.

By purely empirical studies and without paying special attention to oxygen transport properties of the materials under consideration, several groups already observed improved device performance in memristive devices with inserted Al_2O_3 layers, such as improved uniformity of HfO_x- and TaO_x-based devices [204, 205], improved memory windows in TiO_x-based devices [206] and improved retention in GdO_x-based devices [207]. Based on these observations, it can be assumed that the concept of the rationally designed retention-stabilization-layer can be extrapolated from the $SrTiO_3$ model system to technologically more relevant systems.

8.3 The switching mechanism of eightwise resitive switching in oxide heterostructures

Because of the differences in the retention times described above, one may question whether the SrO, $Y{:}ZrO_2$ or Al_2O_3 retention-stabilization-layers might also be actively involved in the resistive switching processes in these heterostructures. For example, the initial resistance of the heterostructures is higher than for the bare $SrTiO_3$ films (Fig. 8.13). But this increased series resistance does not appear to be closely connected to the improved retention times as the highest resistance is observed for $Y{:}ZrO_2/SrTiO_3$-heterostructures followed by $SrO/SrTiO_3$ and $Al_2O_3/SrTiO_3$, which exhibit dramatically different retention behavior.

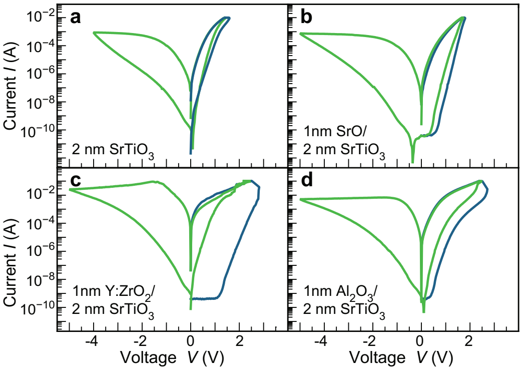

Figure 8.14: Switching characteristics of $SrTiO_3$ thin films and heterostructures. Forming step and representative switching cycle are shown as blue and green lines, respectively. (a) Representative $SrTiO_3$ thin film device. (b) $SrO/SrTiO_3$ heterostructure. (c) $Al_2O_3/SrTiO_3$ heterostructure. (d) $Y{:}ZrO_2/SrTiO_3$ heterostructure.

In a next step, the I-V characteristic of the heterostructures was compared to $SrTiO_3$ thin film devices (Fig. 8.14). If the resistive switching in the heterostructures was dominated by the inserted retention-stabilization-layer rather than by the $SrTiO_3$ film itself, one would expect a different shape or even the opposite switching polarity, as was demonstrated before for resistive switching in Al_2O_3 [206]. Instead, it can be observed that the shape and polarity of the I-V-characteristics as well as the absolute voltages and currents which are typically observed in these heterostructures were still the in the same range as for $SrTiO_3$ thin film devices. For stoichiometric $SrTiO_3$, the forming step can hardly be distinguished, while it is increasingly pronounced for $SrO/SrTiO_3$, $Al_2O_3/SrTiO_3$ and $Y{:}ZrO_2/SrTiO_3$ (Fig. 8.14). In other words, the forming step is more pronounced for higher initial resistances, which is a situation similar to the observations for the $SrTiO_3$ thickness series and stoichiometry comparisons described in chapter 5. As for the initial resistance, one can conclude that the occurrence of the forming step is not responsible for the prolongated retention times. Subsequent Set voltages are around 2 V for each sample (Fig. 8.14). Assigning a specific Reset voltage is unsubstantial because of the gradual Reset. However, all devices can be switched to an HRS with -4 to -5 V.

The LRS state of the $SrTiO_3$ thin film devices and heterostructures is on the order of 10^4 to $10^5\,\Omega$ for all devices (compare Figs. 8.9 and 8.11), orders of magnitude smaller

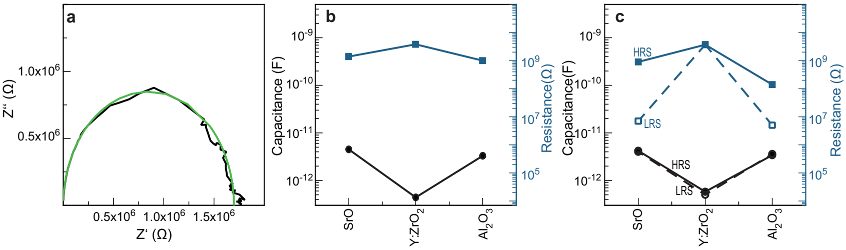

Figure 8.15: Impedance spectroscopy of oxide heterostructure devices. (a) Cole-Cole plot of an exemplary impedance spectroscopy measurement for a 10 × 10 µm Au/SrO/$SrTiO_3$/Nb:$SrTiO_3$ device (black line) and fit using an equivalent circuit consisting of a parallel circuit of capacitor and resistor, representing the device, with a small series resistance, which represents the lead resistances. The fitting was performed using the software Zplot, similar to what was described in ref. 208 (b) Capacitance and resistance determined for the virgin state. (c) Capacitance and resistance determined for the LRS and HRS after switching with 30 mA current limit. The capacitance for each heterostructure does not change between virgin state, HRS and LRS, indicating filamentary switching.

than the initial resistance or the HRS from the $SrTiO_3$ thin film devices. One can therefore conclude that the resistance change in the heterostructures must occur at least partially in the $SrTiO_3$ layer itself, although it cannot ruled out that additional processes take place in the Y:ZrO_2 or Al_2O_3 layers.

Fig. 8.15 shows an exemplary impedance spectroscopy measurement and the resistance and capacitance values extracted for virgin cells and cells in the LRS and HRS for each heterostructure. It is obvious that the capacitance and resistance for HRS and virgin state are fairly similar, as expected. For the LRS, one finds that the capacitance is again almost identical to the HRS, while only the resistance changes between LRS and HRS. Note that for the Y:ZrO_2/$SrTiO_3$ device, the retention time was not sufficient to distinguish between LRS and HRS in these measurements, which were performed on the same devices that were used for Figs. 8.9 and 8.11. These measurements were performed on single devices and do not accurately describe the average resistance as discussed above. Because the capacitance does not change between LRS and HRS, these results confirm that the resistive switching in the heterostructures also occurs within a confined filament [209], similar to the $SrTiO_3$ films themselves.

For filamentary switching, the filaments should be identifiable using spectromicroscopy, as demonstrated for the $SrTiO_3$ thin film devices in chapters 6 and 7. Focusing on the

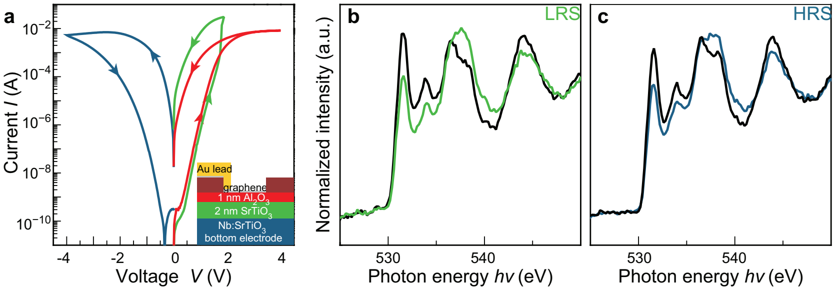

Figure 8.16: Spectromicroscopic fingerprint of the filamentary switching in graphene$Al_2O_3/SrTiO_3$ heterostructures. (a) I-V-characteristic of of a graphene/$Al_2O_3/SrTiO_3/Nb:SrTiO_3$ device with the first Set operation (green line), first Reset operation (blue line) and second Set operation (red line) during the PEEM investigation. Inset: Device schematic (b) O K-edge spectra for the suspected switching filament and a reference area in the LRS (green and black lines, respectively). (c) O K-edge spectra for the suspected switching filament and a reference area in the HRS (blue and black lines, respectively).

heterostructures with the best retention, $Al_2O_3/SrTiO_3/Nb:SrTiO_3$ devices were investigated both *in operando* and after top electrode removal. For the *in operando* characterization, graphene electrodes were employed. Fig. 8.16a shows that graphene electrodes also result in similar switching characteristics for these heterostructures, as also demonstrated in ref. 168. The O K-edge extracted from this devices is shown in Fig. 8.16b and c. On first sight, one may think that the O K-edge from such a heterostructure should contain information from both the Al_2O_3 and the $SrTiO_3$ layer, as the probing depth of 3-5 nm contains both films. But the spectra of a suspected filament and the surrounding are, interestingly, very similar in shape to the spectra collected from bare $SrTiO_3$ surfaces and do not contain any sign of Al_2O_3. The reason for this observation lies in the nature of the O K-edge. As described in section 4.1, the O K-edge can only exist due to covalent overlap between oxygen and metal orbitals. The rather ionic nature of Al_2O_3 compared to $SrTiO_3$ can therefore account for a very weak intensity of the Al_2O_3 O K-edge, which is why the spectra obtained from heterostructures with very thin Al_2O_3 layers are almost identical to $SrTiO_3$ spectra.

In the LRS, the filamentary region shows the signature of reduced $SrTiO_3$ (Fig. 8.16b), which is partially reoxidized when switching to the HRS (smaller $\frac{\mathrm{A}}{\mathbf{B}_2}$-ratio compared to

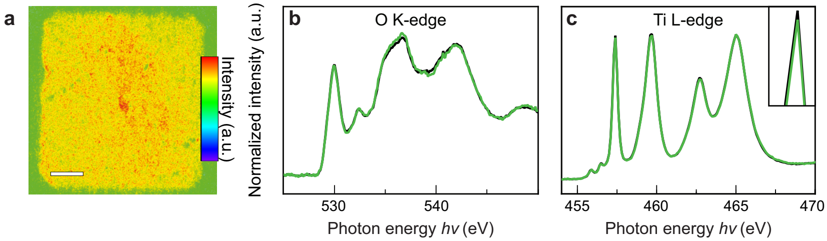

Figure 8.17: Spectromicroscopic fingerprint of the filamentary switching in $Al_2O_3/SrTiO_3$ heterostructures with Au top electrodes. (a) XPEEM image of a Au/$Al_2O_3/SrTiO_3$/Nb:$SrTiO_3$ device for a photon energy of 537 eV after top electrode removal. Scale bar, 2 µm. The suspected filament is the red spot in the center of the device. (b) O K-edge spectra for the suspected switching filament and a reference area (green and black lines, respectively). (c) Ti L-edge spectra for the suspected switching filament and a reference area (green and black lines, respectively). Inset: Zoom to the L_3 t_{2g} edge.

the reference, Fig. 8.16c). This confirms that similar to the $SrTiO_3$ thin film devices, the filamentary switching in $Al_2O_3/SrTiO_3$ heterostructures involves a localized valence change in the $SrTiO_3$ film, as is expected from the reasoning above. Unfortunately, no complete switching cycle LRS $\mapsto$ HRS $\mapsto$ LRS $\mapsto$ HRS was possible for this device to derive reliable quantitative information. During the second Set operation (red curve in Fig. 8.16a), the current limit was not reached, an additional series resistance appeared to be present. After further switching attempts, XPEEM investigation did not show any change in the filament (data not shown). The reason for this may be that the active filament changed or that the entire device suffered from the synchrotron irradiation.

To confirm that the observation of the filamentary valence change in $Al_2O_3/SrTiO_3$ heterostructures in Fig. 8.16 is no artifact, XPEEM analysis was also performed for a device with Au top electrode (the same sample that was used for Fig. 8.11) after top electrode delamination (Fig. 8.17). XPEEM imaging at a photon energy of 537 eV reveals increased intensity in the area where the probe tip contacted the top electrode during switching. Extracting the O K-edge for this region and the surrounding again shows the signature of reduced $SrTiO_3$ for the filament (Fig. 8.17b). Similar to the observations from Fig. 7.14, this valence change in the $SrTiO_3$ can be confirmed using the Ti L-edge (Fig. 8.17c). The observation of the change in the Ti L-edge also provides

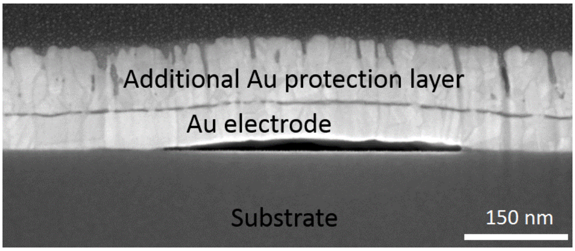

Figure 8.18: TEM image of Au/Al_2O_3/$SrTiO_3$/Nb:$SrTiO_3$ device, switched with 10 mA. In the region of the contact point, the Au top electrode is slightly detached from the film[7].

final evidence that the resistance change in the heterostructures must occur in the $SrTiO_3$ itself. Unfortunately, no clear evidence about the valence state of the Al can be obtained using XPEEM to clarify if additional changes might occur in the Al_2O_3 layer.

After the clarification that a valence change in the Ti is also responsible for resistive switching in Al_2O_3/$SrTiO_3$ heterostructures, one may question the exact switching mechanism. In the absence of *in operando* TEM data for these devices, *ex situ* analysis may shed light on the switching mechanism. Fig. 8.18 shows a low-magnification TEM image of a Au/Al_2O_3/$SrTiO_3$/Nb:$SrTiO_3$ device. The lamella was prepared such that a bubble which emerged during operation was contained in the image. The cavity between electrode and film suggests that the same mechanism as was derived for $SrTiO_3$ thin film devices in section 8.1 can also be responsible for the switching in the heterostructures. Oxygen-species may be released from the active layer towards the Au electrode during Set and reincorporated during Reset. This would also confirm the reason for the retention stabilization using layers with slow oxygen migration, as the oxygen needs to migrate through the thin Al_2O_3 layer during operation and retention failure. High resolution EELS analysis of the filamentary region shown in Fig. 8.12 corroborates the suspected mechanism as a similar Ti^{3+} gradient as described in section 7.3 was identified for the filament (data not shown). However, the extremely small thicknesses of these samples made reliable interpretation of the EELS results impossible due to interface-proximity effects.

---

[7] Image courtesy of Maximilian Kruth, Peter Grünberg Institut and Ernst Ruska-Centre, Forschungszentrum Jülich GmbH, Jülich, Germany.

Because of this suspected mechanism, one might question whether the incorporation of such layers for retention stabilization through slow oxygen migration might not lead to very slow switching times simultaneously. The extreme nonlinearity of oxygen migration with respect to the applied electric field and temperature, however, can yield sufficiently fast switching times even for large oxygen migration activation energies due to Joule heating [57]. Regarding the voltage-time dilemma, the incorporation of such layers may therefore yield the desired fast switching and long retention at the same time, but further experiments are necessary to confirm this expectation.

9 Conclusions and Outlook

The scope of this thesis was the investigation of the microscopic changes of the electronic and chemical structure during resistive switching in $SrTiO_3$ thin films. Spatially resolved spectroscopy and TEM were used both *ex situ* and *in operando* to identify and interpret these changes. Based on the experimental observations, the switching and retention failure mechanisms in $SrTiO_3$ were clarified and a design rule for failure resistant devices was derived.

Devices with different stoichiometries, top electrode materials and film thicknesses were fabricated and the resistive switching behavior was analyzed. All devices investigated here exhibit eightwise resistive switching, but differences in retention times and switching parameters can be observed. A general trend was observed where thicker $SrTiO_3$ films exhibit a more pronounced forming step and higher HRS values while requiring higher switching voltages. Regarding the choice of the top electrode material, differences in the I-V-characteristics between different top electrode materials are small, which can be expected based on a similar work function of the electrode materials investigated here.

Importantly, a dependence of both I-V-characteristics and retention times on the oxygen partial pressure of the external atmosphere was found. Reducing atmospheres lead to improved LRS retention and a less pronounced Reset, which leads to a lower HRS value. This indicates a certain interaction with the surrounding both during and after operation.

This atmosphere-dependence and the observations from *in operando* XPEEM and TEM analysis enable the deduction of a microscopic switching mechanism for the long-debated eightwise switching direction. Electrochemical oxygen evolution and oxygen reduction reactions rather than the typically invoked purely internal redistribution of oxygen vacancies give rise to this switching direction in $SrTiO_3$. During Set (and during forming), oxygen is removed from the $SrTiO_3$ lattice, leaving behind an oxygen-deficient, highly conductive filament, which is visible from the oxygen concentration maps from the TEM analysis. The oxygen species may be stored within the electrode, at the electrode-oxide interface or released as gaseous oxygen to the surrounding atmosphere, depending on the top electrode material and the switching conditions. Driven by this oxygen evolution, the Ti undergoes a valence change from Ti^{4+} to Ti^{3+}, leading to occupied states in the conduction band. These result in a characteristic spectroscopic fingerprint in the Ti L absorption edge and the O K absorption edge, which was detected by EELS as well as XPEEM.

During Reset, oxygen species are reincorporated into the $SrTiO_3$ lattice, oxidizing the filament and causing a valence change from Ti^{3+} to Ti^{4+}. For this incorporation reaction to be completed, oxygen-supply from the ambient appears to be necessary. In reducing atmospheres, only partial Reset was observed.

It can be argued that resistive switching based on oxygen evolution and reincorporation – while potentially causing challenges in the technological implementation – may present a viable route towards a deep Reset which is desirable for technological implementation. At the same time, understanding the origin of eightwise switching will enable the educated design of memristive devices suppressing its complicated contributions during device operation.

Based on the *in operando* XPEEM analysis with graphene electrodes, the carrier density modulation in the conduction band was quantified. The filament was found to contain $9 \pm 2\,\%$ Ti^{3+} in the LRS and $4 \pm 1\,\%$ Ti^{3+} in the HRS. These values were used as an input for nanoionic device simulation and were found to fully explain the resistance change by more than two orders of magnitude. The device simulation revealed that the effective Schottky barrier was strongly modified through this carrier density modulation. Overall, such high carrier concentrations lead to significant tunneling contributions to the current across the barrier, which is also in line with temperature dependent I-V-measurements.

The unprecedented, quantitative agreement between experimental quantification of localized redox reactions and nanoionic device simulation not only contributes to the clarification of the microscopic origin of the resistance change, but also paves the way for educated design and rational implementation of memristive devices for future memory and logic applications, as simulations based on the physical understanding of the switching process are mandatory for the large scale development of devices and integrated circuits.

Ex situ XPEEM analysis of the filament chemistry in $SrTiO_3$ devices with different retention characteristics was used to derive a design rule for failure-resistant memory, elucidating the impact of rationally designed retention-stabilization-layers. It was demonstrated that spatially confined valence changes between Ti^{3+} and Ti^{4+} within the switching filament are also responsible for the resistance change during retention failure. While the low oxygen migration enthalpy of $SrTiO_3$ causes the frequently observed retention failure of the LRS, Joule-heating induced local phase separation within the switching filament can stabilize the retention due to the formation of a $SrTiO_3/SrO$ interface, as observed in spatially resolved Sr 3d XPS and O K-edge absorption spectra. This layer inhibits fast reoxidation due to retarded oxygen transport through the SrO layer. This insight serves as a basis for the design rule for failure-resistant memristive devices: Incorporation of oxide materials with slow oxygen diffusion as retention-stabilization-layer protects the switching filaments from reoxidation and leads to significantly prolongated retention times. This was verified through the fabrication and characterization of devices with intentional SrO and Al_2O_3 layers between $SrTiO_3$ and top electrode. Utilizing good oxygen conductors like $Y{:}ZrO_2$ as the retention-stabilization-layer, on the other hand, yields frequent retention failure. In addition to improved retention, more uniform device performance can be achieved with Al_2O_3 retention-stabilization-layers due to reduced heat generation compared to devices without intentional retention-stabilization-layers, which is also highly desirable for practical applications.

Based on additional electrical measurements and XPEEM and TEM analysis, the switching mechanism in these oxide heterostructures was found to be the same as in regular $SrTiO_3$ thin film devices: oxygen evolution during Set and reincorporation during Reset cause the resistance change due to a carrier density modulation in the $SrTiO_3$ layer.

Overall, these findings present fundamentally new insights about resistive switching in $SrTiO_3$-based devices, as important switching and failure mechanisms could be clarified. Based on this understanding, the design of future devices is facilitated through a physical understanding, the availability of increasingly predictive simulations and the introduction of retention-stabilization-layers.

Outlook

Going beyond a static characterization of each resistance state, the direct *in operando* observation of valence changes during device operation presented in this thesis constitutes an attractive first step and a necessary prerequisite for time-resolved spectromicroscopic characterization of the switching process. This may yield further insights into potential intermediate steps of the mechanisms and the reaction kinetics. In order to achieve time resolution below the minimum integration time of a single PEEM image, which is on the order of seconds and therefore unsuited to study fast phenomena, pump-probe techniques have to be employed. In such experiments the device is electrically excited by a "pump" pulse and measured with a single photon "probe" pulse after a specific delay time, e.g. a single bunch of synchrotron irradiation. Varying the delay time between pump and probe allows the reconstruction of the temporal evolution of the switching.

As a very short probe pulse has to be used, the measurement has to be repeated numerous times for each delay time to achieve a sufficient signal-to-noise ratio. Therefore, the prerequisite for such time-resolved measurement is that the switching can be performed at least 10^6 times, and the location of the switching filament as well as the magnitude of the redox reaction must not vary during these cycles. In principle, this may be possible as very high endurance has been reported, but switching under synchrotron irradiation with devices designed for *in operando* spectromicroscopy rather than ultimate endurance performance complicate such approaches[1]. Alternative *in operando* approaches, which were unsuccessful in the identification of switching filaments, indicate that such performance may be achievable, as was shown for hard X-ray photoelectron spectroscopy [210] and transmission X-ray microscopy [19,20], where millions of switching cycles under synchrotron irradiation have been performed. One way to achieve such stability against beam damage might be the introduction of oxygen into the measurement chamber, as described briefly in section 7.2.

While the *in operando* XPEEM and TEM results presented in this thesis already demonstrate that oxygen must be removed from and reincorporated into the $SrTiO_3$

---

[1] The way towards time-resolved spectromicroscopic characterization of the switching process and the obstacles that will have to be overcome will be described in detail in the PhD thesis of Christoph Schmitz, Peter Grünberg Institute, Forschungszentrum Jülich GmbH, Jülich, Germany.

layer during device operation, the exact mechanism of the corresponding electrochemical reactions have to remain subject of future research. For example, the intermediate steps of oxygen removal and reincorporation are unknown and it needs to be clarified where the oxygen species are stored after removal from the $SrTiO_3$ lattice. It may be very instructive to examine the influence of different chemical species which are likely to be present at the $SrTiO_3$/electrode interface or in the external atmosphere. For example, carbon contaminants at the interface may play a role[2].

Regarding the external atmosphere, it was shown that the presence of water is essential for oxygen evolution and reincorporation [211, 212], i.e., oxygen incorporation rates can be strongly enhanced using water vapor compared to dry oxygen. Switching in atmospheres of varying water partial pressure may be a useful way to determine if this dependence also plays a role for resistive switching in $SrTiO_3$. As demonstrated in ref. 211, oxygen isotope profiles obtained from secondary ion mass spectrometry after exchange with specific atmospheres (e.g. $H_2^{18}O$) can shed light on the exchange rates.

After the mechanistic description of eightwise resistive switching in $SrTiO_3$, its kinetics should be investigated in detail. For this purpose, pulsed measurements similar to those performed for counter-eightwise switching in $SrTiO_3$ [213, 214] can be performed in addition to the pump-probe experiments mentioned above. Such experiments may yield insightful information about mechanisms based on oxygen exchange in comparison with purely internal redistribution of vacancies. While counter-eightwise switching can be explained by the oxygen vacancy migration due to ionic hopping as described by the Mott-Gurney lay [213, 215], the surface exchange could possibly be the rate limiting step for the eightwise switching, i.e., one would expect the kinetics to follow the Butler-Volmer equation, which describes charge transfer at electrode/electrolyte interfaces [4]. Investigation of the switching kinetics may be particularly useful to evaluate if the introduction of retention-stabilization-layers with slow oxygen migration properties impedes fast switching. Based on the extreme nonlinearity of oxygen migration with respect to the applied electric field and temperature, a negative influence of these layers on the switching speed would not be expected, but this assumption requires experimental verification.

---

[2] First hints for the role of carbon species will be presented in the PhD thesis of Nicolas Raab, Peter Grünberg Institute, Forschungszentrum Jülich GmbH, Jülich, Germany.

Regarding the position of the filament, it was observed that while preferred positions exist in the devices investigated here, the filament location may vary from cycle to cycle under certain circumstances (such as the use of graphene electrodes). This filament location variation may be the reason for the observed cycle-to-cycle variability of the LRS and HRS resistances. It may therefore be worthwhile to investigate if pre-defined filaments present a possibility to reduce this variability, similar to the precise and deliberate positioning of the filament by Hayakawa *et al.* [216].

A Appendix: Fabrication details

The following flowchart indicates the necessary steps for sample preparation with metal leads for *in situ* measurements. Follow until step 8 for devices to be contacted by W probes directly.

1. Fabricate $SrTiO_3$ thin film by PLD.
2. Deposit the top electrode onto the $SrTiO_3$ film (*ex situ*). See table A.1 for the different top electrodes tested in this thesis.

Lithography 1

3. Clean the sample using a ultrasonication in acetone followed by 2-propanol for 1 min each. Blow-dry with N_2. Heat to 180 °C for 3 min (dehydration). Cool down to room temperature.
4. Coat the sample with a positive photo resist (AZ5204 for metal electrodes, AZ5214 for graphene). Heat to 90 °C for 3 min. Cool down to room temperature.
5. With the photo mask concealing the future device areas, the rest of the sample is exposed to 500 nm UV light for 15 s (25 s for graphene).
6. Develop the exposed photo resist using the developer MIF 326 for roughly 35 s (45 s for graphene).

7. The exposed metal is dry-etched using argon bombardment in the Reactive Ion Beam Etching tool (Clean room PGI 7). Use recipe ar0lbeam.rec for approximately 3 min (Ar bombardment at an angle of 0° with 70 mA beam current). It is important to use such comparably low currents (compared to the standard settings of this instrument) to avoid excessive heating of the sample. Such heating results in irremovable photo resist.

7. Graphene is dry-etched using oxygen plasma (Clean room PGI 7) with 300 W for 30 s. A 30 nm insulating layer is deposited around the remaining graphene before photo resist lift-off. This step ensures that the next alignment steps are possible (graphene on $SrTiO_3$ is invisible in the light microscope). This way the graphene electrodes and alignment markers can be identified as holes in the insulating layer.

8. To remove the photo resist from the device areas, the sample is heated to 80 °C in dimethyl sulfoxide (DMSO) for roughly 2 hours. Metal electrodes: Ultrasonic cleaning (lowest power available) with hot DMSO for 10 s. Avoid any ultrasonic bath for graphene-containing samples! Place sample in acetone (room temperature) and gently swipe over the sample surface using a "clean room swap". Clean in 2-propanol. Blow-dry with N_2.

Lithography 2

9. Heat to 180 °C for 3 min (dehydration). Cool down to room temperature. Coat the sample with a positive photo resist (AZ5214). Heat to 90 °C for 3 min. Cool down to room temperature.
10. With the photo mask concealing the inner area of the device areas, the rest of the sample is exposed to 500 nm UV light for 25 s.
11. Develop the exposed photo resist using the developer MIF 326 for roughly 45 s.
12. Deposit an insulating layer. Metal electrodes: 100 nm. Graphene: 80 nm. See table A.1 for the different choices for the insulating layer.

13. To remove the photo resist, the sample is heated to 80 °C in dimethyl sulfoxide (DMSO) for roughly 2 hours. Metal electrodes: Ultrasonic cleaning (lowest power available) with hot DMSO for 10 s. Avoid any ultrasonic bath for graphene-containing samples! Place sample in acetone (room temperature) and gently swipe over the sample surface using a "clean room swap". Clean in 2-propanol. Blow-dry with N_2.

Lithography 3

14. Heat to 180 °C for 3 min (dehydration). Cool down to room temperature. Coat the sample with a negative photo resist (AZnLoF). Heat to 90 °C for 3 min. Cool down to room temperature.
15. With the photo mask concealing the areas where metal leads will be deposited in the next step, the rest of the sample is exposed to 500 nm UV light for 10 s.
16. AZnLoF photo resist needs to be baked at 110 °C for 1 min after exposure.
17. Develop the exposed photo resist using the developer MIF 726 for roughly 45 s. Special care has to be taken during alignment and development to later ensure contact between device area and metal lead.
18. Deposit the metal lead. For all devices studied here, 10 nm Pt followed by 130 nm Au were deposited by electron beam evaporation.
19. To remove the photo resist, the sample is heated to 80 °C in TechniStrip Ni555 (MicroChemicals GmbH, Ulm, Germany) for roughly 2 hours. Place sample in acetone (room temperature) and gently swipe over the sample surface using a "clean room swap". Clean in 2-propanol. Blow-dry with N_2.

Table A.1: Materials tested for $SrTiO_3$-based memristive devices with metal leads as described in section 3.2. Top electrode materials which are likely to work in this geometry but which have only been tested without metal leads are included. The phrase "Wire bonding not possible" indicates that the metal lead could not be contacted by wire bonding because each attempt resulted in a short circuit between metal lead and bottom electrode. This can be circumvented by contacting with an Al wire and fast-drying silver paint. However, this results in a non-negligible contact resistant of 100-300 Ω, making wire bonding preferable.

Purpose	**Material**	**Thickness**	**Source**	**Outcome**
Top electrode	Pt	10 nm	Electron beam evaporator (Clean room PGI 7)	√
Top electrode	Rh	2 nm	Electron beam evaporator (Electronic oxide cluster tool PGI 7)	√
Top electrode	Rh	2 nm	Electron beam evaporator (HNF)	√
Top electrode	graphene	1 monolayer	University of Illinois.	√
Top electrode	Au	30 nm	Sputter-gun in PLD setup (PGI 7)	(√) only tested without metal leads.
Top electrode	Au	80 nm	Electron beam evaporator (Clean room PGI 7)	(√) only tested without metal leads.
Top electrode	Pt	30 nm	Electron beam evaporator (Clean room PGI 7)	(√) only tested without metal leads.
Top electrode	Rh	30 nm	Electron beam evaporator (Electronic oxide cluster tool PGI 7)	No forming possible.
Insulating layer	$Y:ZrO_2$	100 nm	PLD (TSST, PGI 7)	√

Insulating layer	MgO_2	40 nm	PLD (TSST, PGI 7)	(√) Wire bonding not possible.
Insulating layer	HfO_2	80 nm	Sputter-tool, PGI 7	(√) Wire bonding not possible.
Insulating layer	Al_2O_3	80 nm	PLD (TSST, PGI 7)	Al_2O_3 loses insulating properties in developer (basic solution).
Insulating layer	Al_2O_3 covered by MgO_2	80 nm Al_2O_3; 20 nm MgO_2	PLD (TSST, PGI 7)	(√) Not tested sufficiently.
Insulating layer	SiO_2	100 nm	Spin-on glass "MSQ"	(√) Not tested sufficiently. Previously shown to degrade under synchrotron irradiation [123].

Metal lead	Pt	130 nm	Electron beam evaporator (Clean room PGI 7)	Peal-off during development.
Metal lead	Pt covered by Au	10 nm Pt; 130 nm Au	Electron beam evaporator (Clean room PGI 7)	√
Metal lead	Pt covered by Au	10 nm Pt; 130 nm Au	Electron beam evaporator (HNF)	√
Metal lead	Pt	50 nm	Sputter-tool, PGI 7	Principally ok, but larger series resistance (≈100 Ω). Results in higher LRS values.

List of Abbreviations

AFM Atomic force microscopy

C-AFM Conductive atomic force microscopy

EDX Energy dispersive X-ray spectroscopy
EEL Electron energy loss
EELS Electron energy loss spectroscopy
EXAFS Extended X-ray absorption fine structure

FIB Focused ion beam

HAADF High-angle annular dark-field
HRS High resistance state

IMFP Inelastic mean free path

LRS Low resistance state

MIM Metal-insulator-metal

PEEM Photoemission electron microscopy
PLD Pulsed laser deposition

RGA Residual gas analyzer
RHEED Reflection high energy electron diffraction
ROI Region of interest

STEM Scanning transmission electron microscopy

TEM Transmission electron microscopy

UHV Ultra-high vacuum

XANES X-ray absorption near edge spectroscopy

XAS X-ray absorption spectroscopy

XPEEM Photoemission electron microscopy with X-ray excitation

XPS X-ray photoelectron spectroscopy

Bibliography

[1] ITRS, *International Technology Roadmap for Semiconductors - 2013 Edition*, 2013.

[2] R. Waser and M. Aono, *Nat. Mater.* **6**, 833 (2007).

[3] A. Sawa, *Mater. Today* **11**, 28 (2008).

[4] R. Waser, R. Dittmann, G. Staikov, and K. Szot, *Adv. Mater.* **21**, 2632 (2009).

[5] J. J. Yang, M. D. Pickett, X. Li, D. A. A. Ohlberg, D. R. Stewart, and R. S. Williams, *Nat. Nanotechnol.* **3**, 429 (2008).

[6] H.-S. P. Wong, H.-Y. Lee, S. Yu, Y.-S. Chen, Y. Wu, P.-S. Chen, B. Lee, F. T. Chen, and M.-J. Tsai, *Proc. IEEE* **100**, 1951 (2012).

[7] E. Linn, R. Rosezin, C. Kügeler, and R. Waser, *Nat. Mater.* **9**, 403 (2010).

[8] A. Marchewka, R. Waser, and S. Menzel, Physical simulation of dynamic resistive switching in metal oxides using a Schottky contact barrier model, in *2015 Int. Conf. Simul. Semicond. Process. Devices (SISPAD)*, pp. 297–300, IEEE, 2015.

[9] S. Larentis, F. Nardi, S. Balatti, D. C. Gilmer, and D. Ielmini, *IEEE Trans. Electron Devices* **59**, 2468 (2012).

[10] S. Lee, J. S. Lee, J.-B. Park, Y. Koo Kyoung, M.-J. Lee, and T. Won Noh, *APL Mater.* **2**, 066103 (2014).

[11] Kan-Hao Xue, B. Traore, P. Blaise, L. R. C. Fonseca, E. Vianello, G. Molas, B. De Salvo, G. Ghibaudo, B. Magyari-Kope, and Y. Nishi, *IEEE Trans. Electron Devices* **61**, 1394 (2014).

[12] A. Marchewka, B. Roesgen, K. Skaja, H. Du, C.-L. Jia, J. Mayer, V. Rana, R. Waser, and S. Menzel, *Adv. Electron. Mater.* **2**, 1500233 (2016).

[13] M. Janousch, G. I. Meijer, U. Staub, B. Delley, S. F. Karg, and B. P. Andreasson, *Adv. Mater.* **19**, 2232 (2007).

[14] J. P. Strachan, M. D. Pickett, J. J. Yang, S. Aloni, a. L. D. Kilcoyne, G. Medeiros-Ribeiro, and R. S. Williams, *Adv. Mater.* **22**, 3573 (2010).

[15] C. Lenser, M. Patt, S. Menzel, A. Köhl, C. Wiemann, C. M. Schneider, R. Waser, and R. Dittmann, *Adv. Funct. Mater.* **24**, 4466 (2014).

[16] A. Koehl, H. Wasmund, A. Herpers, P. Guttmann, S. Werner, K. Henzler, H. Du, J. Mayer, R. Waser, and R. Dittmann, *APL Mater.* **1**, 042102 (2013).

[17] R. Dittmann, R. Muenstermann, I. Krug, D. Park, T. Menke, J. Mayer, A. Besmehn, F. Kronast, C. M. Schneider, and R. Waser, *Proc. IEEE* **100**, 1979 (2012).

[18] M. Sowinska, T. Bertaud, D. Walczyk, S. Thiess, P. Calka, L. Alff, C. Walczyk, and T. Schroeder, *J. Appl. Phys.* **115**, 1 (2014).

[19] S. Kumar, C. E. Graves, J. P. Strachan, A. L. D. Kilcoyne, T. Tyliszczak, Y. Nishi, and R. S. Williams, *J. Appl. Phys.* **118**, 034502 (2015).

[20] S. Kumar, C. E. Graves, J. P. Strachan, E. M. Grafals, A. L. D. Kilcoyne, T. Tyliszczak, J. N. Weker, Y. Nishi, and R. S. Williams, *Adv. Mater.* **28**, 2772 (2016).

[21] H. Tian, H.-Y. Chen, B. Gao, S. Yu, J. Liang, Y. Yang, D. Xie, J. Kang, T.-L. Ren, Y. Zhang, and H.-S. P. Wong, *Nano Lett.* **13**, 651 (2013).

[22] J. Yao, J. Lin, Y. Dai, G. Ruan, Z. Yan, L. Li, L. Zhong, D. Natelson, and J. M. Tour, *Nat. Commun.* **3**, 1101 (2012).

[23] S. Lee, J. Sohn, Z. Jiang, H.-Y. Chen, and H.-S. P. Wong, *Nat. Commun.* **6**, 8407 (2015).

[24] P. A. Cox, *Transition metal oxides: An introduction to their electronic structure and properties*, Oxford University Press, Oxford, 1992.

[25] A. Rothschild, W. Menesklou, H. L. Tuller, and E. Ivers-Tiffée, *Chem. Mater.* **18**, 3651 (2006).

[26] F. M. F. de Groot, M. Grioni, J. C. Fuggle, J. Ghijsen, G. A. Sawatzky, and H. Petersen, *Phys. Rev. B* **40**, 5715 (1989).

[27] X. Guo, X. Chen, Y. Sun, L. Sun, X. Zhou, and W. Lu, *Phys. Lett. A* **317**, 501 (2003).

[28] R. Merkle and J. Maier, *Angew. Chemie Int. Ed.* **47**, 3874 (2008).

[29] F. Kröger, *The Chemistry of Imperfect Crystals*, North-Holland Publishing Company, Amsterdam, 1964.

[30] K. Szot, W. Speier, U. Breuer, R. Meyer, J. Szade, and R. Waser, *Surf. Sci.* **460**, 112 (2000).

[31] F. Gunkel, *The role of defects at functional interfaces between polar and non-polar perovskite oxides*, PhD thesis, RWTH Aachen University, 2013.

[32] S. N. Ruddlesden and P. Popper, *Acta Crystallogr.* **11**, 54 (1958).

[33] W. Luo, W. Duan, S. G. Louie, and M. L. Cohen, *Phys. Rev. B* **70**, 1 (2004).

[34] D. S. Shang, J. R. Sun, L. Shi, J. Wang, Z. H. Wang, and B. G. Shen, *Appl. Phys. Lett.* **94**, 052105 (2009).

[35] C. Park, Y. Seo, J. Jung, and D.-W. Kim, *J. Appl. Phys.* **103**, 054106 (2008).

[36] M.-J. Lee, C. B. Lee, D. Lee, S. R. Lee, M. Chang, J. H. Hur, Y.-B. Kim, C.-J. Kim, D. H. Seo, S. Seo, U.-I. Chung, I.-K. Yoo, and K. Kim, *Nat. Mater.* **10**, 625 (2011).

[37] A. Marchewka, D. Cooper, C. Lenser, S. Menzel, H. Du, R. Dittmann, R. E. Dunin-Borkowski, and R. Waser, *Sci. Rep.* **4**, 6975 (2014).

[38] S. M. Sze and K. K. Ng, editors, *Physics of Semiconductor Devices*, John Wiley & Sons, Inc., Hoboken, NJ, 3 edition, 2006.

[39] F.-C. Chiu, *Adv. Mater. Sci. Eng.* **2014**, 1 (2014).

[40] S. a. Mojarad, K. S. K. Kwa, J. P. Goss, Z. Zhou, N. K. Ponon, D. J. R. Appleby, R. a. S. Al-Hamadany, and A. O'Neill, *J. Appl. Phys.* **111**, 014503 (2012).

[41] E. Mikheev, B. Himmetoglu, A. P. Kajdos, P. Moetakef, T. A. Cain, C. G. Van de Walle, and S. Stemmer, *Appl. Phys. Lett.* **106**, 062102 (2015).

[42] X. Hao, Z. Wang, M. Schmid, U. Diebold, and C. Franchini, *Phys. Rev. B* **91**, 085204 (2015).

[43] Z. Wang, S. McKeown Walker, A. Tamai, Y. Wang, Z. Ristic, F. Y. Bruno, A. de la Torre, S. Riccò, N. C. Plumb, M. Shi, P. Hlawenka, J. Sánchez-Barriga, A. Varykhalov, T. K. Kim, M. Hoesch, P. D. C. King, W. Meevasana, U. Diebold, J. Mesot, B. Moritz, T. P. Devereaux, M. Radovic, and F. Baumberger, *Nat. Mater.* **15**, 835 (2016).

[44] A. Janotti, J. B. Varley, M. Choi, and C. G. Van de Walle, *Phys. Rev. B* **90**, 085202 (2014).

[45] C. Cancellieri, A. S. Mishchenko, U. Aschauer, A. Filippetti, C. Faber, O. S. Barišić, V. A. Rogalev, T. Schmitt, N. Nagaosa, and V. N. Strocov, *Nat. Commun.* **7**, 10386 (2016).

[46] R. Waser, *J. Am. Ceram. Soc.* **74**, 1934 (1991).

[47] R. A. De Souza, V. Metlenko, D. Park, and T. E. Weirich, *Phys. Rev. B* **85**, 174109 (2012).

[48] M. Schie, R. Waser, and R. a. De Souza, *J. Phys. Chem. C* **118**, 15185 (2014).

[49] R. Moos and K. H. Hardtl, *J. Am. Ceram. Soc.* **80**, 2549 (1997).

[50] I. Denk, W. Münch, and J. Maier, *J. Am. Ceram. Soc.* **78**, 3265 (1995).

[51] K. Gömann, G. Borchardt, M. Schulz, A. Gömann, W. Maus-Friedrichs, B. Lesage, O. Kaïtasov, S. Hoffmann-Eifert, and T. Schneller, *Phys. Chem. Chem. Phys.* **7**, 2053 (2005).

[52] V. Metlenko, A. H. H. Ramadan, F. Gunkel, H. Du, H. Schraknepper, S. Hoffmann-Eifert, R. Dittmann, R. Waser, and R. A. De Souza, *Nanoscale* **6**, 12864 (2014).

[53] R. Muenstermann, T. Menke, R. Dittmann, and R. Waser, *Adv. Mater.* **22**, 4819 (2010).

[54] A. Köhl, *Micro-spectroscopic investigation of valence change processes in resistive switching $SrTiO_3$ thin films*, Phd thesis, RWTH Aachen University, 2014.

[55] M. Kubicek, R. Schmitt, F. Messerschmitt, and J. L. M. Rupp, *ACS Nano* **9**, 10737 (2015).

[56] R. Waser, editor, *Nanoelectronics and Information Technology*, Wiley-VCH, Weinheim, 2012.

[57] S. Menzel, M. Waters, A. Marchewka, U. Böttger, R. Dittmann, and R. Waser, *Adv. Funct. Mater.* **21**, 4487 (2011).

[58] D. Ielmini and R. Waser, editors, *Resistive Switching: From Fundamentals of Nanoionic Redox Processes to Memristive Device Applications*, Wiley-VCH, Weinheim, 2016.

[59] K. Shibuya, R. Dittmann, S. Mi, and R. Waser, *Adv. Mater.* **22**, 411 (2010).

[60] R. Bruchhaus, C. Hermes, and R. Waser, *Mater. Res. Soc. Symp. Proc.* **1337**, 73 (2011).

[61] J. J. Yang, J. Borghetti, D. Murphy, D. R. Stewart, and R. S. Williams, *Adv. Mater.* **21**, 3754 (2009).

[62] J. Sung Lee, S. Buhm Lee, B. Kahng, and T. Won Noh, *Appl. Phys. Lett.* **102**, 253503 (2013).

[63] E. Lee, M. Gwon, D.-W. Kim, and H. Kim, *Appl. Phys. Lett.* **98**, 132905 (2011).

[64] R. Buzio, A. Gerbi, A. Gadaleta, L. Anghinolfi, F. Bisio, E. Bellingeri, A. S. Siri, and D. Marrè, *Appl. Phys. Lett.* **101** (2012).

[65] M. Yang, L. Z. Ren, Y. J. Wang, F. M. Yu, M. Meng, W. Q. Zhou, S. X. Wu, and S. W. Li, *J. Appl. Phys.* **115**, 134505 (2014).

[66] J. Park, D.-H. Kwon, H. Park, C. U. Jung, and M. Kim, *Appl. Phys. Lett.* **105**, 183103 (2014).

[67] D.-j. Seong, M. Jo, D. Lee, and H. Hwang, *Electrochem. Solid-State Lett.* **10**, H168 (2007).

[68] Y. H. Wang, K. H. Zhao, X. L. Shi, G. L. Xie, S. Y. Huang, and L. W. Zhang, *Appl. Phys. Lett.* **103**, 031601 (2013).

[69] A. Ohtomo and H. Y. Hwang, *Appl. Phys. Lett.* **84**, 1716 (2004).

[70] C. Rodenbücher, W. Speier, G. Bihlmayer, U. Breuer, R. Waser, and K. Szot, *New J. Phys.* **15**, 103017 (2013).

[71] S. H. Jeon, B. H. Park, J. Lee, B. Lee, and S. Han, *Appl. Phys. Lett.* **89**, 042904 (2006).

[72] R. Schafranek, S. Payan, M. Maglione, and A. Klein, *Phys. Rev. B* **77**, 195310 (2008).

[73] E. Mikheev, B. D. Hoskins, D. B. Strukov, and S. Stemmer, *Nat. Commun.* **5** (2014).

[74] A. Sawa, T. Fujii, M. Kawasaki, and Y. Tokura, *Appl. Phys. Lett.* **86**, 112508 (2005).

[75] T. Fujii, M. Kawasaki, A. Sawa, Y. Kawazoe, H. Akoh, and Y. Tokura, *Phys. Rev. B* **75**, 165101 (2007).

[76] X. Sun, G. Li, L. Chen, Z. Shi, and W. Zhang, *Nanoscale Res. Lett.* **6**, 599 (2011).

[77] K. Dong-Wook, G. Minji, L. Eunsongyi, S. Ahrum, and M. B. El, *J. Korean Phys. Soc.* **57**, 1432 (2010).

[78] M. Noman, W. Jiang, P. A. Salvador, M. Skowronski, and J. A. Bain, *Appl. Phys. A Mater. Sci. Process.* **102**, 877 (2011).

[79] K. Dong-Wook, G. Minji, L. Eunsongyi, S. Ahrum, and M. B. El, *J. Korean Phys. Soc.* **57**, 1432 (2010).

[80] N. Raab, C. Baeumer, and R. Dittmann, *AIP Adv.* **5**, 047150 (2015).

[81] D. Choi, D. Lee, H. Sim, M. Chang, and H. Hwang, *Appl. Phys. Lett.* **88**, 082904 (2006).

[82] T. Ninomiya, S. Muraoka, Z. Wei, R. Yasuhara, K. Katayama, and T. Takagi, *IEEE Electron Device Lett.* **34**, 762 (2013).

[83] T. Ninomiya, Z. Wei, S. Muraoka, R. Yasuhara, K. Katayama, and T. Takagi, *IEEE Trans. Electron Devices* **60**, 1384 (2013).

[84] B. Gao, S. Yu, N. Xu, L. F. Liu, B. Sun, X. Y. Liu, R. Q. Han, J. F. Kang, B. Yu, and Y. Y. Wang, Oxide-based RRAM switching mechanism: A new ion-transport-recombination model, in *Tech. Dig. - Int. Electron Devices Meet. IEDM*, 2008.

[85] B. Gao, J. F. Kang, H. W. Zhang, B. Sun, B. Chen, L. F. Liu, X. Y. Liu, R. Q. Han, Y. Y. Wang, B. Yu, Z. Fang, H. Y. Yu, and D. L. Kwong, Oxide-based RRAM: Physical based retention projection, in *2010 Proc. Eur. Solid State Device Res. Conf. ESSDERC 2010*, pp. 392–395, 2010.

[86] H. Y. Lee, P. S. Chen, T. Y. Wu, Y. S. Chen, C. C. Wang, P. J. Tzeng, C. H. Lin, F. Chen, C. H. Lien, and M. J. Tsai, Low power and high speed bipolar switching with a thin reactive ti buffer layer in robust HfO_2 based RRAM, in *Tech. Dig. - Int. Electron Devices Meet. IEDM*, 2008.

[87] Y. S. Chen, H. Y. Lee, P. S. Chen, P. Y. Gu, C. W. Chen, W. P. Lin, W. H. Liu, Y. Y. Hsu, S. S. Sheu, P. C. Chiang, W. S. Chen, F. T. Chen, C. H. Lien, and M. J. Tsai, Highly scalable hafnium oxide memory with improvements of resistive distribution and read disturb immunity, in *Tech. Dig. - Int. Electron Devices Meet. IEDM*, pp. 1–4, IEEE, 2009.

[88] S. M. Yu, Y. Y. Chen, X. M. Guan, H. S. P. Wong, and J. A. Kittl, *Appl. Phys. Lett.* **100**, 43507 (2012).

[89] Y. Y. Chen, L. Goux, S. Clima, B. Govoreanu, R. Degraeve, G. S. Kar, A. Fantini, G. Groeseneken, D. J. Wouters, and M. Jurczak, *IEEE Trans. Electron Devices* **60**, 1114 (2013).

[90] Z. Wei, Y. Kanzawa, K. Arita, Y. Katoh, K. Kawai, S. Muraoka, S. Mitani, S. Fujii, K. Katayama, M. Iijima, T. Mikawa, T. Ninomiya, R. Miyanaga, Y. Kawashima, K. Tsuji, A. Himeno, T. Okada, R. Azuma, K. Shimakawa, H. Sugaya, T. Takagi, R. Yasuhara, KHoriba, H. Kumigashira, M. Oshima, K. Horiba, H. Kumigashira, and M. Oshima, Highly reliable TaO_x ReRAM and direct evidence of redox reaction mechanism, in *Tech. Dig. - Int. Electron Devices Meet. IEDM*, pp. 1–4, IEEE, 2008.

[91] L. Goux, A. Fantini, Y. Y. Chen, A. Redolfi, R. Degraeve, and M. Jurczak, *ECS Solid State Lett.* **3**, Q79 (2014).

[92] T. Ninomiya, T. Takagi, Z. Wei, S. Muraoka, R. Yasuhara, K. Katayama, Y. Ikeda, K. Kawai, Y. Kato, Y. Kawashima, S. Ito, T. Mikawa, K. Shimakawa, and K. Aono, Conductive filament scaling of TaO_x bipolar ReRAM for long retention with low current operation, in *2012 Symp. VLSI Technol.*, pp. 73–74, IEEE, 2012.

[93] C. Xu, *In-situ study on the Pulsed Laser Deposition growth of complex metal oxides*, Phd thesis, RWTH Aachen University, 2016.

[94] S. Wicklein, *Defect Engineering of $SrTiO_3$ thin films for resistive switching applications*, PhD thesis, Christian-Albrechts-Universität zu Kiel, 2013.

[95] C. Baeumer, C. Xu, F. Gunkel, N. Raab, R. A. Heinen, A. Koehl, and R. Dittmann, *Sci. Rep.* **5**, 11829 (2015).

[96] G. Koster, B. L. Kropman, G. J. H. M. Rijnders, D. H. A. Blank, and H. Rogalla, *Appl. Phys. Lett.* **73**, 2920 (1998).

[97] Y. F. Nie, Y. Zhu, C.-H. Lee, L. F. Kourkoutis, J. A. Mundy, J. Junquera, P. Ghosez, D. J. Baek, S. Sung, X. X. Xi, K. M. Shen, D. A. Muller, and D. G. Schlom, *Nat. Commun.* **5**, 4530 (2014).

[98] C. Baeumer, S. P. Rogers, R. Xu, L. W. Martin, and M. Shim, *Nano Lett.* **13**, 1693 (2013).

[99] J. C. Fuggle and J. E. Inglesfield, editors, *Unoccupied Electronic States*, volume 69 of *Topics in Applied Physics*, Springer, Berlin, 1992.

[100] G. Bunker, *Introduction to XAFS*, Cambridge University Press, Cambridge, UK, 2010.

[101] F. M. F. de Groot, M. O. Figueiredo, M. J. Basto, M. Abbate, H. Petersen, and J. C. Fuggle, *Phys. Chem. Miner.* **19**, 140 (1992).

[102] C. M. Schneider and G. Schönhense, *Reports Prog. Phys.* **65**, 1785 (2002).

[103] D. Briggs and J. Grant, editors, *Surface Analysis by Auger and X-ray Photoelectron Spectroscopy*, Surface Spectra, Manchester, 2003.

[104] S. Tanuma, C. J. Powell, and D. R. Penn, *Surf. Interface Anal.* **21**, 165 (1994).

[105] M. C. Patt, *Bulk and surface sensitive energy-filtered photoemission microscopy using synchrotron radiation for the study of resistive switching memories*, Phd thesis, University of Duisburg-Essen, 2016.

[106] C. Wiemann, M. Patt, I. P. Krug, N. B. Weber, M. Escher, M. Merkel, and C. M. Schneider, *e-Journal Surf. Sci. Nanotechnol.* **9**, 395 (2011).

[107] R. M. Tromp, J. B. Hannon, A. W. Ellis, W. Wan, A. Berghaus, and O. Schaff, *Ultramicroscopy* **110**, 852 (2010).

[108] A. Locatelli, L. Aballe, T. O. Mentes, M. Kiskinova, and E. Bauer, *Surf. Interface Anal.* **38**, 1554 (2006).

[109] B. Ravel and M. Newville, *J. Synchrotron Radiat.* **12**, 537 (2005).

[110] O. Renault, R. Brochier, P.-H. Haumesser, N. Barrett, B. Krömker, and D. Funnemann, *e-Journal Surf. Sci. Nanotechnol.* **4**, 431 (2006).

[111] A. Locatelli, T. O. Mentes, M. Á. Niño, and E. Bauer, *Ultramicroscopy* **111**, 1447 (2011).

[112] C. Baeumer, C. Schmitz, A. Marchewka, D. N. Mueller, R. Valenta, J. Hackl, N. Raab, S. P. Rogers, M. I. Khan, S. Nemsak, M. Shim, S. Menzel, C. M. Schneider, R. Waser, and R. Dittmann, *Nat. Commun.* **7**, 12398 (2016).

[113] F. M. F. de Groot, J. C. Fuggle, B. T. Thole, and G. A. Sawatzky, *Phys. Rev. B* **41**, 928 (1990).

[114] M. Abbate, F. de Groot, J. Fuggle, A. Fujimori, Y. Tokura, Y. Fujishima, O. Strebel, M. Domke, G. Kaindl, J. van Elp, B. Thole, G. Sawatzky, M. Sacchi, and N. Tsuda, *Phys. Rev. B* **44**, 5419 (1991).

[115] D. A. Muller, N. Nakagawa, A. Ohtomo, J. L. Grazul, and H. Y. Hwang, *Nature* **430**, 657 (2004).

[116] F. de Groot, J. Faber, J. Michiels, M. Czyżyk, M. Abbate, and J. Fuggle, *Phys. Rev. B* **48**, 2074 (1993).

[117] N. D. Browning, H. O. Moltaji, and J. P. Buban, *Phys. Rev. B* **58**, 8289 (1998).

[118] A. Fujimori, I. Hase, M. Nakamura, H. Namatame, Y. Fujishima, Y. Tokura, M. Abbate, F. M. F. de Groot, M. T. Czyzyk, J. C. Fuggle, O. Strebel, F. Lopez, M. Domke, and G. Kaindl, *Phys. Rev. B* **46**, 9841 (1992).

[119] A. S. Sefat, G. Amow, M.-Y. Wu, G. A. Botton, and J. Greedan, *J. Solid State Chem.* **178**, 1008 (2005).

[120] E. O. Filatova, A. A. Sokolov, Y. V. Egorova, A. S. Konashuk, O. Y. Vilkov, M. Gorgoi, and A. A. Pavlychev, *J. Appl. Phys.* **113**, 224301 (2013).

[121] A. B. Shah, Q. M. Ramasse, X. Zhai, J. G. Wen, S. J. May, I. Petrov, A. Bhattacharya, P. Abbamonte, J. N. Eckstein, and J. M. Zuo, *Adv. Mater.* **22**, 1156 (2010).

[122] B. P. Andreasson, *Oxygen Vacancies in $SrTiO_3$: An X-ray Absorption Study*, PhD thesis, ETH ZÜRICH, 2009.

[123] C. Lenser, *Investigation of Resistive Switching in Fe-doped $SrTiO_3$ by Advanced Spectroscopy*, Phd thesis, RWTH Aachen University, 2013.

[124] H. P. R. Frederikse, W. R. Thurber, and W. R. Hosler, *Phys. Rev.* **134**, A442 (1964).

[125] J. A. McLeod, R. G. Wilks, N. A. Skorikov, L. D. Finkelstein, M. Abu-Samak, E. Z. Kurmaev, and A. Moewes, *Phys. Rev. B* **81**, 245123 (2010).

[126] D. G. Rickerby, G. Valdrè, and U. Valdrè, editors, *Impact of Electron and Scanning Probe Microscopy on Materials Research*, Springer, Dordrecht, 2012.

[127] C. Scheu, G. Dehm, H. Müllejans, R. Brydson, and M. Rühle, *Microsc. Microanal. Microstruct.* **6**, 19 (1995).

[128] T. J. Pennycook, M. P. Oxley, J. Garcia-Barriocanal, F. Y. Bruno, C. Leon, J. Santamaria, S. T. Pantelides, M. Varela, and S. J. Pennycook, *Eur. Phys. J. Appl. Phys.* **54**, 33507 (2011).

[129] I. M. Ross, W. M. Rainforth, a. J. Scott, a. P. Brown, R. Brydson, and D. W. McComb, *J. Eur. Ceram. Soc.* **24**, 2023 (2004).

[130] N. Aslam, V. Longo, W. Keuning, F. Roozeboom, W. M. M. Kessels, R. Waser, and S. Hoffmann-Eifert, *Phys. status solidi* **211**, 389 (2014).

[131] E. Mikheev, J. Hwang, A. P. Kajdos, A. J. Hauser, and S. Stemmer, *Sci. Rep.* **5**, 11079 (2015).

[132] M. L. Reinle-Schmitt, C. Cancellieri, A. Cavallaro, G. F. Harrington, S. J. Leake, E. Pomjakushina, J. A. Kilner, and P. R. Willmott, *Nanoscale* **6**, 2598 (2014).

[133] D. Li, S. Gariglio, C. Cancellieri, A. Fête, D. Stornaiuolo, and J.-M. Triscone, *APL Mater.* **2**, 012102 (2014).

[134] F. Gunkel, S. Wicklein, S. Hoffmann-Eifert, P. Meuffels, P. Brinks, M. Huijben, G. Rijnders, R. Waser, and R. Dittmann, *Nanoscale* **7**, 1013 (2015).

[135] A. Berlich, H. Strauss, C. Langheinrich, A. Chassé, and H. Morgner, *Surf. Sci.* **605**, 158 (2011).

[136] C. Raisch, T. Chasse, C. Langheinrich, and A. Chasse, *J. Appl. Phys.* **112**, 073505 (2012).

[137] T. Ohnishi, K. Takahashi, M. Nakamura, M. Kawasaki, M. Yoshimoto, and H. Koinuma, *Appl. Phys. Lett.* **74**, 2531 (1999).

[138] T. Ohnishi, K. Shibuya, M. Lippmaa, D. Kobayashi, H. Kumigashira, M. Oshima, and H. Koinuma, *Appl. Phys. Lett.* **85**, 272 (2004).

[139] N. Nakagawa, H. Y. Hwang, and D. A. Muller, *Nat. Mater.* **5**, 204 (2006).

[140] D. Park, A. Herpers, T. Menke, M. Heidelmann, L. Houben, R. Dittmann, and J. Mayer, *Microsc. Microanal.* **20**, 740 (2014).

[141] M. Foerster, R. Bachelet, V. Laukhin, J. Fontcuberta, G. Herranz, and F. Sanchez, *Appl. Phys. Lett.* **100**, 231607 (2012).

[142] J. Fompeyrine, R. Berger, H. P. Lang, J. Perret, E. MaÌˆchler, C. Gerber, and J.-P. Locquet, *Appl. Phys. Lett.* **72**, 1697 (1998).

[143] R. Shimizu, K. Iwaya, T. Ohsawa, S. Shiraki, T. Hasegawa, T. Hashizume, and T. Hitosugi, *ACS Nano* **5**, 7967 (2011).

[144] E. Breckenfeld, R. Wilson, J. Karthik, A. R. Damodaran, D. G. Cahill, and L. W. Martin, *Chem. Mater.* **24**, 331 (2012).

[145] E. Breckenfeld, N. Bronn, J. Karthik, A. R. Damodaran, S. Lee, N. Mason, and L. W. Martin, *Phys. Rev. Lett.* **110**, 196804 (2013).

[146] S. Wicklein, A. Sambri, S. Amoruso, X. Wang, R. Bruzzese, A. Koehl, and R. Dittmann, *Appl. Phys. Lett.* **101**, 131601 (2012).

[147] L. Zhang, D. Wett, R. Szargan, and T. Chassé, *Surf. Interface Anal.* **36**, 1479 (2004).

[148] T. Ohnishi, K. Shibuya, T. Yamamoto, and M. Lippmaa, *J. Appl. Phys.* **103**, 103703 (2008).

[149] J. H. Lee, G. Luo, I. C. Tung, S. H. Chang, Z. Luo, M. Malshe, M. Gadre, A. Bhattacharya, S. M. Nakhmanson, J. A. Eastman, H. Hong, J. Jellinek, D. Morgan, D. D. Fong, and J. W. Freeland, *Nat. Mater.* **13**, 879 (2014).

[150] Y.-E. Sung, S. Thomas, J. A. Tanzer, and A. Wieckowski, Coadsorption of copper and (bi)sulfate anions on (1 1 1) single crystal faces of gold, platinum and rhodium, in *Proc. Sixth Int. Symp. Electrode Process.*, pp. 28–42, Pennington, NJ, 1996, Electrochemical Society.

[151] R. Garg, N. Dutta, and N. Choudhury, *Nanomaterials* **4**, 267 (2014).

[152] C. Baeumer, C. Schmitz, A. H. H. Ramadan, H. Du, K. Skaja, V. Feyer, P. Müller, B. Arndt, C.-L. Jia, J. Mayer, R. A. De Souza, C. M. Schneider, R. Waser, and R. Dittmann, *Nat. Commun.* **6**, 8610 (2015).

[153] C. Baeumer, N. Raab, T. Menke, C. Schmitz, R. Rosezin, P. Müller, M. Andrä, V. Feyer, R. Bruchhaus, F. Gunkel, C. M. Schneider, R. Waser, and R. Dittmann, *Nanoscale* **8**, 13967 (2016).

[154] L. Goux, P. Czarnecki, Y. Y. Chen, L. Pantisano, X. P. Wang, R. Degraeve, B. Govoreanu, M. Jurczak, D. J. Wouters, and L. Altimime, *Appl. Phys. Lett.* **97**, 243509 (2010).

[155] A. A. Sharma, M. Noman, M. Abdelmoula, M. Skowronski, and J. A. Bain, *Adv. Funct. Mater.* **24**, 5522 (2014).

[156] J. Joshua Yang, F. Miao, M. D. Pickett, D. a. a. Ohlberg, D. R. Stewart, C. N. Lau, and R. S. Williams, *Nanotechnology* **20**, 215201 (2009).

[157] D. S. Jeong, H. Schroeder, and R. Waser, *Phys. Rev. B* **79**, 195317 (2009).

[158] Y. Wang, X. Qian, K. Chen, Z. Fang, W. Li, and J. Xu, *Appl. Phys. Lett.* **102**, 042103 (2013).

[159] A. Mehonic, M. Buckwell, L. Montesi, M. S. Munde, D. Gao, S. Hudziak, R. J. Chater, S. Fearn, D. McPhail, M. Bosman, A. L. Shluger, and A. J. Kenyon, *Adv. Mater.* **28**, 7486 (2016).

[160] J. J. Yang, M. D. Pickett, X. Li, D. A. A. Ohlberg, D. R. Stewart, and R. S. Williams, *Nat. Nanotechnol.* **3**, 429 (2008).

[161] L. F. Zagonel, M. Bäurer, A. Bailly, O. Renault, M. Hoffmann, S.-J. Shih, D. Cockayne, and N. Barrett, *J. Phys. Condens. Matter* **21**, 314013 (2009).

[162] R. Meyer, K. Szot, and R. Waser, *Ferroelectrics* **224**, 323 (1999).

[163] R. Meyer, R. Waser, J. Helmbold, and G. Borchardt, *J. Electroceramics* **9**, 101.

[164] B. Rahmati, J. Fleig, W. Sigle, E. Bischoff, J. Maier, and M. Rühle, *Surf. Sci.* **595**, 115 (2005).

[165] C. Lenser, A. Koehl, I. Slipukhina, H. Du, M. Patt, V. Feyer, C. M. Schneider, M. Lezaic, R. Waser, and R. Dittmann, *Adv. Funct. Mater.* **25**, 6360 (2015).

[166] S. Tanuma, C. Powell, and D. Penn, *Surf. Sci.* **192**, L849 (1987).

[167] K. Skaja, C. Baeumer, O. Peters, S. Menzel, M. Moors, H. Du, M. Bornhöfft, C. Schmitz, V. Feyer, C.-L. Jia, C. M. Schneider, J. Mayer, R. Waser, and R. Dittmann, *Adv. Funct. Mater.* **25**, 7154 (2015).

[168] R. Valenta, *Resistive switching devices with ultrathin electrodes for spectroscopic investigations*, Master's thesis, RWTH Aachen University, 2016.

[169] S. McKeown Walker, A. de la Torre, F. Bruno, A. Tamai, T. Kim, M. Hoesch, M. Shi, M. Bahramy, P. King, and F. Baumberger, *Phys. Rev. Lett.* **113**, 177601 (2014).

[170] M. Arita, A. Takahashi, Y. Ohno, A. Nakane, A. Tsurumaki-Fukuchi, and Y. Takahashi, *Sci. Rep.* **5**, 17103 (2015).

[171] M. Kudo, M. Arita, Y. Ohno, and Y. Takahashi, *Appl. Phys. Lett.* **105**, 173504 (2014).

[172] M. Wojcik, M. Hauser, W. Li, S. Moon, and K. Xu, *Nat. Commun.* **6**, 7384 (2015).

[173] J. Kraus, R. Reichelt, S. Günther, L. Gregoratti, M. Amati, M. Kiskinova, A. Yulaev, I. Vlassiouk, and A. Kolmakov, *Nanoscale* **6**, 14394 (2014).

[174] A. Kolmakov, L. Gregoratti, M. Kiskinova, and S. Günther, *Top. Catal.* **59**, 448 (2016).

[175] M. Patt, C. Wiemann, N. Weber, M. Escher, A. Gloskovskii, W. Drube, M. Merkel, and C. M. Schneider, *Rev. Sci. Instrum.* **85**, 113704 (2014).

[176] M. Buckwell, L. Montesi, A. Mehonic, O. Reza, L. Garnett, M. Munde, S. Hudziak, and A. J. Kenyon, *Phys. status solidi* **12**, 211 (2015).

[177] S. Mildner, M. Beleggia, D. Mierwaldt, T. W. Hansen, J. B. Wagner, S. Yazdi, T. Kasama, J. Ciston, Y. Zhu, and C. Jooss, *J. Phys. Chem. C* **119**, 5301 (2015).

[178] J. Kwon, A. A. Sharma, J. A. Bain, Y. N. Picard, and M. Skowronski, *Adv. Funct. Mater.* **25**, 2876 (2015).

[179] J. Norpoth, S. Mildner, M. Scherff, J. Hoffmann, and C. Jooss, *Nanoscale* **6**, 9852 (2014).

[180] Z. Liao, P. Gao, X. Bai, D. Chen, and J. Zhang, *J. Appl. Phys.* **111**, 114506 (2012).

[181] J.-Y. Chen, C.-W. Huang, C.-H. Chiu, Y.-T. Huang, and W.-W. Wu, *Adv. Mater.* **27**, 5028 (2015).

[182] R. J. Kamaladasa, A. A. Sharma, Y.-T. Lai, W. Chen, P. A. Salvador, J. A. Bain, M. Skowronski, and Y. N. Picard, *Microsc. Microanal.* **21**, 140 (2015).

[183] P. Gao, Z. Wang, W. Fu, Z. Liao, K. Liu, W. Wang, X. Bai, and E. Wang, *Micron* **41**, 301 (2010).

[184] W. C. Chueh and S. M. Haile, *Annu. Rev. Chem. Biomol. Eng.* **3**, 313 (2012).

[185] D. Mierwaldt, S. Mildner, R. Arrigo, A. Knop-Gericke, E. Franke, A. Blumenstein, J. Hoffmann, and C. Jooss, *Catalysts* **4**, 129 (2014).

[186] R. Schmiedl, V. Demuth, P. Lahnor, H. Godehardt, Y. Bodschwinna, C. Harder, L. Hammer, H. P. Strunk, M. Schulz, and K. Heinz, *Appl. Phys. A Mater. Sci. Process.* **62**, 223 (1996).

[187] A. Grill, W. Kane, J. Viggiano, M. Brady, and R. Laibowitz, *J. Mater. Res.* **7**, 3260 (1992).

[188] D. S. Jeong, H. Schroeder, U. Breuer, and R. Waser, *J. Appl. Phys.* **104**, 123716 (2008).

[189] B. Govoreanu, G. Kar, Y.-Y. Chen, V. Paraschiv, S. Kubicek, A. Fantini, I. Radu, L. Goux, S. Clima, R. Degraeve, N. Jossart, O. Richard, T. Vandeweyer, K. Seo, P. Hendrickx, G. Pourtois, H. Bender, L. Altimime, D. Wouters, J. Kittl, and M. Jurczak, 10×10nm^2 Hf/HfO$_x$ crossbar resistive RAM with excellent performance, reliability and low-energy operation, in *2011 Int. Electron Devices Meet.*, pp. 31.6.1–31.6.4, IEEE, 2011.

[190] G. S. Brady, H. H. Clauser, and J. A. Vaccari, editors, *Materials Handbook*, McGraw-Hill, New York, NY, 15 edition, 2002.

[191] J. Martin, N. Akerman, G. Ulbricht, T. Lohmann, J. H. Smet, K. von Klitzing, and A. Yacoby, *Nat. Phys.* **4**, 144 (2008).

[192] C. Lenser, a. Kuzmin, J. Purans, a. Kalinko, R. Waser, and R. Dittmann, *J. Appl. Phys.* **111**, 076101 (2012).

[193] A. Mehonic, M. Buckwell, L. Montesi, L. Garnett, S. Hudziak, S. Fearn, R. Chater, D. McPhail, and A. J. Kenyon, *J. Appl. Phys.* **117**, 124505 (2015).

[194] M. Moors, K. K. Adepalli, Q. Lu, A. Wedig, C. Bäumer, K. Skaja, B. Arndt, H. L. Tuller, R. Dittmann, R. Waser, B. Yildiz, and I. Valov, *ACS Nano* **10**, 1481 (2016).

[195] R. Ortega-Hernandez, M. Coll, J. Gonzalez-Rosillo, A. Palau, X. Obradors, E. Miranda, T. Puig, and J. Suñe, *Microelectron. Eng.* **147**, 37 (2015).

[196] M. Scherff, B. Meyer, J. Hoffmann, C. Jooss, M. Feuchter, and M. Kamlah, *New J. Phys.* **17**, 033011 (2015).

[197] C. Y. Chen, L. Goux, A. Fantini, A. Redolfi, G. Groeseneken, and M. Jurczak, Doped Gd-O Based RRAM for Embedded Application, in *2016 IEEE 8th Int. Mem. Work.*, pp. 1–4, IEEE, 2016.

[198] R. Meyer, L. Schloss, J. Brewer, R. Lambertson, W. Kinney, J. Sanchez, and D. Rinerson, Oxide dual-layer memory element for scalable non-volatile cross-point memory technology, in *2008 9th Annu. Non-Volatile Mem. Technol. Symp.*, pp. 1–5, IEEE, 2008.

[199] R. A. De Souza, *Phys. Chem. Chem. Phys.* **8**, 890 (2006).

[200] R. A. De Souza, M. J. Pietrowski, U. Anselmi-Tamburini, S. Kim, Z. A. Munir, and M. Martin, *Phys. Chem. Chem. Phys.* **10**, 2067 (2008).

[201] A. Heuer, *J. Eur. Ceram. Soc.* **28**, 1495 (2008).

[202] H. Du, *Ultramicroscopy* **151**, 62 (2015).

[203] Y. Z. Chen, N. Bovet, T. Kasama, W. W. Gao, S. Yazdi, C. Ma, N. Pryds, and S. Linderoth, *Adv. Mater.* **26**, 1462 (2014).

[204] S. Yu, Y. Wu, Y. Chai, J. Provine, and H. S. P. Wong, Characterization of switching parameters and multilevel capability in HfO_x/AlO_x bi-layer RRAM devices, in *Int. Symp. VLSI Technol. Syst. Appl. Proc.*, pp. 106–107, IEEE, 2011.

[205] Y.-B. Kim, S. R. Lee, D. Lee, C. B. Lee, M. Chang, J. H. Hur, M.-J. Lee, G.-S. Park, C. J. Kim, U.-I. Chung, I.-K. Yoo, and K. Kim, Bi-layered RRAM with unlimited endurance and extremely uniform switching, in *Symp. VLSI Technol. - Dig. Tech. Pap.*, pp. 52–53, 2011.

[206] H. Zhang, N. Aslam, M. Reiners, R. Waser, and S. Hoffmann-Eifert, *Chem. Vap. Depos.* **20**, 1 (2014).

[207] Z. Wang, F. Li, S. Meng, J. Zhang, E. W. Plummer, U. Diebold, and J. Guo, *Phys. Rev. Lett.* **111**, 056101 (2013).

[208] T. Menke, *Investigation of the electroforming and resistive switching mechanisms in Fe-doped $SrTiO_3$ thin films*, Phd thesis, RWTH Aachen University, 2009.

[209] M. Yang, L. Z. Ren, Y. J. Wang, F. M. Yu, M. Meng, W. Q. Zhou, S. X. Wu, and S. W. Li, *J. Appl. Phys.* **115**, 134505 (2014).

[210] T. Bertaud, M. Sowinska, D. Walczyk, S. Thiess, A. Gloskovskii, C. Walczyk, and T. Schroeder, *Appl. Phys. Lett.* **101**, 143501 (2012).

[211] M. Kessel, R. a. De Souza, H.-I. Yoo, and M. Martin, *Appl. Phys. Lett.* **97**, 021910 (2010).

[212] M. J. Pietrowski, R. A. De Souza, M. Fartmann, R. ter Veen, and M. Martin, *Fuel Cells* **13**, 673 (2013).

[213] K. Fleck, U. Bottger, R. Waser, and S. Menzel, *IEEE Electron Device Lett.* **35**, 924 (2014).

[214] K. Fleck, U. Böttger, R. Waser, and S. Menzel, *MRS Proc.* **1790**, 7 (2015).

[215] S. Menzel, U. Böttger, M. Wimmer, and M. Salinga, *Adv. Funct. Mater.* **25**, 6306 (2015).

[216] Y. Hayakawa, A. Himeno, R. Yasuhara, W. Boullart, E. Vecchio, T. Vandeweyer, T. Witters, D. Crotti, M. Jurczak, S. Fujii, S. Ito, Y. Kawashima, Y. Ikeda, A. Kawahara, K. Kawai, Z. Wei, S. Muraoka, K. Shimakawa, T. Mikawa, and S. Yoneda, Highly reliable TaO_x ReRAM with centralized filament for 28-nm embedded application, in *2015 Symp. VLSI Circuits*, pp. T14–T15, IEEE, 2015.

Acknowledgments

This work would not have been possible without the kind help and valuable contributions of many people. I would like to extend my warmest gratitude to everyone who was involved in this work through active participation in the research project or through generally supporting me during my time in Jülich:

First of all, I would like to thank my PhD mentor Prof. Regina Dittmann for the supervision of this thesis. Her continuing support through encouragement, discussion and advice on many different topics and her understanding nature can be expressed metaphorically through her office door which was always open.

My special thanks also go to Prof. Joachim Mayer for agreeing to act as second advisor for this thesis and for the generous support of my research project by providing TEM expertise and instrument time.

I also thank Prof. Rainer Waser for the possibility to work in his institute in this exciting research area, for stimulating discussion, wonderful excursions, inspiring workshops and all his helpful ideas.

After arriving in Jülich, Dr. Annemarie Köhl and Dr. Christian Lenser introduced me to many specific theoretical and practical aspects of electron spectroscopy and spectromicroscopy, for which I am very grateful. I would also like to thank them for laying the groundwork of this thesis through their years of research in the spectro(micro)scopic characterization of $SrTiO_3$-based memristive devices.

During my entire time at the PGI 7, many colleagues were involved in the scientific and experimental details of this work while making every day life very enjoyable. I would like to thank my office mate Dr. Felix Gunkel for a lot of advice and always being available for discussions and/or coffee. I also enjoyed help from the entire PLD group: Katharina Skaja, Nicolas Raab, Dr. Chencheng Xu, Benedikt Arndt, Felix Hensling, Michael Andrä, Thorsten Meiners, Philipp Müller, Richard Valenta and Ronja Heinen. Special thanks go to Nicolas Raab, who shared my interest in resistive switching in $SrTiO_3$. Moreover, I would like to thank Dr. Paul Meuffels for insightful discussions and general support. I thank the PLD group, our soccer team "PGI Turbine Kopfstoß" and all other present and former colleagues in our institute for fruitful discussions and contributing to a nice atmosphere at the institute.

This thesis would not have been possible without the master's students who contributed to the results. Philipp Müller played a major role in the development of the sample design for *in situ* switching and performed the atmosphere and temperature dependent I-V-measurements. Richard Valenta studied resistive switching with thin Rh and graphene electrodes and characterized them using the NanoESCA. Thomas Heisig is continuing this project regarding the details of the switching mechanism. I also would like to thank Nicolas Raab, Katharina Skaja and Thomas Heisig for proofreading this thesis.

For technical support with the PLD systems and the cluster tool I want to thank Georg Pickartz. Special thanks go to Renė Borowski and Alfred Steffen for continuing advice and help in the sample fabrication. I thank Marcel Gerst for help with the electronic setups for device characterization. I am grateful to Maria Garcia and Luise Snyders for

continuing help with administrative issues. My thanks also go to Dr. Christian Rodenbücher and Prof. Krzysztof Szot for the thermal imaging.

Most of the projects performed in this thesis have been in collaboration with colleagues from different groups, without whom this work would not have been possible. Most importantly, I would like to thank all the scientists who were involved in the numerous synchrotron beamtimes, namely Christoph Schmitz, Regina Dittmann, Katharina Skaja, Nicolas Raab, Dr. Vitaliy Feyer, Giovanni Zamborlini, Dr. Slavomir Nemsak, Johanna Hackl, Imtiaz Khan, Dr. Andrea Locatelli, Dr. Onur Mendez, Dr. Alessandro Sala, Richard Valenta and Oliver Peters for sharing the day and night shifts at the synchrotrons and Prof. Claus Michael Schneider for providing excess to different PEEM instruments. Most importantly, I would like to thank Christoph Schmitz who took part in the preparation and execution of (almost) all the beamtimes. His curiosity, dedication to the experiments and desire to understand the details were essential for the experimental success.

For the TEM work in this thesis, my gratitude goes to Dr. Hongchu Du and especially Dr. David Cooper, who spent years on the development and measurement of *in situ* resistive switching in the TEM, a challenging task which was solved with a lot of determination and stamina.

For the interpretation of the experimental results, close collaboration with simulation experts was necessary and helpful. Above all, I would like to thank Dr. Stephan Menzel for continuing advice on how to understand resistive switchinge effects. His team of Astrid Marchewka, Camilla La Torre and Carsten Funck put a lot of effort into simulating and understanding $SrTiO_3$-based devices, for which I am very grateful. Astrid's models were decisive for the interpretation of the spectromicroscopic results. In the same way, I thank Dr. Roger De Souza, Amr Ramadan and Ute Lederer for

their support concerning the understanding of oxygen movement in $SrTiO_3$ and SrO as well as the influence of the surrounding atmosphere.

Finally, I would like to thank my family for their support during my studies and the PhD time. I thank all my friends for the wonderful times we had in Aachen/Jülich. Especially, I thank Laura for always being there for me and always believing in me – regardless of whatever may come.

Band / Volume 137
Surface Potential of Metallic Surfaces and Self-Assembling Organic Monolayers in Various Electrolytes
J. Wang (2016), ii, 58 pp
ISBN: 978-3-95806-188-0

Band / Volume 138
Ab initio investigation of hybrid molecular-metallic interfaces as a tool to design surface magnetic properties for molecular spintronics
R. Friedrich (2016), 277 pp
ISBN: 978-3-95806-194-1

Band / Volume 139
Topological Matter – Topological Insulators, Skyrmions and Majoranas
Lecture Notes of the 48th IFF Spring School 2017
27 March – 07 April 2017, Jülich, Germany
ed. by S. Blügel, Y. Mokrousov, T. Schäpers, Y. Ando (2017), ca 1000 pp
ISBN: 978-3-95806-202-3

Band / Volume 140
In situ studies of the growth and oxidation of complex metal oxides by pulsed laser deposition
C. Xu (2017), iv, 159 pp
ISBN: 978-3-95806-204-7

Band / Volume 141
Intrinsic and extrinsic spin-orbit torques from first principles
G. Géranton (2017), 122 pp
ISBN: 978-3-95806-213-9

Band / Volume 142
Magnetic Proximity Effects in Nanoparticle Composite Systems and Macrocrystals
G. Wilbs (2017), III, 230 pp
ISBN: 978-3-95806-233-7

Band / Volume 143
Etablierung eines Systems aus Cysteinmutanten der Phosphoglycerat-Kinase für Entfaltungsstudien mit Einzelmolekül-FRET
A. Schöne (2017), 137 pp
ISBN: 978-3-95806-237-5

Band / Volume 144
Structural and electronic characterization of hetero-organic NTCDA-CuPc adsorbate systems on Ag(111)
S. Schröder (2017), vi, 154 pp
ISBN: 978-3-95806-239-9

Schriften des Forschungszentrums Jülich
Reihe Schlüsseltechnologien / Key Technologies

Band / Volume 145
Tailoring Molecular Magnetism
T. Esat (2017), viii, 163 pp
ISBN: 978-3-95806-240-5

Band / Volume 146
Spin-wave excitations and electron-magnon scattering in elementary ferromagnets from *ab initio* many-body perturbation theory
M. C. T. D. Müller (2017), vi, 174 pp
ISBN: 978-3-95806-242-9

Band / Volume 147
Neutron Scattering
Lectures of the JCNS Laboratory Course held at Forschungszentrum Jülich and at the Heinz-Maier-Leibnitz Zentrum Garching
edited by T. Brückel, S. Förster, G. Roth, and R. Zorn (Eds.) (2017),
ca 400 pp
ISBN: 978-3-95806-243-6

Band / Volume 148
Neutron scattering
Experimental Manuals of the JCNS Laboratory Course held at Forschungszentrum Jülich and at the Heinz-Maier-Leibnitz Zentrum Garching
edited by T. Brückel, S. Förster, G. Roth, and R. Zorn (Eds.) (2017),
ca 200 pp
ISBN: 978-3-95806-244-3

Band / Volume 149
Kinetic and thermodynamic considerations on the formation of heteromolecular layers on metal surfaces
C. Henneke (2017), vii, 157, XIV pp
ISBN: 978-3-95806-245-0

Band / Volume 150
Spectroscopic characterization of local valence change processes in resistively switching complex oxides
C. Bäumer (2017), x, 206 pp
ISBN: 978-3-95806-246-7

Weitere ***Schriften des Verlags im Forschungszentrum Jülich*** unter
http://wwwzb1.fz-juelich.de/verlagextern1/index.asp

Schlüsseltechnologien /
Key Technologies
Band / Volume 150
ISBN 978-3-95806-246-7

JÜLICH
FORSCHUNGSZENTRUM